Identification and Quantification of Pu and U from Fission Product Gamma-Ray Spectra

by

David H. Beddingfield

A thesis submitted to the Faculty and the Board of Trustees of the Colorado School of Mines in partial fulfillment of the requirements for the degree of Doctor of Philosophy (Materials Science).

Golden, Colorado

Date 3-21-96

Signed: _____
David H. Beddingfield

Approved: _____
Dr. F.E. Cecil
Thesis Advisor

Golden, Colorado

Date 3/21/96

_____
Dr. J. Moore
Professor and Head
Materials Science Department

ABSTRACT

A technique has been developed to distinguish between ^{239}Pu and ^{235}U by observing fission product delayed gamma-rays produced by fissions induced by an external neutron source. If the number of induced fissions per source neutron per unit mass can be determined from Monte Carlo simulation, the material can also be quantified.

Trials were performed with yellowcake, HEU-metal, and Pu-metal samples using a TRIGA reactor and a large ^{252}Cf source as neutron sources. Fission product gamma-ray spectra were collected using a high-resolution hpGe detector over time intervals ranging from 60 s to 3000 s following the end of irradiation. By virtue of being greatly overdetermined, the identity of the Special Nuclear Material (SNM) can be unambiguously determined with a high degree of confidence in all cases by applying a set of Figure of Merit functions. Identification can be made without regard to the properties of the matrix provided a sufficient number of fissions can be induced within the sample to permit observation of the fission product gamma-rays. Once identified, the SNM can be quantified with an accuracy determined mainly by the ability to accurately model the fission response of the system using Monte Carlo simulation, within 3.8 percent in this study.

TABLE OF CONTENTS

LIST OF FIGURES

LIST OF TABLES

LIST OF ACRONYMS

ADC - Analog to Digital Converter

ANDA - Active Nondestructive Assay

AWCC - Active Well Coincidence Counter

BNL - Brookhaven National Laboratory

FOM - Figure Of Merit

HEU - Highly Enriched Uranium

IAEA - International Atomic Energy Agency

LANL - Los Alamos National Laboratory

MCA - Multichannel Analyzer

MCNP - Monte Carlo N-Particle

MECAS - Multi-Energy Californium Assay System

PNDA - Passive Nondestructive Assay

SGS - Segmented Gamma Scanner

SNM - Special Nuclear Material

TGS - Tomographic Gamma Scanner

XRF - X-ray Fluorescence

ACKNOWLEDGEMENTS

I wish to express my gratitude to my committee members, Dr. F.E. Cecil for is years of guidance and Drs. Morse, Anderson, Olsen, Munoz and Menlove for their useful suggestions. My thanks to Los Alamos National Laboratory/DOE for funding this research.

I would like to acknowledge the assistance provided by Mr. T. Debey (USGS) for providing access to the TRIGA reactor facility at the Denver Federal Center. I would like to thank Dr. P. Rinard (LANL) for assisting in the Cf-252 trials. Thanks to Dr. J. Parker (LANL) for his assistance in acquiring the components required to perform the gamma-ray spectroscopy and for many hours of discussion of spectroscopy in general. Special thanks to Dr. H.O. Menlove (LANL) for providing special insight to the study of nondestructive assay in general. Thanks to Mr. K. Manthei for acting as a soundboard throughout the entire project and asking all of the hard questions.

Chapter 1

INTRODUCTION

1.1 Purpose

The objective of this work is to examine the feasibility of identifying and quantifying fissile materials by observing delayed gamma-ray emissions from fission products. The fissions are induced by a well defined neutron source. This study focuses upon distinguishing ^{235}U and ^{239}Pu.

Work of this type is of increasing importance in the modern world. Applications of this and similar technologies exist in nuclear nonproliferation & safeguards, waste characterization and environmental cleanup arenas. The method investigated in the present work is of greatest utility in characterization work. With the necessary clean up of cold-war nuclear facilities world-wide and the very real possibility of nuclear weapons proliferation from the former Soviet Union stockpiles the need to further technological development in the nuclear materials safeguards and characterization areas is heightened.

Interest in fission products extends to the discovery of the fission process itself (P38, M39). A great deal of work has been devoted to the understanding of fission products. Much of this work has intended to aide the interpretation of the physics of the fission process itself and the understanding of nuclear reactor physics. The data collected in this effort has provided a wealth of information useful in nuclear materials safeguards

work. Knowledge of fission product mass distributions and subsequently, isotopic distributions has increased dramatically in recent times (E94).

Despite the existence of a large number of compilations (A65, C77, J79, K92, M88, S93), the use of fission product gamma ray emissions in nuclear safeguards has been relatively limited to date. These efforts have been confined to gross gamma-ray counting techniques and to burnup measurements using the long lived Cm-144 gamma-rays (P95) and Cs-134, Cs-137 and Eu-154 (R91). With the recent completion of the ENDF/B-VI isotopic fission yield sets (E94), sufficient data are now available to exploit delayed fission-product gamma-ray signatures in the differentiation between various fissionable materials.

The majority of the differences between the delayed gamma-ray spectra from ^{235}U and ^{239}Pu fission products occur in the low energy ($E < 500$ keV) gamma emissions. There is little practical use for these gamma-rays in the assay of special nuclear materials (SNM's) due to gamma-ray attenuation in sample matrices and containers. If one has a sample which permits the detection of low energy gamma rays, the large number of gamma-rays emitted from ^{239}Pu at 413 keV and below can be used to distinguish plutonium from uranium and passive neutron counting techniques can be used to quantify the plutonium. However, ^{235}U emits very few gamma rays and a purely passive technique is of little use in this case. Inducing fission may be the only means of identifying and quantifying the ^{235}U present in a sample, particularly if the sample contains both uranium and plutonium.

The differences between ^{235}U and ^{239}Pu fission product gamma ray spectra which exist in the high energy ($E \geq 1$ MeV) portion of the decay spectra are of potential utility in the determination of the identity and quantity of fissionable materials in a variety of samples. These gamma rays are less subject to matrix attenuation than the lower energy components of the spectrum and thus can potentially be used in the assay of bulk and containerized materials.

1.2 Review of Nondestructive Assay Techniques

Nondestructive assay techniques fall into two basic categories: Passive and Active. Passive nondestructive assay (PNDA) techniques measure the naturally occurring radioactive emissions from radioactive materials to identify and quantify the nuclear material contained in a sample. PNDA methods include gamma-ray detection, neutron detection and calorimetry. Active nondestructive assay (ANDA) techniques use radiation sources (gamma-ray, neutron) to stimulate nuclear radiations that can be used to quantify the nuclear material in a sample. PNDA is well suited for the assay of materials with appreciable natural radioactive decays and are generally applied to plutonium compounds (metal, oxide, fluoride, scrap/waste, etc). ANDA methods are suited for the assay of fissile and fertile materials which emit either very few or undetectable natural radiations (e.g. α-decay which cannot escape the sample matrix). Uranium compounds

(HEU metal, oxide, fluoride, LEU, MOX fuels, etc) are typically assayed by ANDA systems.

1.2.1 PNDA Methods

PNDA using Gamma-Ray Detection

Passive gamma-ray methods are used in the determination of ^{235}U enrichment and of Pu isotopics. In both of these cases the gamma-rays of interest are of low energy ($E \leq$ 1 MeV) and thus require physically small sample sizes or gas-phase samples (e.g. $UF_{6(g)}$). Gamma-ray attenuation within the sample matrix is an overwhelming difficulty in passive gamma-ray assay techniques and severely limits their applicability.

The segmented gamma-ray scanner (SGS) system attempts to address the problem of matrix attenuation by using a transmission source of appropriate energy to determine a bulk attenuation coefficient for a sample matrix (M77). This system and the tomographic gamma scanner (TGS) can be used to assay containerized ^{239}Pu and ^{235}U with much greater reliability than a purely passive assay system. The TGS concept allows the accommodation of heterogeneity in the sample matrix (P93). In the cases of isotopes with well known gamma-decay branching ratios, an observed deviation from reported branching ratios can also be utilized to determine an overall attenuation coefficient for the sample matrix.

Gamma-ray measurements are also used in irradiated fuel measurements (R91). This technique can be argued to be active, but is included as a passive method here because the irradiation is incidental to the usage of the fuel and is not a part of the actual assay. Such measurements are related to the technique used in the present work and warrant examination. Gross gamma-ray counting is used to verify operator-declared values for cooling time and burnup and is not of particular interest in the present case. High-resolution gamma-ray spectroscopy is also used in irradiated fuel measurements (R79, R81). The fuel is cooled for approximately two years prior to counting. Thus only abundant and long-lived fission products can be utilized in this type of analysis. These isotopes include ^{106}Ru ($t_{1/2}$ = 366.4 d), ^{137}Cs ($t_{1/2}$ = 30.17 y) and ^{144}Ce ($t_{1/2}$ = 284.5 d). In this method a long collimator tube is used to port the gamma-rays from the top of a fuel assembly to the surface of a storage pit and to a Ge detector. This method is similar to the technique used in this work, but operates in a much later time domain with respect to the cessation of the fission process.

PNDA using Neutron Detection

Passive neutron counting is used in a variety of modes. These are totals-, coincidence- and multiplicity-counting. Totals counting is the simplest mode and involves the scaler counting of neutrons emitted from a sample. Coincidence and multiplicity counting exploit the fact that multiple neutrons are emitted from spontaneous

fission and that they are temporally correlated. When a fission occurs in a sample multiple neutrons are born at the same time and those neutrons which arrive at the detector within a predetermined time window are assumed to have originated from the same fission event. This time correlation methodology provides another observable quantity in the assay. Multiplicity counting looks at higher moments of the fission process to provide an additional observable quantity in the assay. Totals neutron counting is used to assay plutonium metal, UF_6, make holdup measurements and to assay 55-gallon drums. Coincidence neutron counting is well suited for assaying containerized plutonium scrap and bulk plutonium. Multiplicity counting is useful in situations when (α,n) reactions occur (oxides, fluorides) and allow the assay to sort fission neutrons from (α,n) neutrons. Passive neutron counting is broadly applied in verification measurements where the sample is generally well defined (R91).

1.2.2 ANDA Methods

ANDA methods use a wide variety of sources to excite radioactive emissions in sample matrices. These include isotopic gamma sources, isotopic neutron sources, accelerators, and nuclear reactors. As such, ANDA is arguably a more flexible methodology and can be tailored to the specific application.

ANDA using Gamma-ray Sources

ANDA methods using gamma-ray sources include densitometry and X-ray fluorescence (XRF) and are generally used to compliment other assay techniques. These methods are plagued by matrix attenuation difficulties when the observed radiations are gamma- or x-rays. One can use gamma sources to produce reactions such as (γ,n) and (γ,f) and observe the escaping neutrons, but these techniques are generally hampered by the necessary gamma-ray background interfering with the neutron counting. As previously mentioned, a related application of gamma-ray sources is their usage as transmission sources to characterize sample matrices (P93).

ANDA using Neutron Sources

ANDA methods using neutron sources can be categorized by the type of emission which is observed. One can measure prompt-neutron or prompt-gamma emission from fissions in the sample, delayed neutron production from fission products, delayed gamma-ray production as in the present work and also characterize the sample matrix by source neutron transmission. Techniques which fall into the prompt neutron category include the active well coincidence counter (AWCC) and the random driver system for the assay of HEU and Pu metal and oxides (M79), the active neutron coincidence collar for measuring HEU fuel assemblies (M81) and the MECAS system which induces fissions in a sample matrix and counts gross gamma-ray emission from the fission products (M75). The ^{252}Cf shuffler system measures delayed fission neutrons from

containerized fissile U and Pu samples (R92).

1.3 Conclusion

There are a large number of existing assay technologies, each exploiting specific attributes characteristic of a given assay situation. The common attribute in each of the techniques which have been described is that the identity of the SNM is known and the sample is generally well defined prior to the assay. The present technique is useful in situations where the identity of the SNM is unknown or needs to be verified.

Chapter 2

GENERAL CONCEPTS

2.1 Fission Yields

Data on fission product yield distributions has been collected for many years. The most well known compilations are those of Rider (R87) and Crouch (C77). Since his retirement, Rider's work has been taken over by T.R. England. Rider and England have compiled the ENDF/B-VI data sets that are used in this work. These data sets include the thermal, epithermal and fast neutron fission yields for fissioning materials. The data contained in the ENDF/B-VI compilation provides the cumulative and independent yields of approximately 1200 nuclides resulting from neutron induced and spontaneous fission of the 36 fissioning nuclides. The ENDF/B-VI compilations include all measured data through early 1992 and represent the most complete compilations to date (E93). The values reported in the ENDF/B-VI files arise from theoretical calculations merged and correlated with measured values when possible and are expected to conform with experimental observation. The data files are available on-line from the National Nuclear Data Center at BNL (bnlnd2.dne.bnl.gov) and from the IAEA.

There are a variety of types of fission product yields which are reported in the literature. These include the independent yield, the cumulative yield, the total chain yield and the mass yield. The independent yield is defined as the distribution of fission

products produced directly from the fission process before the emission of delayed neutrons. The cumulative yield is defined as the distribution of fission products after all of the delayed neutrons have been emitted prior to any β-decay. The total chain yield is defined as the sum of the cumulative yields of the stable end products of a given mass chain. The mass yield is defined as the sum of the independent yields of a given mass chain. Table 2.1 illustrates the various yields for the A=92 mass chain. The chain yield is not a simple sum of the cumulative yields, but accounts for the decay of Br-92, Kr-92 and Rb-92 by either neutron emission or β^- decay. In this work, the cumulative yield and occasionally the independent yield are of interest.

Table 2.1. ^{235}U fission yields for the A=92 mass chain

Isotope	Independent Yield (/fission)	Cumulative Yield (/fission)
As-92	3.5476×10^{-12}	3.5476×10^{-12}
Se-92	4.1697×10^{-7}	4.1697×10^{-7}
Br-92	2.6771×10^{-4}	2.6813×10^{-4}
Kr-92	1.6581×10^{-2}	1.6742×10^{-2}
Rb-92	3.1317×10^{-2}	4.8152×10^{-2}
Sr-92	1.0752×10^{-2}	5.9379×10^{-2}
Y-92	7.1483×10^{-4}	6.0093×10^{-2}
Zr-92	1.1898×10^{-4}	6.0213×10^{-2}
Nb-92	2.2698×10^{-13}	2.2698×10^{-13}
Mass Yield (/fission):	5.9752×10^{-2}	
Chain Yield (/fission):		2.4479×10^{-1}

Figure 2.1 shows the cumulative thermal fission product yields as a function of the product mass number (A) for ^{235}U and ^{239}Pu derived from the ENDF/B-VI data compilation. The differences in the low-mass group between the ^{235}U and ^{239}Pu are significant. Of particular interest in the differentiation of ^{239}Pu and ^{235}U are the gamma rays resulting from the decay of the light-mass group components (A=80 through A=115). It is significantly more probable that the low mass portion of this group (A=80 through 95) will be produced in ^{235}U fission than in ^{239}Pu fission. The higher mass

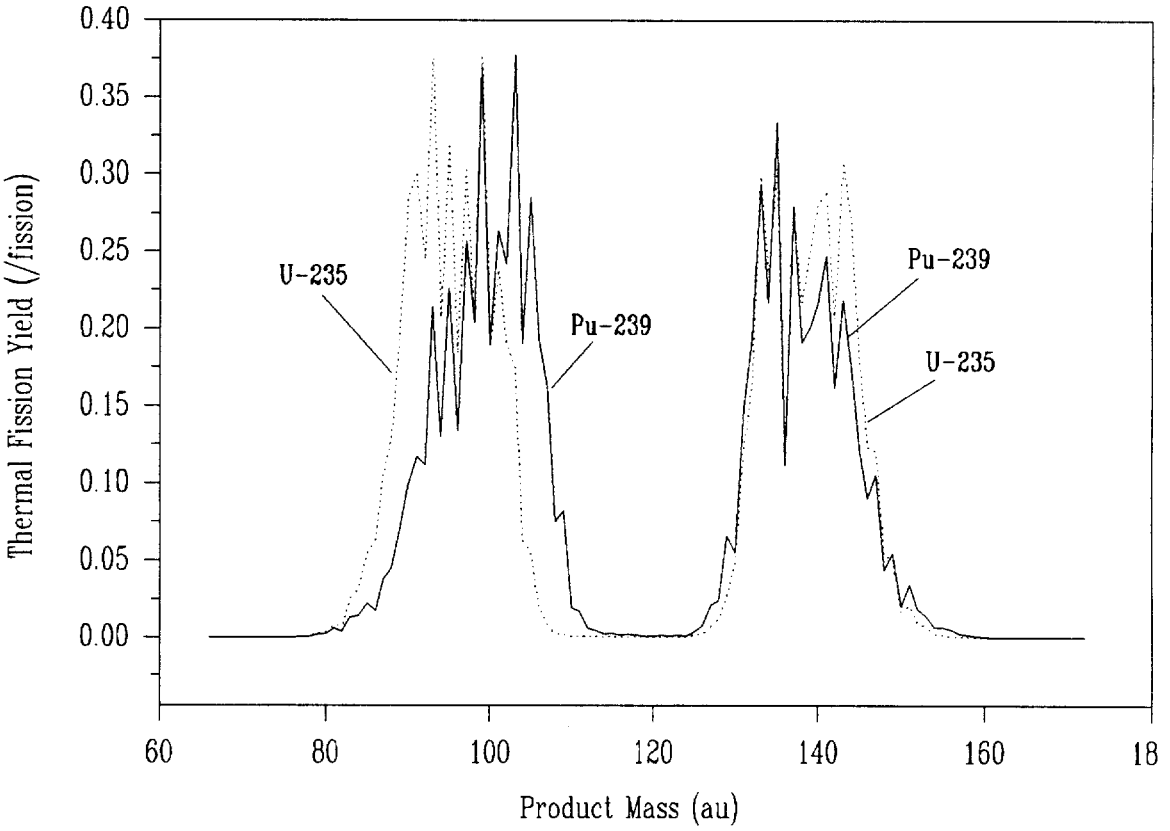

Figure 2.1. Cumulative thermal fission product yield for ^{235}U and ^{239}Pu.

contributions to the light-mass group (A=96 through 115) are favored in ^{239}Pu fission. Gamma-ray signatures from these mass groups which are unique to the SNM may be found in the fission product decay spectrum. Also, the ratio of the intensities of gamma rays from these two groups may also be used to differentiate plutonium and uranium.

Within each isobar (decay chain of isotopes with the same mass), the fission product yields exhibit a generally hyperbolic distribution about the stable member(s) of that isobar. Figure 2.2 shows the cumulative fission product distribution within the A=91

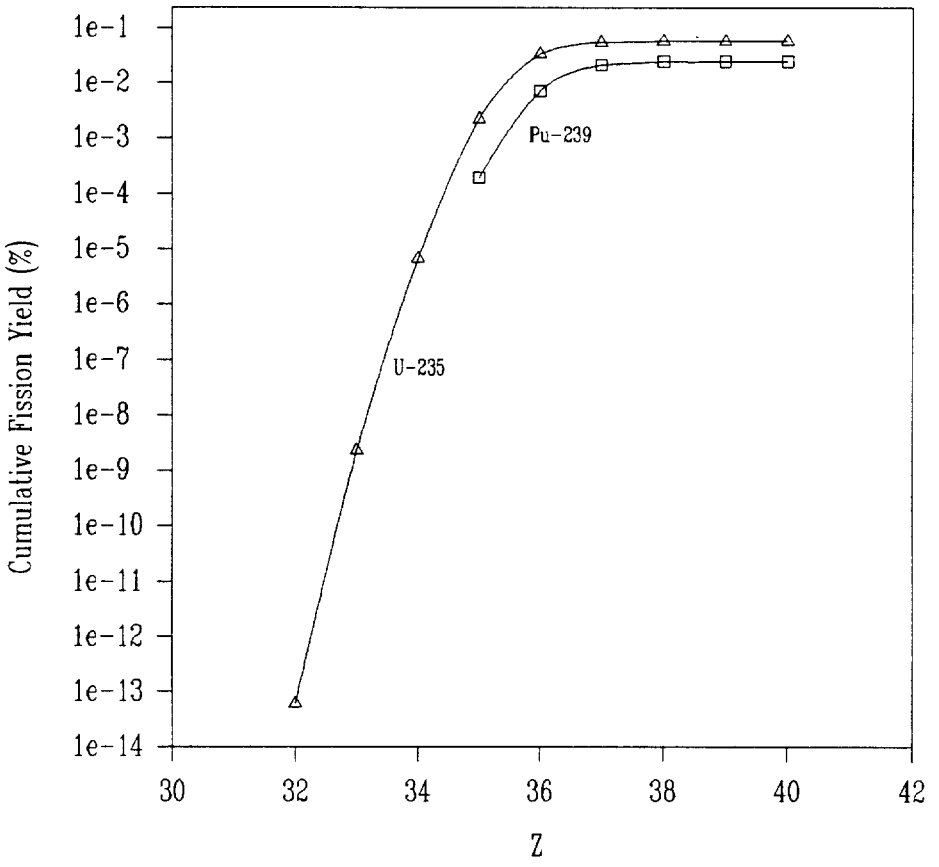

Figure 2.2. Distribution of cumulative fission product yields within the A=91 isobar

isobar. The trend of the yield steeply dropping off a few members up the decay chain is repeated for every isobar.

2.2 Effect of Neutron Energy on Fission Yields

In the case of thermal fission, the bimodal mass distribution shown in Figure 2.1 is produced. As the fission-inducing neutron energy increases, the bimodal distribution shifts to favor symmetric fission. Figures 2.3 and 2.4 show the cumulative fission yields for U-235 and Pu-239 resulting from thermal, epithermal and high energy neutrons. If necessary, one could use gamma-rays emitted from mass A=110 through A=122 isotopes to determine the average fission energy to adjust the isotopic yields accordingly. Such a correction might be necessary if a neutron generator were used as the neutron source. In some situations the use of a Cf-252 source may result in the a shift in the fission energy but the required correction would be within the measurement error. Monte Carlo modeling has shown that ~80 percent of fissions from a Cf-252 source in contact with a sample will be from thermal neutrons and the balance from epithermal neutrons. The difference in the yields from thermal to epithermal fission are insignificant in the regions of interest. If necessary, it is sufficient to merely check for notable 'trough' gamma rays to insure that the fissions were from thermal neutrons or to determine the mean fission energy and adjust the expected yield values accordingly.

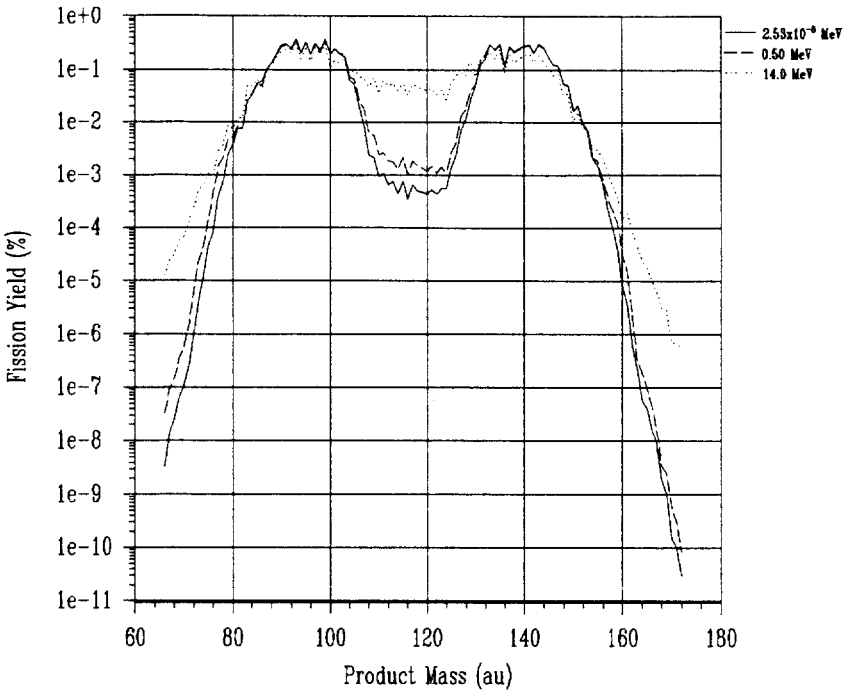

Figure 2.3. U-235 cumulative fission yield at various energies

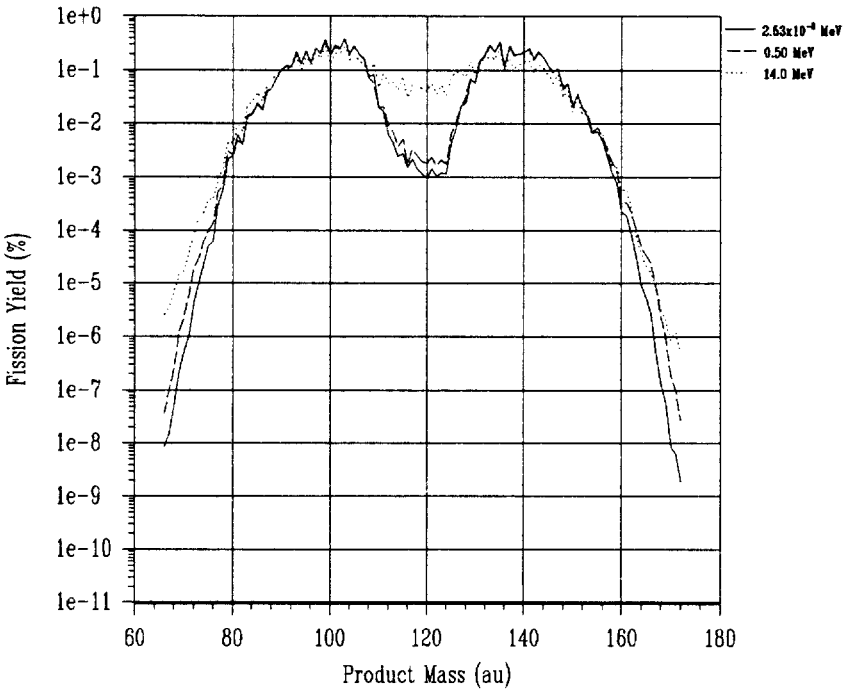

Figure 2.4. Pu-239 cumulative fission yield at various energies

While the fission yields in the mass chains of interest are not particularly sensitive to the fission energy unless an unmoderated neutron generator (high energy) source in employed, the fission energy is still important from the standpoint of quantification. Because the fission reaction cross section goes as $\sim 1/E_n$, the prediction of the number of fissions per source neutron is strongly dependent upon knowing the energy of the fission inducing neutrons. Using a thermal neutron source eliminates this potential difficulty and also eliminates the need to account for neutron moderation within the matrix when attempting to quantify the number of induced fission.

2.3 Delayed Neutrons

Less than one percent of fission neutron are delayed, but these neutrons play a central roll in the steady state operation of a nuclear reactor. Delayed neutrons are traditionally categorized in six half-life groups. Each of these groups contains specific isotopes that are termed delayed-neutron precursors. In the present work, attempts were made to minimize the cooling time of the samples and as such the observed yields are expected to be in between the independent and the cumulative yields. Table 2.2 presents some of the 271 known delayed-neutron precursors, their half-lives and their group assignments. All of the members of groups 1 and 2 are presented, only representative members of the other groups are provided.

Table 2.2. Delayed-neutron precursor groups

Precursor	Half-life (sec)	Group Assignment
^{87}Br ^{91}Rb	55.7 58.2	Group 1
^{88}Br ^{134}Sb ^{136}Te ^{137}I ^{141}Cs ^{146}La	16.0 10.2 19.0 24.5 24.8 11.1	Group 2
^{89}Br ^{92}Rb ^{93}Rb ^{94}Rb ^{97}Y ^{104}Nb ^{138}I Others	4.37 4.54 5.85 2.73 3.7 4.8 6.33	Group 3
I^{139} Br^{90} Br^{92} Kr^{93} Others	2.3 1.96 0.365 1.29	Group 4
I^{140} Others	0.86	Group 5
Br, Rb, As, Others	0.2	Group 6

Typical cool-down times in the experiments performed in this study ranged from thirty seconds to one minute, it is evident from Table 2.2 that not all of the delayed-neutrons in the samples had been emitted prior to counting. The data expected from these experiments will thus lie between the observed independent yield and the

cumulative yield. Groups 3-6 can be assumed to have fully decayed before the start of counting, but the same assumption cannot be made of groups 1 and 2. As a result, caution must be exhibited when analyzing the yields in mass chains 86, 87, 88, 90, 133, 135,136, 137, 140 and 145 from short cooling time data. The remaining mass chains can be considered to have attained their assigned cumulative yield values.

2.4 Fission Product Half-Lives

Fission products have half-lives ranging from a few microseconds to many years. The distribution of fission product half-lives is an important consideration when designing the timing aspects of gamma-ray measurements. Figure 2.5 shows the distribution of half-lives of radioactive fission products. From the trend, it is reasonable to expect to observe some of the longer-lived members of the 10-100 second group, members of the 100-1000 second group and short-lived members of the 1000 to 10,000 second group. Products with shorter half-lives are difficult to observe and impossible to reliably quantify because the half-life is close to or less than the expected irradiation period. Isotopes with half-lives greater than a few thousand seconds will have too low an activity to produce useful signal strengths.

Another useful consideration of fission product half-lives lies in an observed trend within the individual isobars. The half-life of isotopes far from the line-of-stability is invariably less than the half-life of isotopes close to the line-of-stability. That is, the

half life decreases as one moves down a given isobar. The result is that after a sample has cooled for more than a few hours, the majority of the observed gamma-rays are emitted for isobar members adjacent the stable member of the decay chain.

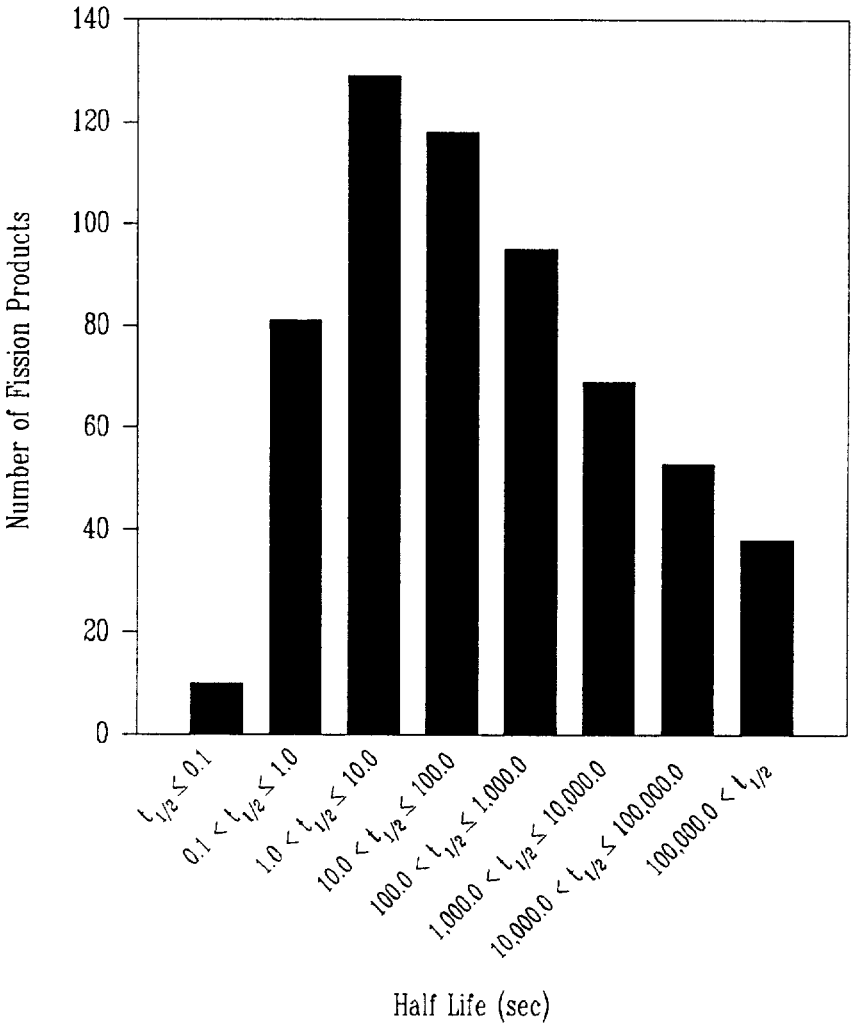

Figure 2.5. Temporal distribution of fission product half-lives

2.5 Matrix Effects

The sample which is being interrogated invariably has some effect upon both the source neutron field and the exiting gamma-rays. If these phenomena are not considered a severe systematic bias can develop.

Materials present in the sample matrix may alter the incident neutron flux and cause the number of induced fissions to differ from expected values. Low-Z materials such as hydrogen, graphite, beryllium and many plastics may shield source neutrons and bias subsequent measurements. There may also be neutron absorbing materials such as boron, cadmium or fertile nuclear materials present within the matrix which can reduce the neutron flux below anticipated values. These potential difficulties can be quite serious in the case of poorly characterized matrices in large containers (e.g.. 55-gallon drums).

A possible means of mitigating the neutron attenuation dilemma is to measure neutron transmission during the irradiation to observe irregularities or bulk variations in the transmitted neutron distribution (B92). Optimally, an uncorrelated neutron source should be employed and singles neutrons corrected for doubles neutrons (arising from induced fissions) should be observed.

Gamma-Ray attenuation is of serious consequence in all sample matrices. This results from both attenuation in the sample matrix, especially if the sample is physically large, and self-absorption in the nuclear material which is the object of the assay.

A straight-forward solution to the gamma-ray attenuation problem for containerized matrices is to use collimated gamma-ray transmission sources to determine an effective linear attenuation coefficient (μ_l) for the matrix within the useful energy range (700 keV to 1.5 MeV).

If a direct measurement of a value of μ_l for a matrix cannot be made, as in the case of an in-situ soil assay, and a representative calibration standard cannot be prepared, the known branching ratio of the observed gamma-ray peaks can be exploited to determine relative μ_l values. The methodology is prone to the production of a systematic bias in quantified results. This bias would not represent a difficulty in determining the material identity, but could introduce serious errors in attempts to quantify the material.

Chapter 3.

METHODS

3.1 Approaches to Signal Differentiation

A variety of methodologies can be employed to distinguish between ^{235}U and ^{239}Pu using the signals from fission product gamma-ray emissions. The most straight forward technique is to identify peaks which are only present in the ^{235}U and/or the ^{239}Pu spectra. Other techniques exploiting the relative intensity of selected peaks in the spectra can also be exploited.

The first case of identifying peaks which are unique to a particular SNM has difficulties. Such peaks need to be of relatively high energy to minimize attenuation within the sample matrix and these peaks need to be unobscured by other decays in any of the possible SNM's. Peaks which are wholly unique to one SNM do not actually exist, however peaks which are dominated by a particular SNM can be identified. This allows the usage of a system of linear equations to determine the identity of a fissioning material. Such relations have the form:

$$I_{obs} = \alpha I_U + \beta I_{Pu}.$$

The values of α and β are known from combining the known fission yields and decay branching ratios for a well defined peak. Peaks which are potentially useful in such a

balance include ^{90}Kr at 1118.7 keV, ^{136}I and ^{136*}I at 1313.0 keV and ^{94}Sr at 1428.3 keV which are dominated by the α term and ^{82}Br at 1317.5 keV which is dominated by the β term. Other substantial differences exist at and below 600 keV, but these peaks are not useful in most applications because of matrix attenuation difficulties.

A simpler means of exploiting the fission yields differences to discriminate between SNM's when the matrix is comprised of only a single species lies in the intensity ratios of peaks from the low-mass group to invariant peaks in the high-mass group. Alternatively, intensity ratios from opposite sides of the low-mass maxima (A~100) may be exploited. Optimally, whatever ratio is used, the peaks should be of similar energy and originate from isotopes of similar half-life. The energy similarity requirement allows the omission of attenuation considerations as the peaks would be equally attenuated. The similar half-life requirement produces an intensity ratio that is invariant over time. The ratio of the relative intensity of the corresponding gamma peaks would allow the observer to readily distinguish between uranium and plutonium signals and thus identify the fissioning material if the theoretical differences are sufficient. Another important criterion in choosing suitable peaks is that the peaks remain visible and unobscured throughout the count period. Peaks which theoretically meet these rigid requirements are included in Table 3.1 although the visibility of these peaks has yet to be determined.

Any activity ratio which produces significant differences between uranium and plutonium can actually be used. These may be more difficult to utilize because

Table 3.1. Gamma-rays potentially useful for obtaining intensity ratios which determine SNM identity and meet the most rigid criteria.

^{84m}Br E=1462 keV $t_{1/2}$=360s	^{101}Mo E=1532 keV $t_{1/2}$=876s
^{85}Br E=924.6 keV $t_{1/2}$=172.2s ^{85}Br E=802.4 keV $t_{1/2}$=172.2s	^{130*}Sb E=793.4 keV $t_{1/2}$=390s ^{130*}Sb E=839.4 keV $t_{1/2}$=390s
^{86}Br E=1564.6keV $t_{1/2}$=55.7s	^{101}Mo E=1532 keV $t_{1/2}$=876s
^{87}Br E=1419.8 keV $t_{1/2}$=55.6s	^{138m}Cs E=1436.0 keV $t_{1/2}$=174.0s
^{88}Rb E=1836.0 keV $t_{1/2}$=1066.8s	^{138}Xe E=1768.3 keV $t_{1/2}$=850.2s ^{138}Xe E=2004.8 keV $t_{1/2}$=850.2s ^{138}Xe E=2015.8 keV $t_{1/2}$=850.2s
^{89}Kr E=904.3 keV $t_{1/2}$=190.8s	^{108}Rh E=901.4 keV $t_{1/2}$=360s ^{154}Pm E=921.6 keV $t_{1/2}$=102s ^{154}Pm E=1017.6 keV $t_{1/2}$=102s
^{89}Rb E=1248.1 keV $t_{1/2}$=909.0s	^{147}Pr E=1261.2 keV $t_{1/2}$=816.0s ^{138}Cs E=1283.2 keV $t_{1/2}$=571.0s
^{92}Sr E=1383.9 keV $t_{1/2}$=9,756s	^{141}La E=1354.5 keV $t_{1/2}$=14,040s ^{139}Pr E=1347.3 keV $t_{1/2}$=15,876s
^{94}Sr E=1428.3 keV $t_{1/2}$=74.1s	^{138m}Cs E=1436 keV $t_{1/2}$=174s ^{154m}Pm E=1440.3 keV $t_{1/2}$=159s
^{94}Y E=918.8 keV $t_{1/2}$=1122s	^{133m}Te E=912 keV $t_{1/2}$=3324s ^{133m}Te E=915 keV $t_{1/2}$=3324s

significant energy differences would require the use of attenuation corrected counts in the ratio. If peaks which have largely differing half-lives are chosen, the theoretical intensity ratio becomes a function of time. In any case, whatever peaks are actually chosen, the value of the ratio must be tracked over several time periods to enhance confidence of the resulting identity determination.

3.2 Quantification of Materials

To quantify the fissionable materials present in a sample the number of induced fissions must be well known and the relationship between the number of source neutrons and the number of induced fissions as a function of SNM mass must also be determined. If the sample matrix is well defined this is an attainable goal and the number of induced fissions per source neutron per unit mass of SNM can be determined by modeling the system and using Monte Carlo methods. The number of fissions can be determined from each unobscured peak in the spectrum and thus is sufficiently overdetermined that this quantity can be confidently calculated. It is not generally the case that when the SNM identity is unknown, that the matrix is sufficiently well-defined that modeling can be reliably employed. Errors resulting from uncertainty in this relation can easily dominate the resulting mass determination. Attempts have been made to address matrix effects on neutron transport within waste drums (B92). Further work in this area is needed to investigate matrix phenomena for both neutron transport and gamma-ray attenuation.

Another aspect of quantification of the SNM in a sample lies in the correlation of the observed gamma-rays to the actual number of gamma-ray emissions to obtain the corrected counts. In a situation where quantification is not obscured by matrix ambiguity one can use the observed gamma ray peaks to determine the number of decays of a given species within the observation period. One can then use the chain-decay relations derived in Appendix A to iterate the number of fissions induced in the sample and

subsequently determine the mass of SNM present in the sample. This approach allows the systematic and material-dependent aspects of the calculations to be separated and can allow results to be refined in the material iteration independently from the systematic parameters of the actual measurement.

3.2.1 Correction of Observed Gamma-Ray Counts

The first step in reducing the observed data from an assay of this type is the correction of the observed gamma decays in each peak of interest to obtain the actual number of decays represented by the observed value. The correction requires no supposition regarding the identity of the isotope emitting the gamma-rays. The various correction terms are those stemming from the experiment itself and include all of the systematic aspects of the measurement. If one ignores the matrix attenuation considerations discussed earlier, the systematic correction required in a typical experiment is given in equation 3.1.

$$n_{\gamma} = \frac{n_{\gamma\,obs}\ \left(\frac{t_r}{t_l}\right)}{\Omega_{det}\ \epsilon(E_{\gamma})\ e^{-\mu_{Pb}(E_{\gamma})\ t_{Pb}}} \qquad \textbf{(3.1)}$$

Where: n_{γ} = the corrected number of gamma decays of the isotope during the count period [decays],

$n_{\gamma\ obs}$ = the background corrected area of the identified peak observed during the count period [decays],
t_r = real time elapsed during the count period [s],
t_l = the detector live time during the count period [s],
Ω_{det} = the solid angle subtended by the detector [spheres],
$\epsilon(E_\gamma)$ = the detector absolute counting efficiency at E_γ [],
$\mu_{Pb}(E_\gamma)$ = the gamma ray attenuation coefficient in lead at E_γ [cm^{-1}],
t_{Pb} = thickness of lead filter [cm]. (placed in front of the detector head)

The attenuation correction term in the denominator is added to accommodate the typical use of a thin lead filter placed over the detector face to reduce dead-time difficulties associated with the abundant low energy gamma-rays which are not of interest. Other terms which are typically included in correction equations which are omitted from equation 3.1 are matrix attenuation corrections and a correction term for the attenuation of the container itself. The matrix attenuation term will be presented later. The correction for attenuation in the container is functionally identical to the lead filter correction term, except the value of μ corresponds to the container material and the known container thickness is used.

3.2.2 Theoretical Gamma-Ray Decay Trends

Once a particular peak has been associated with a specific isotope, a reliable means of assuring the identity is to track the theoretical decays of that isotope over the various time windows through which the data were collected. A specific isotope which is observed generally does not decay in a simple logarithmic fashion. The fission products

are distributed along a given isobar and as a result the decay of an observed peak is a member of a multi-level serial decay chain.

The value of n_γ can also be represented as,

$$n_\gamma = \nu_\gamma^{-1} \int_{t_1}^{t_2} \left(\frac{dN}{dt}\right)_{\beta^-} dt \qquad \textbf{(3.2)}$$

where: N = the number of atoms present at time t [atoms],
ν_γ = the fraction of decays of the supposed isotope which produce the observed gamma ray [] (the branching ratio),
t_1 = the time at the start of the count period [s],
t_2 = the time at the end off the count period [s].

The β^--subscript on the dN/dt term in the integral is added as a reminder that contributions to the time-change in the number of atoms of the isotope other than beta-decay are not to be included here. The value of N(t) is a material balance of production and decay terms, this is reflected in dN/dt. In equation 3.2, $(dN/dt)_{\beta^-}$ represents only the β-decay portion of the balance and not the production terms. The values for the times (t_1 and t_2) are chosen using a time datum at the end of the sample irradiation. The value of N(t) is given in Appendix A. By virtue of the choice of temporal datums, the serial decay equations can be used to iterate a value of the number of fissions associated with the corrected observed counts for a particular isotope. Appendix A contains the derivation of the equations of serial decay with excited states for a five-member decay chain. While these equations still represent an approximation in many cases, they are a substantial

improvement over a one- or two-member decay correction.

In order to minimize the possibility of misidentifying a given peak it is useful to perform a trend analysis upon a given peak as it appears in the various observed spectra over time. If the peak is incorrectly associated with a specific isotope, the calculated trend will not parallel observation over time. If the theoretical and observed trends agree, one can be reasonably assured that the peak has been properly identified. Further, multiple determinations along the temporal decay trend allows for the identification of individual data points which greatly deviate from the trend. Once identified, these outlier data points can be omitted from subsequent analysis to minimize error propagation.

3.2.3 MCNP Modeling to Determine the Number of Induced Fissions

The Monte Carlo neutron transport code, MCNP (B93), provides a convenient means for determining the number of induced fissions in a sample. Even the simplest matrix is sufficiently complex that the number of induced fissions cannot be directly calculated as a function of the number of source neutrons and mass of SNM without oversimplifying assumptions which may introduce large errors. In contrast, the Monte Carlo method can converge upon the correct results without making any significant assumptions.

The MCNP package itself facilitates performing Monte Carlo calculations on complex systems. Any conceivable geometry and material composition can be easily

modeled using the descriptive spatial geometry language that is incorporated into the package. MCNP also allows a wide variety of result tallies to be generated, in this case fissions per source neutron per g-SNM. The result can be binned into energy groups based upon incident neutron energy to allow precise determination of the expected fission product distribution. Yet another attribute of the MCNP package is the performance of statistical checking of result tallies to insure that the problem has converged to a stable result. Of course, the validity of the result is determined by the accuracy of the model and the `fairness of the game` (B93).

Chapter 4

EXPERIMENTAL

4.1 Experimental Trials

Five series of experimental trials were performed in this study. The first series of experiments were performed using a TRIGA reactor (USGS facility at the Denver Federal Center) as a neutron source and yellowcake powder (U_3O_8, unenriched) as the sample material. The remaining series were performed using a large Cf-252 neutron source in a specially designed irradiation apparatus using HEU- and Pu-metal disks as the samples.

4.1.1 TRIGA Reactor and Yellowcake Trials

Two trials involving the placement of a small sample of yellowcake into a large thermal neutron flux for short irradiation times and monitoring the resulting fission product spectra were performed at the Denver Federal Center TRIGA Reactor facility. These trials were preliminary in nature and were intended to determine the number of fissions required to produce sufficient signal strength to provide useful fission product spectra, appropriate count periods, source-to-detector distances and to provide a general

familiarity with the nature of fission product spectra.

The nuclear reactor employed in these trials is a 1.0MW TRIGA facility operated by the USGS located on the Denver Federal Center Site. Small samples (0.5250g & 0.0526g) of yellowcake (U_3O_8) were placed in a $7.5x10^{11}$ n/cm^2 s thermal neutron flux for ten second irradiations. The samples were then delivered to a sample counting area via the reactor pneumatic rabbit tube system. The gamma-ray activity of each sample was then monitored using a hpGe (high purity Germanium) detector attached to the EG&G Nomad electronics package using Maestro (EGGware) for windows as the MCA software.

Tables 4.1 and 4.2 list the count periods used while obtaining spectra for the 0.5250 gram and 0.0526 gram yellowcake samples.

Table 4.1. Count times for DFC yellowcake sample 1 (0.5250 g)

Real Time (sec)	Live Time (sec)	Cool Time (sec)
224	51	60
330	164	284
600	482	1751
1000	856	2413
1508	1360	3414
1500	1221	4922
413	341	7150

Table 4.2. Count times for DFC yellowcake sample 2 (0.0526 g)

Real Time (sec)	Live Time (sec)	Cool Time (sec)
200	167	35
600	576	269
1500	1418	928
8657	8502	2493

4.1.2 Cf-252 and HEU- & Pu-metal Trials

Four series of trials using enriched U-235 metal and Pu metal were performed at LANL (NIS-5 hotcell facility). In these trials, a large Cf-252 source (4.05×10^8 n/s) was used. The apparatus used as the irradiation chamber was optimized to make best use of the nominal source term. The HEU sample was a bare uranium (93.15% U-235, 6.85% U-238) thin metal disk (2.00 in. diameter, 0.022 in. thick) weighing 20.797 grams. The Pu sample was a copper clad (98.87% Pu-239, 0.058% Pu-240, 0.00335% Pu-241, 0.000179% Pu-242, 1.00% Ga) thin metal disk (2.00 in. diameter, 0.020 in. thick surrounded by 0.020 in. cladding) weighing 16.09 g-Pu. The samples were individually placed into the irradiation chamber and the Cf-252 source was shuttled into a position adjacent to the sample for 100 second irradiations. The samples were then moved to a counting apparatus. The gamma-ray activity of each sample was then monitored using a PGT hpGe detector, Canberra Spectral Amplifier and ADC, and Canberra S-100 for windows as the MCA software. Tables 4.3 through 4.6 list the count periods used in the

various LANL trials.

Table 4.3. Count times for LANL HEU sample, experiment 1.

Real Time (sec)	Live Time (sec)	Cool Time (sec)
100	33	563
100	37	663
100	50	763
100	66	863
100	67	963
500	354	1063
500	376	1563
500	394	2063
1000	829	2563

Table 4.4. Count times for LANL HEU sample, experiment 2.

Real Time (sec)	Live Time (sec)	Cool Time (sec)
25	7	45
25	9	70
25	11	95
25	13	120
50	30	145
50	33	195
50	35	245
50	37	295
50	38	345
50	39	395
50	40	445
50	41	495

Table 4.5. Count times for LANL Pu sample, experiment 1.

Real Time (sec)	Live Time (sec)	Cool Time (sec)
100	35	600
100	43	700
100	51	800
100	66	900
100	66	1000
500	333	1100
500	336	1600
500	340	2100
1441	1000	2600

Table 4.6. Count times for LANL Pu sample, experiment 2.

Real Time (sec)	Live Time (sec)	Cool Time (sec)
25	10	49
25	12	74
25	14	99
25	15	124
50	33	149
50	35	199
50	36	249
50	37	299
50	38	349
50	38	399
50	39	449
50	39	499

The irradiation apparatus used in the LANL trials consisted of a optimized moderating polyethylene block which housed the Cf-252 source and the sample. Drawings of the apparatus are shown in Appendix B. In the optimization of the apparatus, MCNP was used to determine the most efficient source-to-target coupling and to mitigate leakage of neutrons from the system. The source-to-target coupling was optimized by modeling a ^{252}Cf source centered within a monolithic polyethylene block with a target disk of fissionable metal. The source-to-target distance was varied and the optimum target placement with respect to the source was determined by maximizing the number of fissions per source neutron in pure ^{239}Pu and ^{235}U metal . These optimization trials indicated that the neutron source is in contact with the target material at the maximum of the number of induced fissions per source neutron. The next series of optimization trials involved reducing the size of the polyethylene moderator to determine the nominal dimensions of the apparatus. Beginning from the monolithic case, the polyethylene dimensions were individually reduced until the number of induced fissions began to fall due to leakage. It was determined that the nominal poly thickness between the sample and an edge was 18.52 cm, Dimensions of 25.4x25.4x21.0 cm were used in the actual construction of the apparatus. With the as-built dimensions, the system was modeled again using the isotopics of the actual target disks. In the ^{239}Pu sample the fission rate was determined by Monte Carlo simulation to be 0.033215 fissions per source neutron; hence, 1.345×10^{7} fissions per second. In the ^{235}U sample the fission rate was determined by Monte Carlo simulation to be, 0.037455 fissions per source neutron, thus,

1.517×10^7 fissions per second.

4.2 Analysis of Gamma-Ray Spectra

The data from the LANL trials was analyzed and reduced as per the discussion in Chapter 3. Peaks which existed in multiple time windows were corrected using equation 3.1. The peaks were then tentatively identified and compared to the theoretical trends. Once the peak identity was confirmed the intensity ratios were formed to determine the identity of the SNM, then the number of induced fissions was determined and subsequently the mass of the SNM was calculated

4.2.1 Identification of Peaks

The peaks were identified from those peaks located by performing a peak search in the MCA package. The identification process was aided by using a large database written specifically for this task. The database contains all gamma-rays within 20 percent relative intensity of the maxima for all fission products listed in the ENDF/B-VI compilation for which decay data is available. Figures 4.1 through 4.4 show representative spectra in the energy range of interest for each of the LANL trials. Tables 4.7 through 4.10 list the identities of the numbered peaks in the associated spectra.

Complete spectra are shown in Appendix C on a larger scale.

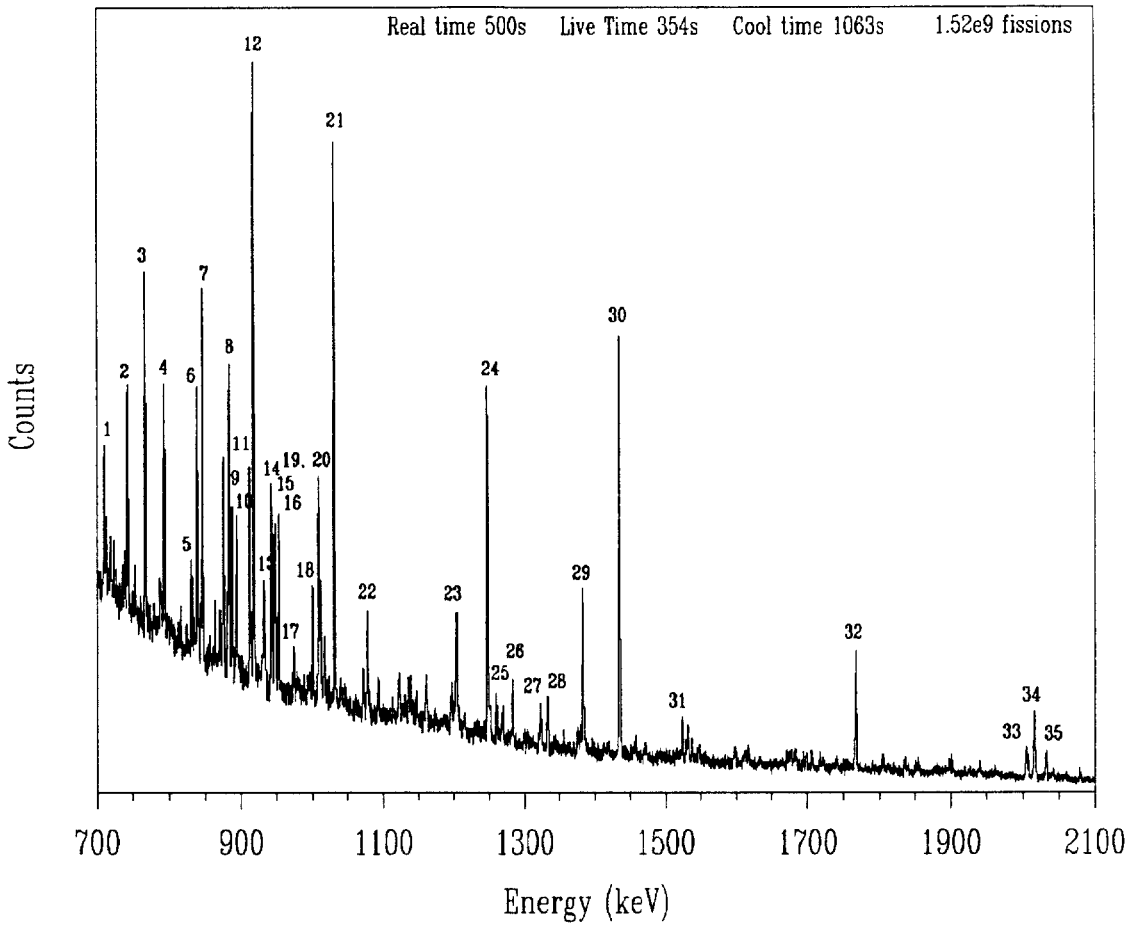

Figure 4.1. Fission product spectrum from HEU experiment 1.

Table 4.7. Identities of labeled peaks from Figure 4.1.

Peak Number	Parent Isotope	Peak Energy (keV)	Half-Life (s)
1	Ce-145	725.0	180
2	Mo-99/ Sn-130	739.4/743.1	23,7672/221.4
3	Te-134	767.2	2508
4	Sb-130*	793.4	390
5	Sn-127	823.1	7776
6	Rb-90/Rb-90m	831.7	153/258
7	Sb-130/ Sb-130*	839.4	2454/390
8	Sr-93	875.9	26748
9	I-134	884.1	3150
10	Sr-93	888.3	26,748
11	Te-133m	912.7	3324
12	Y-94	918.8	1122
13	Sb-131	933.1	1382
14	Sb-131	943.4	1382
15	Ba-142	948.8	639
16	Y-95	954.2	618
17	Sb-132/Sb-132*	973.9	252/168
18	Ba-142	1000.9	639
19	Cs-138	1009.8	1932
20	Mo-101	1012.5	876
21	Rb-89	1031.9	909
22	Ba-142	1078.5	639
23	Ba-142	1204.1	639
24	Rb-89	1248.1	909
25	I-135	1260.4	23,796
26	Cs-139	1283.2	572
27	I-136/I-136*	1313.0	83.4/44.8
28	I-136	1321.1	83.4
29	Sr-92	1383.9	9756
30	Sr-94	1428.3	74.1
31	Mo-101	1532.3	876
32	Xe-138	1768.3	850
33	Xe-138	2004.8	850
34	Xe-138	2015.82	850
35	Mo-101	2032.0	876

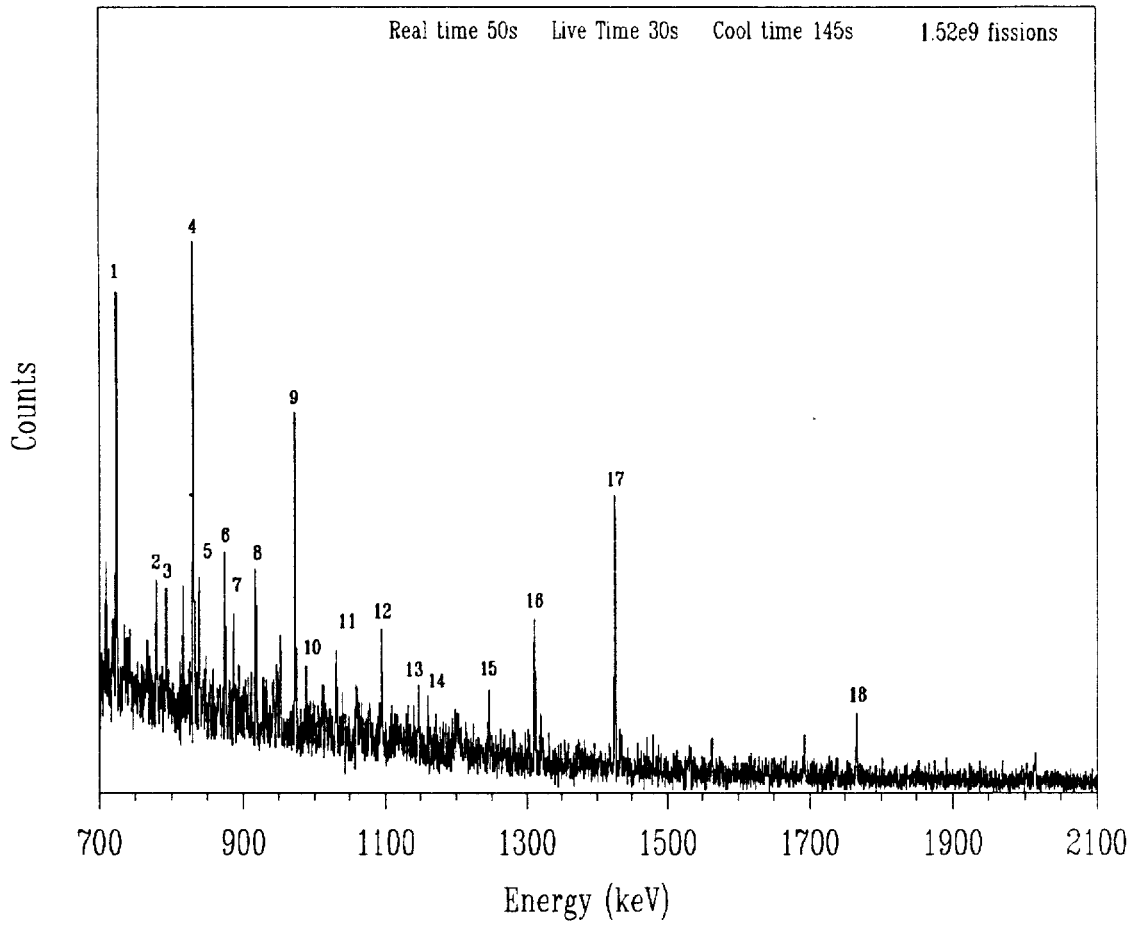

Figure 4.2. Fission product spectrum from HEU experiment 2.

Table 4.8. Identities of labeled peaks from Figure 4.2.

Peak Number	Parent Isotope	Peak Energy (keV)	Half-Life (s)
1	Ce-145	725.0	180
2	Sn-130	779.8	221.4
3	Sb-130*	793.4	390
4	Rb-90/Rb-90m	831.7	153/258
5	Sb-130/Sb-130*	839.4	2454/390
6	Sr-93	875.9	26,748
7	Ba-142	894.9	639
8	Y-94	918.8	1122
9	Y-95	954.2	618
10	Sb-132/Sb-132*	973.9	252/168
11	Mo-101	1012.5	876
12	Kr-90	1118.7	32
13	Pm-154	1148.1	102
14	Sn-129*	1162.0	450
15	Rb-89	1248.1	909
16	I-136	1321.1	83.4
17	Sr-94	1428.3	74.1
18	Xe-138	1768.3	850.2

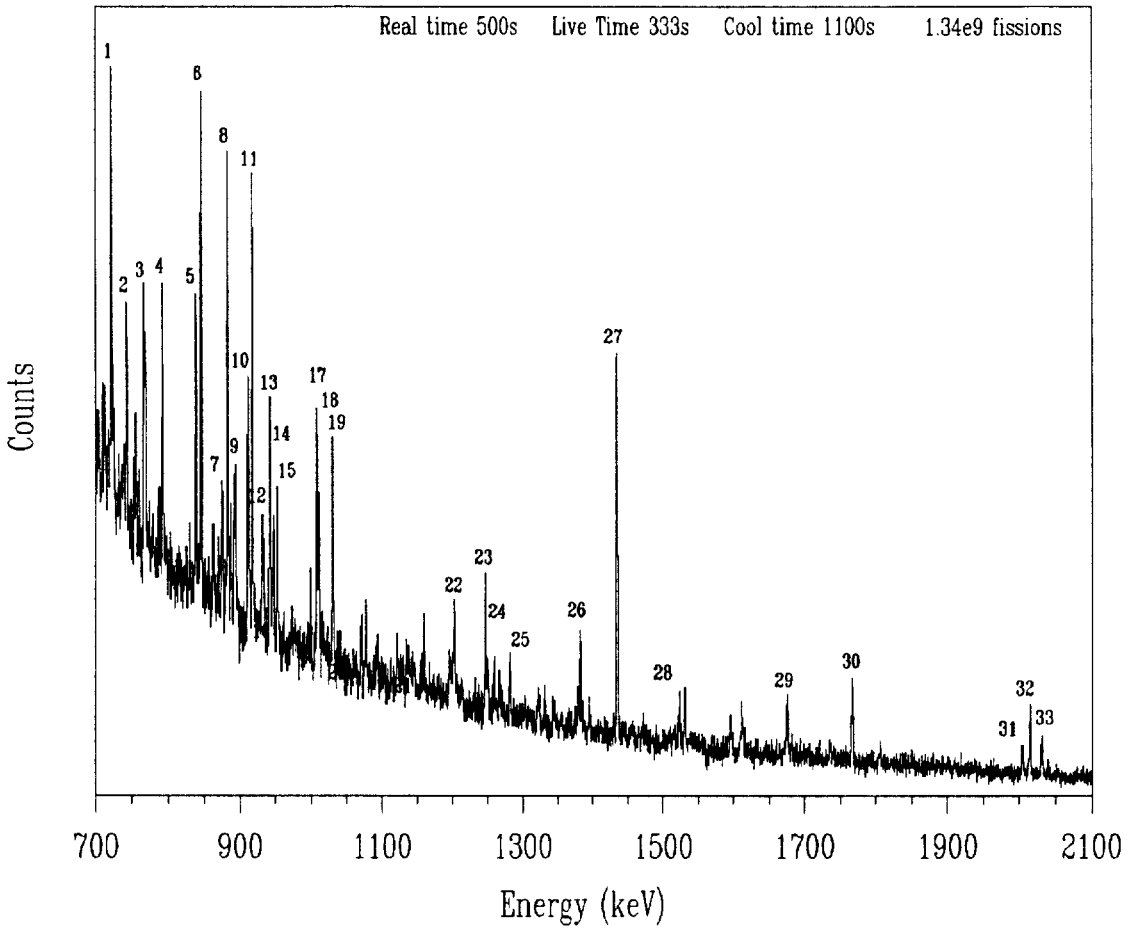

Figure 4.3. Fission product spectrum from Pu-metal experiment 1.

Table 4.9. Identities of labeled peaks from Figure 4.3.

Peak Number	Parent Isotope	Peak Energy (KeV)	Half-Life (s)
1	Ce-145	725.0	180
2	Mo-99/Sn-130	739.4/743.1	237,672/221.4
3	Te-134	767.2	2508
4	Sb-130*	793.4	390
5	Rb-90/Rb-90m	831.7	153/258
6	Sb-130/Sb-130*	839.4	2454/390
7	I-134	884.1	3150
8	Sr-93	888.3	26,748
9	Ba-142	894.9	639
10	Te-133m	912.7	3324
11	Y-94	918.8	1122
12	Sb-131	933.1	1381.8
13	Sb-131	943.4	1381.8
14	Ba-142	948.8	639
15	Y-95	954.2	618
16	Ba-142	1000.9	639
17	Cs-138	1009.8	1932
18	Mo-101	1012.5	876
19	Rb-89	1031.9	909
20	Ba-142	1078.5	639
21	Sn-129*	1162.0	450
22	Ba-142	1204.1	639
23	Rb-89	1248.1	909
24	I-135	1260.4	23,796
25	Cs-139	1283.2	571.8
26	Sr-92	1383.9	9756
27	Cs-138/Cs-138*	1438.9/1436.0	1932/174
28	Mo-101	1532.3	876
29	I-135	1678.0	23,796
30	Xe-138	1732.3	850.2
31	Xe-138	2004.8	850.2
32	Xe-138	2015.8	850.2
33	Mo-101	2032.0	876

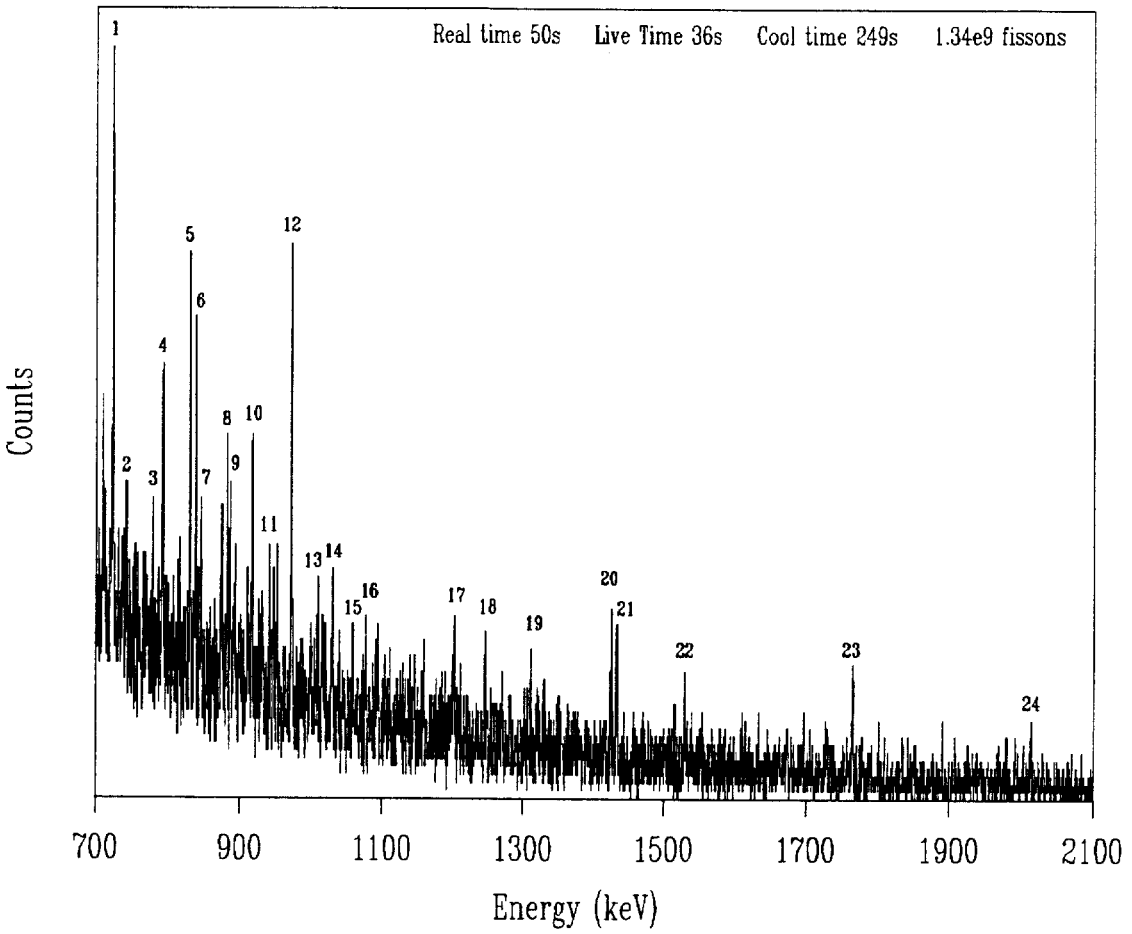

Figure 4.4. Fission product spectrum from Pu-metal experiment 2.

Table 4.10. Identities of labeled peaks from Figure 4.4.

Peak Number	Parent Isotope	Peak Energy (keV)	Half-Life (s)
1	Ce-145	725.0	180
2	Te-134	742.6	2508
3	Sn-130	743.1	221.4
4	Sb-130*	793.4	390
5	Rb-90/Rb-90m	831.7	153/258
6	Sb-130/Sb-130*	839.4	2454/390
7	I-134	847.0	3150
8	I-134	884.1	3150
9	Sr-93	888.3	26,748
10	Y-94	918.8	1122
11	Sb-131	933.1	1381.8
12	Y-95	954.2	618
13	Ba-142	1000.9	639
14	Mo-101	1012.5	876
15	Rb-89	1031.9	909
16	Ba-142	1078.5	639
17	Ba-142	1204.1	639
18	Rb-89	1248.1	909
19	I-136	1321.1	83.4
20	Sr-94	1428.3	74.1
21	Cs-138/Cs-138m	1438.9/1436.0	1932/174
22	Mo-101	1532.3	876
23	Xe-138	1768.3	850.2
24	Xe-138	2015.8	850.2

4.2.2 Comparison of Observations to Theoretical Trends

Once the peaks have been tentatively identified using those listed in the fission product database, the identities can be confirmed by comparing the observed temporal behavior of each peak to theoretical expectation. The number of observed counts for each peak over time must parallel the expected theoretical trend for the identification to be considered valid.

Many hundreds of gamma-rays exist in the fission product spectrum. These decays each have different time constants and can possibly superimpose to create false peaks and erroneous count rates which may be incorrectly associated with a particular peak. To be useful in this analysis a particular peak must remain unobscured in both the uranium and plutonium spectra throughout the data collection period.

While the fission-product database used in the tentative identification is large, it is not wholly inclusive. To insure that a particular peak is correctly identified and remains unobscured over the count period, the corrected counts from the various time windows must be compared to theoretical trends. Figure 4.5, parts a through r, compares the trends in the corrected observed data to the theoretical trends for the long time period HEU and Pu-metal trials. Figure 4.6, parts a through p compares the corrected observed values to the theory for the short time period HEU and Pu-metal trials. The theoretical curves superimposed over the observed data result from the serial decay equations derived in Appendix A using the ENDF/B-VI fission yield data. The error bars on the

theoretical curves are associated with the errors ascribed to the ENDF/B-VI data compilations. Numerous other peaks were identified in the various spectra. These peaks are not included in Figures 4.5 and 4.6 because they did not meet the criteria of remaining unobscured throughout the count period and as a result did not follow the theoretical trends over the count period. The gamma-ray peaks which are included in Figures 4.5 and 4.6 are those whhich met the identification criteria and they are used in the subsequent analysis.

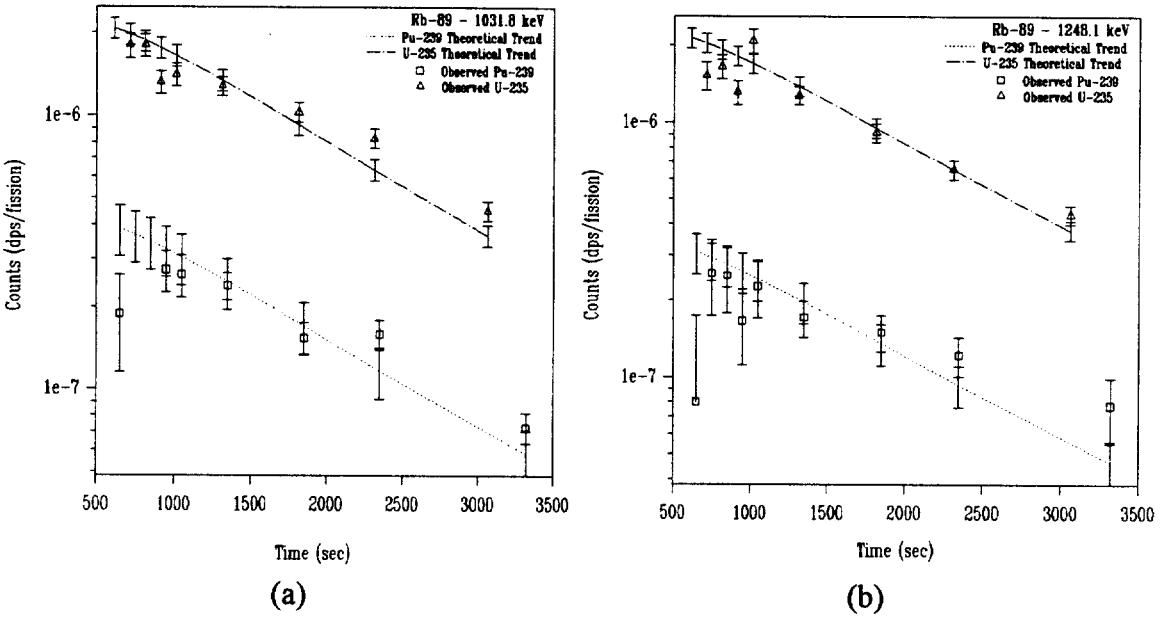

Figure 4.5a-b. Observed gamma-ray activities for U-235 and Pu-239 from LANL experimental series 1 with theoretical trends superimposed.

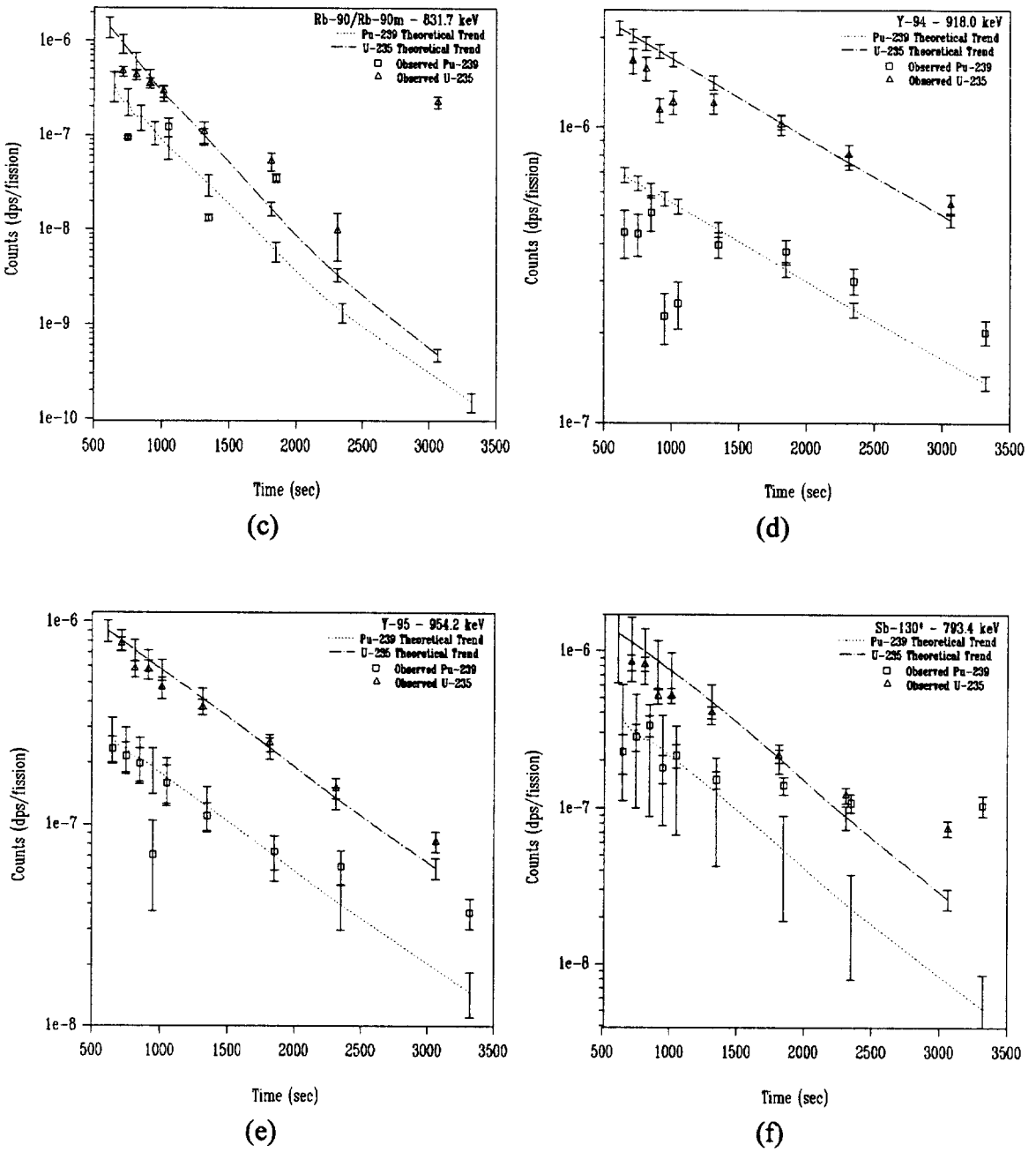

Figure 4.5c-f. Observed gamma-ray activities for U-235 and Pu-239 from LANL experimental series 1 with theoretical trends superimposed.

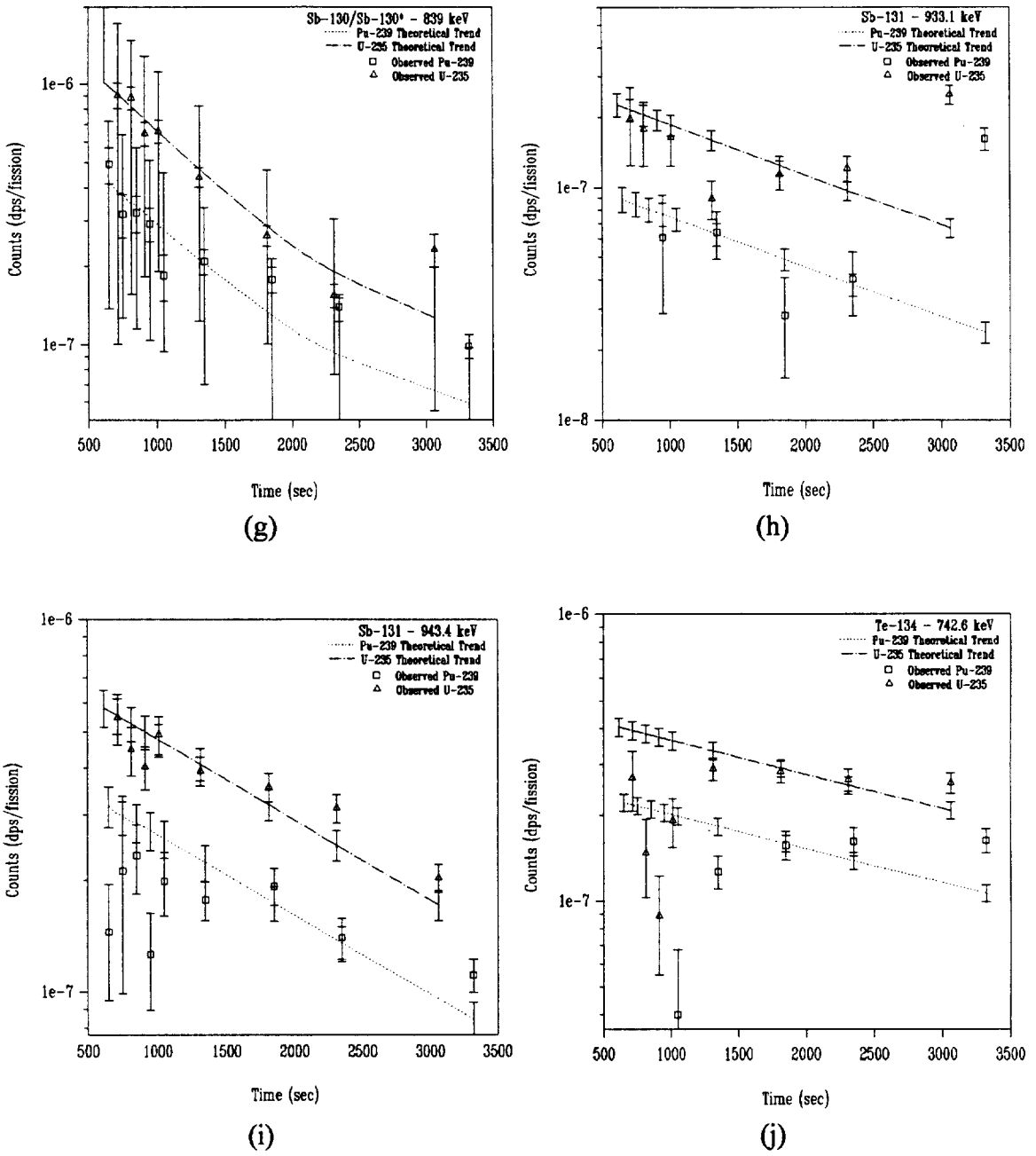

Figure 4.5g-j. Observed gamma-ray activities for U-235 and Pu-239 from LANL experimental series 1 with theoretical trends superimposed.

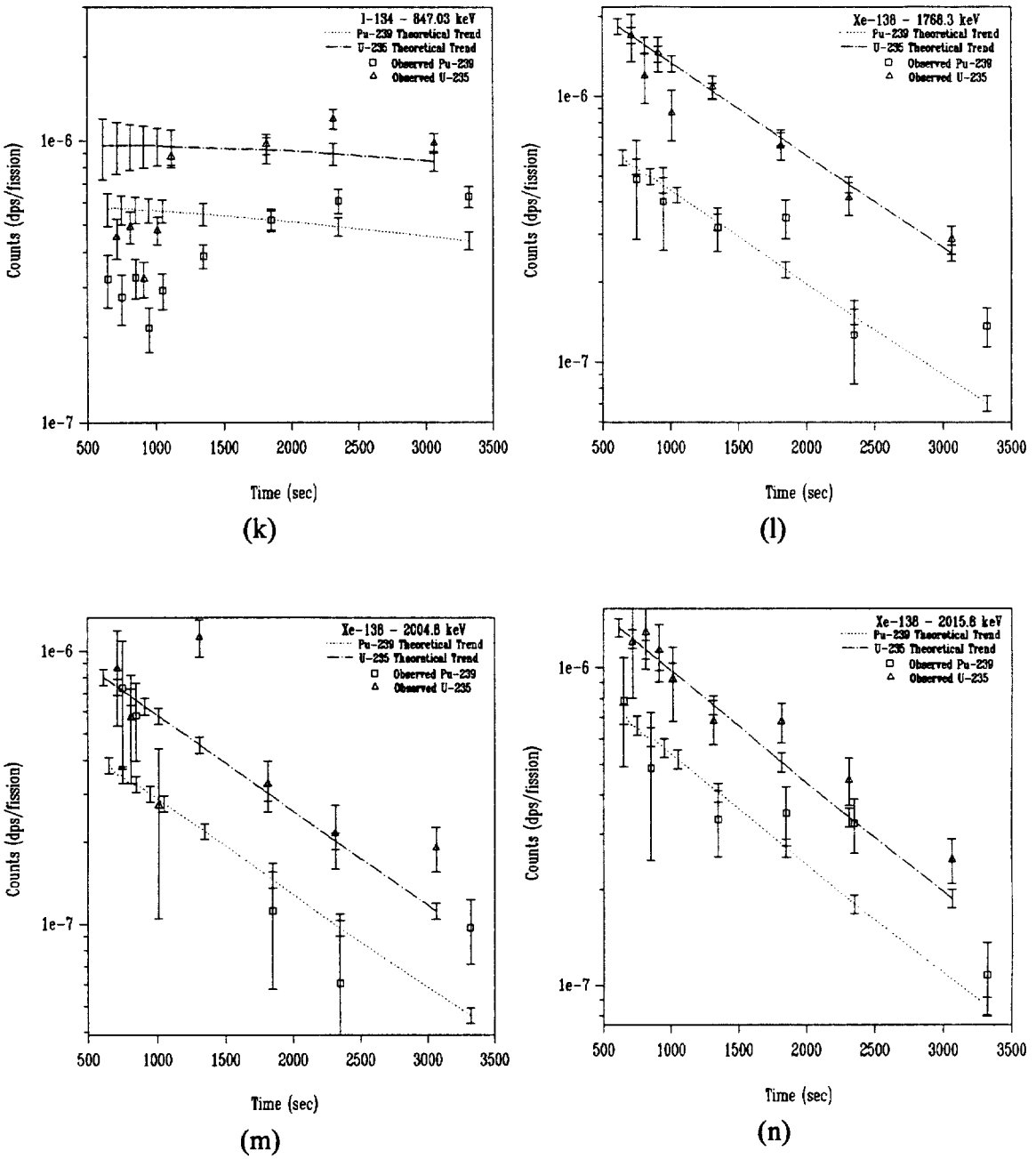

Figure 4.5k-n. Observed gamma-ray activities for U-235 and Pu-239 from LANL experimental series 1 with theoretical trends superimposed.

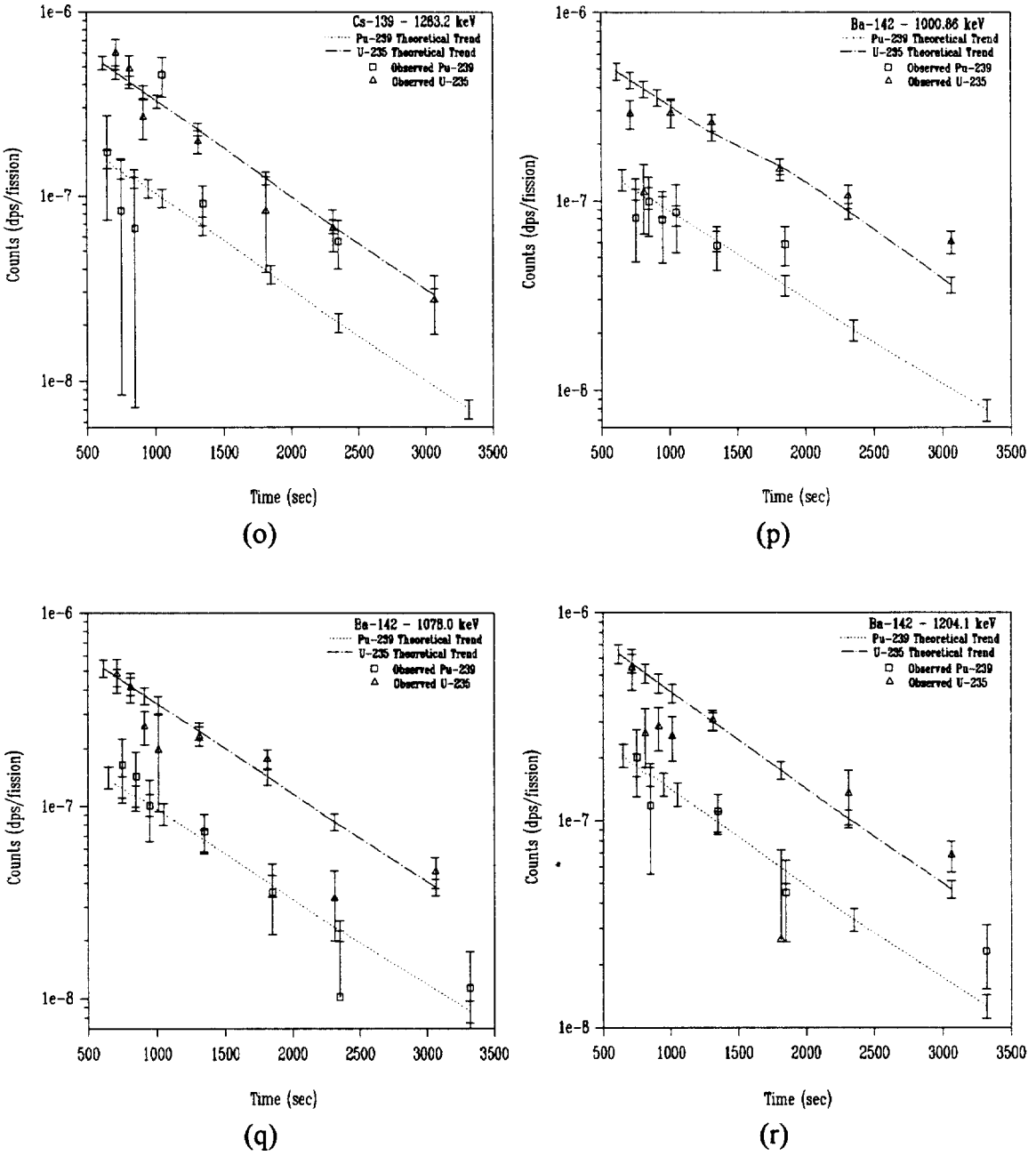

Figure 4.5o-r. Observed gamma-ray activities for U-235 and Pu-239 from LANL experimental series 1 with theoretical trends superimposed.

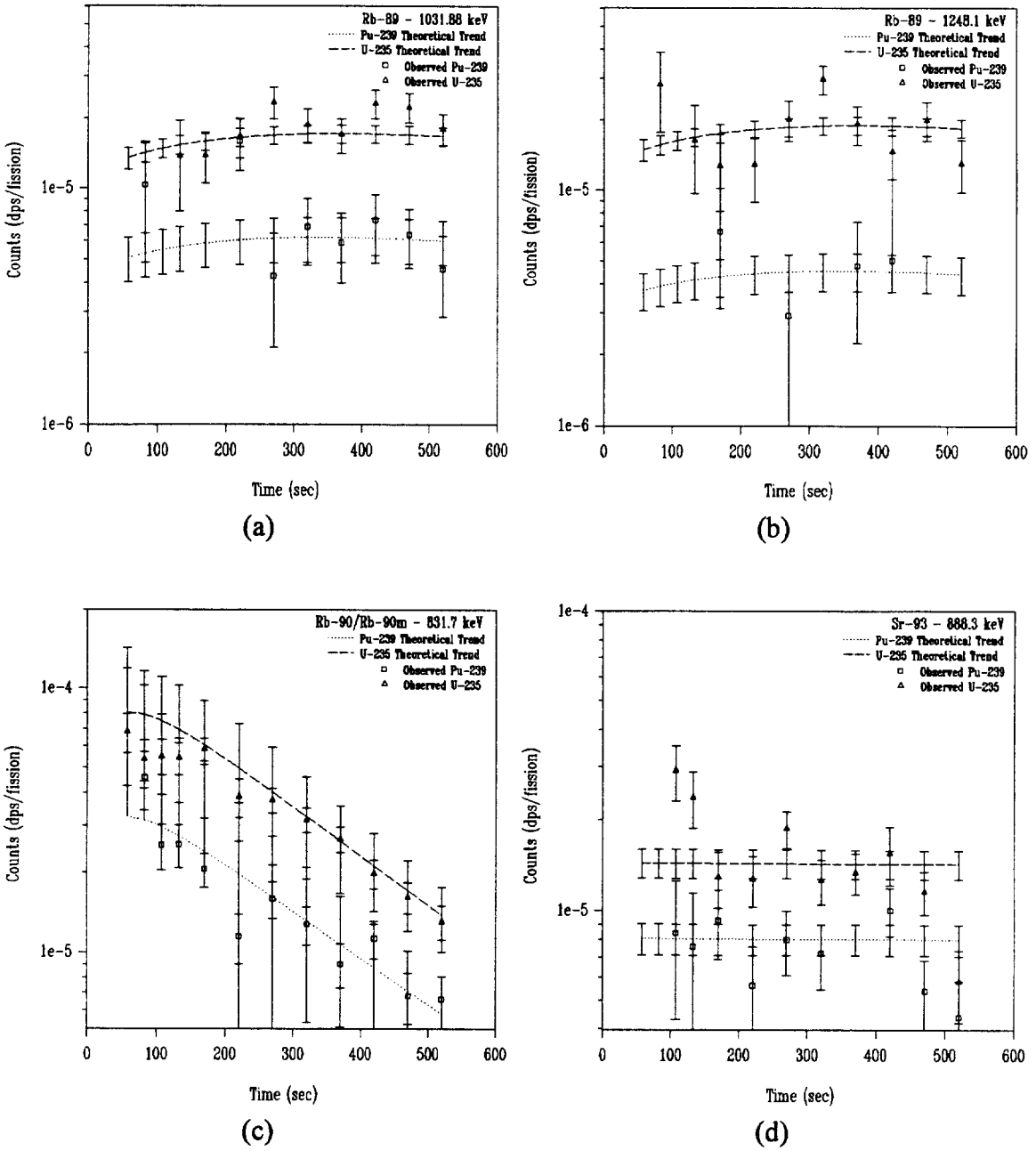

Figure 4.6a-d. Observed gamma-ray activities for U-235 and Pu-239 from LANL experimental series 2 with theoretical trends superimposed.

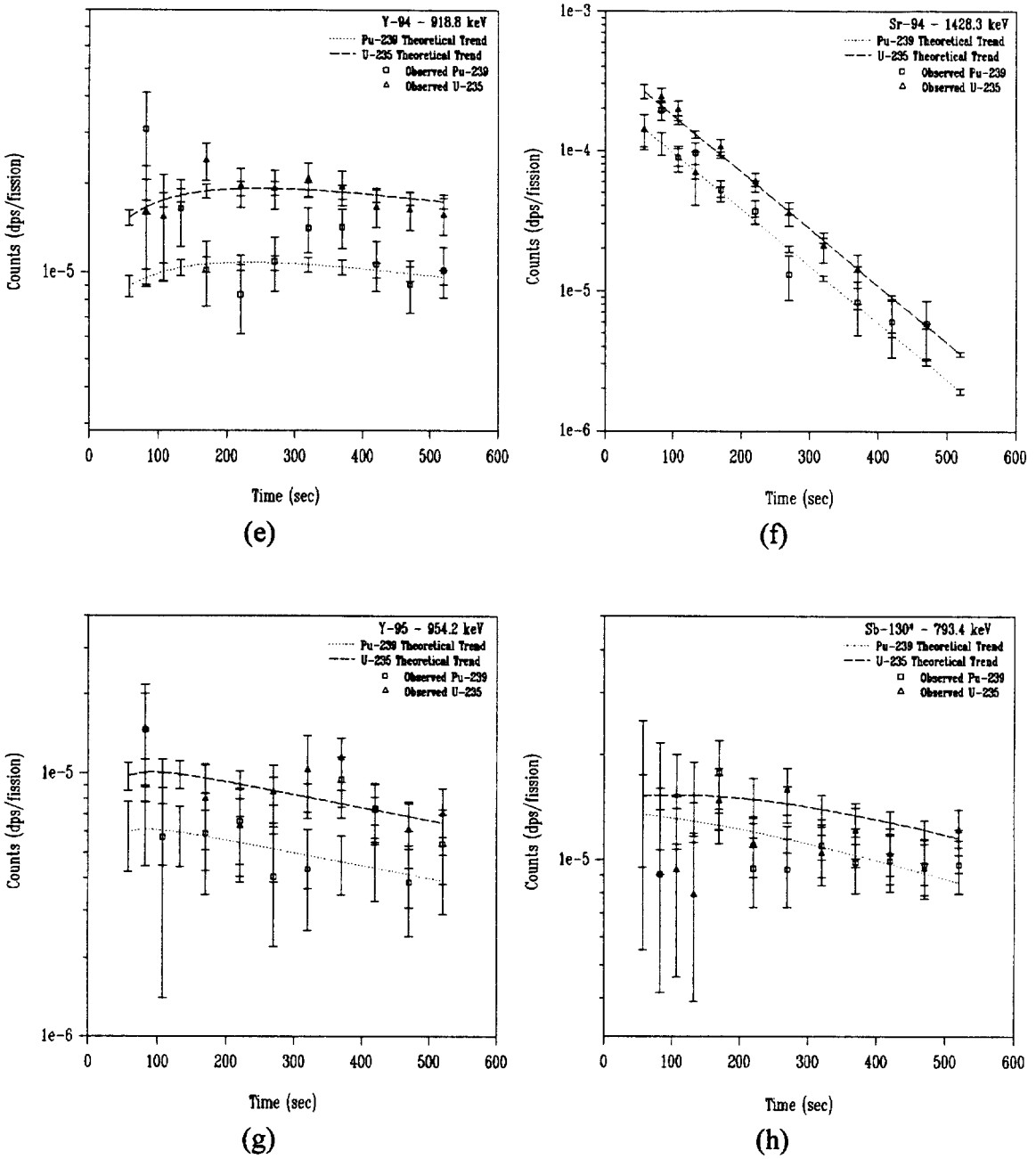

Figure 4.6e-h. Observed gamma-ray activities for U-235 and Pu-239 from LANL experimental series 2 with theoretical trends superimposed.

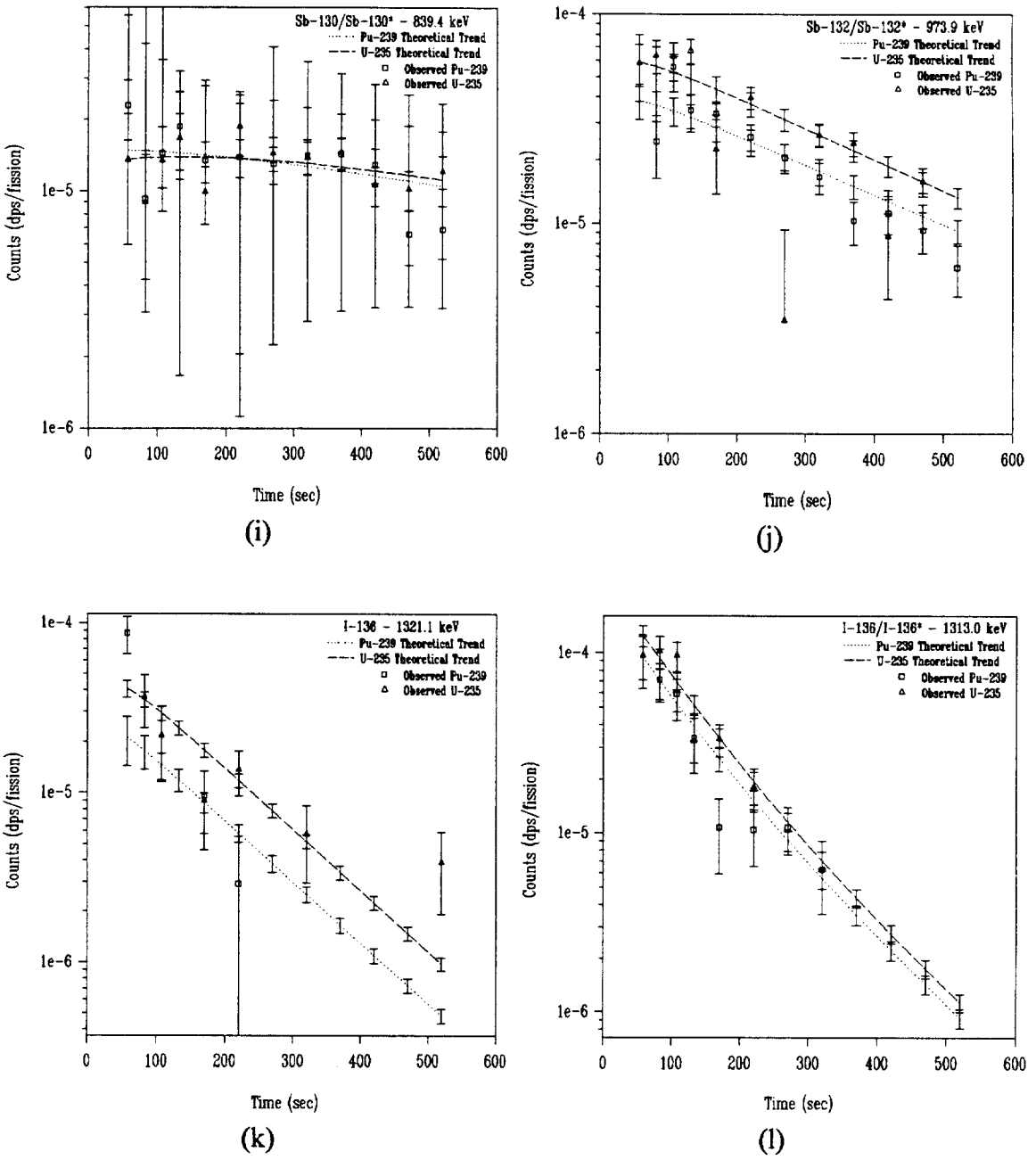

Figure 4.6i-l. Observed gamma-ray activities for U-235 and Pu-239 from LANL experimental series 2 with theoretical trends superimposed.

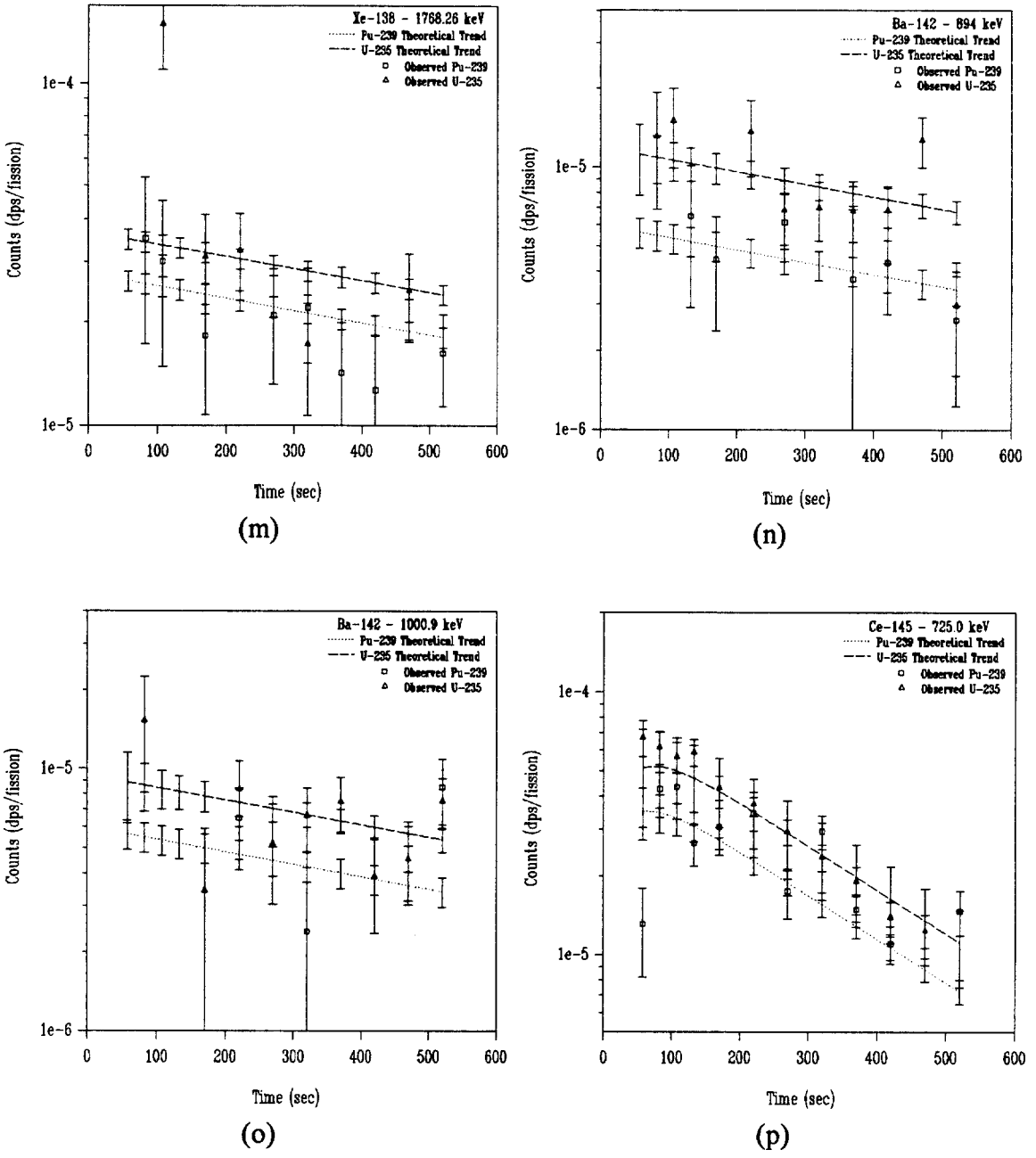

Figure 4.6m-p. Observed gamma-ray activities for U-235 and Pu-239 from LANL experimental series 2 with theoretical trends superimposed.

4.3 Material Identification

As discussed in Chapter 3, the signals from plutonium and uranium fission products can be distinguished by examining the ratio of observed intensities from the spectra. The confirmed gamma-ray peaks from Figures 4.5 and 4.6 serve as the source for a selection set of intensity ratios which can lead to the identification of the material.

From the early time period data using the peaks confirmed in Figure 4.6, the low mass group members available for use include Rb-89 (1031.9 keV), Rb-89 (1248.1 keV), Sr-93 (888.3 keV), Sr-94 (1428.3 keV), Y-94 (918.8 keV), and Y-95 (954.2 keV). If the intensity ratios of these low-mass peaks to all other useable peaks are examined, a majority of the resulting theoretical trends do not exhibit significant differences between the expected values for uranium and plutonium and thus cannot be used to distinguish uranium from plutonium. Some examples of the case where materials cannot be distinguished by virtue of nearly identical theoretical uranium and plutonium trends are shown in Figure 4.7.

From close examination of the theoretical trends in the intensity ratios in the early time period, it would seem that there is little to be gained from striving to collect short count period data immediately following the irradiation. Within the available selection set, the early time period spectra are not yet sufficiently mature that the differences in the theoretical intensity ratios of the uranium and plutonium peaks are significant enough to allow the material to be conclusively identified.

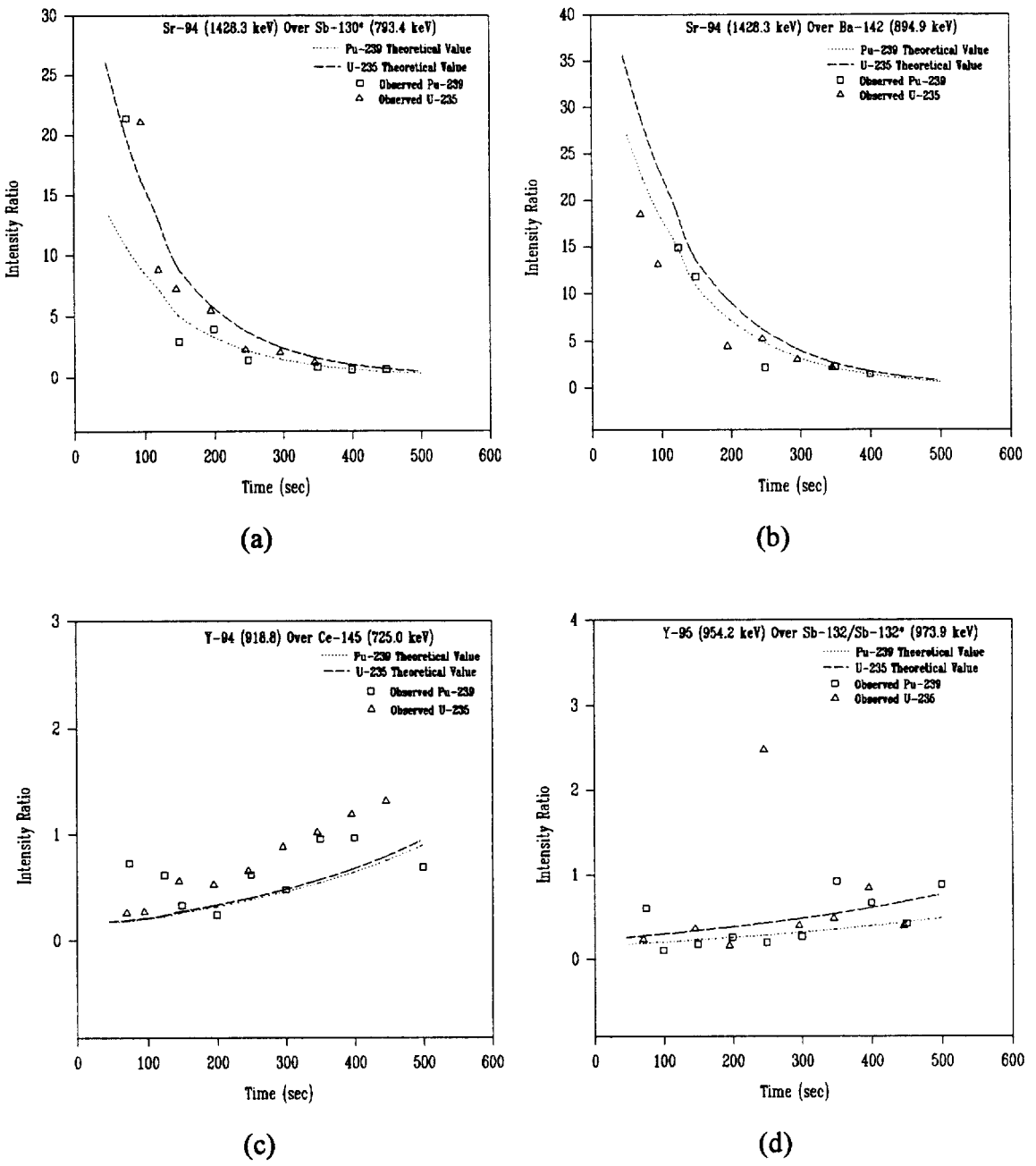

Figure 4.7a-d. Observed and theoretical intensity ratios for early time periods that do not permit identification of the material

There are a few noteworthy exceptions to the inability to distinguish early time period spectra. These distinguishable cases are shown in Figure 4.8. The existence of useful activity ratios where both members are in the low-mass group was an unexpected result, but the requirement that the theoretical trends be significantly different is met in these cases.

In the later time period data there are many cases in the available selection set where the theoretical differences between the uranium and the plutonium ratios remain

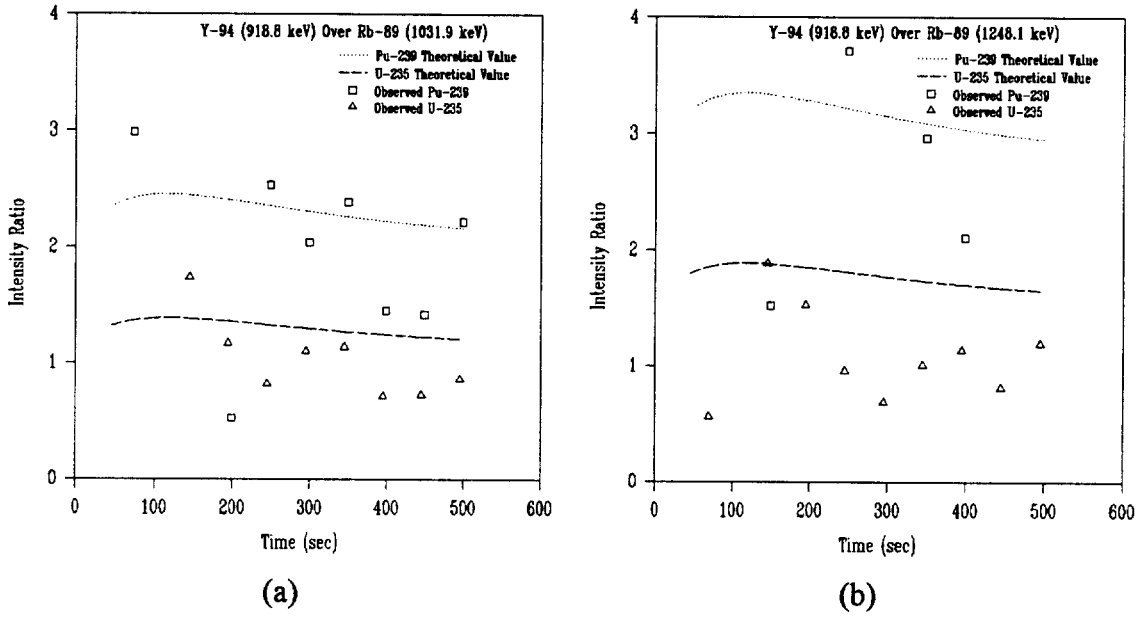

Figure 4.8a-b. Observed and theoretical intensity ratios for early time periods that can permit identification of the material.

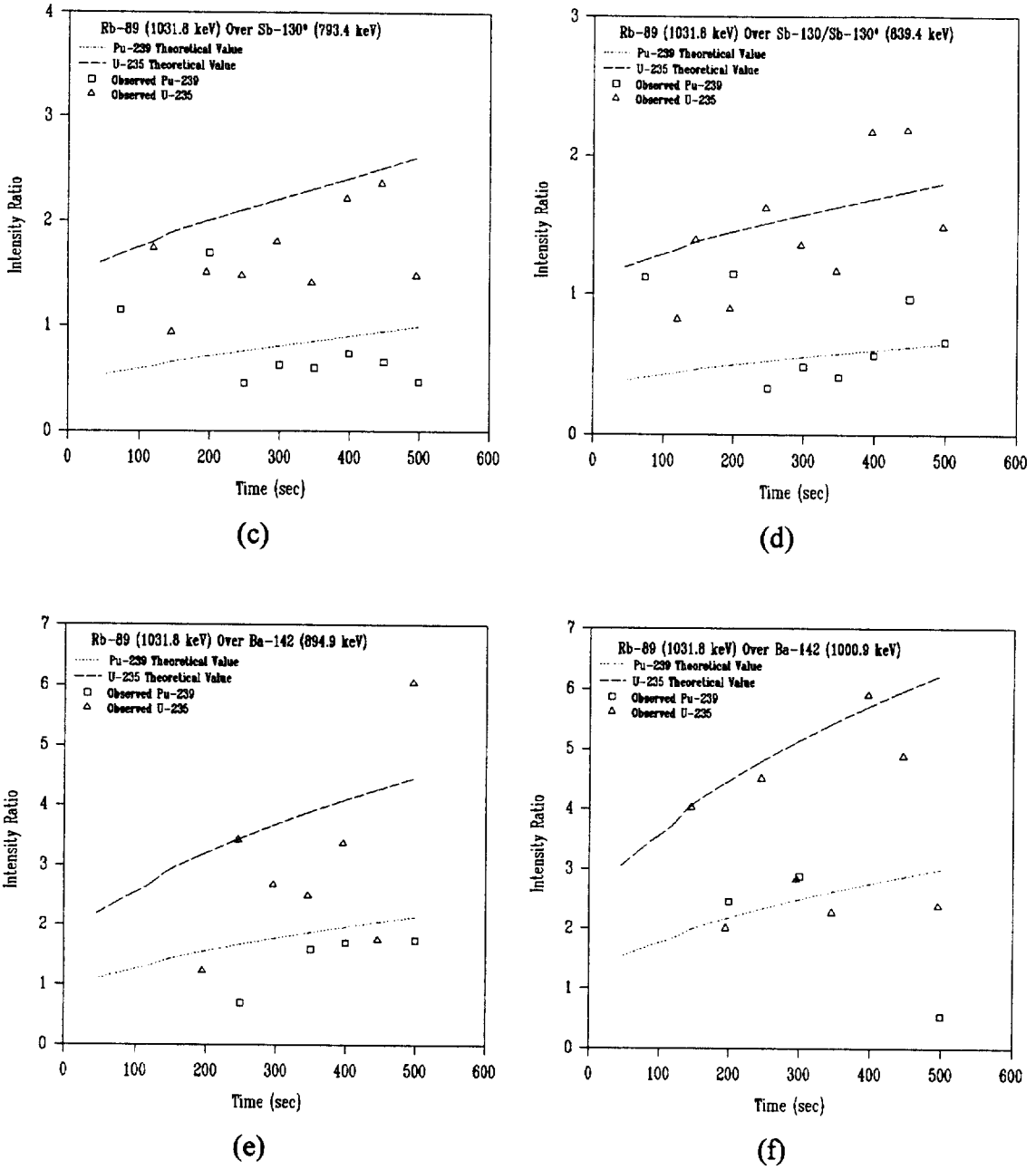

Figure 4.8c-f. Observed and theoretical intensity ratios for early time periods that can permit identification of the material.

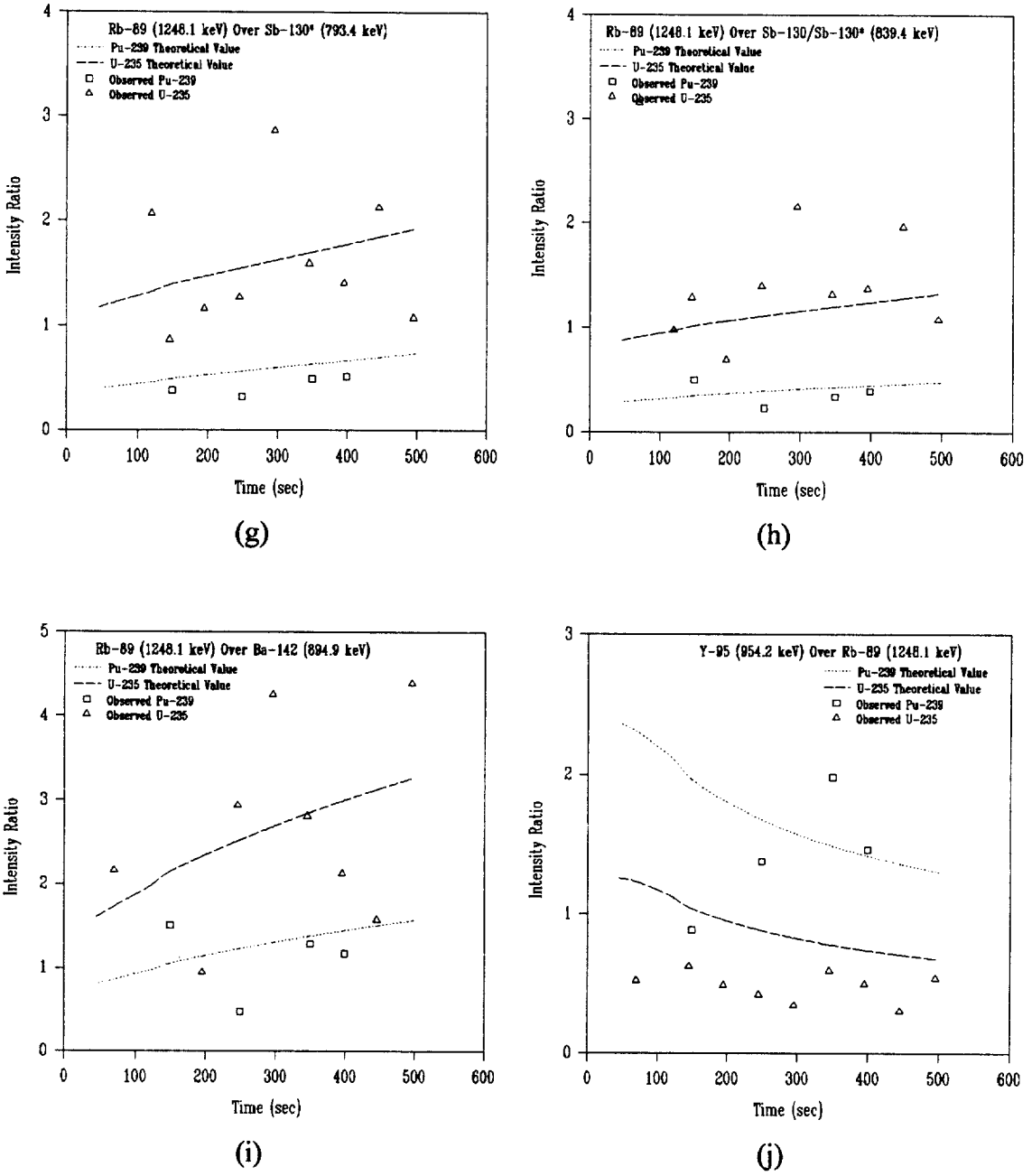

Figure 4.8g-j. Observed and theoretical intensity ratios for early time periods that can permit identification of the material.

insufficient to discriminate between the materials. There are also many cases where the differences are sufficient to allow material identification. Figure 4.9 shows the later time period data which allow discrimination between ^{235}U and ^{239}Pu.

Clearly there is no individual ratio which can be relied upon to conclusively identify the material. However by examining multiple ratios over a lengthy time period, the confidence in determining the material identity increases dramatically.

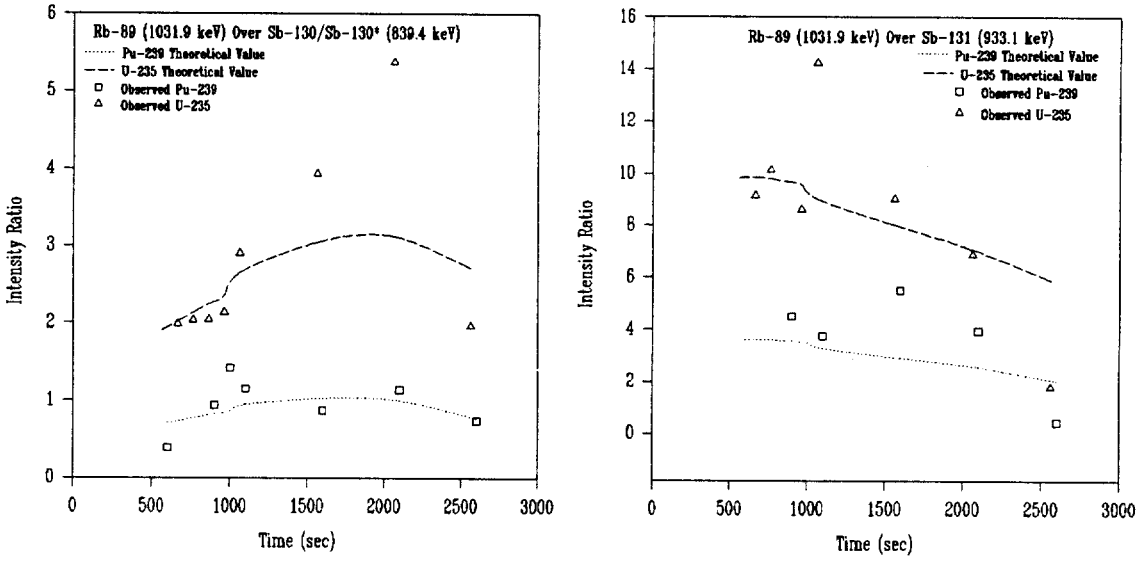

Figure 4.9a-b. Observed and theoretical intensity ratios for later time periods that can permit identification of the material.

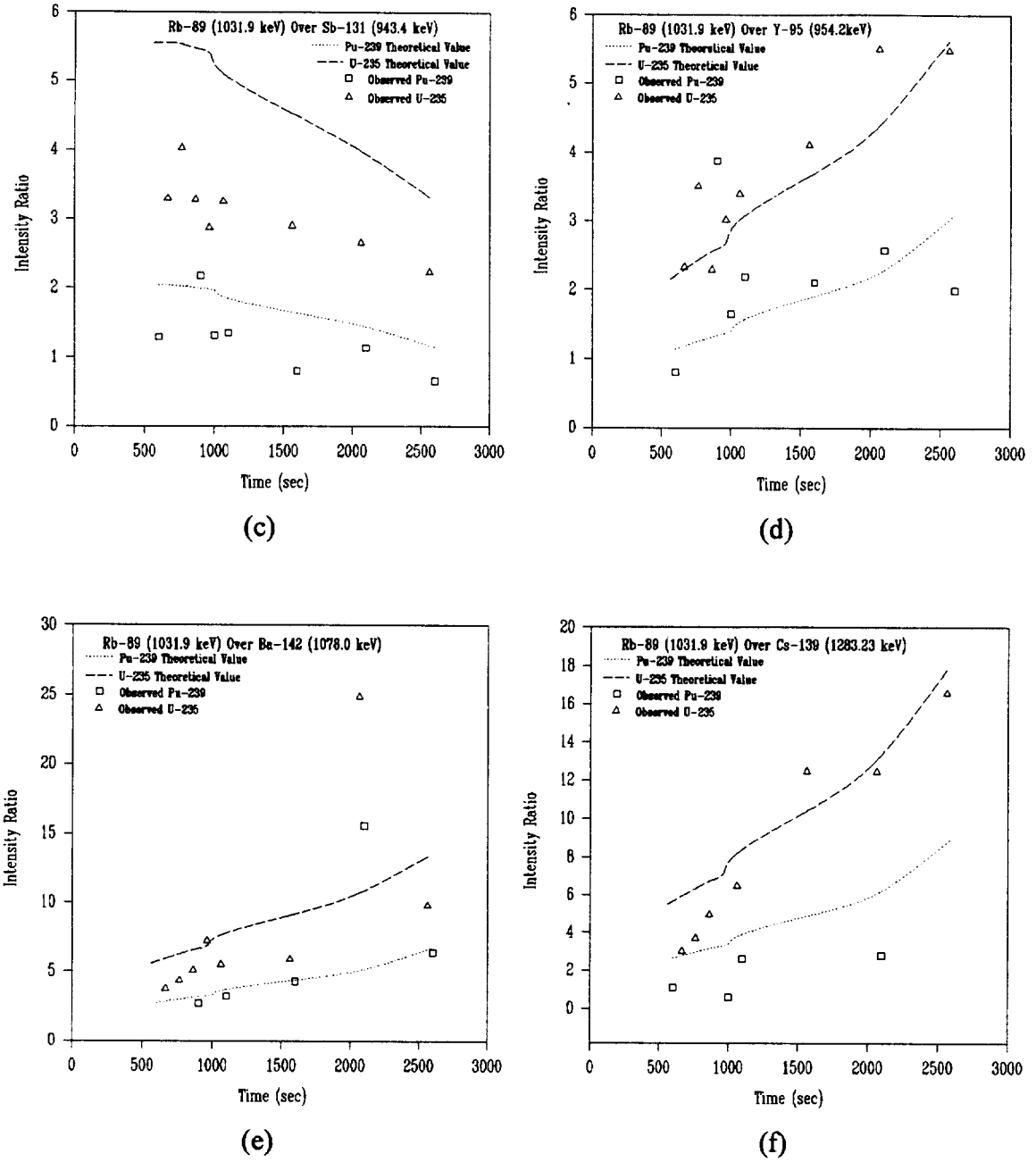

Figure 4.9c-f. Observed and theoretical intensity ratios for later time periods that can permit identification of the material.

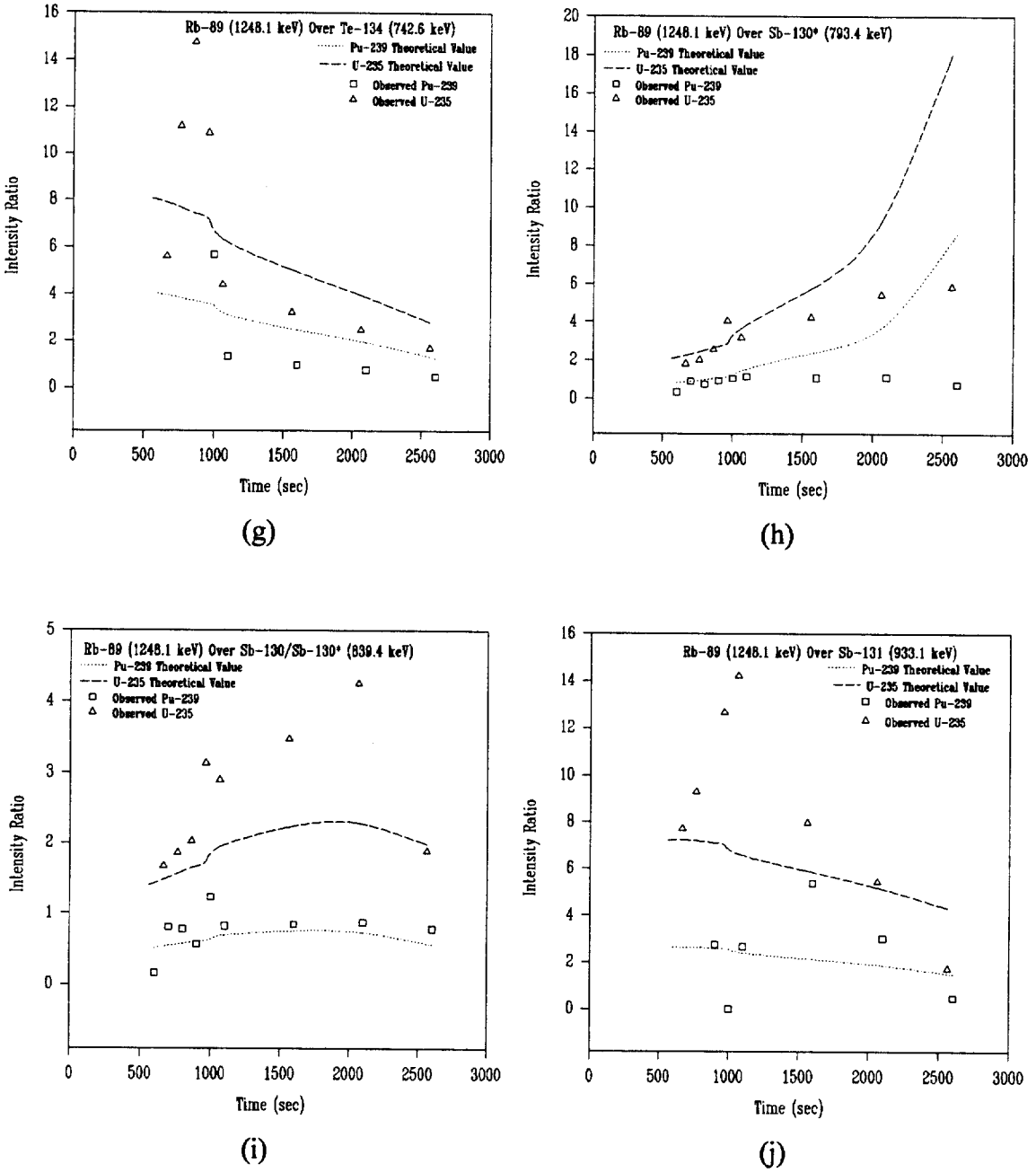

Figure 4.9g-j. Observed and theoretical intensity ratios for later time periods that can permit identification of the material.

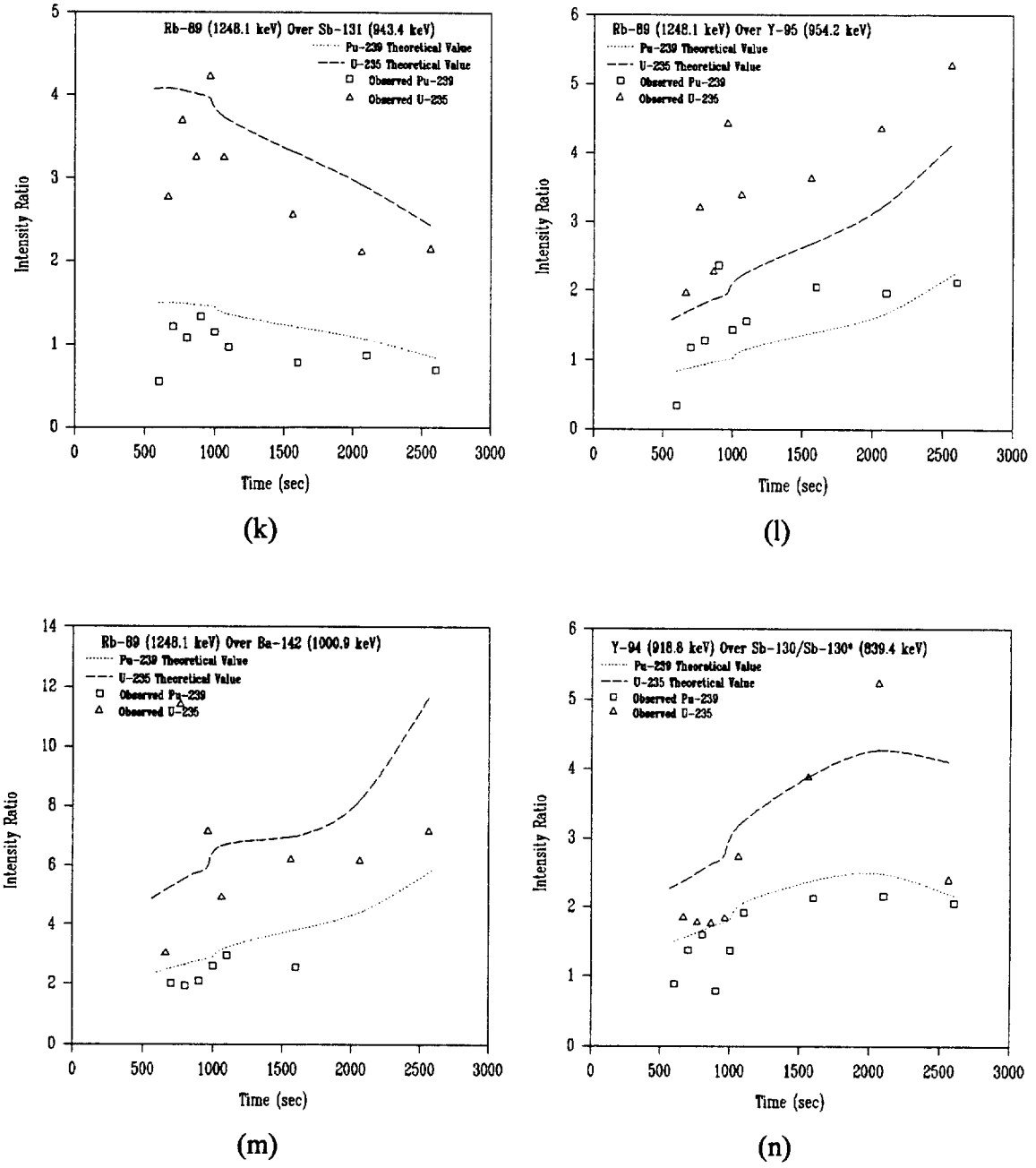

Figure 4.9k-n. Observed and theoretical intensity ratios for later time periods that can permit identification of the material.

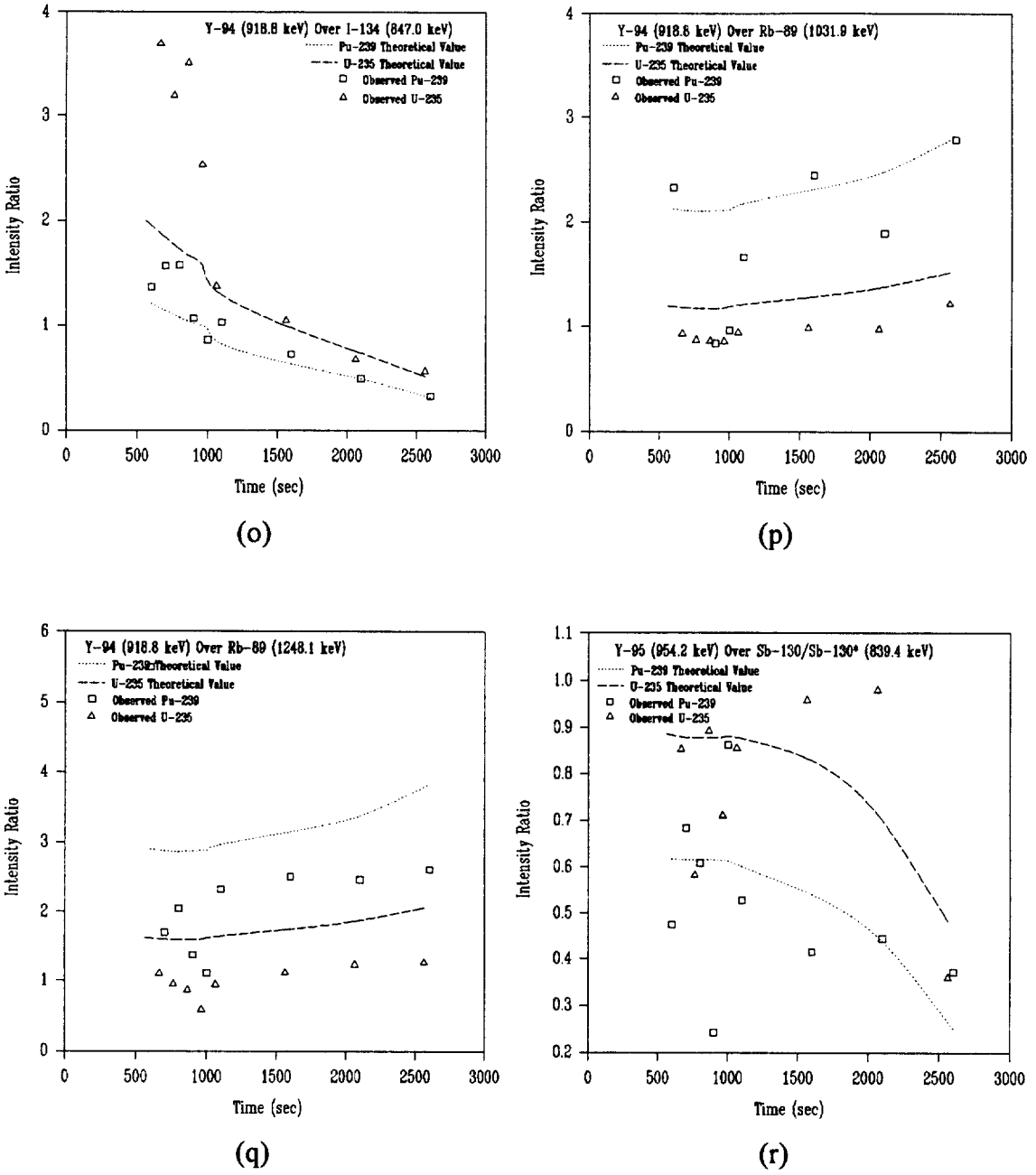

Figure 4.9o-r. Observed and theoretical intensity ratios for later time periods that can permit identification of the material.

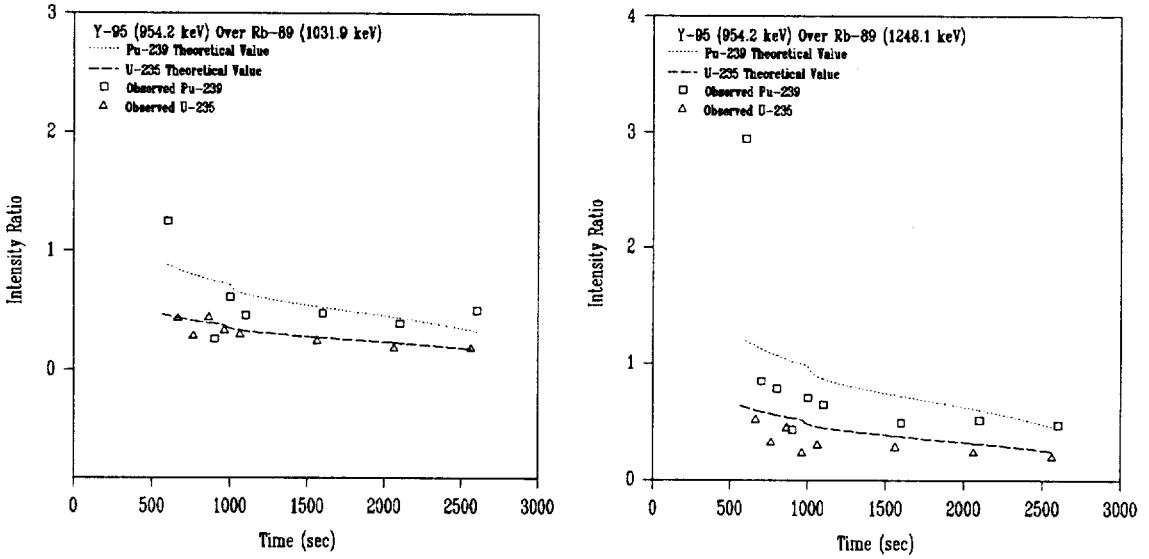

Figure 4.9s-t. Observed and theoretical intensity ratios for later time periods that can permit identification of the material.

A means of numerically assessing the data to arrive at a determination of identity is required for the differences shown in Figures 4.8 and 4.9 to be useful. One can define figure of merit functions, FOM_{Pu} and FOM_{U}, to assess the deviation of an observed value from the theoretically expected results for Pu-239 and U-235. The FOM functions are applied to each intensity ratio at every time step over the entire data set. Comparison of the two values averaged over the entire data set should permit identification of the fissioning material.

Possible forms of the FOM functions are,

$$FOM_{Pu} = \left(1 - \left|\frac{n_{obs} - n_{Pu}}{n_{Pu} - n_{U}}\right|\right) 100\% \qquad (4.1)$$

and

$$FOM_{U} = \left(1 - \left|\frac{n_{obs} - n_{U}}{n_{Pu} - n_{U}}\right|\right) 100\% \qquad (4.2)$$

where:

n_{obs} = the observed value of a given isotopic intensity ratio at a given time interval,

n_{Pu} = the theoretical value of the isotopic intensity ratio for Pu-239 in the same time interval,

n_{U} = the theoretical value of the isotopic intensity ratio for U-235 in the same time interval.

The values of FOM_{Pu} and FOM_{U} can range from $-\infty$ to 100% where 100% is an exact match with the theoretical expectation.

Applying the confidence functions to all of the early time period data shown in Figure 4.8 and averaging the results over the entire data set yields, $FOM_{U} = 47.3$ and $FOM_{Pu} = -7.4$ for the HEU sample data, and $FOM_{Pu} = 61.3$ and $FOM_{U} = 3.2$ for the Pu-metal sample. For the later time period data shown in Figure 4.9, the results for the HEU sample averaged over the entire data set are, $FOM_{U} = 41.29$ and $FOM_{Pu} = -20.28$. The later time period results for the Pu-metal sample averaged over the entire data set are, $FOM_{Pu} = 56.9$ and $FOM_{U} = -1.47$. In all four cases, by examining the associated pair of

FOM values, the fissioning material is correctly and unambiguously identified.

It is instructive to examine the FOM values from each intensity ratio, rather than only the average of the entire data set. Table 4.11 shows the results of applying the FOM functions to each of the individual ratios in the later time period data shown Figure 4.9. The stated value of the FOM's are the average over all of the time steps for which data were available. In general, each of the ratios produced FOM values which clearly identified the SNM, though a small number of the results are ambiguous.

Table 4.11. FOM values using late time period data

Numerator	E (keV)	Denominator	E (keV)	FOM:				
				Pu Sample:		U Sample:	
				Pu	U	Pu	U
Rb-89	1031.9	Sb-130/Sb-130*	839.4	85.7	3.9	-20.9	67.9
		Sb-131	933.1	70.7	12.8	7.7	67.3
		Sb-131	943.4	82.3	-16.2	63.8	45.7
		Y-95	954.2	47.0	0.0	-55.6	64.4
		Ba-142	1078	55.8	-4.2	-12.8	12.1
		Cs-139	1283.2	47.5	-52.5	4.4	47.8
Rb-89	1248.1	Te-134	742.6	43.7	-32.5	8.0	18.3
		Sb-130*	793.4	70.7	-29.1	-4.4	26.6
		Sb-130/Sb-130*	839.4	79.2	11.1	-75.4	30.8
		Sb-131	933.1	62.8	6.2	-37.5	30.9
		Sb-131	943.4	84.9	-15.1	33.3	73.7
		Y-95	954.2	49.2	22.0	-142.2	-14.8
		Ba-142	1000.9	79.3	-20.7	-15.5	12.1
Y-94	918.8	Sb-130/Sb-130*	839.4	64.1	-35.9	31.7	27.9
		I-134	847.03	72.4	24.0	-65.9	-11.8
		Rb-89	1248.1	6.9	35.5	-49.2	47.0
		Rb-89	1031.9	42.8	30.8	-27.1	69.1
Y-95	954.2	Sb-130/Sb-130*	839.4	51.1	-10.3	20.0	52.3
		Rb-89	1031.9	31.3	-2.6	-21.0	87.6
		Rb-89	1248.1	14.6	7.6	-42.1	70.1

4.4 Determination of the Number of Induced Fissions

Once the nuclear material has been identified, the serial decay equations from Appendix A can be used to iterate the number of fissions induced in the sample by comparing the observed number of decays to theoretical results. The ENDF/B-VI fission yields, the timings of the individual trials and a seed value of the number of fissions are used as input values and the resulting predicted number of decays for a particular isotope is compared to observation. The number of fissions is adjusted until the theoretical number of decays matches observation. Tables 4.12 through 4.15 show the iterated values of the number of fissions associated with each observed number of decays for each of the four LANL experiments. From the MCNP modeling of these samples, the number of fissions actually induced in the samples were $1.5169 \times 10^9 \pm 1.1340 \times 10^8$ fissions for the HEU sample in both experiments and $1.3452 \times 10^9 \pm 1.1340 \times 10^8$ fission for the Pu-metal sample in both experiments.

The serial decay equations used in the iteration process use the assumption that all of the fissions occurred immediately prior to $t_{cool}=0$. The reality is that the samples were irradiated over a 100 second period prior to $t_{cool}=0$. The assumption ends up being fatal in the early time periods and results in a severe underestimate of the number of induced fissions. After a lengthy cooling period (~2500s) the error introduced by this assumption becomes negligible and the iterated value converges upon the correct result.

Table 4.12. Number of fissions iterated from early time period Pu-metal experiment

Cool Time (s)	Ce-145 725 keV	Sb-130* 793.4 keV	Sr-93 888.3 keV	Ba-142 894.9 keV	Y-94 918.8 keV	Y-95 954.2 keV	Sb-132 973.9 keV	Ba-142 1000.9 keV	Rb-89 1031.9 keV	Rb-89 1248.1 keV	I-136/I-136* 1313.0 keV	I-136 1321.1 keV	Sr-94 1428.3 keV	Xe-138 1768.3 keV	Row Averages
49	1.53e+08											4.08e+09			2.12e+9
74	5.04e+08	7.37e+07			1.94e+09	8.07e+07	4.25e+08		1.52e+09		7.22e+08		1.57e+09	5.46e+08	8.19e+8
99	5.38e+08		3.53e+08			2.78e+08	1.10e+09				8.06e+08		9.12e+08	4.78e+08	6.38e+8
124	3.54e+08		3.17e+08	1.27e+09	9.48e+08		7.30e+08				6.14e+08		1.25e+09		7.83e+8
149	4.60e+08	1.54e+08	3.89e+08	9.00e+08	5.71e+08	2.99e+08	7.89e+08			1.21e+09	2.91e+08	1.09e+09	9.51e+08	3.05e+08	6.18e+8
199	6.23e+08	8.54e+07	2.36e+08		4.64e+08	3.50e+08	7.15e+08	1.95e+09	2.05e+09		4.81e+08	5.01e+08	1.07e+09		7.75e+8
249	3.80e+08	8.92e+07	3.37e+08	1.39e+09	6.04e+08	2.27e+08	6.71e+08		5.43e+08	5.06e+08	8.21e+08		6.11e+08	3.79e+08	5.47e+8
299	7.74e+08	1.10e+08	3.03e+08		7.94e+08	2.58e+08	6.39e+08	8.01e+08	8.68e+08		7.77e+08			4.14e+08	5.74e+8
349	4.74e+08	1.04e+08		9.40e+08	8.17e+08	5.97e+08	4.70e+08		7.47e+08	8.22e+08			9.83e+08	2.80e+08	6.23e+8
399	4.25e+08	1.12e+08	4.22e+08	1.15e+09	6.27e+08	4.91e+08	5.98e+08		9.30e+08	8.71e+08			1.14e+09	2.60e+08	6.38e+8
449		1.16e+08	2.27e+08		5.48e+08	2.71e+08	5.84e+08		8.19e+08				1.78e+09		6.20e+8
499	8.31e+08	1.24e+08	1.85e+08	7.76e+08	6.30e+08	4.01e+08	4.58e+08	3.54e+09	5.94e+08					3.60e+08	7.90e+8
Column Averages:	5.01e+08	1.08e+08	3.08e+08	1.07e+09	7.94e+08	3.25e+08	6.53e+08	2.10e+09	1.01e+09	8.52e+08	6.44e+08	1.89e+09	1.14e+09	3.78e+08	
Set Average:	6.97e+08														

Table 4.13. Number of fissions iterated from late time period Pu-metal experiment

Cool Time (s)	Te-134 742.6 keV	Sb-130* 793.4 keV	I-134 847.0 keV	Y-94 918.8 keV	Sb-131 933.1 keV	Sb-131 943.4 keV	Y-95 954.2 keV	Ba-142 1000.9 keV	Rb-89 1031.9 keV	Ba-142 1078.0 keV	Ba-142 1204.1 keV	Rb-89 1248.1 keV	Cs-139 1283.2 keV	Xe-138 1768.3 keV	Xe-138 2004.8 keV	Xe-138 2015.8 keV	Row Averages
600		4.13e+07	5.18e+08	5.86e+08		4.46e+08	4.42e+08		5.16e+08			2.09e+08	9.28e+08			1.06e+09	5.27e+08
700		5.95e+07	4.48e+08	6.16e+08		6.82e+08	4.56e+08	8.46e+08		1.25e+09	8.61e+08	7.05e+08	5.07e+08	5.17e+08	1.19e+09		6.26e+08
800		8.16e+07	5.28e+08	7.74e+08		7.88e+08	4.59e+08	9.55e+08		1.21e+09	5.59e+08	7.31e+08	4.57e+08		1.03e+09	7.68e+08	6.95e+08
900		5.10e+07	3.52e+08	3.68e+08	3.85e+08	4.49e+08	1.86e+08	6.57e+08	8.94e+08	9.59e+08		5.19e+08		5.01e+08			4.43e+08
1000	1.79e+08	7.15e+07	4.81e+08	4.30e+08		7.45e+08	4.69e+08	7.98e+08	9.14e+08			7.58e+08	3.97e+09				8.02e+08
1100	6.18e+08	7.97e+07	6.56e+08	8.15e+08	4.93e+08	7.69e+08	4.48e+08	8.13e+08	1.03e+09	1.07e+09	8.96e+08	7.01e+08	1.13e+09	5.50e+08		7.87e+08	7.24e+08
1600	8.73e+08	1.70e+08	9.20e+08	1.05e+09	2.78e+08	1.08e+09	5.24e+08	1.42e+09	9.62e+08	8.89e+08	6.27e+08	8.95e+08		8.99e+08	4.45e+08	1.24e+09	8.18e+08
2100	1.04e+09	3.16e+08	1.14e+09	1.14e+09	5.14e+08	1.01e+09	7.72e+08		1.45e+09	4.34e+08		1.06e+09	2.36e+09	4.92e+08	3.63e+08	1.73e+09	9.86e+08
2600	1.36e+09	1.34e+09	1.32e+09	1.36e+09	3.29e+09	1.28e+09	1.24e+09		1.33e+09	1.27e+09	1.46e+09	1.35e+09		1.12e+09	1.21e+09	1.21e+09	1.44e+09
Column Averages:	8.13e+08	2.45e+08	7.07e+08	7.94e+08	9.92e+08	8.05e+08	5.54e+08	9.15e+08	1.01e+09	1.01e+09	8.80e+08	7.69e+08	1.56e+09	6.80e+08	8.47e+08	7.54e+08	
Set Average:	8.04e+08																

Table 4.14. Number of fissions iterated from early time period HEU experiment

Cool Time (s)	Ce-145 725 keV	Sb-130* 793.4 keV	Sr-93 888.3 keV	Ba-142 894.9 keV	Y-94 918.8 keV	Y-95 954.2 keV	Sb-132 973.9 keV	Ba-142 1000.9 keV	Rb-89 1031.9 keV	Rb-89 1248.1 keV	I-136/I-136* 1313.0 keV	I-136 1321.1 keV	Sr-94 1428.3 keV	Xe-138 1768.3 keV	Row Averages
45	5.79e+08						9.89e+08				5.84e+08		5.50e+08		6.75e+08
70	5.27e+08			1.87e+09	7.09e+08	9.83e+08	1.14e+09	1.22e+09		2.33e+09	8.27e+08	1.76e+08	1.18e+09		1.10e+09
95	5.02e+08	4.58e+08	3.45e+09	2.20e+09	6.43e+08		1.20e+09				1.04e+09	1.26e+08	1.22e+09	2.14e+10	3.22e+09
120	5.54e+08	3.89e+08	2.82e+09				1.39e+09		7.69e+08	1.25e+09	4.67e+08		5.44e+08		1.02e+09
145	4.57e+08	7.34e+08	1.53e+09		9.35e+08	5.58e+08	5.20e+08	3.02e+08	7.44e+08	9.35e+08	7.23e+08	8.56e+07	1.17e+09	4.66e+09	1.03e+09
195	4.73e+08	5.63e+08	1.50e+09	2.25e+09	7.48e+08	4.65e+08	1.09e+09	7.72e+08	8.64e+08	9.08e+08	6.74e+08	1.96e+08	1.06e+09	5.04e+09	1.19e+09
245	4.47e+08	8.30e+08	2.22e+09	1.20e+09	7.38e+08	6.60e+08	1.12e+08	5.08e+08	1.19e+09	1.39e+09			1.00e+09		9.35e+08
295	4.33e+08	5.65e+08	1.49e+09	1.29e+09	7.99e+08	8.47e+08	1.02e+09	6.85e+08	9.38e+08	2.04e+09		1.87e+08	9.42e+08	2.92e+09	1.09e+09
345	4.26e+08	6.84e+08	1.59e+09	1.33e+09	7.62e+08	9.94e+08	1.11e+09	8.17e+08	8.49e+08	1.31e+09			1.03e+08		9.06e+08
395	3.77e+08	6.16e+08	1.84e+09	1.41e+09	6.67e+08	6.69e+08	4.02e+08	4.50e+08	1.15e+09	9.95e+08					8.58e+08
445	4.06e+08	5.87e+08	1.37e+09	2.75e+09	6.71e+08	5.93e+08	1.02e+09	5.52e+08	1.12e+09	1.38e+09				4.71e+09	1.38e+09
495		8.01e+08	6.88e+08	6.81e+08	6.60e+08	7.23e+08		9.68e+08	9.19e+08	9.10e+08		6.80e+08			7.81e+08
Column Averages:	4.71e+08	6.23e+08	1.85e+09	1.66e+09	7.33e+08	7.21e+08	9.08e+08	6.97e+08	9.49e+08	1.34e+09	7.19e+08	2.42e+08	8.64e+08	7.74e+09	
Set Average:	1.20e+09														

Table 4.15. Number of fissions iterated from late time period HEU experiment

Cool Time (s)	Te-134 742.6 keV	Sb-130* 793.4 keV	I-134 847.0 keV	Y-94 918.8 keV	Sb-131 933.1 keV	Sb-131 943.4 keV	Y-95 954.2 keV	Ba-142 1000.9 keV	Rb-89 1031.9 keV	Ba-142 1078.0 keV	Ba-142 1204.1 keV	Rb-89 1248.1 keV	Cs-139 1283.2 keV	Xe-138 1768.3 keV	Xe-138 2004.8 keV	Xe-138 2015.8 keV	Row Averages
663	3.85e+08	3.93e+08	6.09e+08	1.11e+09	3.88e+08	1.23e+09	9.90e+08	1.19e+09	1.10e+09	1.28e+09	1.45e+09	8.05e+08	2.22e+09	2.36e+09	1.83e+09	1.15e+09	1.16e+09
763	2.37e+08	4.49e+08	6.63e+08	1.11e+09	3.70e+08	1.06e+09	7.35e+08	3.82e+08	1.17e+09	1.23e+09	5.33e+08	9.28e+08	2.05e+09	1.79e+09	1.32e+09	1.34e+09	9.61e+08
863	1.33e+08	3.19e+08	4.36e+08	8.54e+08		1.00e+09	9.20e+08		9.08e+08	8.60e+08	6.42e+08	7.81e+08	1.26e+09	2.38e+09		1.27e+09	9.05e+08
963	2.96e+08	3.70e+08	6.46e+08	9.66e+08	3.75e+08	1.29e+09	8.37e+08	9.54e+08	1.04e+09	7.24e+08	6.41e+08	1.32e+09		1.53e+09	7.43e+08	1.12e+09	8.57e+08
1063	4.86e+08	4.55e+08	1.20e+09	1.15e+09	2.38e+08	1.19e+09	9.28e+08	1.16e+09	1.15e+09	1.17e+09	1.06e+09	9.95e+08	1.50e+09	2.44e+09	3.89e+09	1.05e+09	1.25e+09
1563	5.47e+08	5.49e+08	1.37e+09	1.32e+09	3.90e+08	1.39e+09	1.09e+09	1.13e+09	1.34e+09	1.53e+09	1.56e+08	1.03e+09	1.15e+09	2.20e+09	1.70e+09	1.57e+09	1.15e+09
2063	5.89e+08	7.31e+08	1.74e+09	1.43e+09	5.30e+08	1.57e+09	1.14e+09	1.41e+09	1.58e+09	4.96e+08	1.38e+09	1.08e+09	1.70e+09	2.10e+09	1.68e+09	1.55e+09	1.29e+09
2563	1.48e+09	1.51e+09	1.52e+09	1.53e+09	1.59e+09	1.47e+09	1.39e+09	1.75e+09	1.49e+09	1.49e+09	1.50e+09	1.24e+09	1.65e+09	2.66e+09	2.69e+09	1.56e+09	1.66e+09
Column Average:	5.20e+08	5.98e+08	1.02e+09	1.18e+09	5.55e+08	1.27e+09	1.00e+09	1.14e+09	1.22e+09	1.10e+09	9.20e+08	1.02e+09	1.65e+09	2.18e+09	1.98e+09	1.33e+09	
Set Average:	1.16e+09																

4.5 Determination of SNM Mass

Once the number of fissions has been determined, the mass of the SNM can be determined using the number of fissions and the results of Monte Carlo calculations. The Monte Carlo modeling determined that in the case of the Pu-metal sample the number of fissions is related to the SNM mass by the constant, 2.08793×10^{-3} fissions per source neutron per gram Pu-239. In the case of the HEU, a value of 1.93345×10^{-3} fissions per source neutron per gram U-235 was calculated.

Using the data from the longest cooling period trial from the long count experiments, the SNM mass has been calculated. The results, shown in Table 4.16, are that the mass of the uranium sample is 19.64 g U-235 and the mass of the plutonium sample is 15.32 g Pu-239. The mass calculation was refined by omitting results which were more than one standard deviation from the mean of the full set and computing a new average value. The actual mass values of the samples were 19.37 g U-235 and 15.91 g Pu-239.

Table 4.16. SNM mass determined from the number of induced fissions

Isotope:	Te-134	Sb-130*	I-134	Y-94	Sb-131	Sb-131	Y-95	Ba-142	Rb-89	Ba-142	Ba-142	Rb-89	Cs-139	Xe-138	Xe-138	Xe-138
Gamma Energy:	742.6 keV	793.4 keV	847.0 keV	918.8 keV	933.1 keV	943.4 keV	954.2 keV	1000.9 keV	1031.9 keV	1078.0 keV	1204.1 keV	1248.1 keV	1283.2 keV	1768.3 keV	2004.8 keV	2015.8 keV
Uranium																
Number of Fissions:	1.48e+09	1.51e+09	1.52e+09	1.53e+09	1.59e+09	1.47e+09	1.39e+09	1.75e+09	1.49e+09	1.49e+09	1.50e+09	1.24e+09	1.65e+09	2.66e+09	2.69e+09	1.56e+09
U-235 mass (g):	18.95	19.34	19.44	19.52	20.32	18.78	17.75	22.37	19.05	19.05	19.21	15.89	21.07	33.94	34.33	19.92
Average mass value:	21.18															
Standard Deviation:	5.08															
Average of values within 1 standard deviation of the mean:				19.64	grams U-235											
Revised Standard Deviation:				1.14												
Plutonium																
Number of Fissions:	1.36e+09	1.34e+09	1.32e+09	1.36e+09	3.29e+09	1.28e+09	1.24e+09		1.33e+09	1.27e+09	1.46e+09	1.35e+09		1.12e+09	1.21e+09	1.21e+09
Pu-239 mass (g):	16.08	15.81	15.66	16.10	38.88	15.12	14.61		15.71	15.00	17.23	15.96		13.24	14.31	14.33
Average mass value:	15.87															
Standard Deviation:	7.29															
Average of values within 1 standard deviation of the mean:				15.32	grams Pu-239											
Revised Standard Deviation:				0.99												

Chapter 5

CONCLUSION

5.1 Effectiveness of Material Identification

The material identification technique using relative intensity ratios of observed peaks analyzed by the FOM functions (equations 4.1 and 4.2) conclusively identified the material in each of the four LANL trials. Despite this, the methodology is not without difficulties.

For the identification to be conclusive, as in this work, a relatively large number of intensity ratios should be examined. The ratios require unobscured peaks from the low-mass group to be used in the numerator. Here, only four such peaks proved useful in the later time period data. However, from Table 4.11, every pair of FOM values correctly identified both possible SNM's. Tables 5.1 and 5.2 show the average values of the FOM functions using all of the late time period data for each of the four numerator peaks. A tentative conclusion can be made from any one of these possible numerator options. However, confidence in the determination is enhanced by using multiple peak intensity ratios.

Table 5.1. Average FOM values determined for each numerator isotope for HEU

Numerator:	Rb-89 (1031 keV)	Rb-89 (1248 keV)	Y-94 (919 keV)	Y-95 (954 keV)
FOM_U	50.6	25.5	33.0	70.0
FOM_{Pu}	-2.6	-33.6	-27.6	-14.4

Table 5.2. Average FOM values determined for each numerator isotope for Pu-metal

Numerator:	Rb-89 (1031 keV)	Rb-89 (1248 keV)	Y-94 (919 keV)	Y-95 (954 keV)
FOM_U	-7.2	-6.6	12.6	-1.7
FOM_{Pu}	66.5	68.4	46.8	32.4

A potential difficulty associated with using intensity ratios to identify the SNM in large containers is that if peaks of greatly differing energy are used, rather than energetically similar peaks like those listed in Table 3.1, matrix attenuation must be considered. If the peaks are not energetically similar, the intensity ratios must be constructed from corrected counts using equation 3.1 including a matrix attenuation term. Whereas if the peaks are energetically similar, the matrix attenuation cancels from the ratio and need not be considered.

The FOM functions defined in equations 4.1 and 4.2 are well suited for the required analysis in that an unambiguous identification can be made from the result. Normally, the deviation between an observed and theoretical result can be handled by a more conventional statistical analysis. The difficulty in the present analysis is that the

theoretical results are different for each time interval and each intensity ratio for each material. As such there is no normal distribution of the data which can be exploited in a more conventional analysis. While better methods surely exist, examining the percent deviation from the theoretical expectations for each observed data point is a reasonable approach and does produce unambiguous results.

A convenient attribute of the relative values of FOM_{Pu} and FOM_U is that both results will converge upon ~50 in the case of a matrix containing nearly equal quantities of ^{239}Pu and ^{235}U. If both FOM_{Pu} and FOM_U are strongly positive throughout the entire data set, this sends up a flag that the matrix may be a mixture of SNM's. If this is the case the relative quantities can be determined using the system of linear equations method discussed in section 3.1.

The material identification can be refined by rejecting outlier data. For a given isotope used in an intensity ratio, when the observed temporal trend is compared to the theoretical trends, individual outlier points can be identified and discarded as necessary based upon deviation from the theoretical decay trends. For example, in Figure 4.5f both the ^{235}U and ^{239}Pu observed values in the 2500 second time bin are outliers. The same is true in Figure 4.5l in the 2500 second time bin. These particular outliers produced lower than expected ratio values in the same time bin as seen in Figures 4.9b, 4.9h, and 4.9j. Of particular concern is the identification of outlier data in the low-mass isotopes used as numerators in the ratios as these will propagate throughout the analysis.

5.2. Effectiveness of Material Quantification

Quantification of a containerized SNM using the methods described in Chapter 3 and applied in Chapter 4 hinges upon a number of factors. The SNM, or mix of SNMs, and the energy distribution of the fissions must be precisely determined so that the correct fission yields can be applied in the determination of the number of induced fissions. The attenuation of gamma-rays in the matrix must be accurately accounted for and corrected. The crucial factor which must be determined is modeling the relationship between the number of source neutrons and the number of induced fissions per unit mass of SNM. Difficulties in any of these aspects of the problem will result in an inability to reliably quantify the SNM.

The factor of material identification has been discussed in the previous section. The energy distribution of the fissions can only be determined by Monte Carlo modeling. The matrix attenuation and matrix modeling factors will be addressed in sections 5.3 and 5.4.

5.3. Matrix Attenuation of Gamma-Rays in Cylindrical Samples

The issue of matrix attenuation in samples has been addressed somewhat completely in the past (R91, P86). Transmission corrected passive gamma-ray spectroscopy is typically used to address this problem (P86). However, analytical

solutions to simple cases exist and can be used. The matrix is assumed to have the SNM homogeneously distributed throughout the volume and solutions are generally given for the far-field case. The far-field case assumes that the detector is sufficiently far away that all lines in the plane of the detector from the matrix to the detector are essentially parallel, that is the source-to-detector distance is much greater than the radius of the cylindrical sample.

First consider the planar example shown in Figure 5.1. The drum is of radius, R, and the detector is located to the right. Gamma-Rays must travel through a length of material, L, prior to exiting the drum. The functional form of $L(r,\Theta)$ must first be determined. From Figure 5.1 it is clear that in the far-field approximation that $L = |AB| = |OD| - |OC|$. Simplifying, one arrives at,

$$L(r,\Theta) = R\cos\left(\sin^{-1}\left(\frac{r}{R}\sin(\Theta)\right)\right) - r\cos(\Theta). \qquad \textbf{(5.1)}$$

Once the path length, $L(r,\Theta)$, is defined it remains to integrate the gamma-ray attenuation relation over the area of the circle,

$$\frac{N}{N_0} = \int_A \exp(-\mu L)\, dA. \qquad \textbf{(5.2)}$$

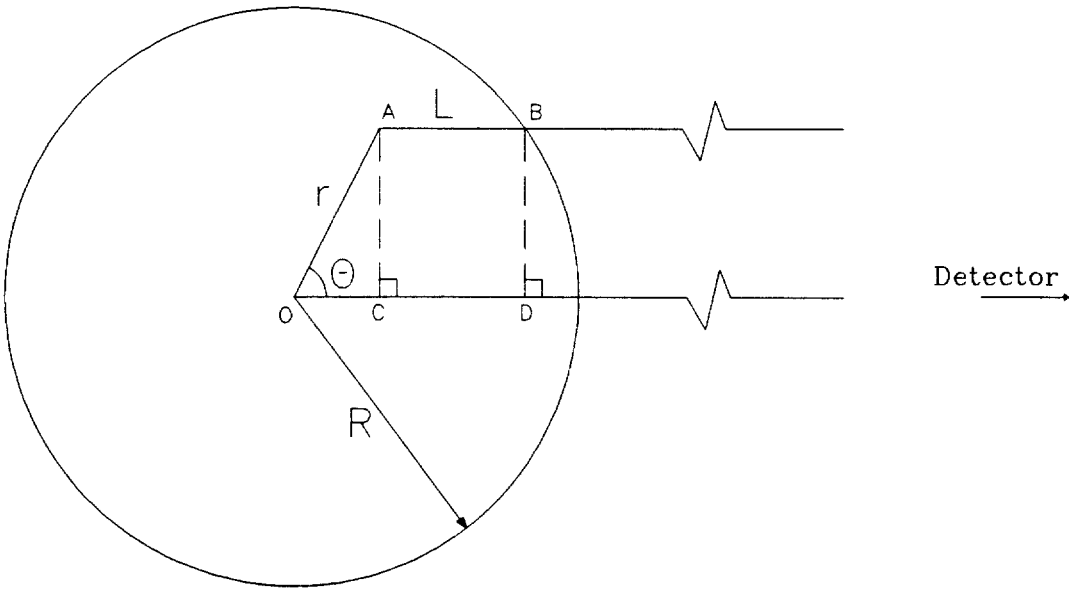

Figure 5.1. Diagram of planar attenuation example.

In polar coordinates, dA = r dr dΘ. Inserting equation 5.1 into the integral equation, one arrives at,

$$\frac{N}{N_0} = \int_0^{2\pi}\int_0^{R} r\exp\left[-\mu\left(R\cos\left(\sin^{-1}\left(\frac{r}{R}\sin(\Theta)\right)\right) - r\cos(\Theta)\right]dr\,d\Theta. \qquad \textbf{(5.3)}$$

Equation 5.3 requires a numeric solution for each value of μ. Figure 5.2 shows the result of numerically integrating equation 5.3 at R = 30 cm for various values of μ.

The cylindrical case has been solved in a closed form in the far-field

approximation (R91). For this case, if the entire drum is in the field of view of the detector the attenuation by the matrix is given by,

$$\frac{N}{N_0} = \frac{hR^2}{2d^2}\left[\frac{I_1(2\mu R) - \mathfrak{L}_1(2\mu R)}{2\mu R}\right] \tag{5.4}$$

where:

h = the height of the cylinder,
R = the radius of the cylinder,
d = the distance between the cylinder and the detector,
μ = the linear attenuation coefficient of the matrix,
I_1 = a modified Bessel function of the first kind.
$\mathfrak{L}_1$ = a modified Struve function.

The modified Bessel function has the form:

$$I_n(x) = \sum_{k=0}^{\infty} \frac{(x/2)^{n+2k}}{k!\,\Gamma(n+k+1)} \tag{5.5}$$

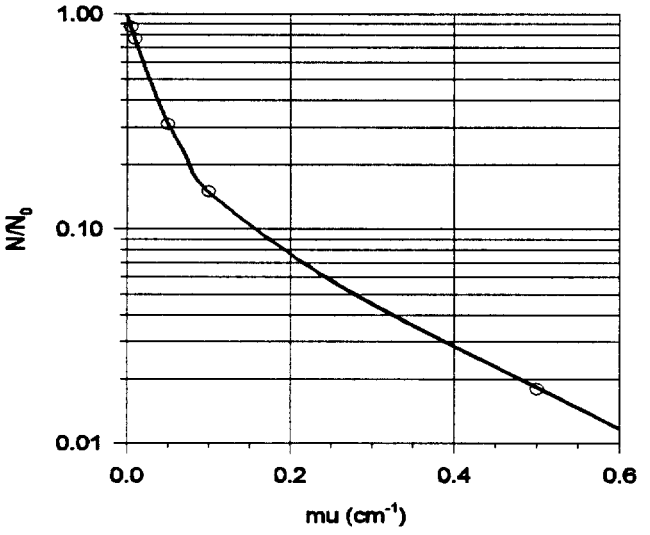

Figure 5.2. Result of Numerically integrating equation 5.3 at R=30 cm

and the modified Struve function has the form,

$$\mathcal{L}_n(x) = (x/2)^{n+1} \sum_{k=0}^{\infty} \frac{(x/2)^{2k}}{\Gamma(k+3/2)\,\Gamma(k+n+3/2)}. \qquad \textbf{(5.6)}$$

A less cumbersome approximate solution for the near-field geometry has also been presented (W72). If $\mu < 0.1$ cm^{-1}, the solution becomes,

$$\frac{N}{N_0} = \frac{d + \dfrac{(3\pi/8)\,R}{3\pi/8 + 1/2\sqrt{\mu R}}}{d + R} \exp\left[\frac{(3\pi/8)\,\mu R}{(3\pi/8) + 1/2\sqrt{\mu R}}\right] \qquad \textbf{(5.7)}$$

5.4 Determination of the Relation Between the Number of Source Neutrons and the Number of Induced Fissions

Even in the simplest matrices, the term, η_f, the number of induced fissions per source neutron per unit mass can only be accurately determined using Monte Carlo methods. Unfortunately, if a container is so poorly characterized that the identity of the SNM is in question, there is little possibility that the matrix is sufficiently well-defined that it can be adequately modeled to determine the value of η_f.

There exist a few cases of interest where the matrix may be sufficiently well-defined to permit modeling of the fission response of the system where the SNM could be

unknown. Tables 5.3 and 5.4 show the results of modeling polyethylene shavings (1/10th nominal density), ordinary concrete, diatomaceous earth and glass in a rotating 55-gallon drum with ^{235}U and ^{239}Pu homogeneously distributed throughout the matrix. The source neutron energies were modeled using a ^{252}Cf fission spectrum. For SNM masses greater than 10 g the fission response develops non-linearities which would require additional modeling and the development of a higher order relation for η_f.

Table 5.3. Fission response in various matrices for ^{235}U masses ≤ 10.0 g.

Matrix	η_f (g^{-1}) (thermal)	η_f (g^{-1}) (epithermal)	η_f (g^{-1}) (14 MeV)	η_f (g^{-1}) Total
Polyethylene	1.487×10^{-5}	1.823×10^{-7}	4.662×10^{-11}	1.503×10^{-5}
Concrete	2.673×10^{-5}	1.026×10^{-7}	1.479×10^{-11}	2.684×10^{-5}
D.E.	1.946×10^{-8}	1.015×10^{-7}	1.792×10^{-11}	1.209×10^{-7}
Glass	1.107×10^{-6}	1.510×10^{-6}	1.667×10^{-10}	2.617×10^{-6}

Table 5.4. Fission response in various matrices for ^{239}Pu masses ≤ 10.0 g.

Matrix	η_f (g^{-1}) (thermal)	η_f (g^{-1}) (epithermal)	η_f (g^{-1}) (14 MeV)	η_f (g^{-1}) Total
Polyethylene	2.3352×10^{-5}	2.677×10^{-7}	5.729×10^{-11}	2.362×10^{-5}
Concrete	4.124×10^{-5}	1.503×10^{-7}	1.813×10^{-11}	4.139×10^{-5}
D.E.	2.175×10^{-8}	1.491×10^{-7}	2.202×10^{-11}	1.708×10^{-7}
Glass	1.093×10^{-6}	$2.212 \times 10^{-}$	3.305×10^{-10}	3.305×10^{-6}

5.5 Effect of Matrix and SNM heterogeneity

If the SNM is present in the matrix in a heterogeneous distribution a myriad of difficulties ensue. If the matrix itself is heterogeneous the situation worsens. Unfortunately, typical compacted facilities waste falls into this category, and older mixed wastes which were not stabilized will have settled into a heterogeneous distribution and thus cannot be quantified by the present method.

Matrix and SNM heterogeneity create a situation where the fission response, η_f, of the system cannot be adequately modeled. Without this information, quantification becomes impossible. Even if the matrix is sufficiently well-defined to permit accurate modeling, if the SNM is dispersed in only a few small lumps within a moderating matrix, the mass determination may be lower than the true value. This is due to the inability to adequately interrogate the entire volume down to a sufficiently small scale to induce enough fissions to produce an adequate signal strength. If large lumps of SNM are present in the sample, the mass determination will again be lower than reality. This is caused by the fact that a thermal neutron will only penetrate 0.25 - 0.38 mm in a metallic SNM before inducing a fission and as a result, only the surface of a lump of dimension greater than ~0.7 mm is interrogated.

Matrix heterogeneity also complicates the gamma-ray counting portion of the analysis. The gamma-ray attenuation discussed in section 5.3 becomes null and void.

The matrix no longer has a unique value of μ, and in the case of a heterogeneous distribution of the SNM, the path length of the exiting gamma-rays is unknown. These difficulties can be alleviated to some extent by using the transmission corrected gamma-ray counting techniques developed by Jack Parker at Los Alamos National Laboratory (P86). The method involves counting a calibrated gamma-ray source transmitted through the matrix during the actual gamma count. The transmission source needs to be similar in energy to the peak of interest so that the value of μ associated with the calibration peak can be considered equal to μ of the observed peak. The transmission correction method also provides an improved means of making dead-time and detector efficiency corrections to the raw data by virtue of knowing the number of transmission gamma-rays emitted from the calibrated source. In the present method, gamma-ray peaks in a wide energy range are potentially of interest. If this is the case, the basic transmission correction method is of limited usefulness. The use of multiple transmission sources worsens counting statistics by increasing the dead-time of the system requiring increased real counting times. Also, the peak density of a fission product gamma-ray spectrum is so high that one is hard pressed to find a number of energies where the transmission source will not overlap the existing peaks. However, one can modify the transmission correction method and use a small number of transmission sources to obtain values of μ at a few energies throughout the energetic region of interest. From this data and knowledge of the general trends of μ(E), values of μ can be reliably determined. One possible isotopic gamma-ray source which would prove useful in this application is ^{60}Co

with gamma-rays at 1173 keV and 1332 keV.

If a sample has a heterogeneous nature, the present method, without employing transmission correction techniques, is not well suited for quantification of the SNM. Other techniques such as the TGS should be employed in this case. However, the SNM identity can still be determined if the intensity ratios are calculated from energetically similar gamma-rays such as those listed in table 3.1. This fact may make the present method useful when used in conjunction with more robust quantification techniques.

5.6 Correction of Serial Decay Equations for Finite Irradiation Times

The serial decay equations derived in Appendix A and employed in Chapter 4 included the basic assumption that the fissions occurred in a burst fashion immediately prior to t=0. It was observed in Tables 4.12 through 4.15 that this assumption resulted in low estimates of the number of induced fissions until a cooling period of ~$25t_{irr}$ had lapsed. This is a reasonable observation, after such a protracted cooling period the irradiation time period is of little consequence. However, in larger samples with lesser quantities of SNM, the required irradiation periods to obtain adequate signal intensity will increase significantly and one may not be able to wait for this needless assumption to become valid.

The equations derived in Appendix A are completely valid, it is only the values of N_{X0} which require modification to accommodate the finite irradiation period. If the time

datum is left at t=0 at the cessation of the irradiation, the revised values of N_{X0} can simply be inserted in the existing equations.

The governing differential equation for simultaneous production and decay of an isotope, X, is,

$$dN_X = -\lambda_X N_X dt + R_X dt \tag{5.8}$$

where,

N_X = number of atoms of isotope X,
λ_X = the decay constant of isotope X,
R_X = the production rate of isotope X
= (fission rate)(fission yield)$_X$ = constant.

Using the substitution,

$$v = \exp(\lambda_X t) \tag{5.9}$$

equation 5.8 reduces to,

$$N_X = \frac{1}{v}\int_{-t_{irr}}^{t} vR_X dt + \frac{C}{v}. \tag{5.10}$$

Solving the integral,

$$N_X = \frac{R_X}{\lambda_X}\left(1 - \exp(-\lambda_X(t_{irr} + t))\right) + C\exp(-\lambda_X t). \tag{5.11}$$

Applying the boundary condition that at $t = -t_{irr}$, $N_X = 0$, one determines that C=0. Thus,

$$N_X = \frac{R_X}{\lambda_X}\left(1 - \exp(-\lambda_X(t_{irr} + t))\right) \quad \textbf{(5.12)}$$

and at t = 0,

$$N_{X0} = \frac{R_X}{\lambda_X}\left(1 - \exp(-\lambda_X t_{irr})\right). \quad \textbf{(5.13)}$$

The differential equation for isotope A in the decay scheme depicted in Figure A1 becomes,

$$\frac{dN_A}{dt} - \lambda_A N_A = f_{A1}^{IT} R_{A1}\left[1 - \exp(-\lambda_{A1}(t_{irr} + t))\right] + f_{A2}^{IT} R_{A2}\left[1 - \exp(-\lambda_{A2}(t_{irr} + t))\right] + R_A \quad \textbf{(5.14)}$$

where all terms are as defined above and in Appendix A.

Making the appropriate substitution ($v = \exp(\lambda_A t)$) and solving one arrives at,

$$\begin{aligned} N_A = {} & f_{A1}^{IT} R_{A1}\left[\frac{1}{\lambda_A}\left(1 - \exp(-\lambda_A(t_{irr} + t))\right) - \frac{1}{\lambda_A - \lambda_{A1}}\left(\exp(-\lambda_{A1}(t_{irr} + t)) - \exp(-\lambda_A(t_{irr} + t))\right)\right] \\ & + f_{A2}^{IT} R_{A2}\left[\frac{1}{\lambda_A}\left(1 - \exp(-\lambda_A(t_{irr} + t))\right) - \frac{1}{\lambda_A - \lambda_{A2}}\left(\exp(-\lambda_{A2}(t_{irr} + t)) - \exp(-\lambda_A(t_{irr} + t))\right)\right] \\ & + \frac{R_A}{\lambda_A}\left(1 - \exp(-\lambda_A(t_{irr} + t))\right) + C\exp(-\lambda_A t). \end{aligned}$$

Applying the boundary condition that at $t = -t_{irr}$, $N_A = 0$ yields C=0. Thus at t = 0,

$$N_{A0} = f_{A1}^{IT} R_{A1}\left[\frac{1}{\lambda_A}\left(1 - \exp(-\lambda_A t_{irr})\right) - \frac{1}{\lambda_A - \lambda_{A1}}\left(\exp(-\lambda_{A1} t_{irr}) - \exp(-\lambda_A t_{irr})\right)\right]$$
$$+ f_{A2}^{IT} R_{A2}\left[\frac{1}{\lambda_A}\left(1 - \exp(-\lambda_A t_{irr})\right) - \frac{1}{\lambda_A - \lambda_{A2}}\left(\exp(-\lambda_{A2} t_{irr}) - \exp(-\lambda_A t_{irr})\right)\right] \quad \textbf{(5.15)}$$
$$+ \frac{R_A}{\lambda_A}\left(1 - \exp(-\lambda_A t_{irr})\right)$$

The rest of the N_{X0} correction terms from the decay scheme shown in Figure A1 are provided without derivation in Appendix D.

5.7 Conclusion

The methods developed in this work make it feasible to distinguish ^{235}U and ^{239}Pu in an unknown matrix by examining fission product gamma-ray intensity ratios. If the matrix is sufficiently well-defined and homogeneous with the SNM evenly dispersed the SNM can also be quantified. Even in the heterogeneous case, if the required fission product gamma-rays can be observed, the material can be identified.

If the material is contained in a 55-gallon drum and the drum is rotated, from Tables 5.1 and 5.2, approximately 10^{15} neutrons need to be introduced into the system to produce sufficient signal strength to perform an analysis. This requires a substantial neutron source be used to avoid protracted irradiation periods. A 0.5 gram ^{252}Cf source (1.3×10^{12} n/s) would meet the requirement and result in irradiation periods on the order of 1000 seconds. There also exist very high flux neutron generators based upon a

continuous (d,t) reaction which can produce source terms of 10^{12} n/s.

While difficulties exist in the material quantification aspect of this technique, in nearly any type of matrix, homogeneous or heterogeneous, provided a sufficient number of fissions can be induced (~ 10^9 - 10^{10}), the SNM can be unambiguously identified with a high degree of confidence. As such, this technique could be used in conjunction with a less matrix dependent quantification methodology. For example, an uncorrelated neutron source (AmLi, (d,t) neutron generator) could be used to induce fissions while simultaneously employing neutron coincidence counting. Subsequent gamma-ray spectroscopy can identify the SNM via the present method and thereby allow interpretation of the active coincidence counting data to determine the mass of the SNM.

REFERENCES CITED

A65 Anderson, C.A., "Fission Product Yields from Fast (~1 MeV) Neutron Fission of Pu-239", Los Alamos Scientific Laboratory Report, LA-3383, 1965.

A93 Attrep, M., "Fission Product Chemistry", Los Alamos National Laboratory Report, LA-UR-93-4177, 1993.

B79 Blachot, J., "Fission Yields from Spectroscopic Measurements", in Nuclear Spectroscopy of Fission Products, Inst. of Physics, Bristol & London, Conf. Series #51, (1979) 161.

B92 Beddingfield, D.H. and Menlove, H.O., "Statistical Data Filtration in Neutron Coincidence Counting," Los Alamos National Laboratory report, LA-12451-MS, 1992.

B93 Briesmeister, J., Ed., "MCNP--A General Monte Carlo N-Particle Code, Version 4A," Loa Alamos National Laboratory Report, LA-12625-M, 1993.

C77 Crouch, A.C., "Fission-Product Yields from Neutron-Induced Fission", Atomic Data and Nuclear Data Tables, 19 (1977) 417.

C82 Cobb, D., Phillips, J., Bosler, G., et al, "Nondestructive Verification and Assay Systems for Spent Fuels," Los Alamos National Laboratory report, LA-9041, Vol. 1, 1982.

D93 Dewey, H.J., "Chemical Separation of Transuranics and Fission Products", Los Alamos National Laboratory Report, LA-UR-93-873, 1993.

E79 England, T.R., "Fission Product Yield Status", Los Alamos National Laboratory Report, LA-UR-79-1222, 1979.

E79a England, T.R., "Data Testing of Preliminary Fission Product Decay File Data", Los Alamos National Laboratory Report, LA-UR-79-1193, 1979

E93 England, T.R. and Rider, B.F., "Evaluation and Compillation of Fission Product Yields", Los Alamos National Laboratory Report, LA-UR-94-3106, 1994.

E94 England, T.R., "Fission Product Yield Evaluation for the U.S.A. Evaluated Nuclear Data Files", Los Alamos National Laboratory Report, LA-UR-94-3318, 1994.

G81 Gonzani, T., Active Nondestructive Assay of Nuclear Materials - Principles and Applications, NUREG/CR-0602, U.S. Nuclear Regulatory Commision, Washington DC, 1981.

J79 Jurney, E.T., Bendt, P.J., England, T.R., "Fission Product Gamma Spectra", Los Alamos Scientific Report, LA-7620-MS, 1979.

K91 Katakura, J., England, T.R., "Augmentation of ENDF/B Fission Product Gamma-Ray Spectra by Calculated Spectra", Los Alamos National Laboratory Report, LA-12125-MS, 1991.

K92 Kawai, M., Iijima, S., Nakagawa, T., et al, "JENDL-3 Fission Product Nuclear Data Library", Nucl. Sci. & Tech., 29 (1992) 195.

L77 LaBauve, R.J., England, T.R., Stamatelatos, M.G., and George, D.C., "Approximations to Summation Calculations of Delayed Energy and Spectra from Fission Products", Los Alamos National Laboratory Report, LA-6684-MS, 1977.

L81 LaBauve, R.J., England, T.R., George, D.C. and Maynard, C.W., "Fission Product Analytic Impulse Source Functions", Los Alamos National Laboratory Report, LA-UR-81-908, 1981.

L81a LaBauve, R.J., George, D.C. and England, T.R., "Delayed Photon Spectra from ENDF/B-V Fission Product Data", Los Alamos National Laboratory Report, LA-UR-81-123, 1981.

L81b LaBauve, R.J., England, T.R. and George, D.C., "Integral Data Testing of ENDF/B Fission Product Data with Other Fission Product Data Files", Los Alamos National Laboratory Report, LA-9090-MS, 1981.

M39 Meitner,L. and Frisch, O.R., Disintegration of Uranium by Neutrons: A New Type of Nuclear Reaction," Natuure, 143, (1939) 239.

M75 Martin, E.R. and Menlove, H.O., "Multienergy Californium Assay System (MECAS)," in "Nuclear Analysis Research and Development," Los Alamos Scientific Laboratory report, LA-6142-PR, pp 6-9, 1975.

M77 Martin, E.R., Jones, D.F., and Parker, J.L., "Gamma-Ray Measurements with the Segmanted Gamma Scan," Los Alamos Scientific Laboratory report, LA-7059-M, 1977.

M79 Menlove, H.O., "Description and Operation Manual for the Active Well Coincidence Counter," Los Alamos Scientific Laboratory report, LA-7823-M, 1979.

M81 Menlove, H.O., "Description and Performance Characteristics for the Neutron Coincidence Collar for the Verification of Reactor Fuel Assemblies," Los Alamos National Laboratory report, LA-8939-MS, 1981.

M88 Moss, C.E., Atwater, H.F., Deplitch, J.E., et al, "Survey of Delayed Fission Product Gamma Rays", Los Alamos National Laboratory Report, LA-UR-87-4280, 1988.

P38 Pool, M.L. and Quill, L.L., "Radioactivity Induced in the Rare Earth Elements by Fast Neutrons," Phys Rev, 53 (1938) 437.

P86 Parker, J.L., "The Use of Calibration Standards and the Correction for Sample Self-Attenuation in Gamma-Ray Nondestructive Assay," Los Alamos National Laboratory Report, LA-10045, Rev., 1986.

P82 Phillips, J.R., Barnes, B.K. and Barnes, M.L., "Nondestructive Measurement of the radial Two-Dimensional Distributions of Fission Products in Irradiated Fuel Materials", Los Alamos National Laboratory Report, LA-UR-82-1247, 1982.

P92 Petrzhak, K.A., Platygina, E.V., Solonkin, A.A., Teplykh, V.F., Frolov, S.V., and Nebogatikov, V.B., "Mass-Spectrometric Investigation of Fission Product Yields for Neutron Induced Fission of Z-Odd Nuclei", in Fiftieth Anniversary of Nuclear Fission, Nove Science Publishers, Inc. (1992) 607.

P93 Prettyman, T.H., Sprinkle, J.K. Jr., and Sheppard, G.A., "A Weighted Least-Squares Lump Correction Algorithm for Transmission-Corrected Gamma-Ray Nondestructive Assay," Nucl. Mat. Man. XXII, 682, 1993.

P93 Prettyman, T.H., Estep, R.J., and Sheppard, G.A., "Developement of a Tomagraphic Instrument for Gamma-Ray Nondestructive Assay," Los Alamos National Laboratory report, LA-UR-93-2580, Rev. 1, 1993.

P95 Parker, J.L., Private communication, Los Alamos National Laboratory, October, 1995.

R79 Ramalho, A.J.G. and Payne, W.E., "Spent fuel Measurments using High-Resolution Gamma Systems," Nuc. Mat. Man., 8, (1979) 76.

R83 Rogers, D.R., Ed., Handbook of Nuclear Safeguard Measurements Methods, NUREG/CR-2078, U.S. Nuclear Regulatory Commission, Washington, DC, 1983.

R87 Rider, B.J. and England, T.R., "Evaluation of Fission Product Yields for the USA National Nuclear Data Files", Los Alamos National Laboratory Report, LA-UR-87-2462, 1987.

R90 Rudstam, G. and England, T.R., "Test of Pre-ENDF/B-VI Decay Data and Fission Yields", Los Alamos National Laboratory Report, LA-11909-MS, 1990.

R91 Reilly, D., Ensslin, N., and Smith, H., Passive Nondestructive Assay of Nuclear Materials, U.S. Nuclear Regulatory Commision, Washington DC, 1991.

R92 Rinard, P.M., Adams, E.L., Menlove, H.O. and Sprinkle, J.K., Jr., "The Nondestructive Assay of 55-Gallon Drums Containing Uranium and Transuranic Waste Using Passive-Active Shufflers," Los Alamos National Laboratory report, LA-12446-MS, 1992.

S75 Seigert, G., Greif, J., Wollnik, H., et al, "Nuclear Charge Distributionis in the Isobars 92 to 100 Resulting from Thermal Neutron Fission of Uranium-235", Phys. Rev. Lett., 34 (1975) 1034.

S86 Sampson, T.E., "Plutonium Isotopic Composition by Gamma-Ray Spectroscopy: A Review", Los Alamos National Laboratory Report, LA-10750-MS, 1986.

S92 Schillebeeckx, P., Wagemans, C., Deruytter, A.J. and Barthelemy, R., "Comparitive Study of the Fragments' mass and Energy Characteristics in the Spontaneous fission of ^{238}Pu, ^{240}Pu and ^{242}Pu and in the Thermal-Neutron-Induced fission of ^{239}Pu", Nucl. Phys. A, 545 (1992) 623.

S93 Schier, W.A., Campbell, J.M., Couchell, G.P., et al, "Gamma-Ray Study of Short-Lived Aggregate Fission Products From $^{235}U(n,f)$", Los Alamos National Laboratory Report, LA-UR-93-2232, 1993.

W62 Wahl, A.C., Ferguson, R.L., Nethaway, D.R., et al, "Nuclear-Charge Distribution in Low-Energy Fission", Phys. Rev, 126 (1962) 1112.

W72 Whitted, E. , "Derivation of a Near Field Passive γ-Ray Correction Factor", LANL Office Memorandum, Group A-1, April 25, 1972.

W81 Wilson, W.B., England, T.R., LaBauve, R.J., and Boicourt, R.M., "The TOAFEW-V Multigroup Cross-Section Collapsing Code and Library of 154-Group Processed ENDF/B-V Fission Product and Actinide Cross Sections", Los Alamos National Laboratory Report, LA-UR-81-1762, 1981.

APPENDIX A.

Derivation of Serial Decay Equations

Consider the decay scheme depicted in figure A1 that eventually terminates at some stable isotope. At time, t = 0, the various isotopes are present in quantities, N_{A0},

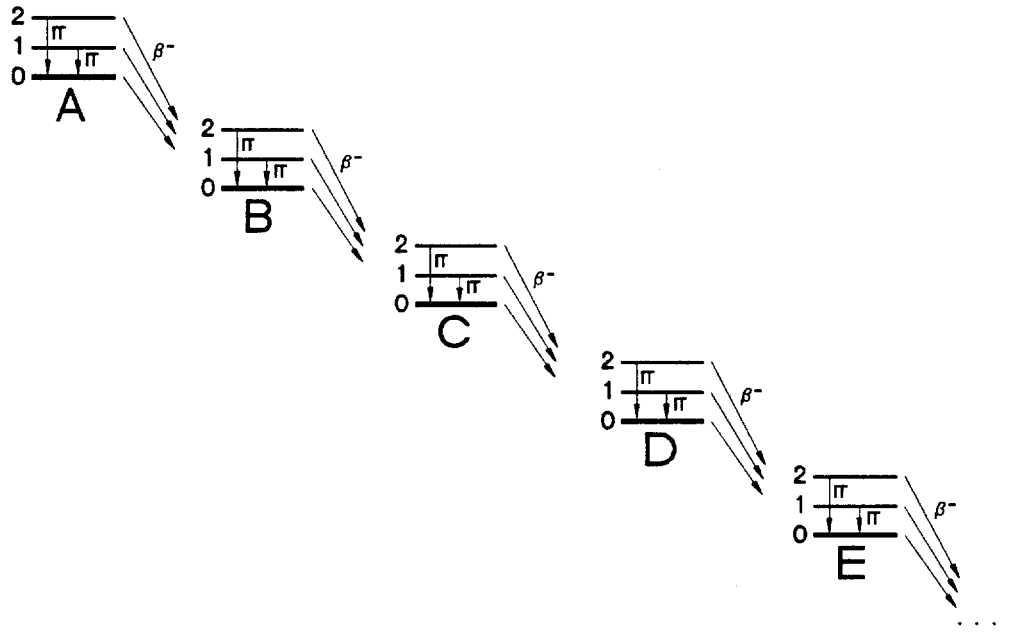

Figure A1. Hypothetical radioactive decay scheme

N_{B0}, N_{C0}, N_{D0}, N_{E0}, etcetera. A derivation of the quantities of each isotope in the decay chain as a function of time is provided below.

Case 1. $N_A(t)$

For the relatively trivial case of isotope A with no metastable components, the change in the number of atoms of A is given by,

$$dN_A = -\lambda_A N_A \, dt$$

where:

N_A is the number of atoms of isotope *A*,
λ_A is the decay constant of isotope *A*,
t is the elapsed time.

Separating variables,

$$\frac{dN_A}{N_A} = -\lambda_A \, dt.$$

Using the boundary condition that at t=0, $N_A = N_{A0}$, the solution of this first order, linear, homogeneous differential equation is given by,

$$N_A(t) = N_{A0} \exp(-\lambda_A t) . \qquad \textbf{(A1)}$$

In the case of two excited/metastable states (*A1* and *A2*), and assuming that all internal conversions produce the ground state isotope, *A*, the balance becomes,

$$\frac{dN_A}{dt} = -\lambda_A N_A + f_{A1}^{IT} \lambda_{A1} N_{A1} + f_{A2}^{IT} \lambda_{A2} N_{A2} .$$

Where,

f_{A1}^{IT} = the fraction of decays of metastable isotope *A1* via internal conversion,
f_{A2}^{IT} = the fraction of decays of metastable isotope *A2* via internal conversion,

and all other terms are as previously defined.

This equation is more readily solved by using the substitution,

$$v = e^{\lambda_A t} \quad \rightarrow \quad \frac{dv}{dt} = \lambda_A e^{\lambda_A t}.$$

Inserting into the balance,

$$v \frac{dN_A}{dt} + N_A d\frac{v}{dt} = v f_{A1}^{IT} \lambda_{A1} N_{A1} + v f_{A2}^{IT} \lambda_{A2} N_{A2}.$$

Applying the boundary conditions that at t=0, $N_A = N_{A0}$, $N_{A1} = N_{A10}$ and $N_{A2} = N_{A20}$,

$$N_A(t) = + f_{A1}^{IT} N_{A10} \frac{\lambda_{A1}}{\lambda_A - \lambda_{A1}} (e^{-\lambda_{A1} t} - e^{-\lambda_A t}) + f_{A2}^{IT} N_{A20} \frac{\lambda_{A2}}{\lambda_A - \lambda_{A2}} (e^{-\lambda_{A2} t} - e^{-\lambda_A t}) + N_{A0} e^{-\lambda_A t}.$$

If one defines,

$$\tilde{\lambda}_{XY} \equiv \frac{\lambda_X}{\lambda_Y - \lambda_X} = \frac{t_{1/2Y}}{t_{1/2X} - t_{1/2X}}$$

and,

$$\Lambda_{XY} \equiv \tilde{\lambda}_{XY} (e^{-\lambda_X t} - e^{-\lambda_Y t}),$$

the result reduces to,

$$N_A(t) = f_{A1}^{IT} N_{A10} \Lambda_{A1A} + f_{A2}^{IT} N_{A20} \Lambda_{A2A} + N_{A0} \exp(-\lambda_A t). \qquad \textbf{(A1')}$$

Case 2. $N_B(t)$

For the case of isotope B, which is being produced by the decay of isotope A and simultaneously decaying, the time rate of change of the number of atoms of B is given by,

$$\frac{dN_B}{dt} = \lambda_A N_A - \lambda_B N_B .$$

Separating variables,

$$\frac{dN_B}{dt} + \lambda_B N_B = \lambda_A N_A .$$

Using the substitution,

$$v = e^{\lambda_B t} \quad \rightarrow \quad \frac{dv}{dt} = \lambda_B e^{\lambda_B t} .$$

the equation becomes,

$$v \frac{dN_B}{dt} + N_B \frac{dv}{dt} = v \lambda_A N_A .$$

Using the boundary conditions that at time t = 0, $N_A = N_{A0}$ and $N_B = N_{B0}$, the equation reduces to,

$$\begin{aligned} N_B(t) &= \left(\frac{\lambda_A N_{A0}}{\lambda_B - \lambda_A} \right) (e^{-\lambda_A t} - e^{-\lambda_B t}) + N_{B0} e^{-\lambda_B t} \\ &= N_{A0} \Lambda_{AB} + N_{B0} \exp(-\lambda_B t) . \end{aligned} \qquad \textbf{(A2)}$$

In the case of the existance of the excited states, *A1*, *A2*, *B1* and *B2*, assuming that the beta decays of *A1* and *A2* produce ground state *B*, the balance becomes,

$$\frac{dN_B}{dt} = f_A^{\beta^-}\lambda_A N_A - \lambda_B N_B + f_{A1}^{\beta^-}\lambda_{A1} N_{A1} + f_{A2}^{\beta^-}\lambda_{A2} N_{A2} + f_{B1}^{IT}\lambda_{B1} N_{B1} + f_{B2}^{IT}\lambda_{B2} N_{B2} .$$

Solving the equation and applying the boundary conditions at t=0,

$$\begin{aligned} N_B(t) = {} & f_A^{\beta^-} f_{A1}^{IT}\tilde{\lambda}_{A1A} N_{A10}\left[\frac{\lambda_A}{\lambda_{A1}}\Lambda_{A1B} - \Lambda_{AB}\right] + f_A^{\beta^-} f_{A2}^{IT}\tilde{\lambda}_{A2A} N_{A20}\left[\frac{\lambda_A}{\lambda_{A2}}\Lambda_{A2B} - \Lambda_{AB}\right] \\ & + f_A^{\beta^-} N_{A0}\Lambda_{AB} + f_{A1}^{\beta^-} N_{A10}\Lambda_{A1B} + f_{A2}^{\beta^-} N_{A20}\Lambda_{A2B} + f_{B1}^{IT} N_{B10}\Lambda_{B1B} \\ & + f_{B2}^{IT} N_{B20}\Lambda_{B2B} + N_{B0}\exp(-\lambda_B t) . \end{aligned} \qquad \textbf{(A2')}$$

Case 3. $N_C(t)$

For the case of isotope *C*, which is being produced by the decay of isotopes *A*, *B* and the metastable isotopes, *B1*, *B2*, *C1* and *C2* , the time rate of change of the number of atoms of *C* is given by,

$$\frac{dN_C}{dt} = f_B^{\beta^-}\lambda_B N_B + f_{B1}^{\beta^-}\lambda_{B1} N_{B1} + f_{B2}^{\beta^-}\lambda_{B2} N_{B2} + f_{C1}^{IT}\lambda_{C1} N_{C1} + f_{C2}^{IT}\lambda_{C2} N_{C2} - \lambda_C N_C .$$

Using the substitution,

$$v = e^{\lambda_C t} \quad \rightarrow \quad \frac{dv}{dt} = \lambda_C e^{\lambda_C t},$$

and the boundary conditions at t=0, the result reduces to,

$$\begin{aligned}
N_C(t) = {} & f_B^{\beta^-} f_A^{\beta^-} f_{A1}^{IT} \tilde{\lambda}_{A1A} N_{A10} \left[\frac{\lambda_A}{\lambda_{A1}} \tilde{\lambda}_{A1B} \left(\frac{\lambda_B}{\lambda_{A1}} \Lambda_{A1C} - \Lambda_{BC} \right) - \tilde{\lambda}_{AB} \left(\frac{\lambda_B}{\lambda_A} \Lambda_{AC} - \Lambda_{BC} \right) \right] \\
& + f_B^{\beta^-} f_A^{\beta^-} f_{A2}^{IT} \tilde{\lambda}_{A2A} N_{A20} \left[\frac{\lambda_A}{\lambda_{A2}} \tilde{\lambda}_{A2B} \left(\frac{\lambda_B}{\lambda_{A2}} \Lambda_{A2C} - \Lambda_{BC} \right) - \tilde{\lambda}_{AB} \left(\frac{\lambda_B}{\lambda_A} \Lambda_{AC} - \Lambda_{BC} \right) \right] \\
& + f_B^{\beta^-} f_A^{\beta^-} \tilde{\lambda}_{AB} N_{A0} \left(\frac{\lambda_B}{\lambda_A} \Lambda_{AC} - \Lambda_{BC} \right) + f_B^{\beta^-} f_{A1}^{\beta^-} \tilde{\lambda}_{A1B} N_{A10} \left(\frac{\lambda_B}{\lambda_{A1}} \Lambda_{A1C} - \Lambda_{BC} \right) \\
& + f_B^{\beta^-} f_{A2}^{\beta^-} \tilde{\lambda}_{A2B} N_{A20} \left(\frac{\lambda_B}{\lambda_{A2}} \Lambda_{A2C} - \Lambda_{BC} \right) + f_B^{\beta^-} f_{B1}^{IT} \tilde{\lambda}_{B1B} N_{B10} \left(\frac{\lambda_B}{\lambda_{B1}} \Lambda_{B1C} - \Lambda_{BC} \right) \\
& + f_B^{\beta^-} f_{B2}^{IT} \tilde{\lambda}_{B2B} N_{B20} \left(\frac{\lambda_B}{\lambda_{B2}} \Lambda_{B2C} - \Lambda_{BC} \right) + f_B^{\beta^-} N_{B0} \Lambda_{BC} + f_{B1}^{\beta^-} N_{B10} \Lambda_{B1C} \\
& + f_{B2}^{\beta^-} N_{B20} \Lambda_{B2C} + f_{C1}^{IT} N_{C10} \Lambda_{C1C} + f_{C2}^{IT} N_{C20} \Lambda_{C2C} + N_{C0} \exp(-\lambda_C t)
\end{aligned} \tag{A3}$$

Case 4. $N_D(t)$

Anologous to the previous cases, the balance for the number of atoms of D considering the metastable states is,

$$\frac{dN_D}{dt} = -\lambda_D N_D + f_C^{\beta^-} \lambda_C N_C + f_{C1}^{\beta^-} \lambda_{C1} N_{C1} + f_{C2}^{\beta^-} \lambda_{C2} N_{C2} + f_{D1}^{IT} \lambda_{D1} N_{D1} + f_{D2}^{IT} \lambda_{D2} N_{D2}.$$

Solving and applying the boundary condition that at $t = 0$, one obtains,

$$
\begin{aligned}
N_D(t) \;=\; & f_C^{\beta^-} f_B^{\beta^-} f_A^{\beta^-} \tilde{\lambda}_{AB} N_{A0} \left[\frac{\lambda_B}{\lambda_A} \tilde{\lambda}_{AC} \left(\frac{\lambda_C}{\lambda_A} \Lambda_{AD} - \Lambda_{CD} \right) - \tilde{\lambda}_{BC} \left(\frac{\lambda_C}{\lambda_B} \Lambda_{BD} - \Lambda_{CD} \right) \right] \\
& + f_C^{\beta^-} f_B^{\beta^-} f_A^{\beta^-} f_{A1}^{IT} \tilde{\lambda}_{A1A} \tilde{\lambda}_{A1B} N_{A10} \frac{\lambda_A}{\lambda_{A1}} \left[\frac{\lambda_B}{\lambda_{A1}} \tilde{\lambda}_{A1C} \left(\frac{\lambda_C}{\lambda_{A1}} \Lambda_{A1D} - \Lambda_{CD} \right) - \tilde{\lambda}_{BC} \left(\frac{\lambda_C}{\lambda_B} \Lambda_{BD} - \Lambda_{CD} \right) \right] \\
& - f_C^{\beta^-} f_B^{\beta^-} f_A^{\beta^-} f_{A1}^{IT} \tilde{\lambda}_{A1A} \tilde{\lambda}_{AB} N_{A10} \left[\frac{\lambda_B}{\lambda_A} \tilde{\lambda}_{AC} \left(\frac{\lambda_C}{\lambda_A} \Lambda_{AD} - \Lambda_{CD} \right) - \tilde{\lambda}_{BC} \left(\frac{\lambda_C}{\lambda_B} \Lambda_{BD} - \Lambda_{CD} \right) \right] \\
& + f_C^{\beta^-} f_B^{\beta^-} f_{A1}^{\beta^-} \tilde{\lambda}_{A1B} N_{A10} \left[\frac{\lambda_B}{\lambda_{A1}} \tilde{\lambda}_{A1C} \left(\frac{\lambda_C}{\lambda_{A1}} \Lambda_{A1D} - \Lambda_{CD} \right) - \tilde{\lambda}_{BC} \left(\frac{\lambda_C}{\lambda_B} \Lambda_{BD} - \Lambda_{CD} \right) \right] \\
& + f_C^{\beta^-} f_B^{\beta^-} f_A^{\beta^-} f_{A2}^{IT} \tilde{\lambda}_{A2A} \tilde{\lambda}_{A2B} N_{A20} \frac{\lambda_A}{\lambda_{A2}} \left[\frac{\lambda_B}{\lambda_{A2}} \tilde{\lambda}_{A2C} \left(\frac{\lambda_C}{\lambda_{A2}} \Lambda_{A2D} - \Lambda_{CD} \right) - \tilde{\lambda}_{BC} \left(\frac{\lambda_C}{\lambda_B} \Lambda_{BD} - \Lambda_{CD} \right) \right] \\
& - f_C^{\beta^-} f_B^{\beta^-} f_A^{\beta^-} f_{A2}^{IT} \tilde{\lambda}_{A2A} \tilde{\lambda}_{AB} N_{A20} \left[\frac{\lambda_B}{\lambda_A} \tilde{\lambda}_{AC} \left(\frac{\lambda_C}{\lambda_A} \Lambda_{AD} - \Lambda_{CD} \right) - \tilde{\lambda}_{BC} \left(\frac{\lambda_C}{\lambda_B} \Lambda_{BD} - \Lambda_{CD} \right) \right] \\
& + f_C^{\beta^-} f_B^{\beta^-} f_{A2}^{\beta^-} \tilde{\lambda}_{A2B} N_{A20} \left[\frac{\lambda_B}{\lambda_{A2}} \tilde{\lambda}_{A2C} \left(\frac{\lambda_C}{\lambda_{A2}} \Lambda_{A2D} - \Lambda_{CD} \right) - \tilde{\lambda}_{BC} \left(\frac{\lambda_C}{\lambda_B} \Lambda_{BD} - \Lambda_{CD} \right) \right] \\
& + f_C^{\beta^-} f_B^{\beta^-} f_{B1}^{IT} \tilde{\lambda}_{B1B} N_{B10} \left[\frac{\lambda_B}{\lambda_{B1}} \tilde{\lambda}_{B1C} \left(\frac{\lambda_C}{\lambda_{B1}} \Lambda_{B1D} - \Lambda_{CD} \right) - \tilde{\lambda}_{BC} \left(\frac{\lambda_C}{\lambda_B} \Lambda_{BD} - \Lambda_{CD} \right) \right] \\
& + f_C^{\beta^-} f_B^{\beta^-} f_{B2}^{IT} \tilde{\lambda}_{B2B} N_{B20} \left[\frac{\lambda_B}{\lambda_{B2}} \tilde{\lambda}_{B2C} \left(\frac{\lambda_C}{\lambda_{B2}} \Lambda_{B2D} - \Lambda_{CD} \right) - \tilde{\lambda}_{BC} \left(\frac{\lambda_C}{\lambda_B} \Lambda_{BD} - \Lambda_{CD} \right) \right] \\
& + f_C^{\beta^-} f_B^{\beta^-} \tilde{\lambda}_{BC} N_{B0} \left(\frac{\lambda_C}{\lambda_B} \Lambda_{BD} - \Lambda_{CD} \right) + f_C^{\beta^-} f_{B1}^{\beta^-} \tilde{\lambda}_{B1C} N_{B10} \left(\frac{\lambda_C}{\lambda_{B1}} \Lambda_{B1D} - \Lambda_{CD} \right) \\
& + f_C^{\beta^-} f_{B2}^{\beta^-} \tilde{\lambda}_{B2C} N_{B20} \left(\frac{\lambda_C}{\lambda_{B2}} \Lambda_{B2D} - \Lambda_{CD} \right) + f_C^{\beta^-} f_{C1}^{IT} \tilde{\lambda}_{C1C} N_{C10} \left(\frac{\lambda_C}{\lambda_{C1}} \Lambda_{C1D} - \Lambda_{CD} \right) \\
& + f_C^{\beta^-} f_{C2}^{IT} \tilde{\lambda}_{C2C} N_{C20} \left(\frac{\lambda_C}{\lambda_{C2}} \Lambda_{C2D} - \Lambda_{CD} \right) + f_C^{\beta^-} N_{C0} \Lambda_{CD} \\
& + f_{C1}^{\beta^-} N_{C10} \Lambda_{C1D} + f_{C2}^{\beta^-} N_{C20} \Lambda_{C2D} + f_{D1}^{IT} N_{D10} \Lambda_{D1D} \\
& + f_{D2}^{IT} N_{D20} \Lambda_{D2D} + N_{D0} \exp(-\lambda_D t)
\end{aligned}
\qquad \textbf{(A4)}
$$

Case 5. $N_E(t)$

The balance for the time rate of change of N_E is,

$$\frac{dN_E}{dt} = -\lambda_E N_E + f_D^{\beta^-} \lambda_D N_D + f_{D1}^{\beta^-} \lambda_{D1} N_{D1} + f_{D2}^{\beta^-} \lambda_{D2} N_{D2} + f_{E1}^{IT} \lambda_{E1} N_{E1} + f_{E2}^{IT} \lambda_{E2} N_{E2}$$

Solving this balance and applying the boundary conditions at t=0, the result reduces to,

$$
\begin{aligned}
N_E(t) \;=\; & f_D^{\beta^-} f_C^{\beta^-} f_B^{\beta^-} f_A^{\beta^-}\, \tilde{\lambda}_{AB}\, N_{A0} \Big[\Big[\frac{\lambda_B}{\lambda_A}\tilde{\lambda}_{AC}\Big[\frac{\lambda_C}{\lambda_A}\tilde{\lambda}_{AD}\Big(\frac{\lambda_D}{\lambda_A}\Lambda_{AE} - \Lambda_{DE}\Big) - \tilde{\lambda}_{CD}\Big(\frac{\lambda_D}{\lambda_C}\Lambda_{CE} - \Lambda_{DE}\Big)\Big] \\
& - \tilde{\lambda}_{BC}\Big[\frac{\lambda_C}{\lambda_B}\tilde{\lambda}_{BD}\Big(\frac{\lambda_D}{\lambda_B}\Lambda_{BE} - \Lambda_{DE}\Big) - \tilde{\lambda}_{CD}\Big(\frac{\lambda_D}{\lambda_C}\Lambda_{CE} - \Lambda_{DE}\Big)\Big]\Big] \\
& + f_D^{\beta^-} f_C^{\beta^-} f_B^{\beta^-} f_A^{\beta^-} f_{A1}^{IT}\, \tilde{\lambda}_{A1A}\, \tilde{\lambda}_{A1B}\, N_{A10}\, \frac{\lambda_A}{\lambda_{A1}} \Big[\Big[\frac{\lambda_B}{\lambda_{A1}}\tilde{\lambda}_{A1C}\Big[\frac{\lambda_C}{\lambda_{A1}}\tilde{\lambda}_{A1D}\Big(\frac{\lambda_D}{\lambda_{A1}}\Lambda_{A1E} - \Lambda_{DE}\Big) - \tilde{\lambda}_{CD}\Big(\frac{\lambda_D}{\lambda_C}\Lambda_{CE} - \Lambda_{DE}\Big)\Big] \\
& - \tilde{\lambda}_{BC}\Big[\frac{\lambda_C}{\lambda_B}\tilde{\lambda}_{BD}\Big(\frac{\lambda_D}{\lambda_B}\Lambda_{BE} - \Lambda_{DE}\Big) - \tilde{\lambda}_{CD}\Big(\frac{\lambda_D}{\lambda_C}\Lambda_{CE} - \Lambda_{DE}\Big)\Big]\Big] \\
& - f_D^{\beta} f_C^{\beta} f_B^{\beta} f_A^{\beta^-} f_{A1}^{IT}\, \tilde{\lambda}_{A1A}\, \tilde{\lambda}_{AB}\, N_{A10} \Big[\Big[\frac{\lambda_B}{\lambda_A}\tilde{\lambda}_{AC}\Big[\frac{\lambda_C}{\lambda_A}\tilde{\lambda}_{AD}\Big(\frac{\lambda_D}{\lambda_A}\Lambda_{BE} - \Lambda_{CE}\Big) - \tilde{\lambda}_{CD}\Big(\frac{\lambda_D}{\lambda_C}\Lambda_{CE} - \Lambda_{DE}\Big)\Big] \\
& - \tilde{\lambda}_{BC}\Big[\frac{\lambda_C}{\lambda_B}\tilde{\lambda}_{BD}\Big(\frac{\lambda_D}{\lambda_B}\Lambda_{BE} - \Lambda_{DE}\Big) - \tilde{\lambda}_{CD}\Big(\frac{\lambda_D}{\lambda_C}\Lambda_{CE} - \Lambda_{DE}\Big)\Big]\Big] \\
& + f_D^{\beta} f_C^{\beta} f_B^{\beta} f_{A1}^{\beta^-}\, \tilde{\lambda}_{A1B}\, N_{A10} \Big[\Big[\frac{\lambda_B}{\lambda_{A1}}\tilde{\lambda}_{A1C}\Big[\frac{\lambda_C}{\lambda_{A1}}\tilde{\lambda}_{A1D}\Big(\frac{\lambda_D}{\lambda_{A1}}\Lambda_{A1E} - \Lambda_{DE}\Big) - \tilde{\lambda}_{CD}\Big(\frac{\lambda_D}{\lambda_C}\Lambda_{CE} - \Lambda_{DE}\Big)\Big] \\
& - \tilde{\lambda}_{BC}\Big[\frac{\lambda_C}{\lambda_B}\tilde{\lambda}_{BD}\Big(\frac{\lambda_D}{\lambda_B}\Lambda_{BE} - \Lambda_{DE}\Big) - \tilde{\lambda}_{CD}\Big(\frac{\lambda_D}{\lambda_C}\Lambda_{CE} - \Lambda_{DE}\Big)\Big]\Big] \\
& + f_D^{\beta^-} f_C^{\beta^-} f_B^{\beta^-} f_{A2}^{IT}\, \tilde{\lambda}_{A2A}\, \tilde{\lambda}_{A2B}\, N_{A20}\, \frac{\lambda_A}{\lambda_{A2}} \Big[\Big[\frac{\lambda_B}{\lambda_{A2}}\tilde{\lambda}_{A2C}\Big[\frac{\lambda_C}{\lambda_{A2}}\tilde{\lambda}_{A2D}\Big(\frac{\lambda_D}{\lambda_{A2}}\Lambda_{A2E} - \Lambda_{DE}\Big) - \tilde{\lambda}_{CD}\Big(\frac{\lambda_D}{\lambda_C}\Lambda_{CE} - \Lambda_{DE}\Big)\Big] \\
& - \tilde{\lambda}_{BC}\Big[\frac{\lambda_C}{\lambda_B}\tilde{\lambda}_{BD}\Big(\frac{\lambda_D}{\lambda_B}\Lambda_{BE} - \Lambda_{DE}\Big) - \tilde{\lambda}_{CD}\Big(\frac{\lambda_D}{\lambda_C}\Lambda_{CE} - \Lambda_{DE}\Big)\Big]\Big] \\
& - f_D^{\beta} f_C^{\beta} f_B^{\beta} f_A^{\beta^-} f_{A2}^{IT}\, \tilde{\lambda}_{A2A}\, \tilde{\lambda}_{AB}\, N_{A20} \Big[\Big[\frac{\lambda_B}{\lambda_A}\tilde{\lambda}_{AC}\Big[\frac{\lambda_C}{\lambda_A}\tilde{\lambda}_{AD}\Big(\frac{\lambda_D}{\lambda_A}\Lambda_{AE} - \Lambda_{DE}\Big) - \tilde{\lambda}_{CD}\Big(\frac{\lambda_D}{\lambda_C}\Lambda_{CE} - \Lambda_{DE}\Big)\Big] \\
& - \tilde{\lambda}_{BC}\Big[\frac{\lambda_C}{\lambda_B}\tilde{\lambda}_{BD}\Big(\frac{\lambda_D}{\lambda_B}\Lambda_{BE} - \Lambda_{DE}\Big) - \tilde{\lambda}_{CD}\Big(\frac{\lambda_D}{\lambda_C}\Lambda_{CE} - \Lambda_{DE}\Big)\Big]\Big] \\
& + f_D^{\beta} f_C^{\beta} f_B^{\beta} f_{A2}^{\beta^-}\, \tilde{\lambda}_{A2B} N_{A20} \Big[\Big[\frac{\lambda_B}{\lambda_{A2}}\tilde{\lambda}_{A2C}\Big[\frac{\lambda_C}{\lambda_{A2}}\tilde{\lambda}_{A2D}\Big(\frac{\lambda_D}{\lambda_{A2}}\Lambda_{A2E} - \Lambda_{DE}\Big) - \tilde{\lambda}_{CD}\Big(\frac{\lambda_D}{\lambda_C}\Lambda_{CE} - \Lambda_{DE}\Big)\Big] \\
& - \tilde{\lambda}_{BC}\Big[\frac{\lambda_C}{\lambda_B}\tilde{\lambda}_{BD}\Big(\frac{\lambda_D}{\lambda_B}\Lambda_{BE} - \Lambda_{DE}\Big) - \tilde{\lambda}_{CD}\Big(\frac{\lambda_D}{\lambda_C}\Lambda_{CE} - \Lambda_{DE}\Big)\Big]\Big] \\
& + f_D^{\beta} f_C^{\beta} f_B^{\beta} \tilde{\lambda}_{BC}\, N_{B0}\Big[\frac{\lambda_C}{\lambda_B}\tilde{\lambda}_{BD}\Big(\frac{\lambda_D}{\lambda_{B2}}\Lambda_{BE} - \Lambda_{DE}\Big) - \tilde{\lambda}_{CD}\Big(\frac{\lambda_D}{\lambda_C}\Lambda_{CE} - \Lambda_{DE}\Big)\Big] \\
& + f_D^{\beta} f_C^{\beta} f_B^{\beta} f_{B1}^{IT} \tilde{\lambda}_{B1B}\, N_{B10}\Big[\Big[\frac{\lambda_B}{\lambda_{B1}}\tilde{\lambda}_{B1C}\Big[\frac{\lambda_C}{\lambda_{B1}}\tilde{\lambda}_{B1D}\Big(\frac{\lambda_D}{\lambda_{B1}}\Lambda_{B1E} - \Lambda_{DE}\Big) - \tilde{\lambda}_{CD}\Big(\frac{\lambda_D}{\lambda_E}\Lambda_{CE} - \Lambda_{DE}\Big)\Big] \\
& - \tilde{\lambda}_{BC}\Big[\frac{\lambda_C}{\lambda_B}\tilde{\lambda}_{BD}\Big(\frac{\lambda_D}{\lambda_B}\Lambda_{BE} - \Lambda_{DE}\Big) - \tilde{\lambda}_{CD}\Big(\frac{\lambda_D}{\lambda_C}\Lambda_{CE} - \Lambda_{DE}\Big)\Big]\Big] \\
& + f_D^{\beta} f_C^{\beta} f_{B1}^{\beta} \tilde{\lambda}_{B1C}\, N_{B10}\Big[\frac{\lambda_C}{\lambda_{B1}}\tilde{\lambda}_{B1D}\Big(\frac{\lambda_D}{\lambda_{B1}}\Lambda_{B1E} - \Lambda_{DE}\Big) - \tilde{\lambda}_{CD}\Big(\frac{\lambda_D}{\lambda_C}\Lambda_{CE} - \Lambda_{DE}\Big)\Big]
\end{aligned}
\qquad \textbf{(A6)}
$$

$$+ f_D^{\beta^-} f_C^{\beta^-} f_B^{\beta^-} f_{B2}^{IT} \tilde{\lambda}_{B2B} N_{B20} \left[\left[\frac{\lambda_B}{\lambda_{B2}} \tilde{\lambda}_{B2C} \left[\frac{\lambda_C}{\lambda_{B2}} \tilde{\lambda}_{B2D} \left(\frac{\lambda_D}{\lambda_{B2}} \Lambda_{B2E} - \Lambda_{DE} \right) - \tilde{\lambda}_{CD} \left(\frac{\lambda_D}{\lambda_D} \Lambda_{CE} - \Lambda_{DE} \right) \right] \right. \right.$$

$$\left. \left. - \tilde{\lambda}_{BC} \left[\frac{\lambda_C}{\lambda_B} \tilde{\lambda}_{BD} \left(\frac{\lambda_D}{\lambda_B} \Lambda_{BE} - \Lambda_{DE} \right) - \tilde{\lambda}_{CD} \left(\frac{\lambda_D}{\lambda_C} \Lambda_{CE} - \Lambda_{DE} \right) \right] \right] \right]$$

$$+ f_D^{\beta^-} f_C^{\beta^-} f_{B2}^{\beta^-} \tilde{\lambda}_{B2C} N_{B20} \left[\frac{\lambda_C}{\lambda_{B2}} \tilde{\lambda}_{B2D} \left(\frac{\lambda_D}{\lambda_{B2}} \Lambda_{B2E} - \Lambda_{DE} \right) - \tilde{\lambda}_{CD} \left(\frac{\lambda_D}{\lambda_C} \Lambda_{CE} - \Lambda_{DE} \right) \right]$$

$$+ f_D^{\beta^-} f_C^{\beta^-} f_{C1}^{IT} \tilde{\lambda}_{C1C} N_{C10} \left[\frac{\lambda_C}{\lambda_{C1}} \tilde{\lambda}_{C1D} \left(\frac{\lambda_D}{\lambda_{C1}} \Lambda_{C1E} - \Lambda_{CE} \right) - \tilde{\lambda}_{CD} \left(\frac{\lambda_D}{\lambda_C} \Lambda_{CE} - \Lambda_{DE} \right) \right]$$

$$+ f_D^{\beta^-} f_C^{\beta^-} f_{C2}^{IT} \tilde{\lambda}_{C2C} N_{C20} \left[\frac{\lambda_C}{\lambda_{C2}} \tilde{\lambda}_{C2D} \left(\frac{\lambda_D}{\lambda_{C2}} \Lambda_{C2E} - \Lambda_{DE} \right) - \tilde{\lambda}_{CD} \left(\frac{\lambda_D}{\lambda_C} \Lambda_{CE} - \Lambda_{DE} \right) \right]$$

$$+ f_D^{\beta^-} f_C^{\beta^-} \tilde{\lambda}_{CD} N_{C0} \left(\frac{\lambda_D}{\lambda_C} \Lambda_{CE} - \Lambda_{DE} \right) + f_D^{\beta^-} f_{C1}^{\beta^-} \tilde{\lambda}_{C1D} N_{C10} \left(\frac{\lambda_D}{\lambda_{C1}} \Lambda_{C1E} - \Lambda_{DE} \right)$$

$$+ f_D^{\beta^-} f_{C2}^{\beta^-} N_{C20} \tilde{\lambda}_{C2D} N_{C20} \left(\frac{\lambda_D}{\lambda_{C2}} \Lambda_{C2E} - \Lambda_{DE} \right) + f_D^{\beta^-} f_{D1}^{IT} \tilde{\lambda}_{D1D} N_{D10} \left(\frac{\lambda_D}{\lambda_{D1}} \Lambda_{D1E} - \Lambda_{DE} \right)$$

$$+ f_D^{\beta^-} f_{D2}^{IT} \tilde{\lambda}_{D2D} N_{D20} \left(\frac{\lambda_D}{\lambda_{D2}} \Lambda_{D2E} - \Lambda_{DE} \right) + f_D^{\beta^-} N_{D0} \Lambda_{DE}$$

$$+ f_{D1}^{\beta^-} N_{D10} \Lambda_{D1E} + f_{D2}^{\beta^-} N_{D20} \Lambda_{D2E} + f_{E1}^{IT} N_{E10} \Lambda_{E1E}$$

$$+ f_{E2}^{IT} N_{E20} \Lambda_{E2E} + N_{E0} \exp(-\lambda_E t) .$$

APPENDIX B

Lanl Irradiation Apparatus Design

Figures B1 and B2 show the design dimensions of the irradiation apparatus used in the LANL Cf-252 irradiation trials.

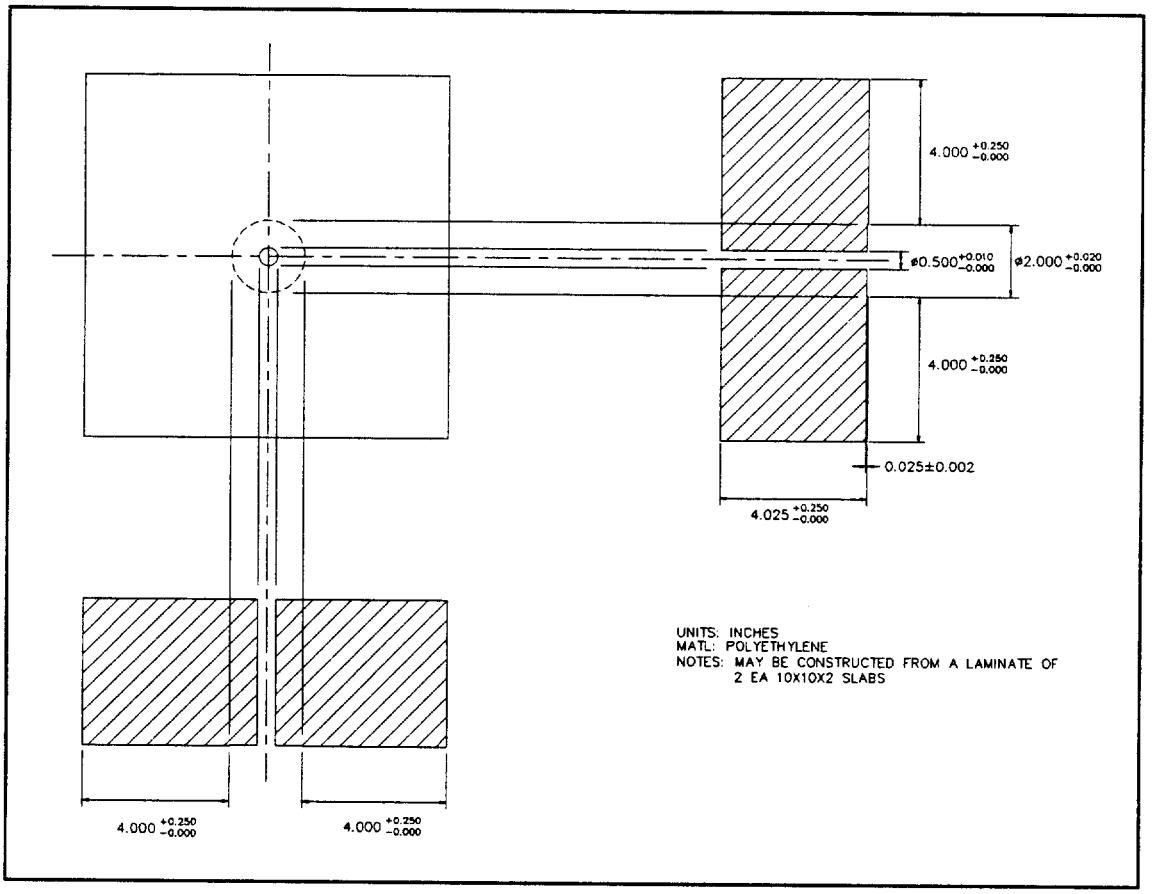

Figure B1. Top assembly of Cf-252 irradiation apparatus

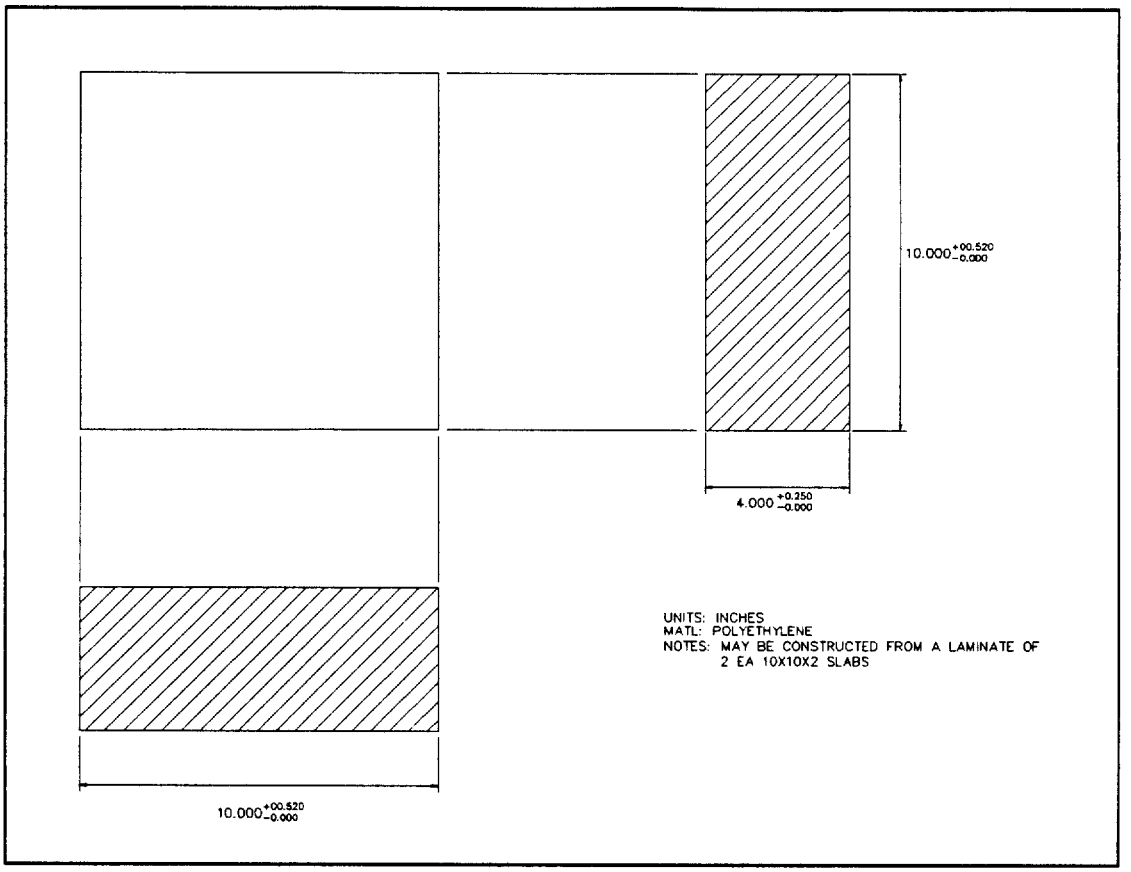

Figure B2. Bottom assembly of Cf-252 irradiation aparatus

APPENDIX C

Fission Product Gamma-Ray Spectra

This appendix contains complete fission product gamma-ray spectra from the LANL Cf-252 late time period trials. Both ^{235}U and ^{239}Pu spectra are provided at three cooling times. Each spectrum is shown in a complete figure followed by ten figures showing the spectrum in 250 keV increments.

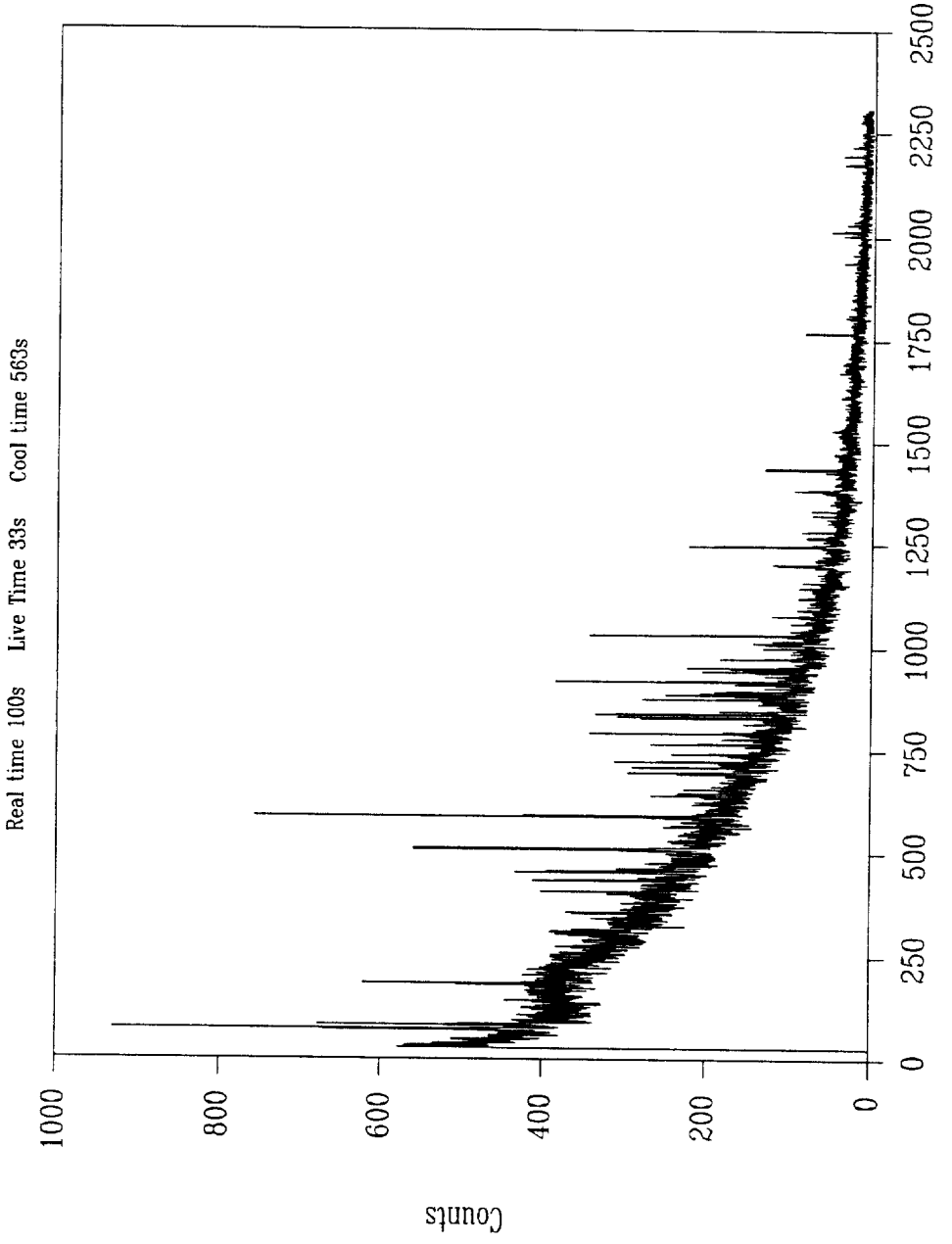

Figure C1. Entire U-235 fission product gamma-ray spectrum

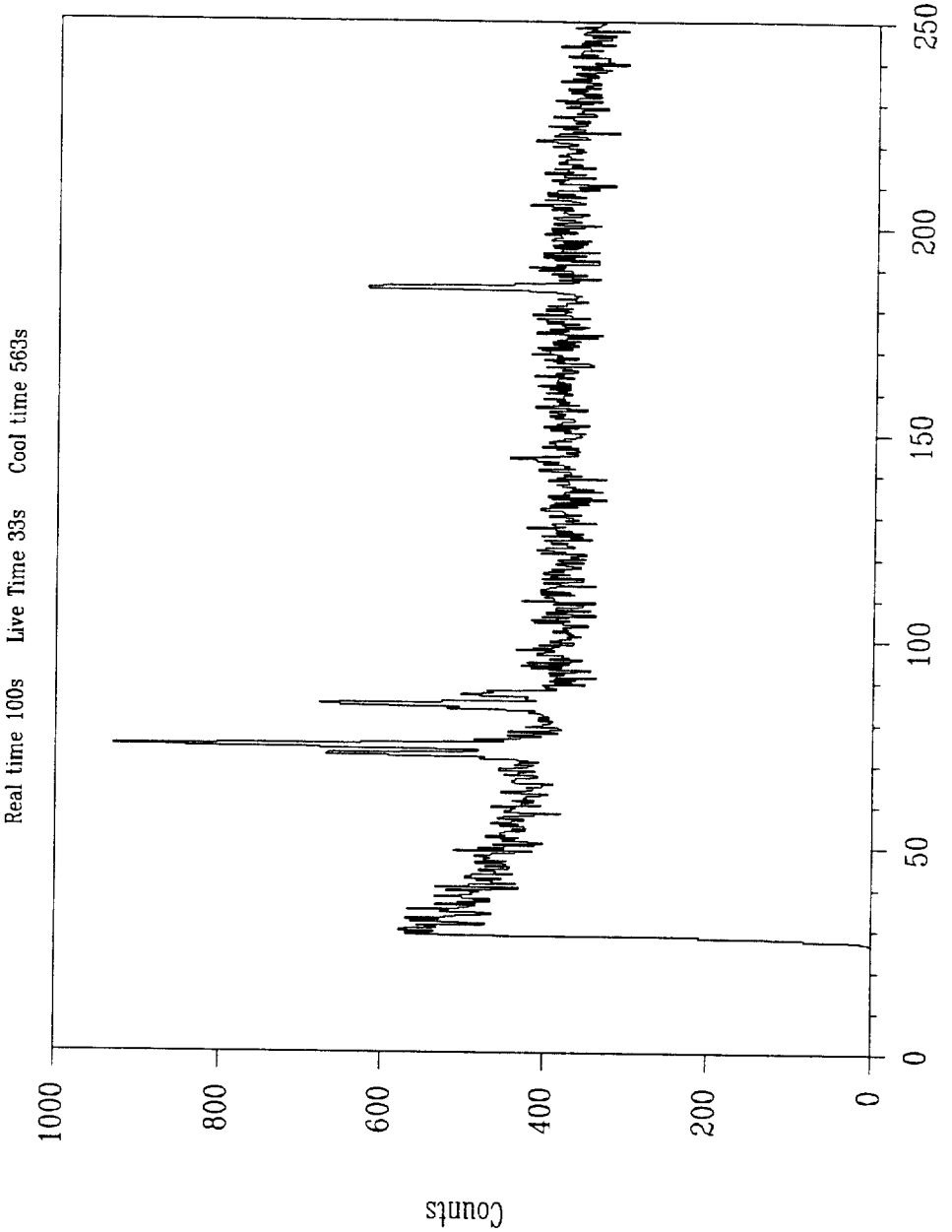

Figure C2. U-235 fission product gamma-ray spectrum from 0 - 250 keV

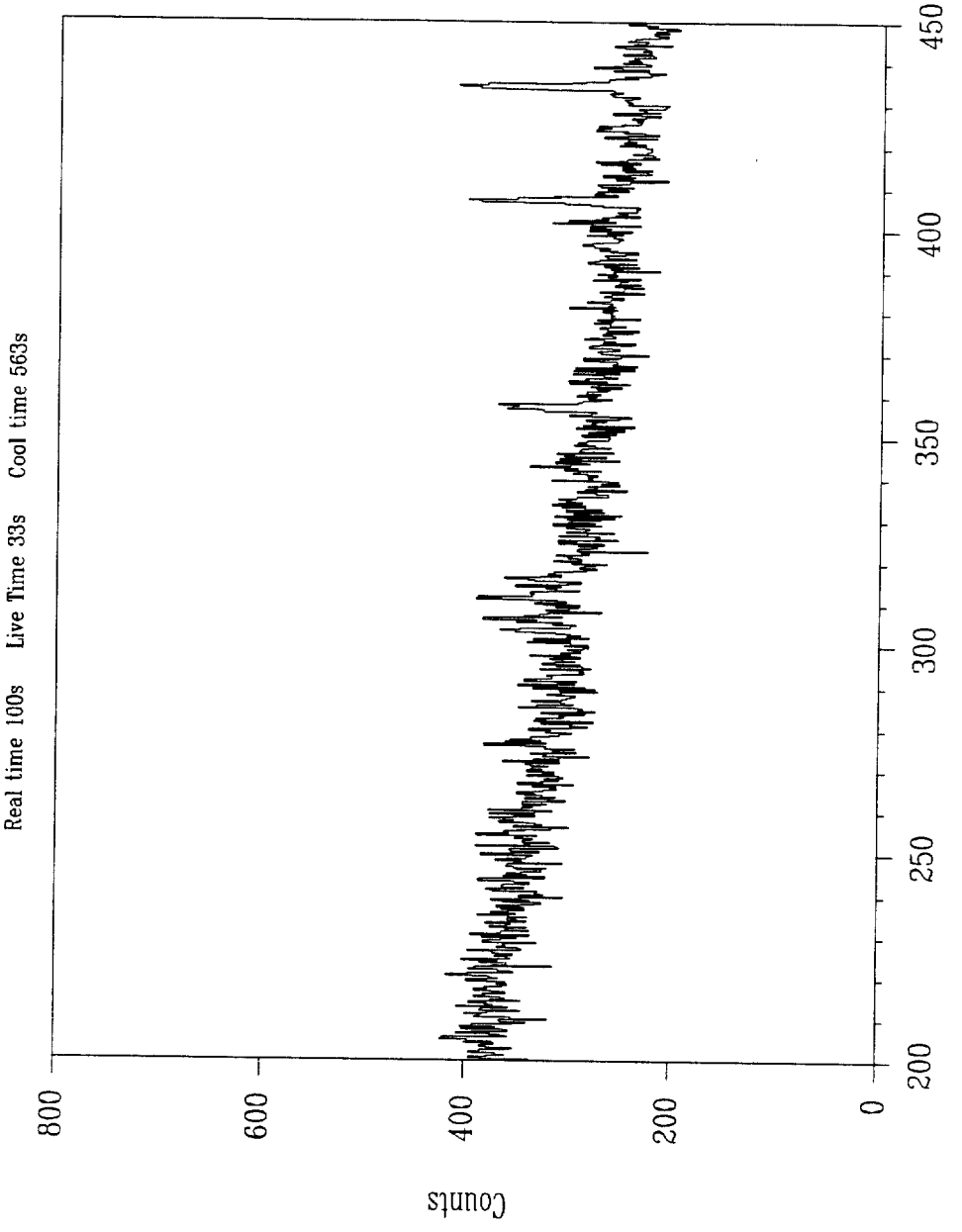

Figure C3. U-235 fission product gamma-ray spectrum from 200 - 450 keV

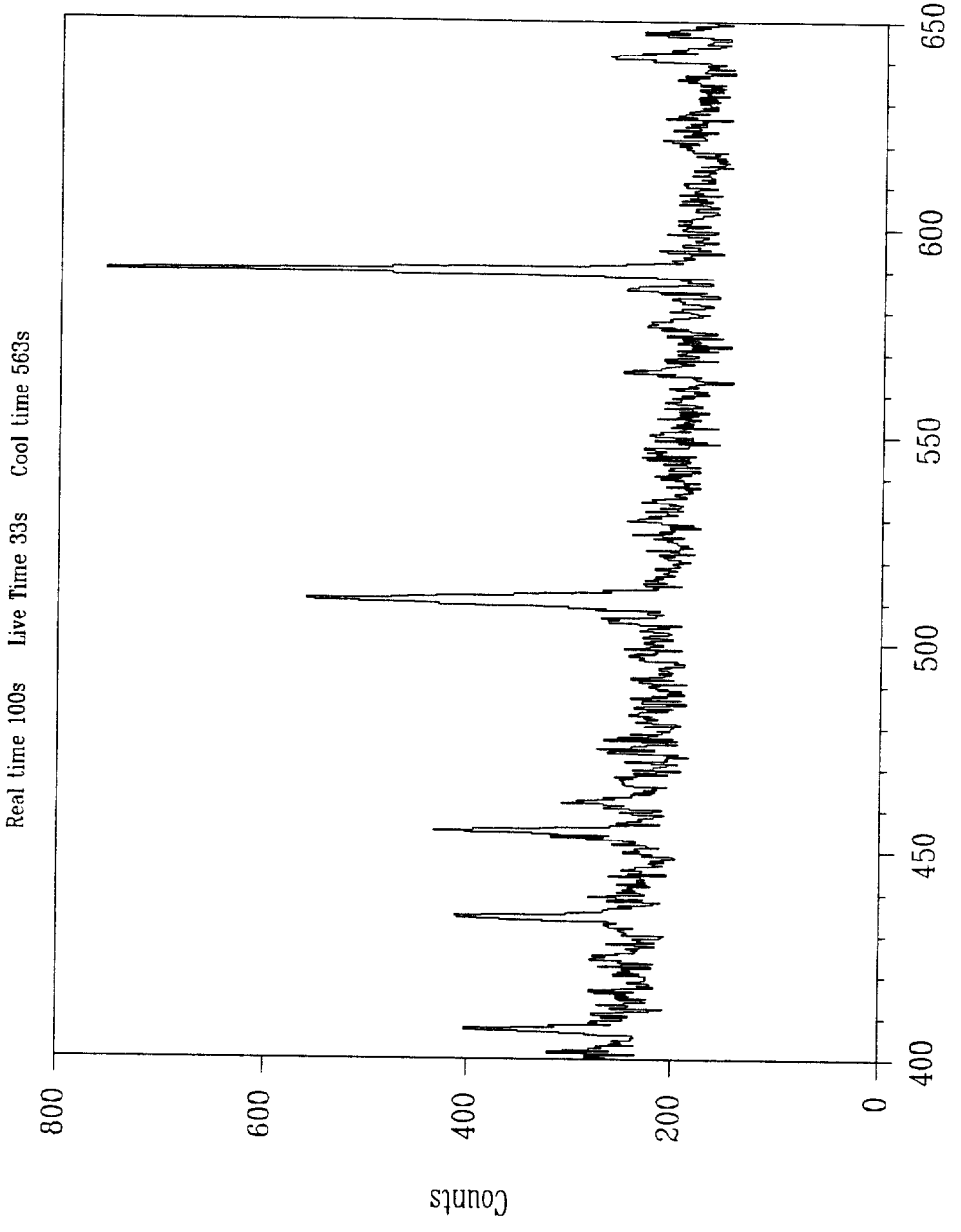

Figure C4. U-235 fission product gamma-ray spectrum from 400 - 650 keV

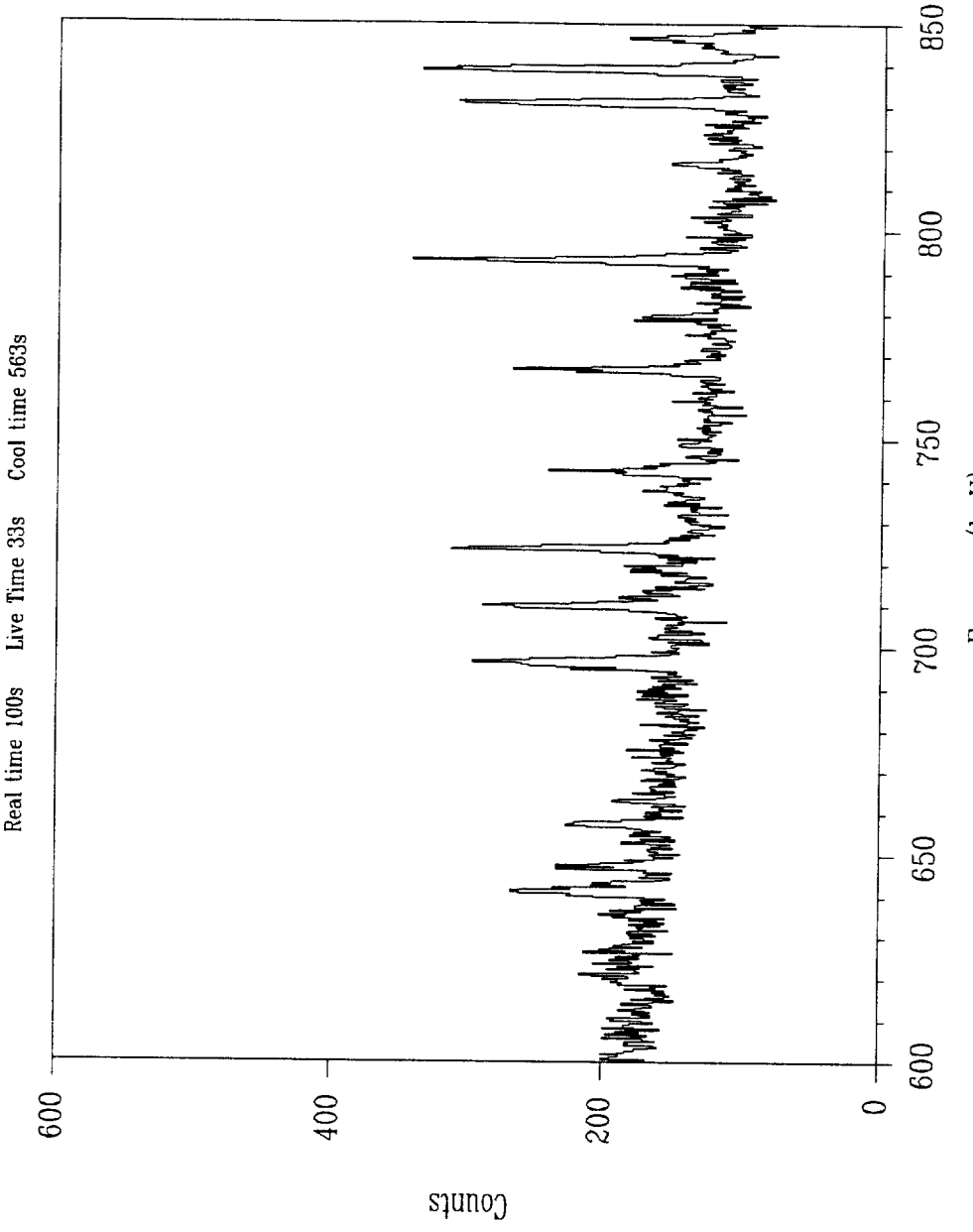

Figure C5. U-235 fission product gamma-ray spectrum from 600 - 850 keV

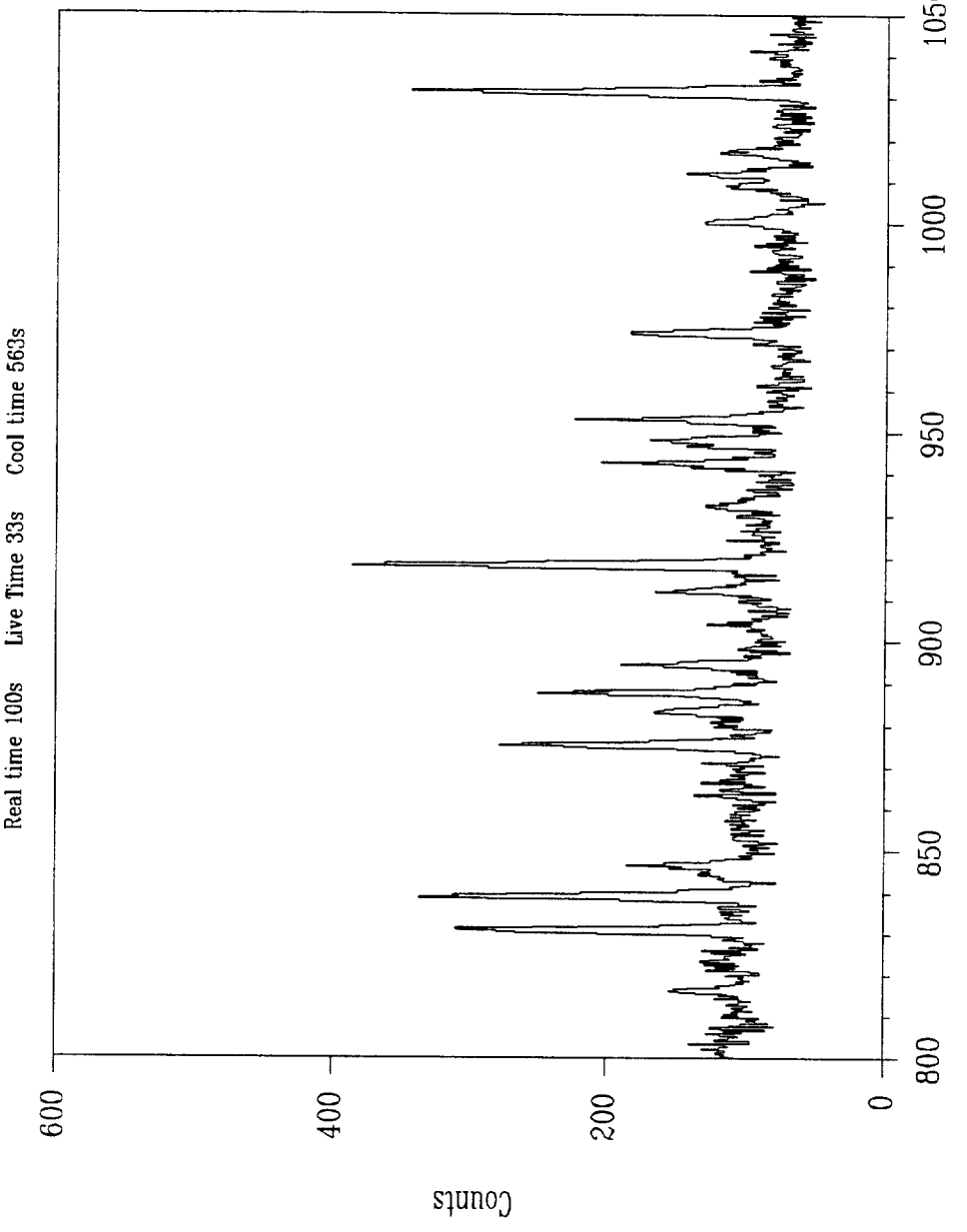

Figure C6. U-235 fission product gamma-ray spectrum from 800 - 1050 keV

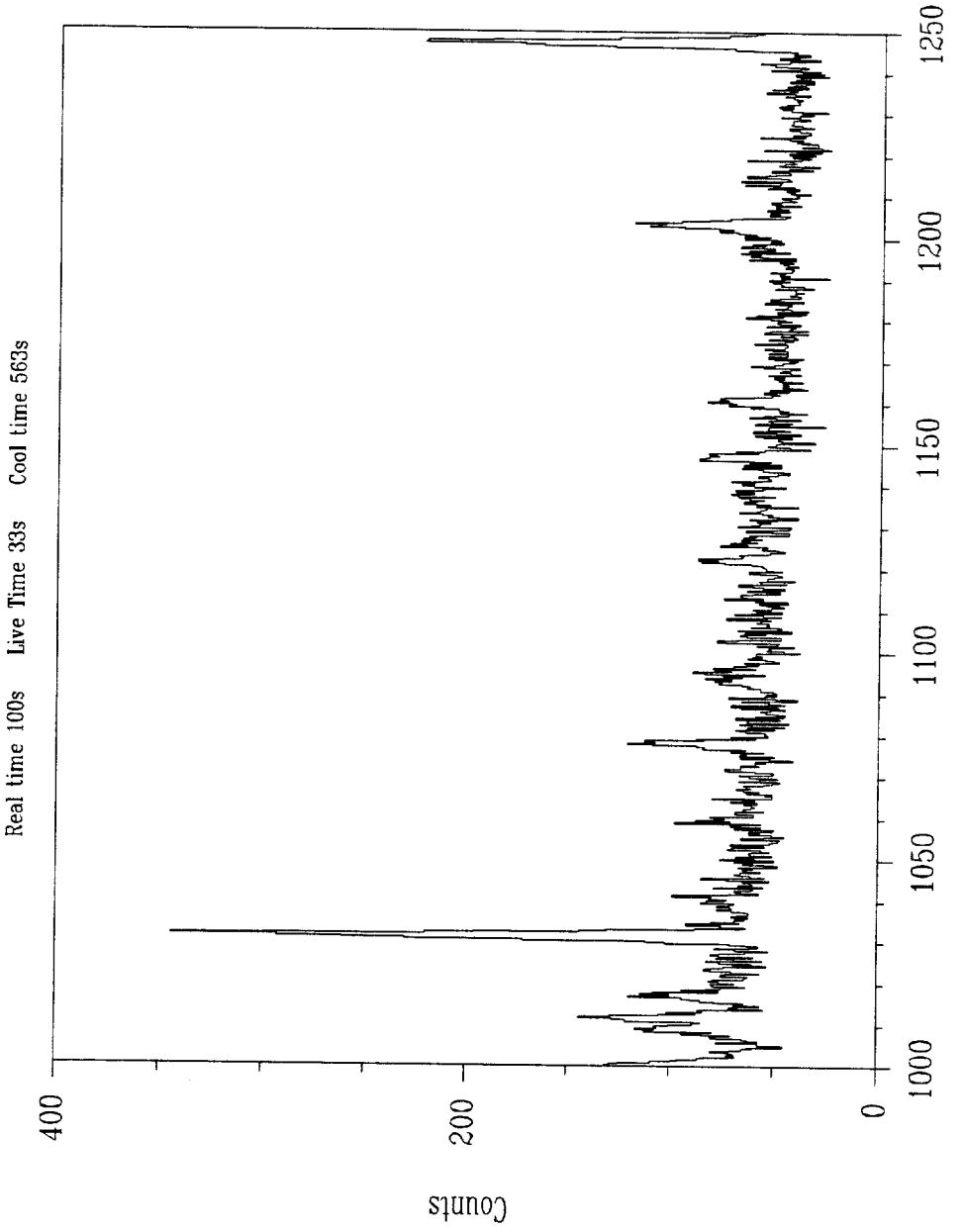

Figure C7. U-235 fission product gamma-ray spectrum from 1000 - 1250 keV

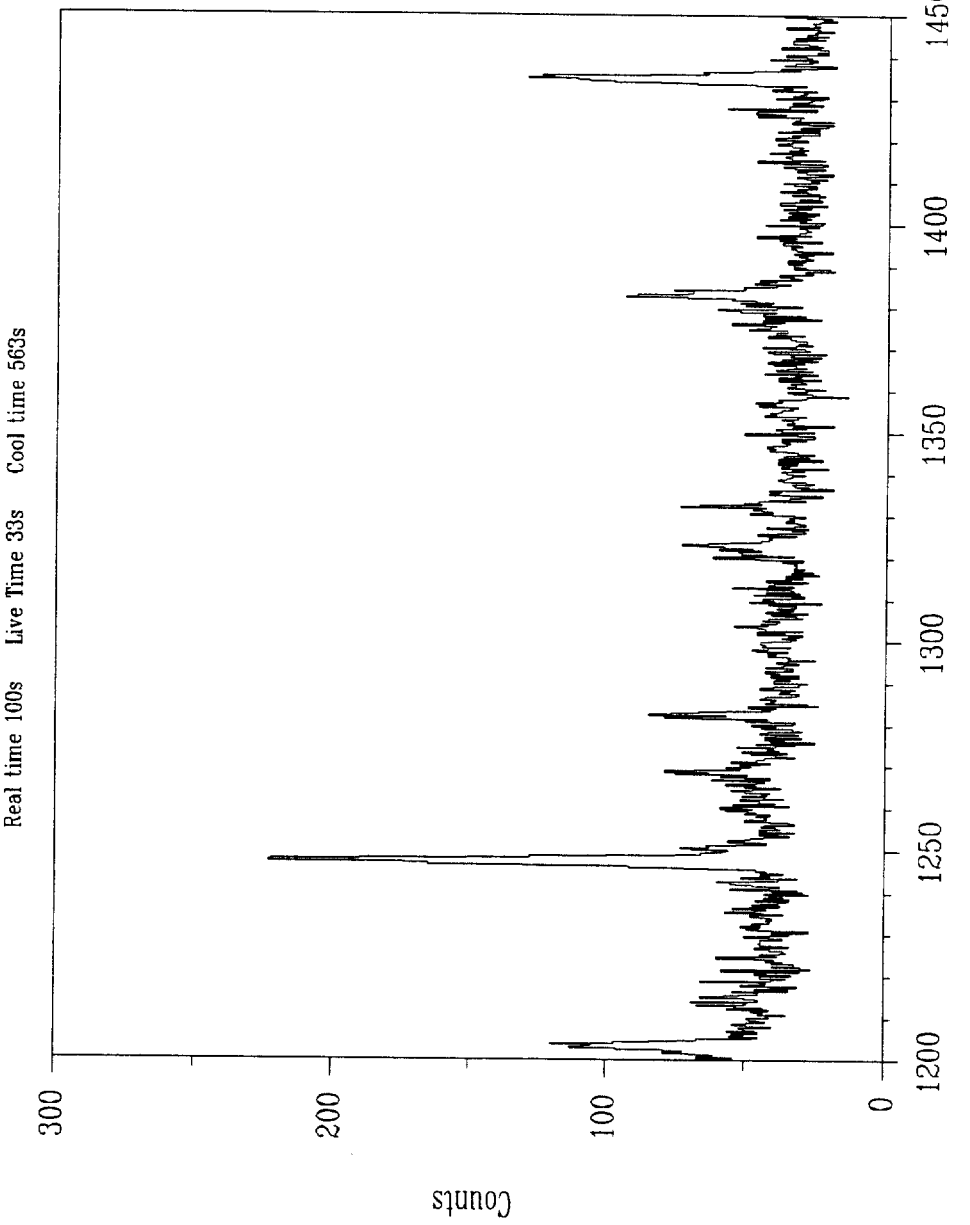

Figure C8. U-235 fission product gamma-ray spectrum from 1200 - 1450 keV

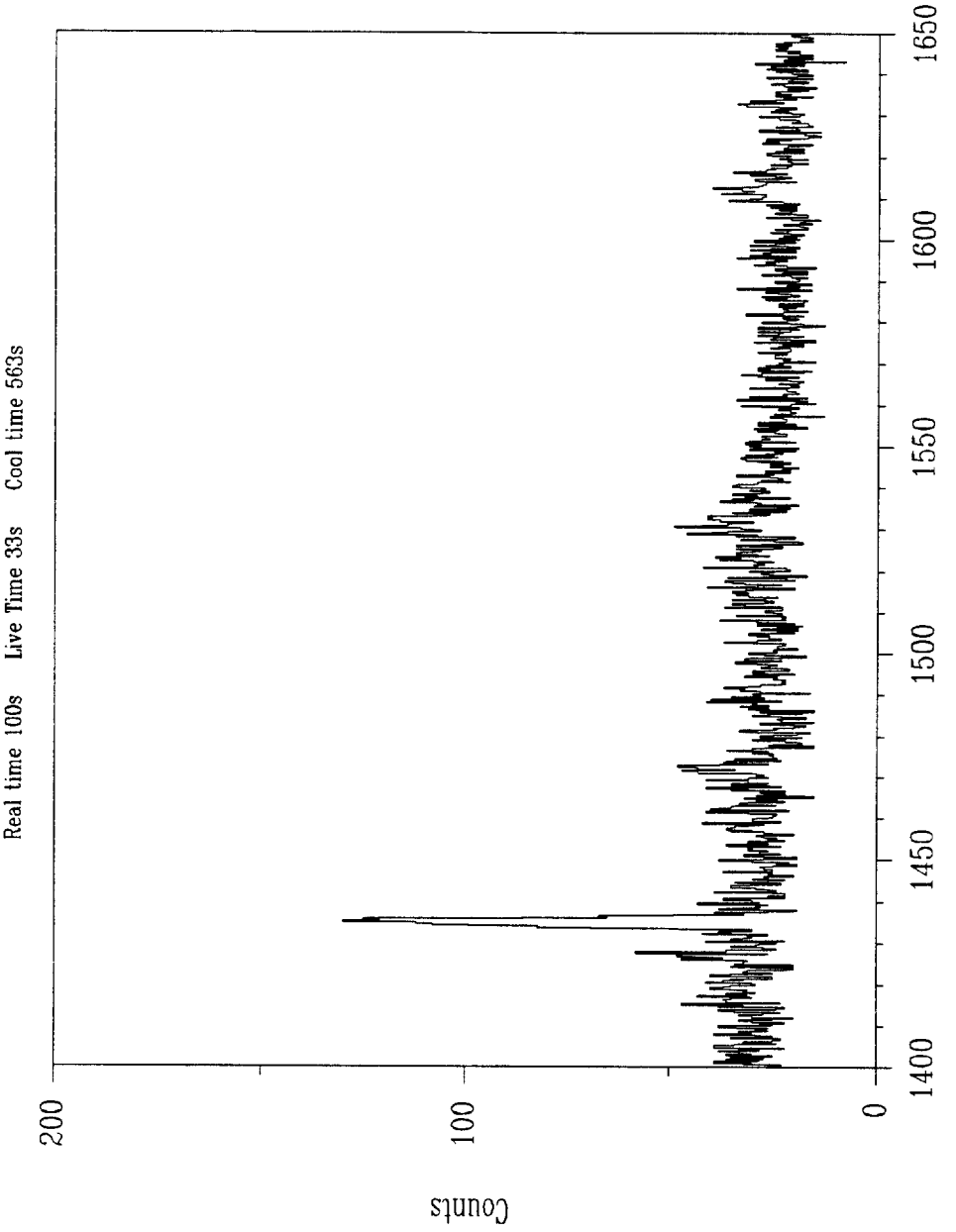

Figure C9. U-235 fission product gamma-ray spectrum from 1400 - 1650 keV

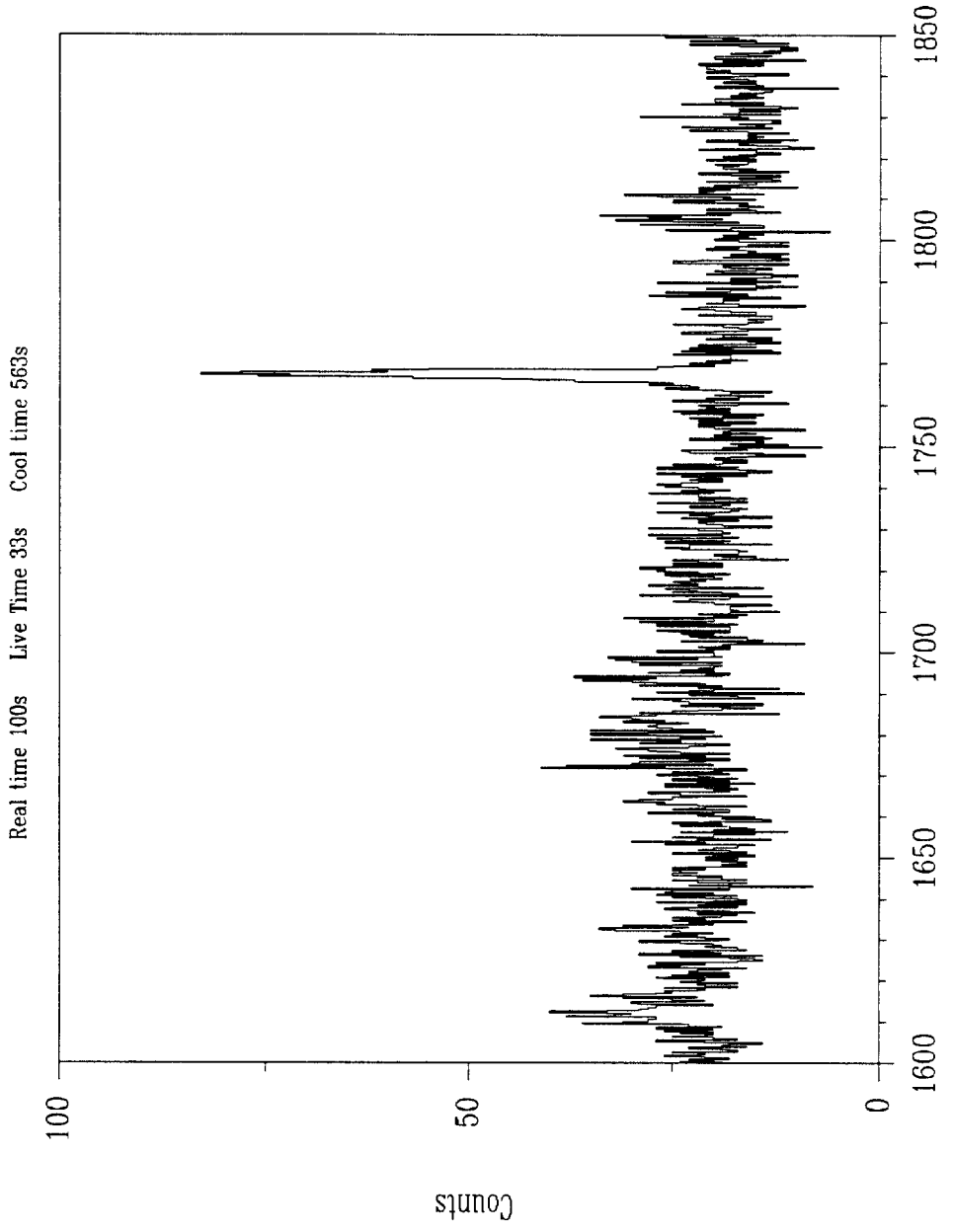

Figure C10. U-235 fission product gamma-ray spectrum from 1600 - 1850 keV

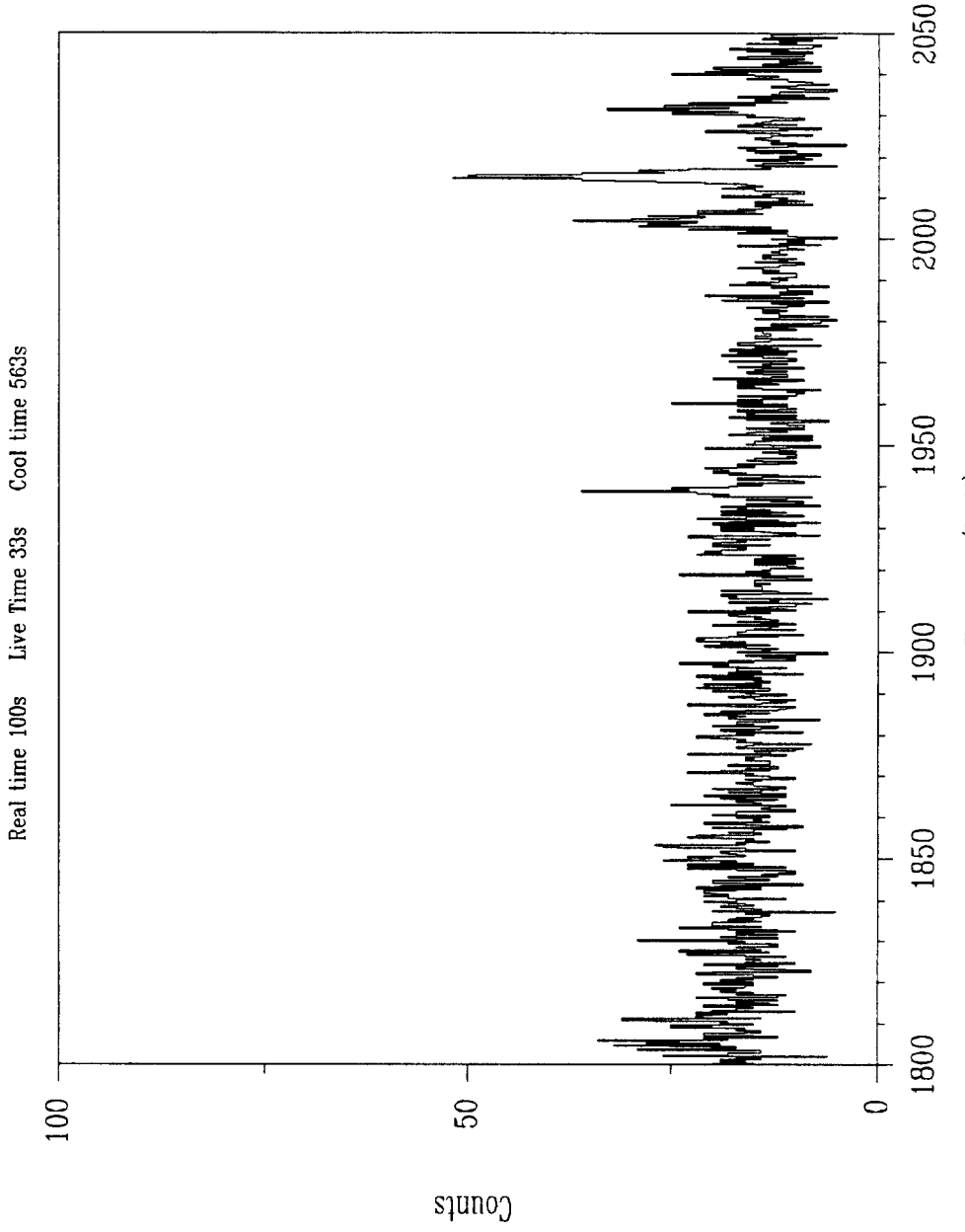

Figure C11. U-235 fission product gamma-ray spectrum from 1800 - 2050 keV

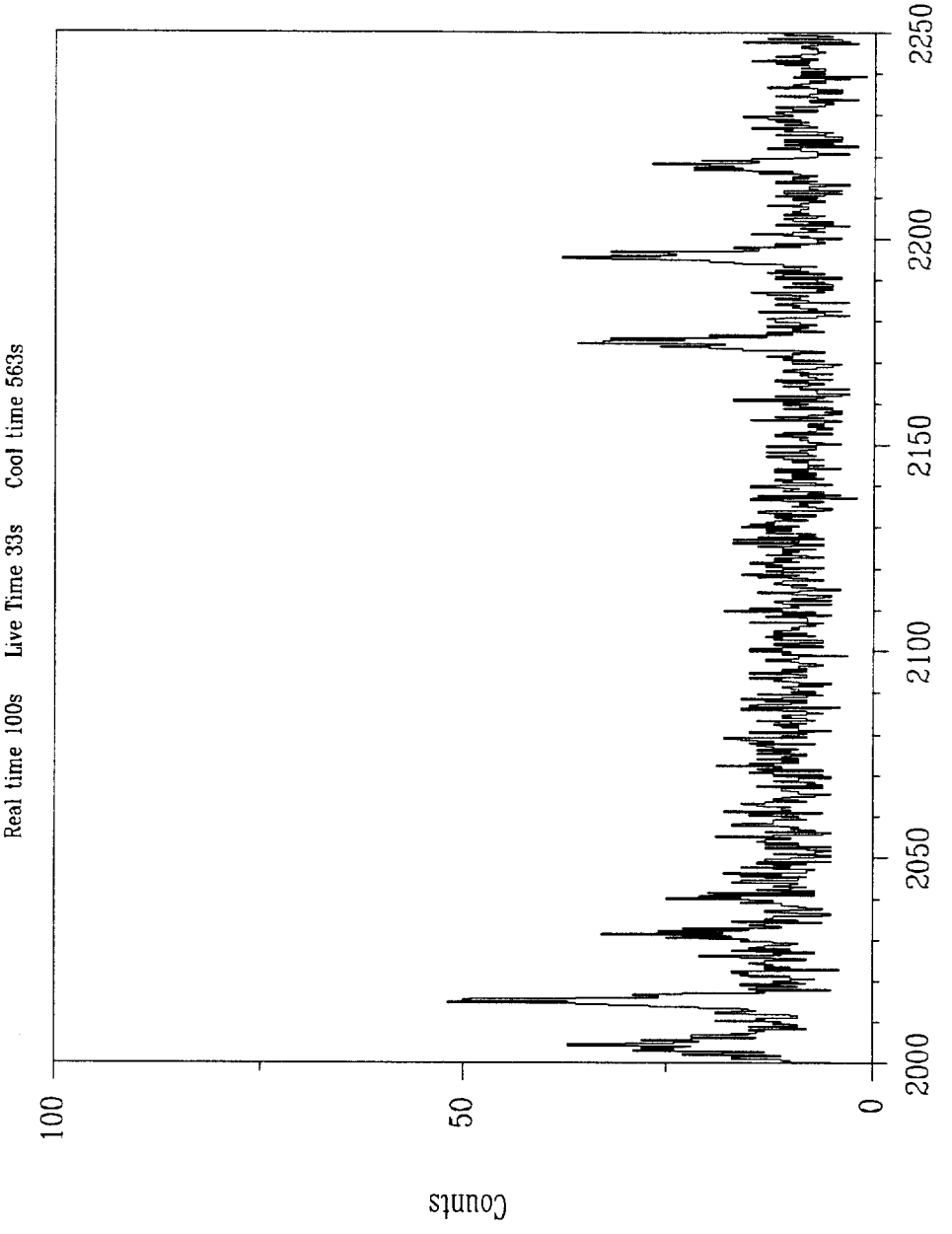

Figure C12. U-235 fission product gamma-ray spectrum from 2000 - 2250 keV

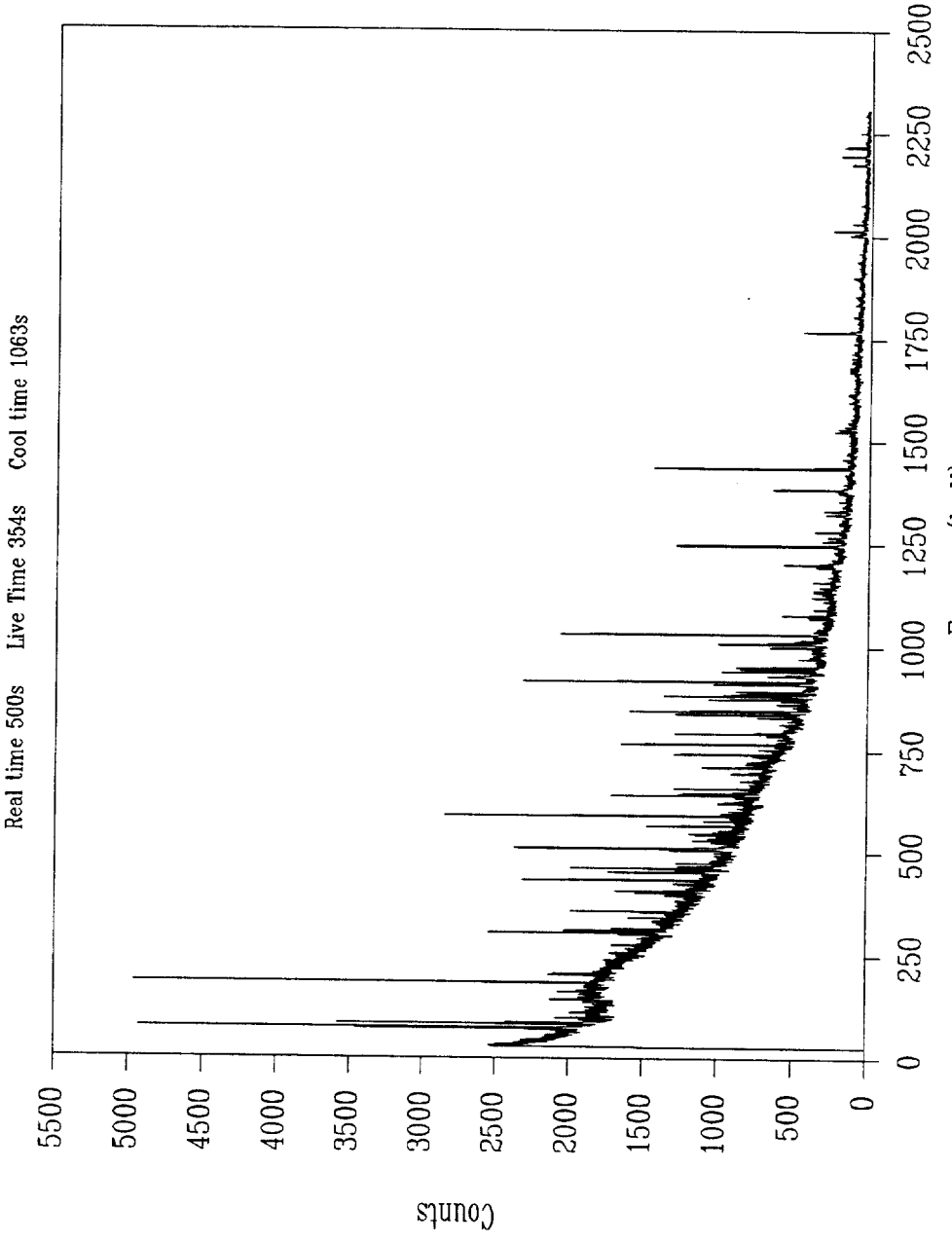

Figure C13. Entire U-235 fission product gamma-ray spectrum

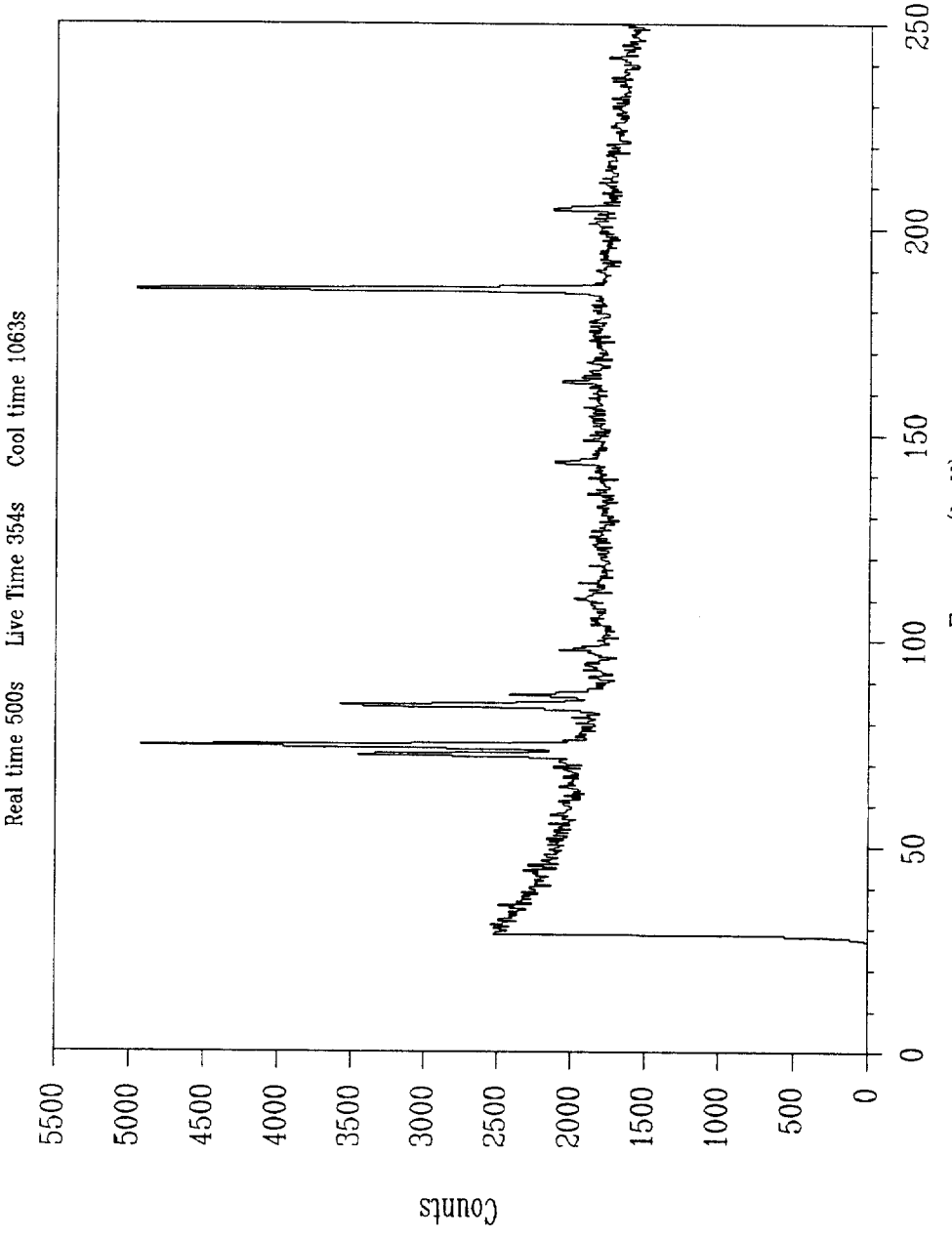

Figure C14. U-235 fission product gamma-ray spectrum from 0 - 250 keV

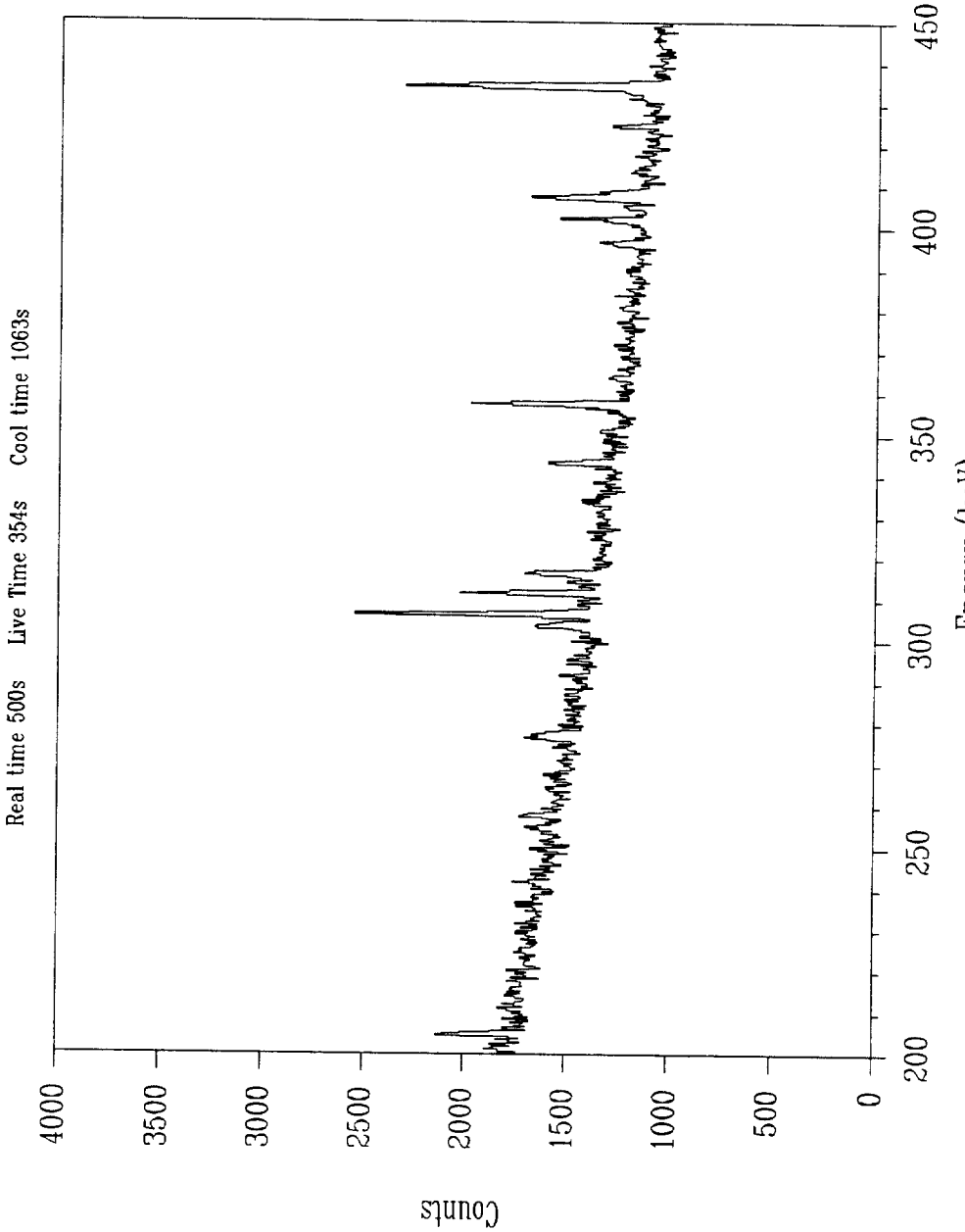

Figure C15. U-235 fission product gamma-ray spectrum from 200 - 450 keV

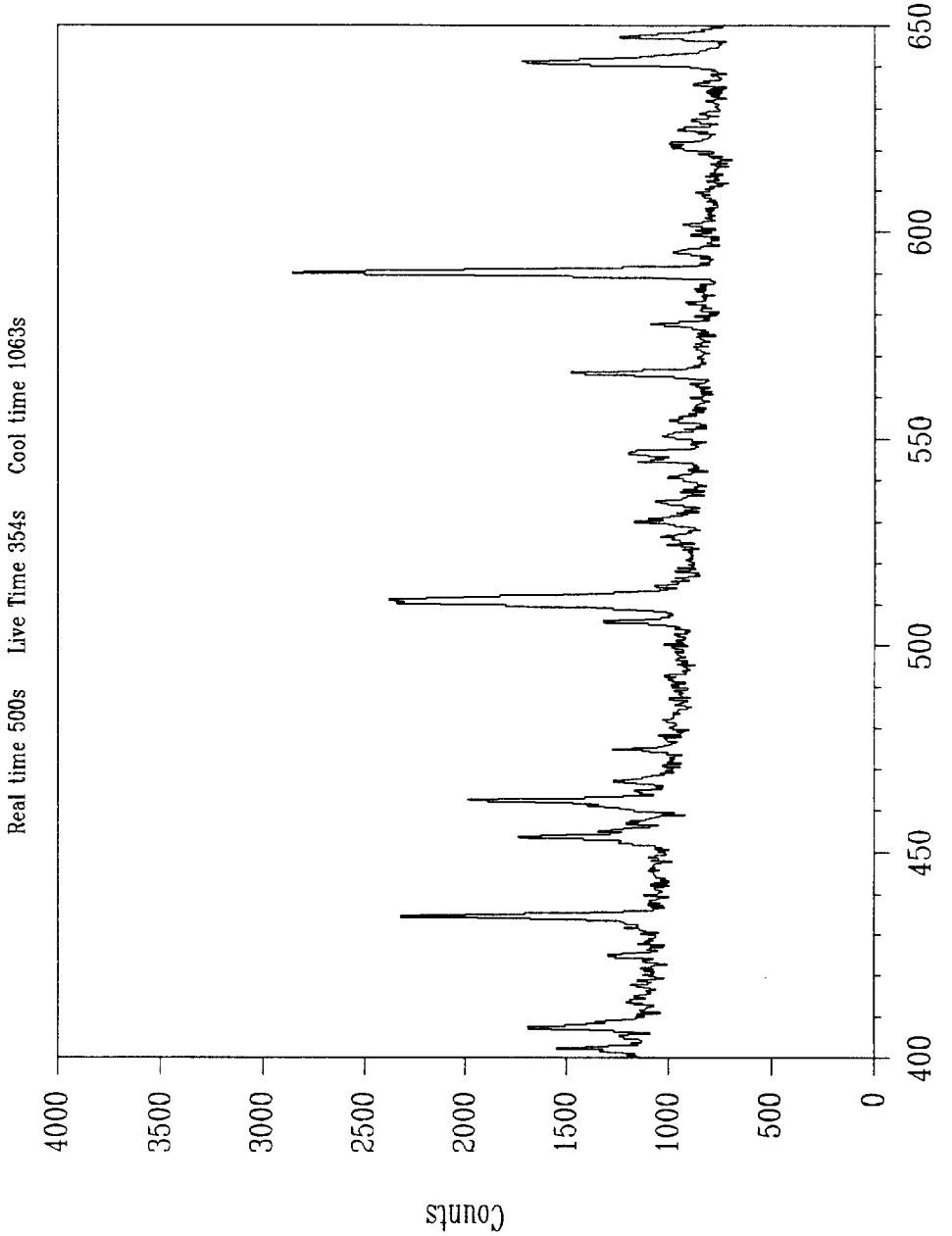

Figure C16. U-235 fission product gamma-ray spectrum from 400 - 650 keV

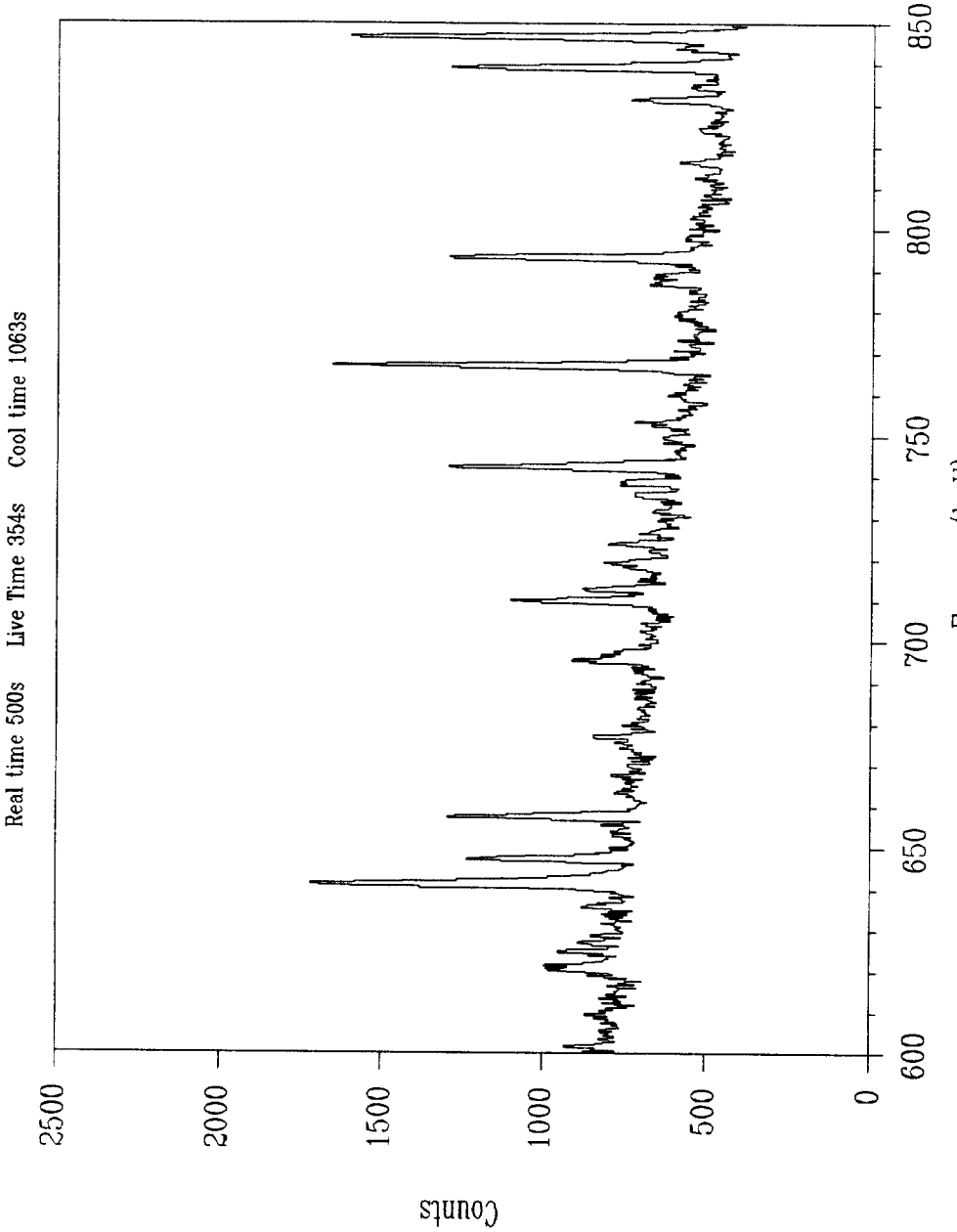

Figure C17. U-235 fission product gamma-ray spectrum from 600 - 850 keV

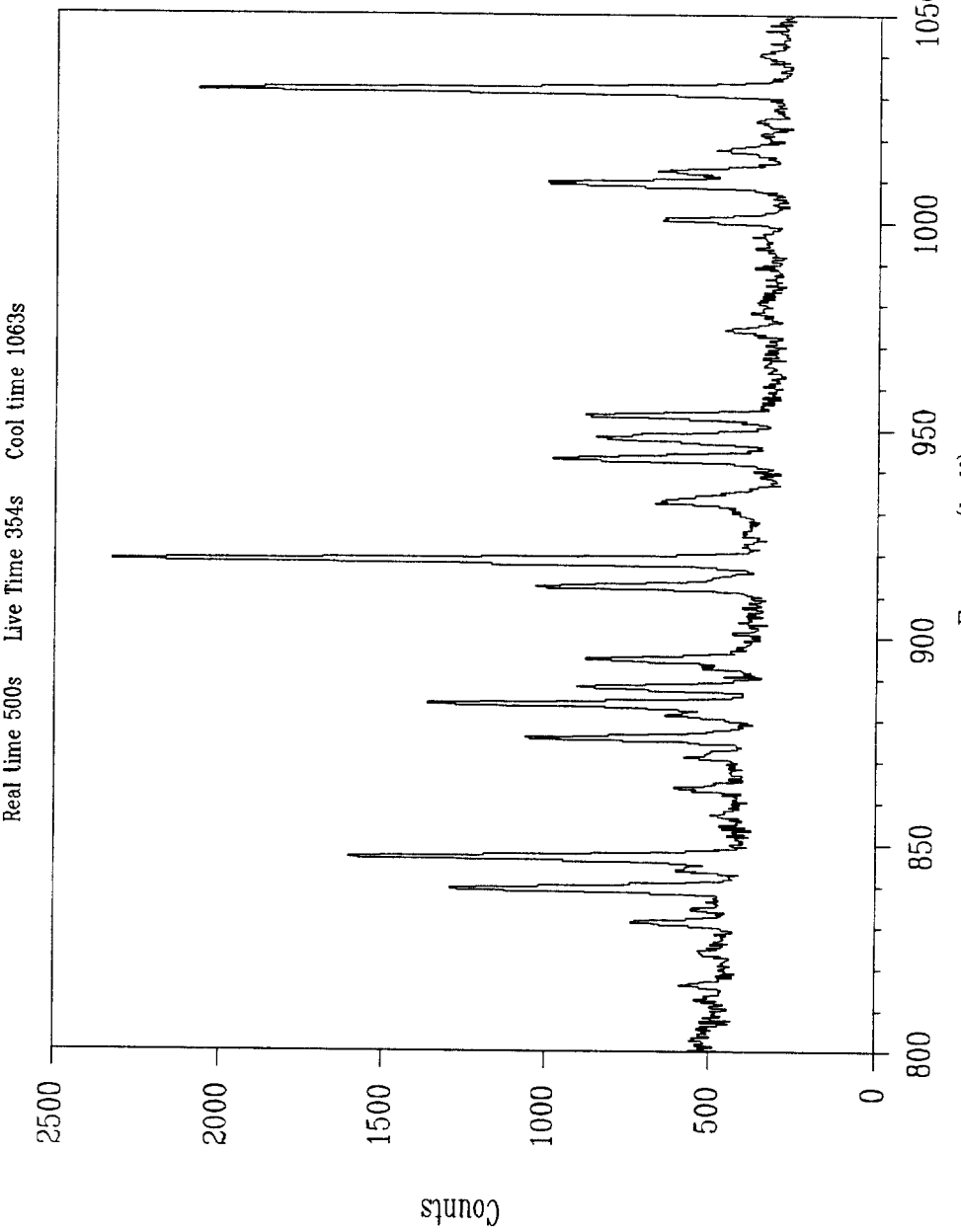

Figure C18. U-235 fission product gamma-ray spectrum from 800 - 1050 keV

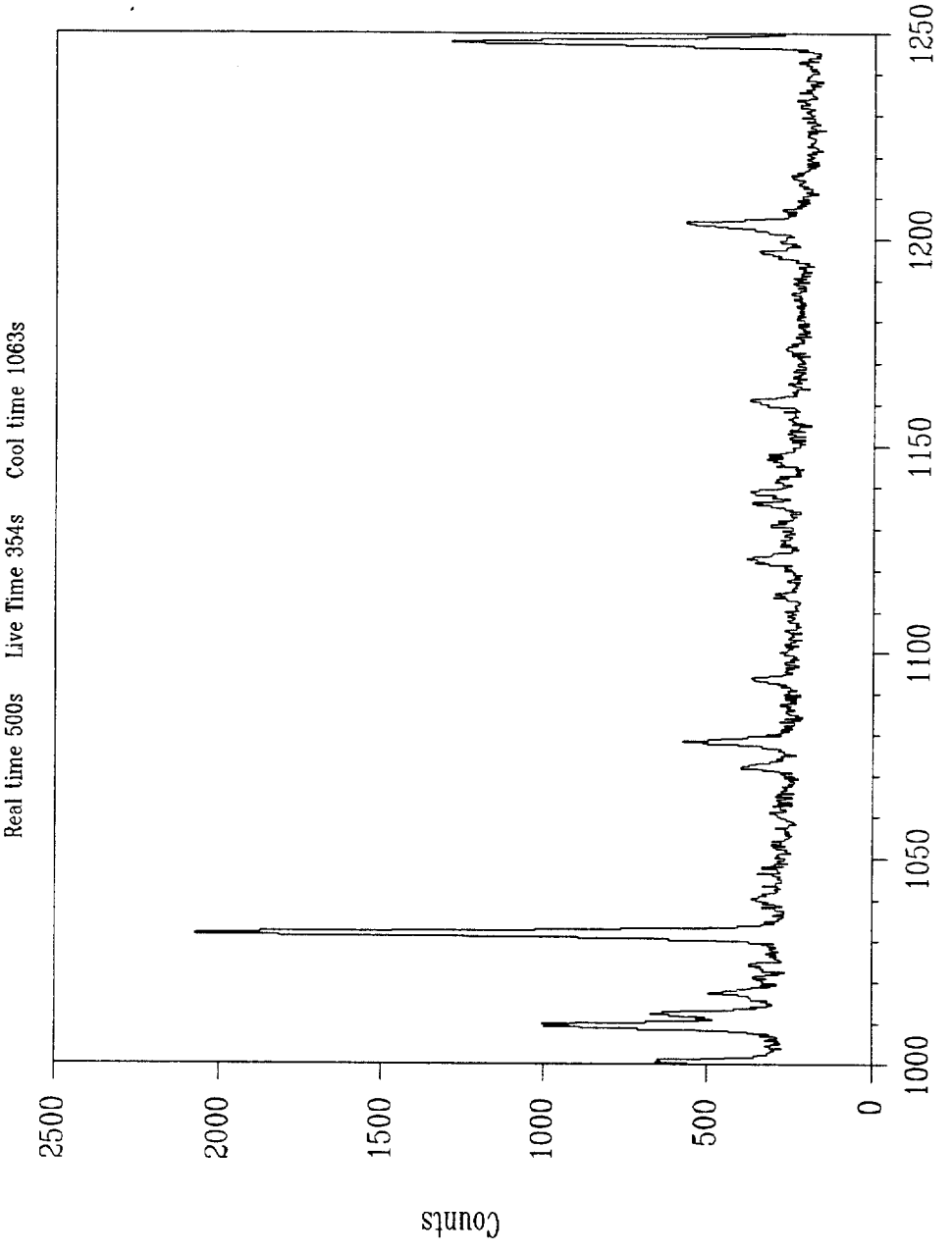

Figure C19. U-235 fission product gamma-ray spectrum from 1000 - 1250 keV

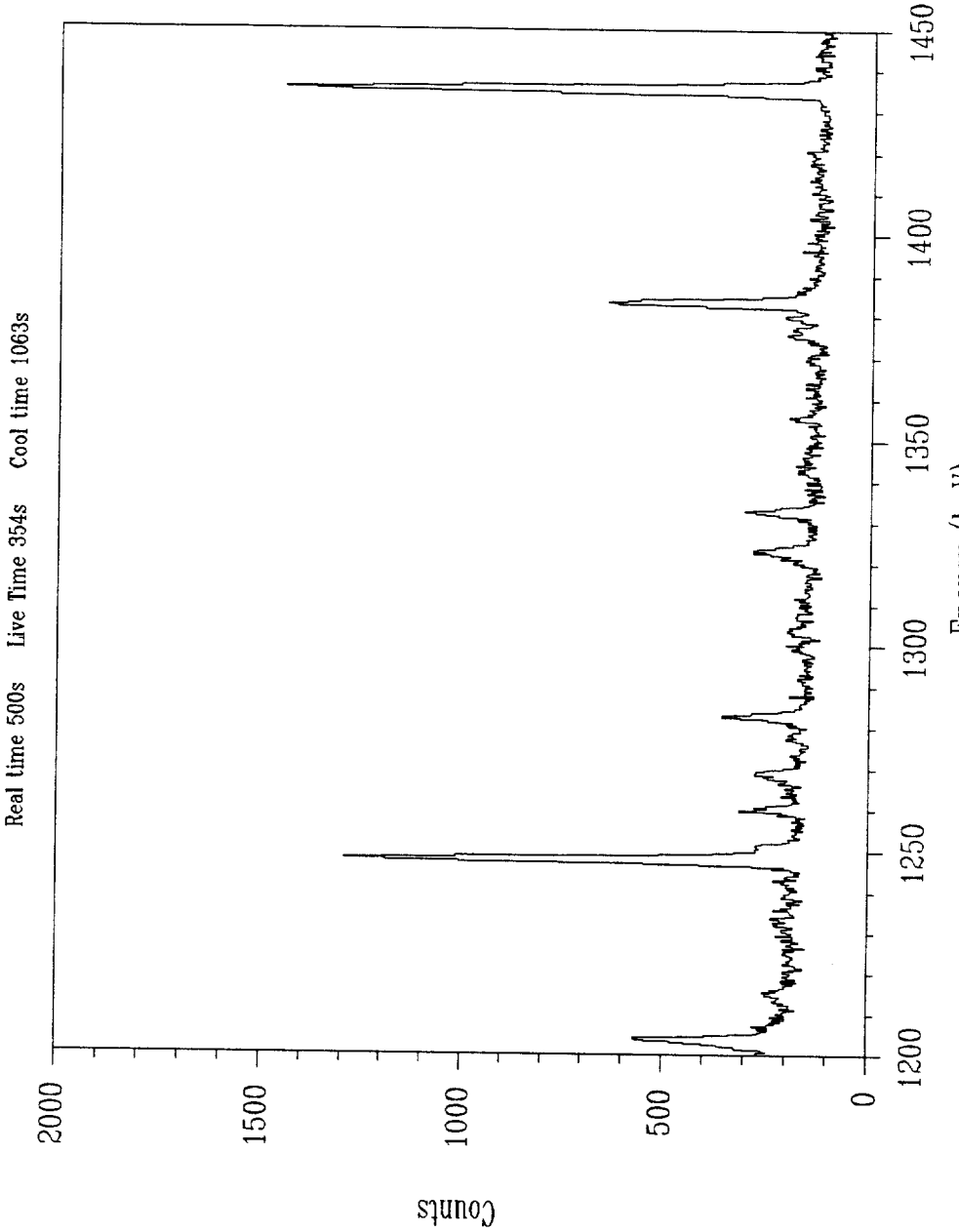

Figure C20. U-235 fission product gamma-ray spectrum from 1200 - 1450 keV

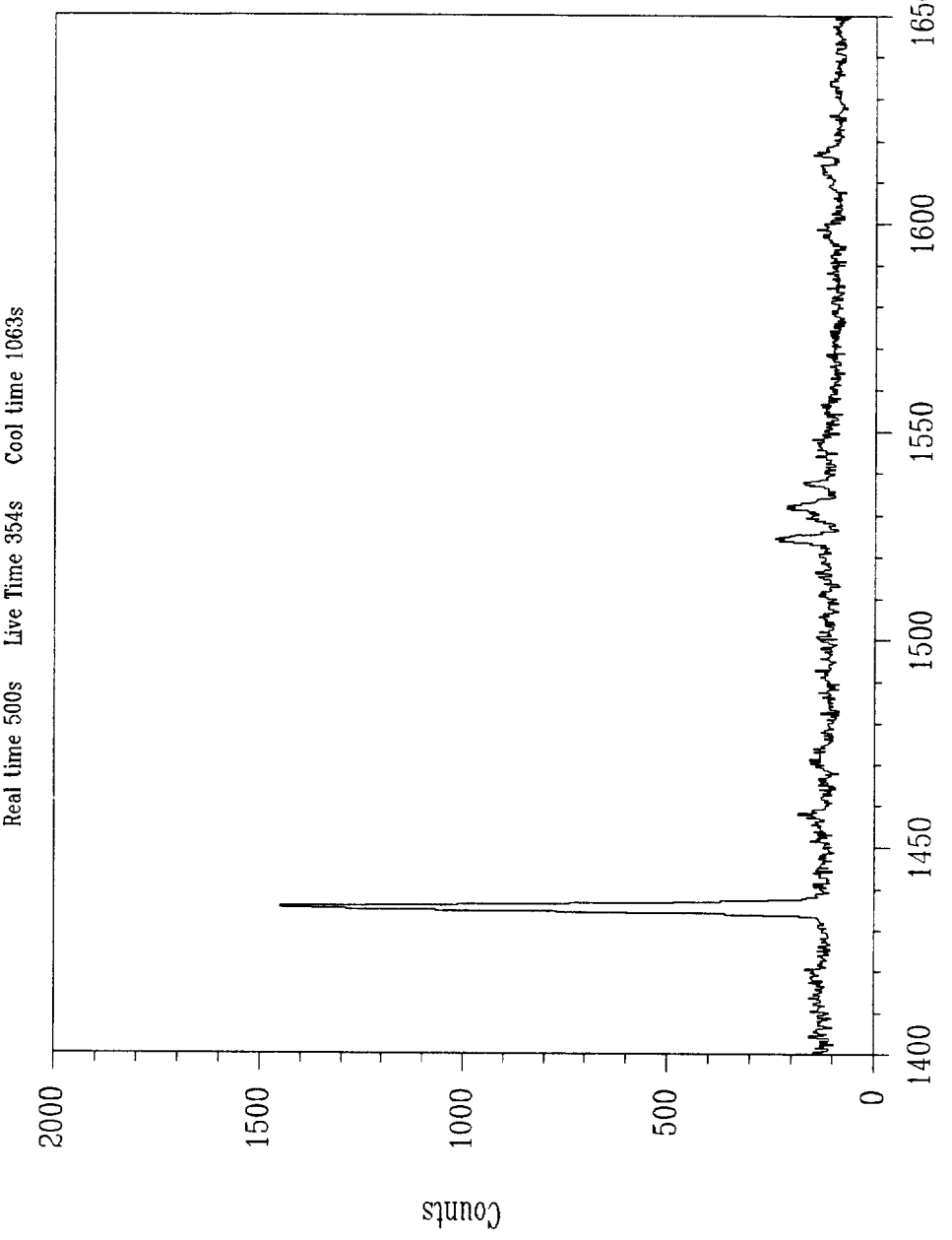

Figure C21. U-235 fission product gamma-ray spectrum from 1400 - 1650 keV

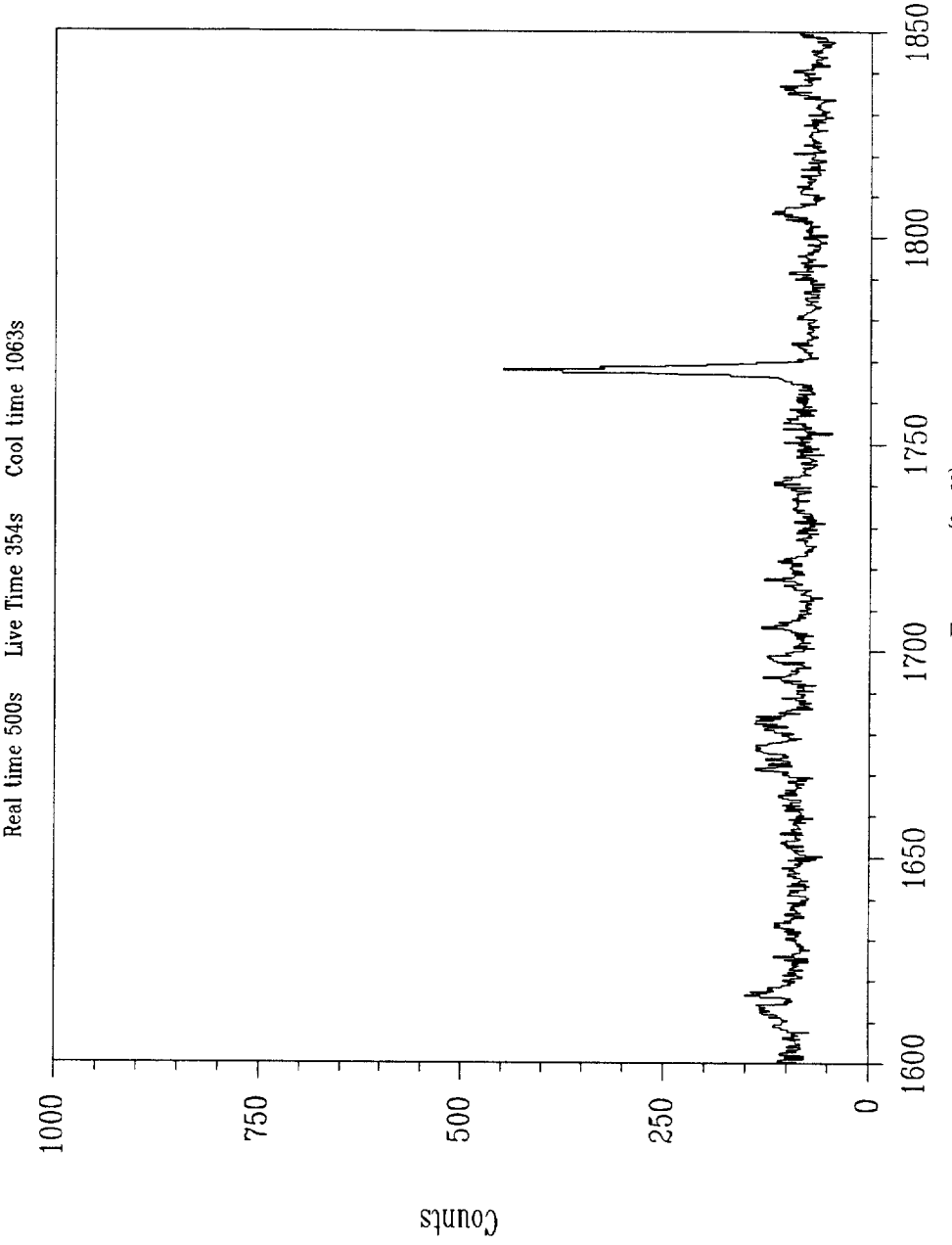

Figure C22. U-235 fission product gamma-ray spectrum from 1600 - 1850 keV

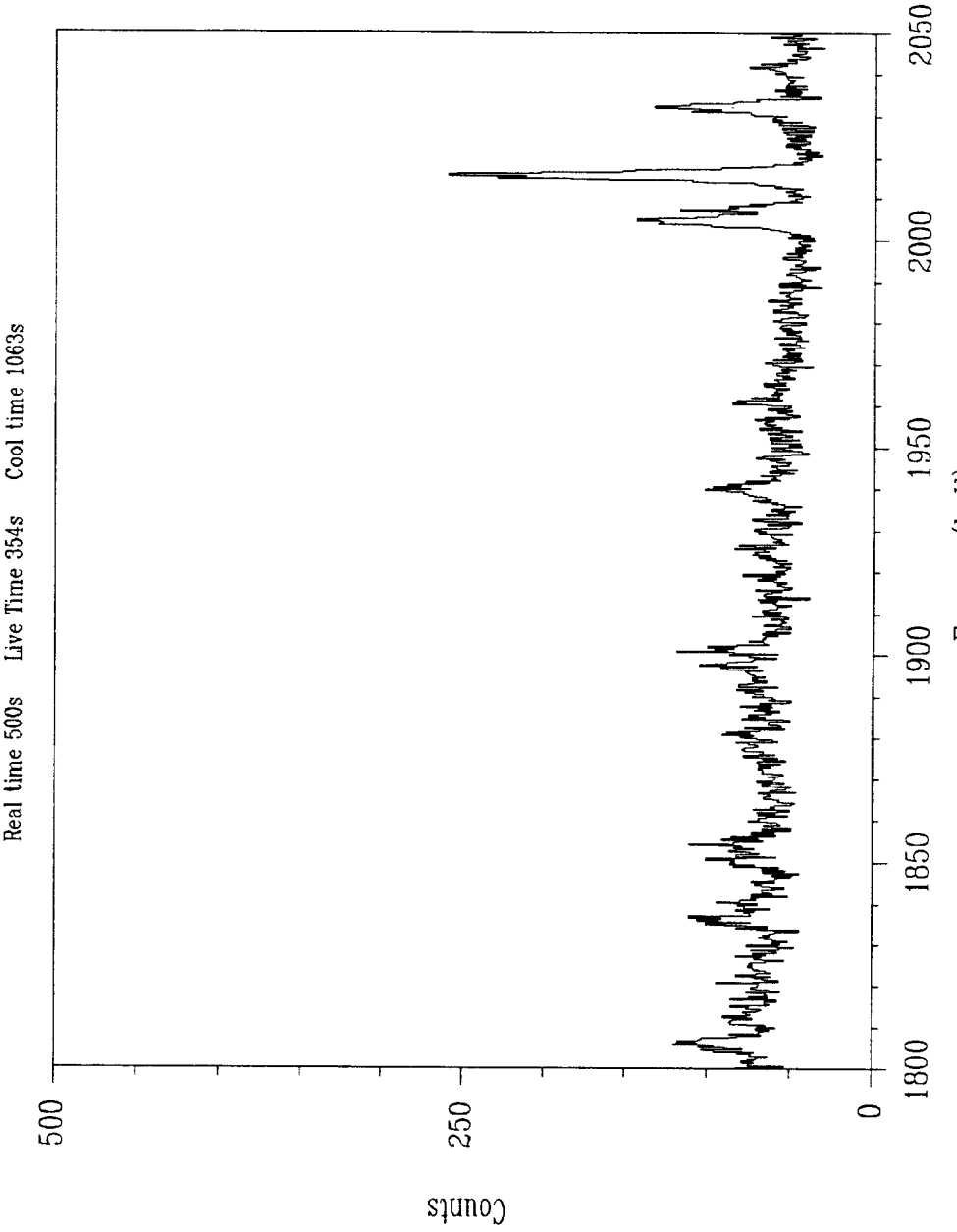

Figure C23. U-235 fission product gamma-ray spectrum from 1800 - 2050 keV

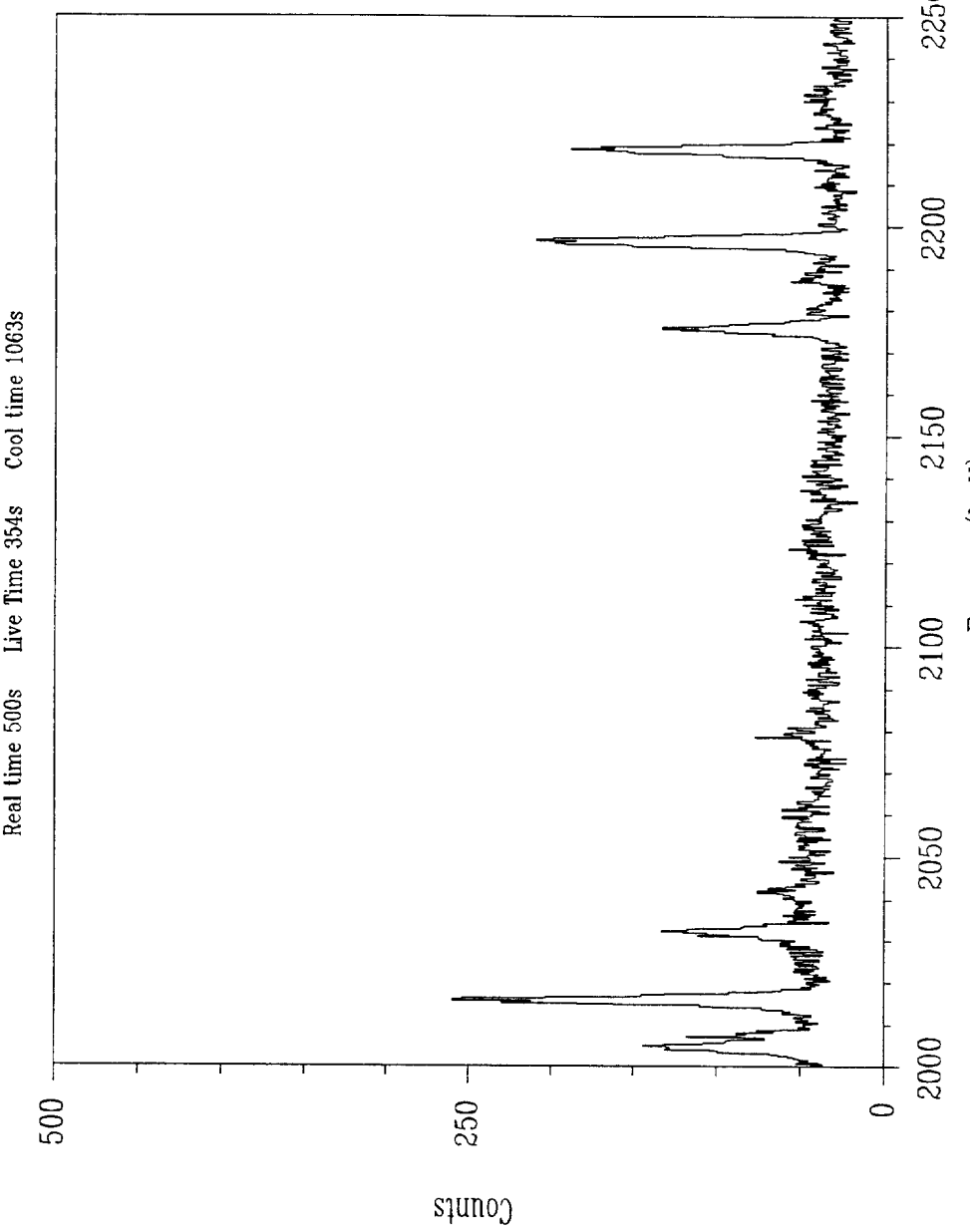

Figure C24. U-235 fission product gamma-ray spectrum from 2000 - 2250 keV

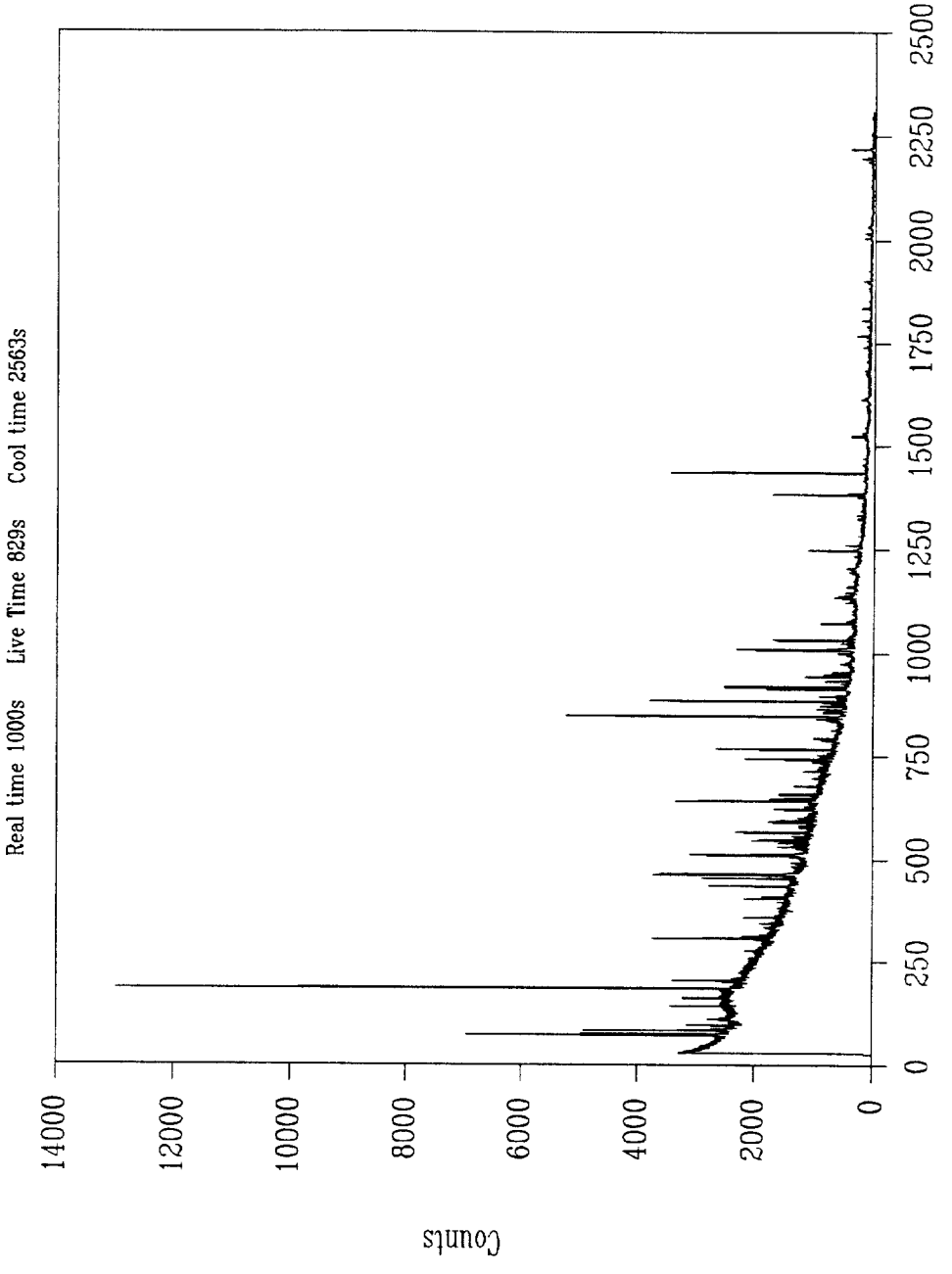

Figure C25. Entire U-235 fission product gamma-ray spectrum

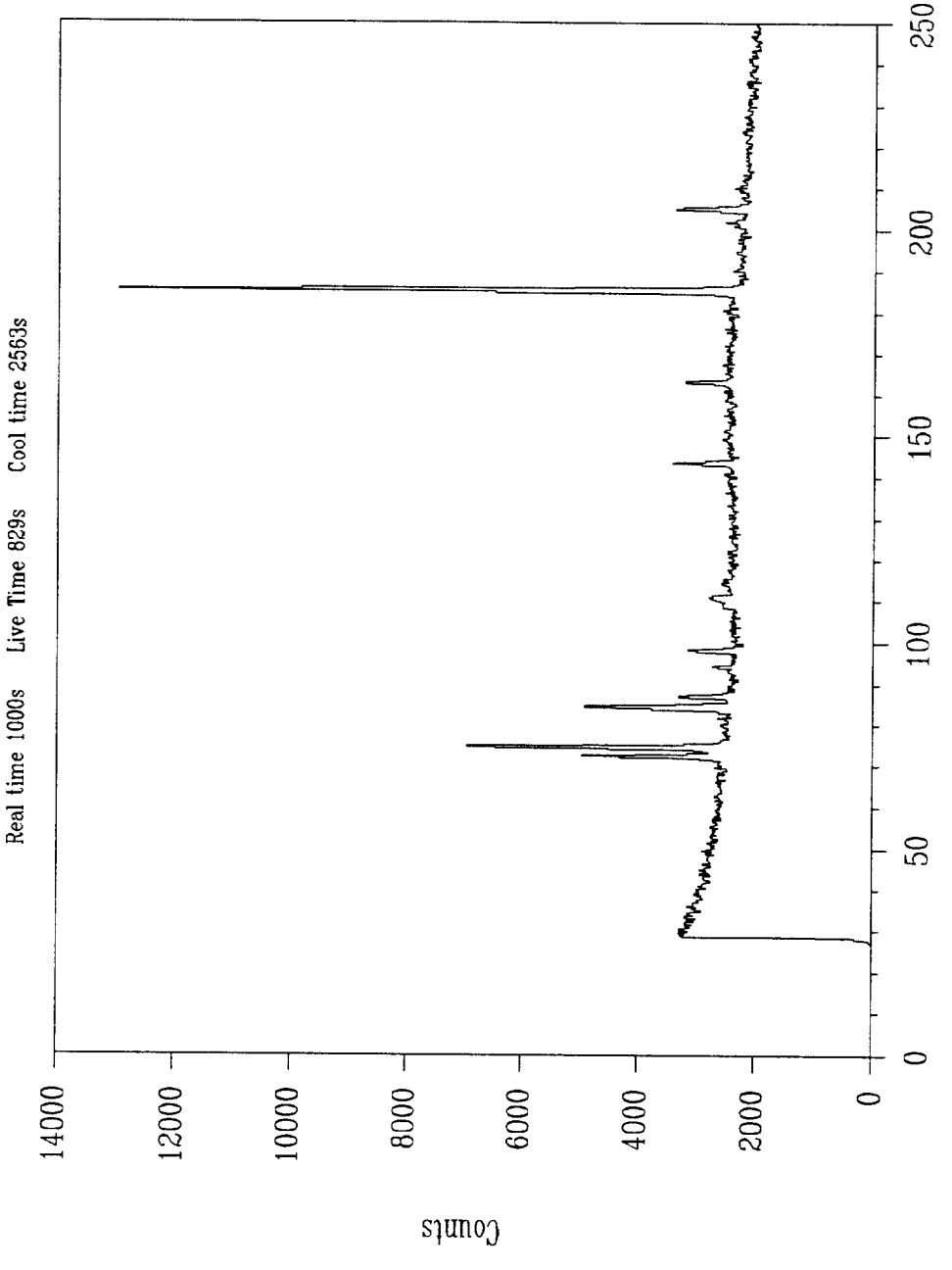

Figure C26. U-235 fission product gamma-ray spectrum from 0 - 250 keV

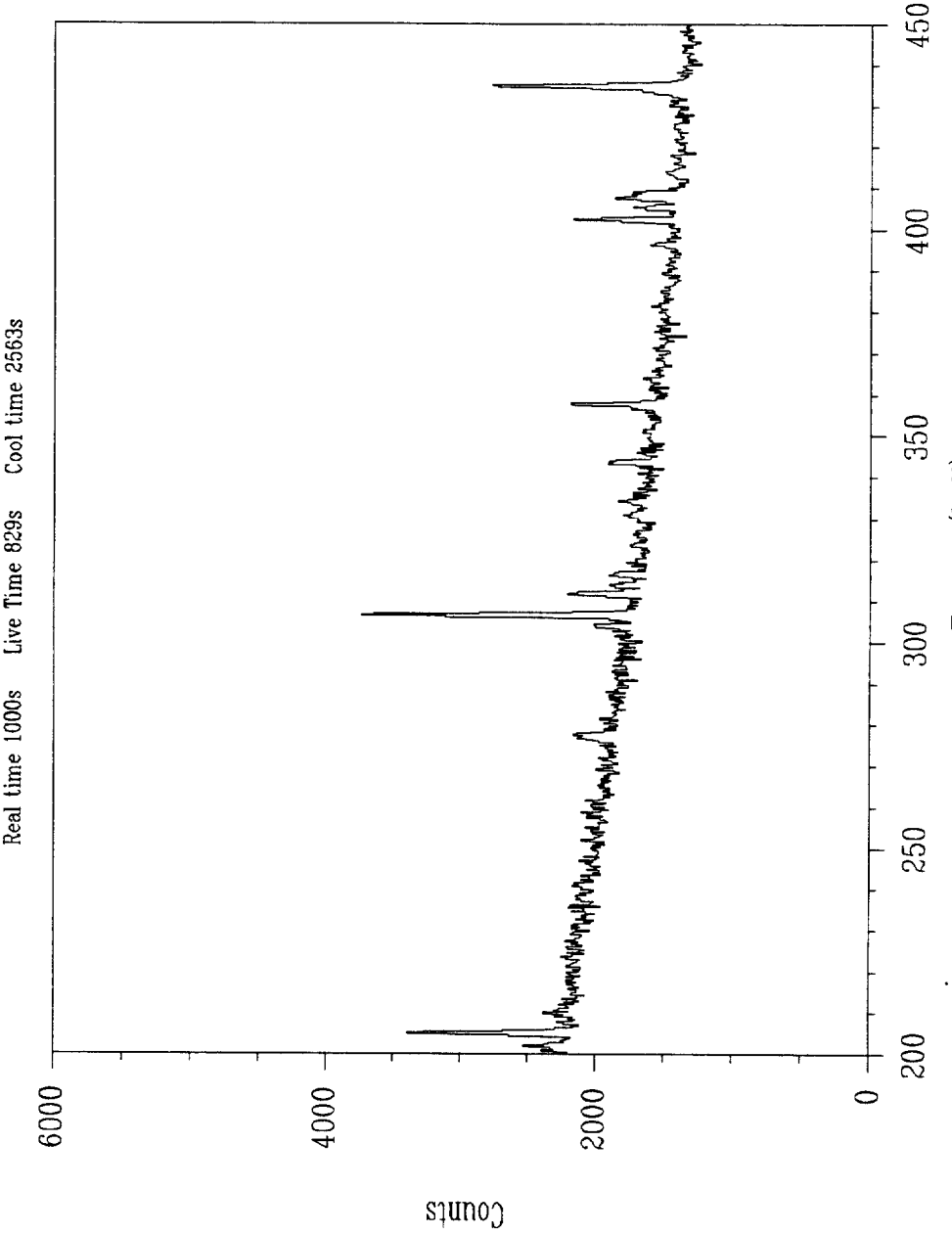

Figure C27. U-235 fission product gamma-ray spectrum from 200 - 450 keV

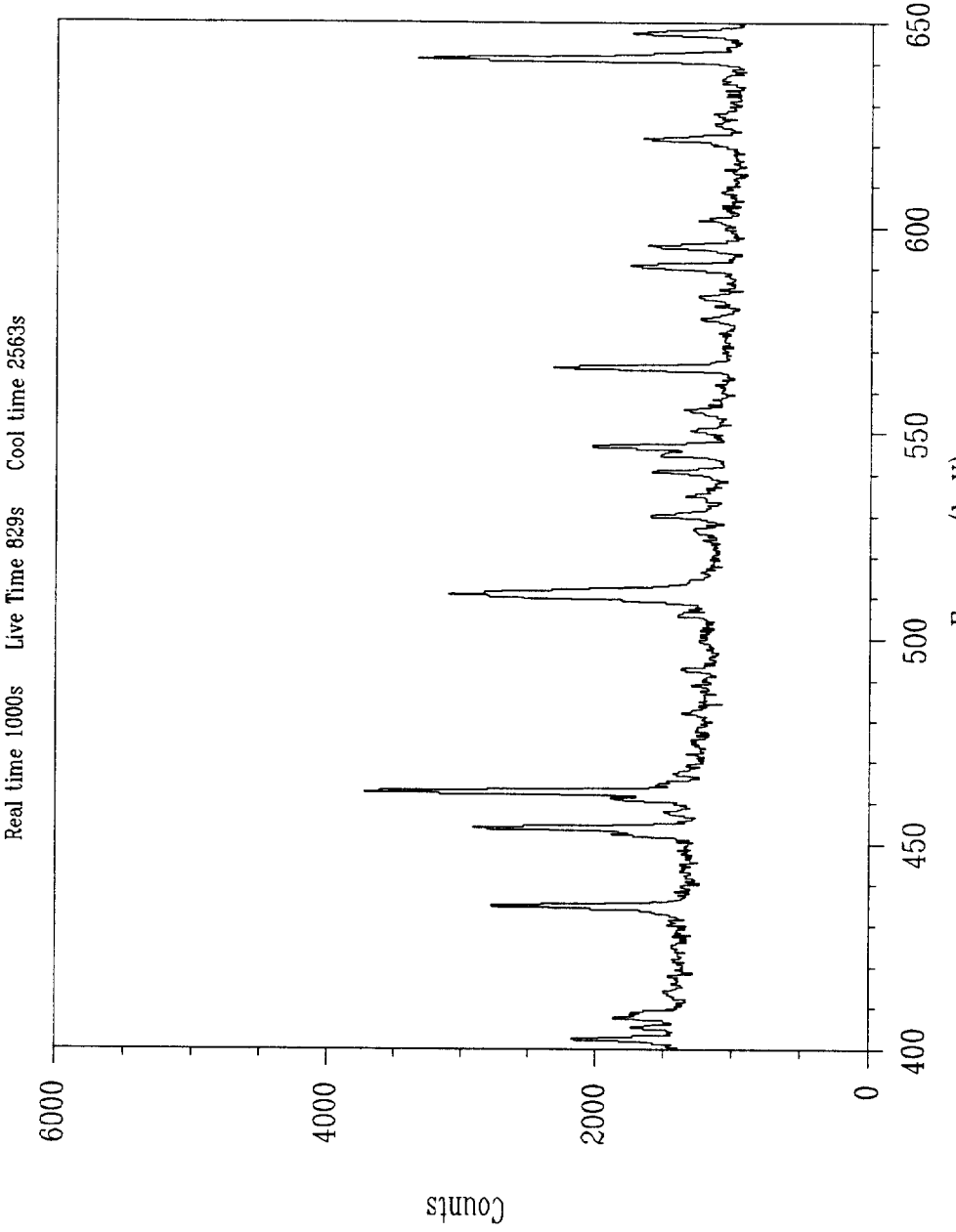

Figure C28. U-235 fission product gamma-ray spectrum from 400 - 650 keV

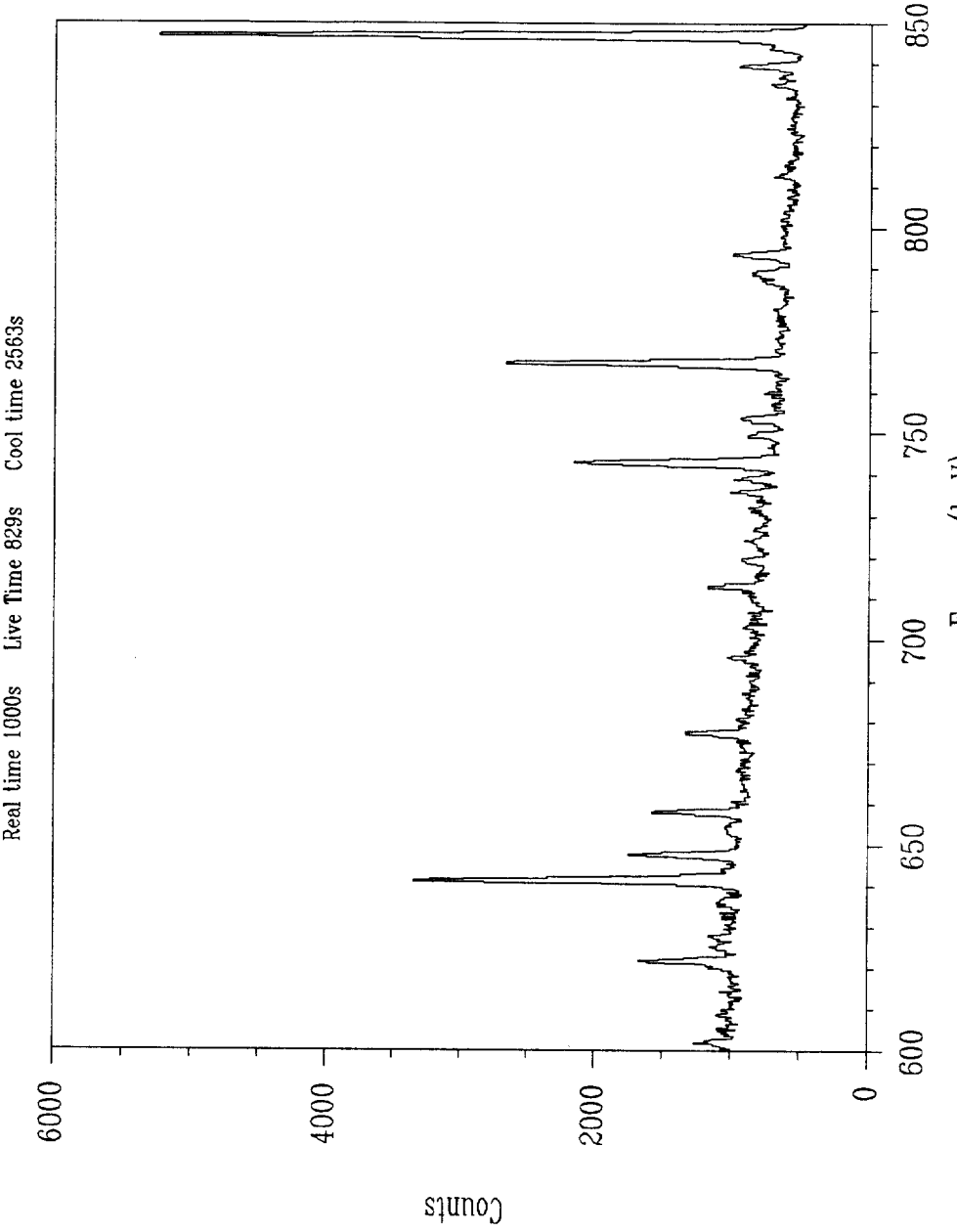

Figure C29. U-235 fission product gamma-ray spectrum from 600 - 850 keV

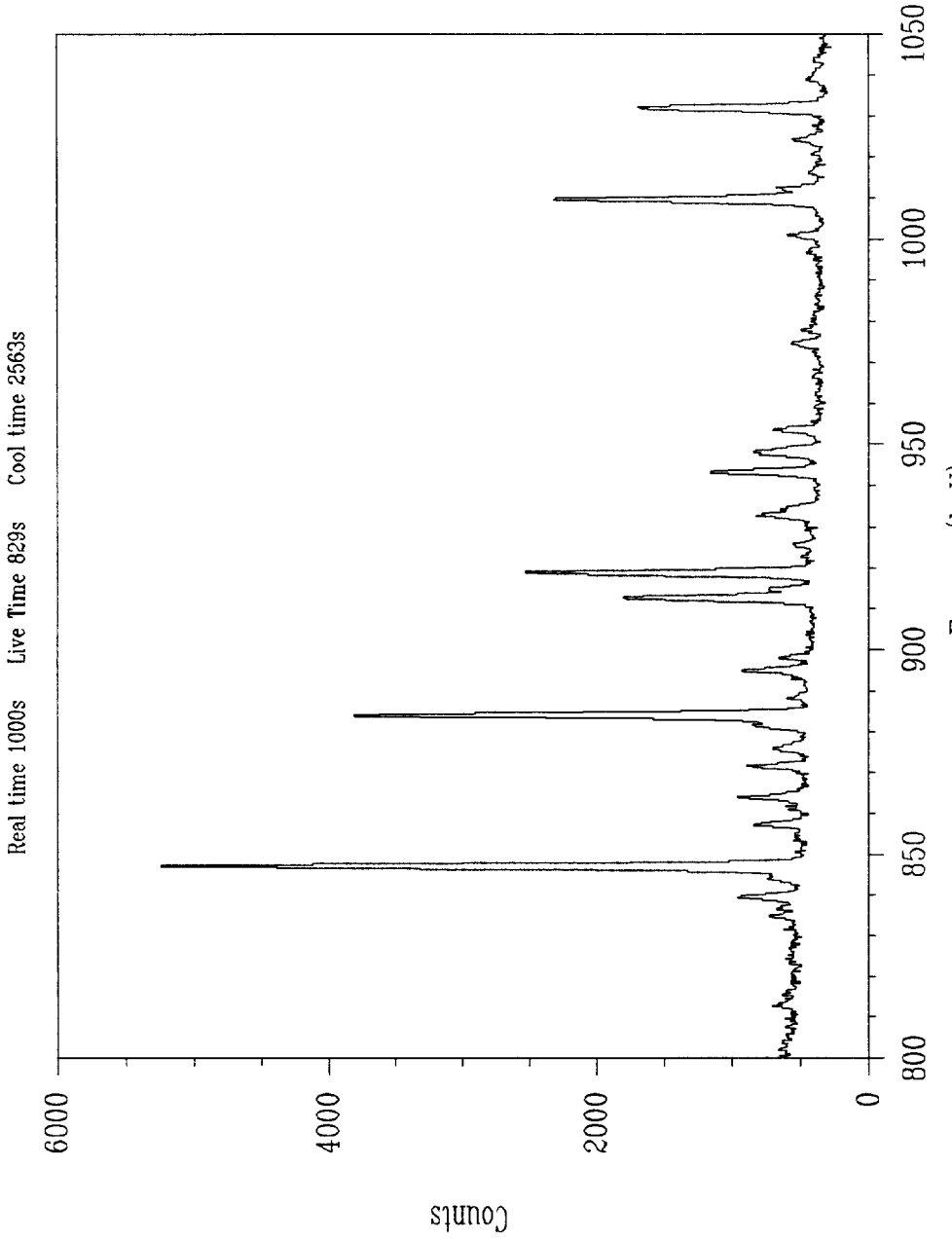

Figure C30. U-235 fission product gamma-ray spectrum from 800 -1050 keV

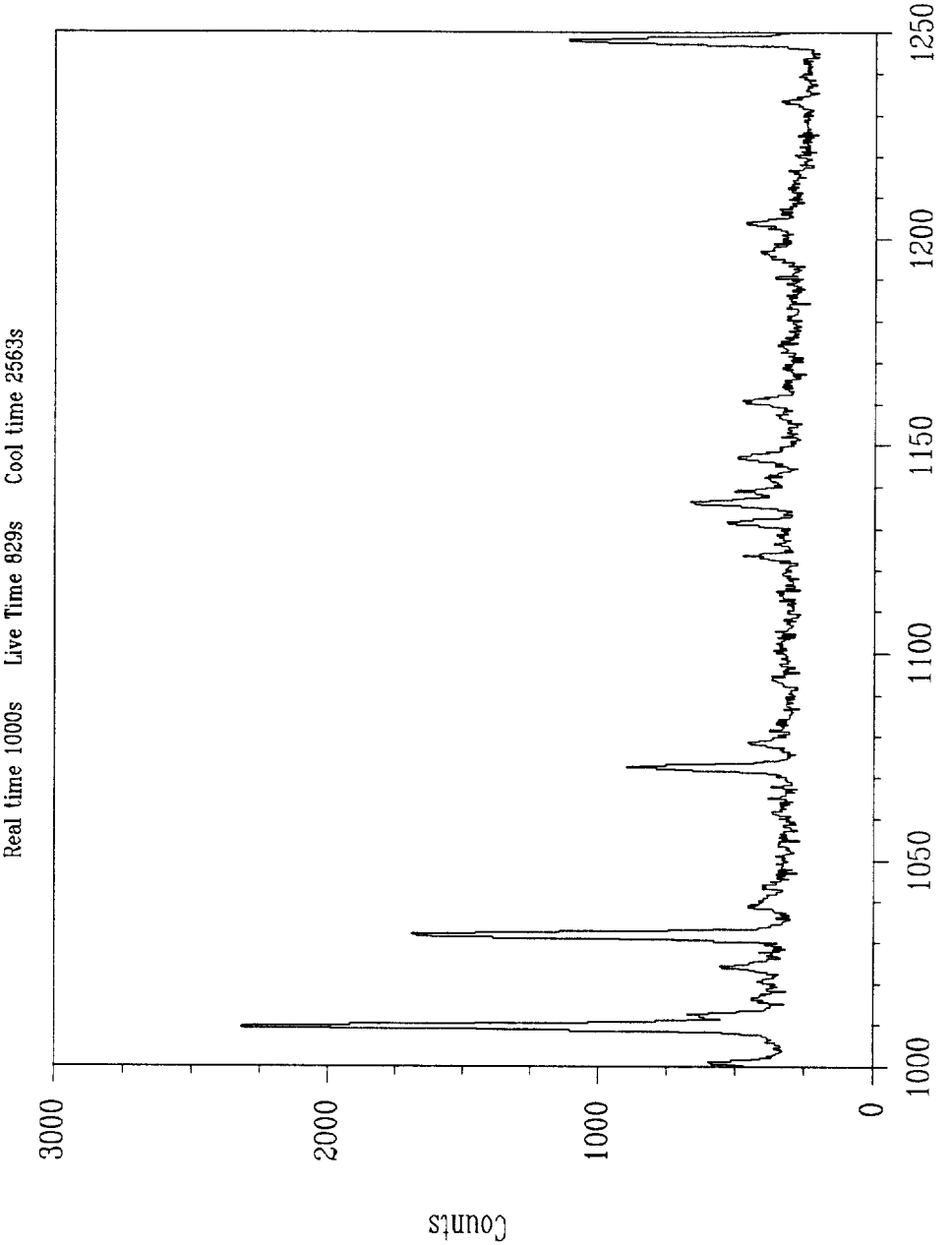

Figure C31. U-235 fission product gamma-ray spectrum from 1000 -1250 keV

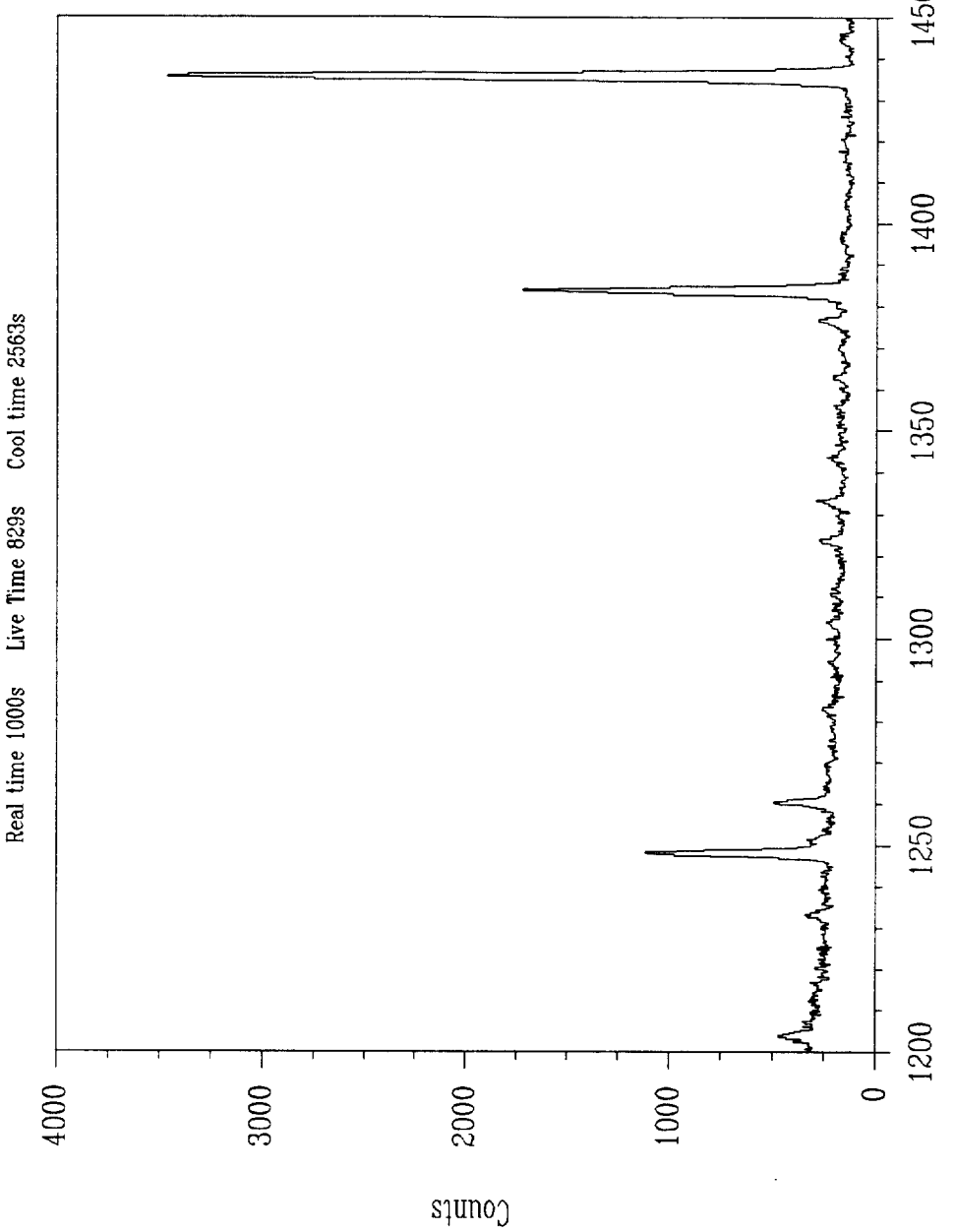

Figure C32. U-235 fission product gamma-ray spectrum from 1200 -1450 keV

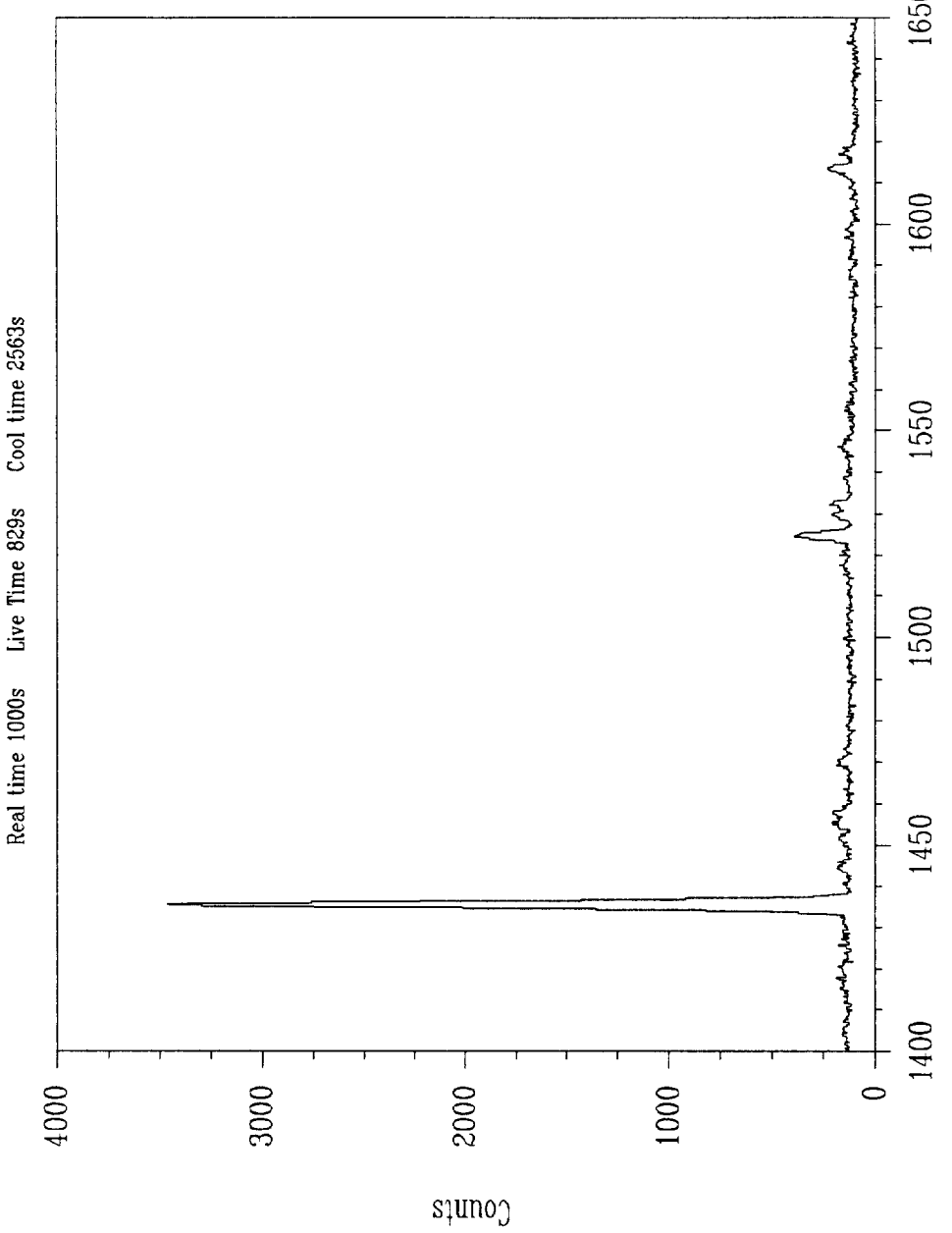

Figure C33. U-235 fission product gamma-ray spectrum from 1400 -1650 keV

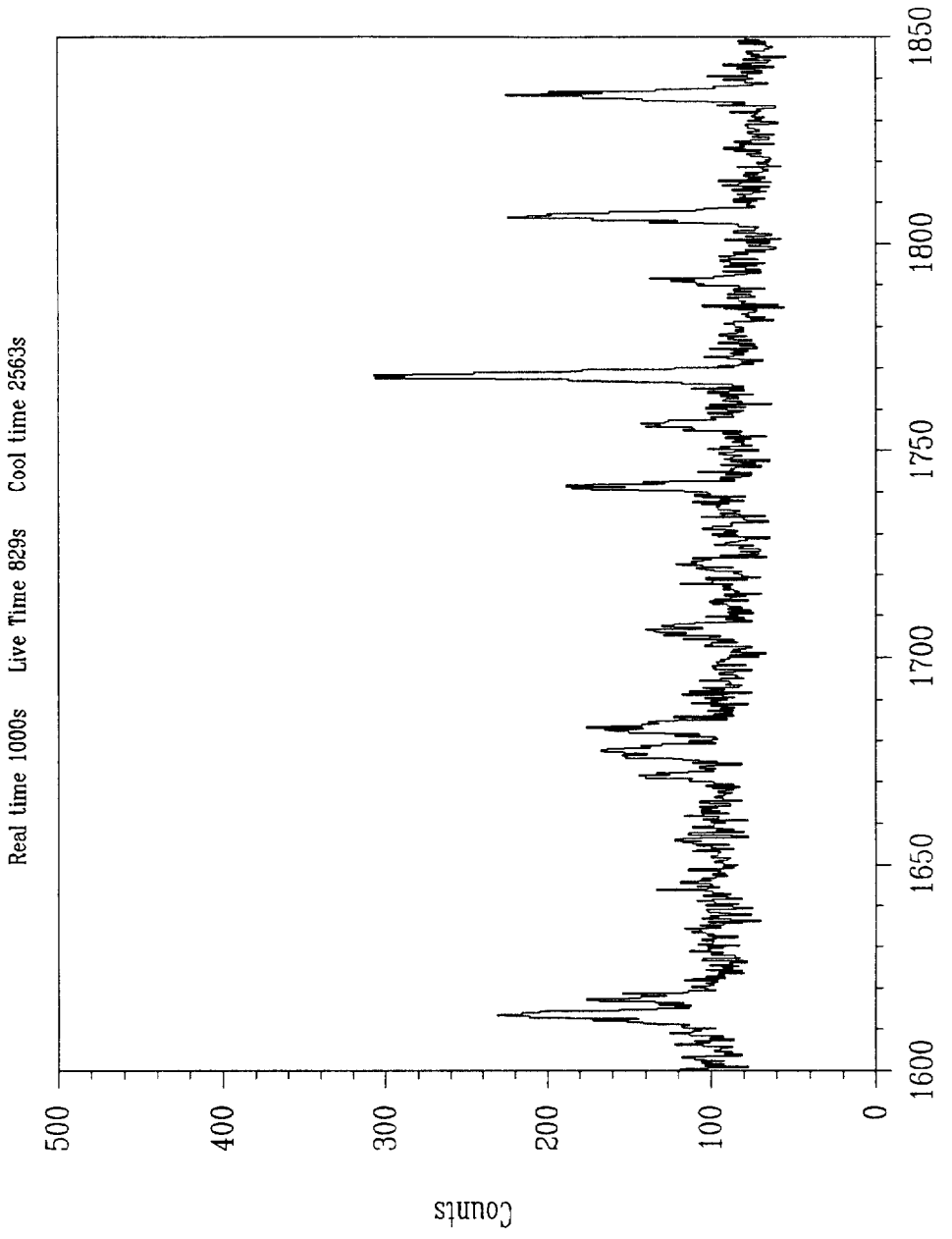

Figure C34. U-235 fission product gamma-ray spectrum from 1600 -1850 keV

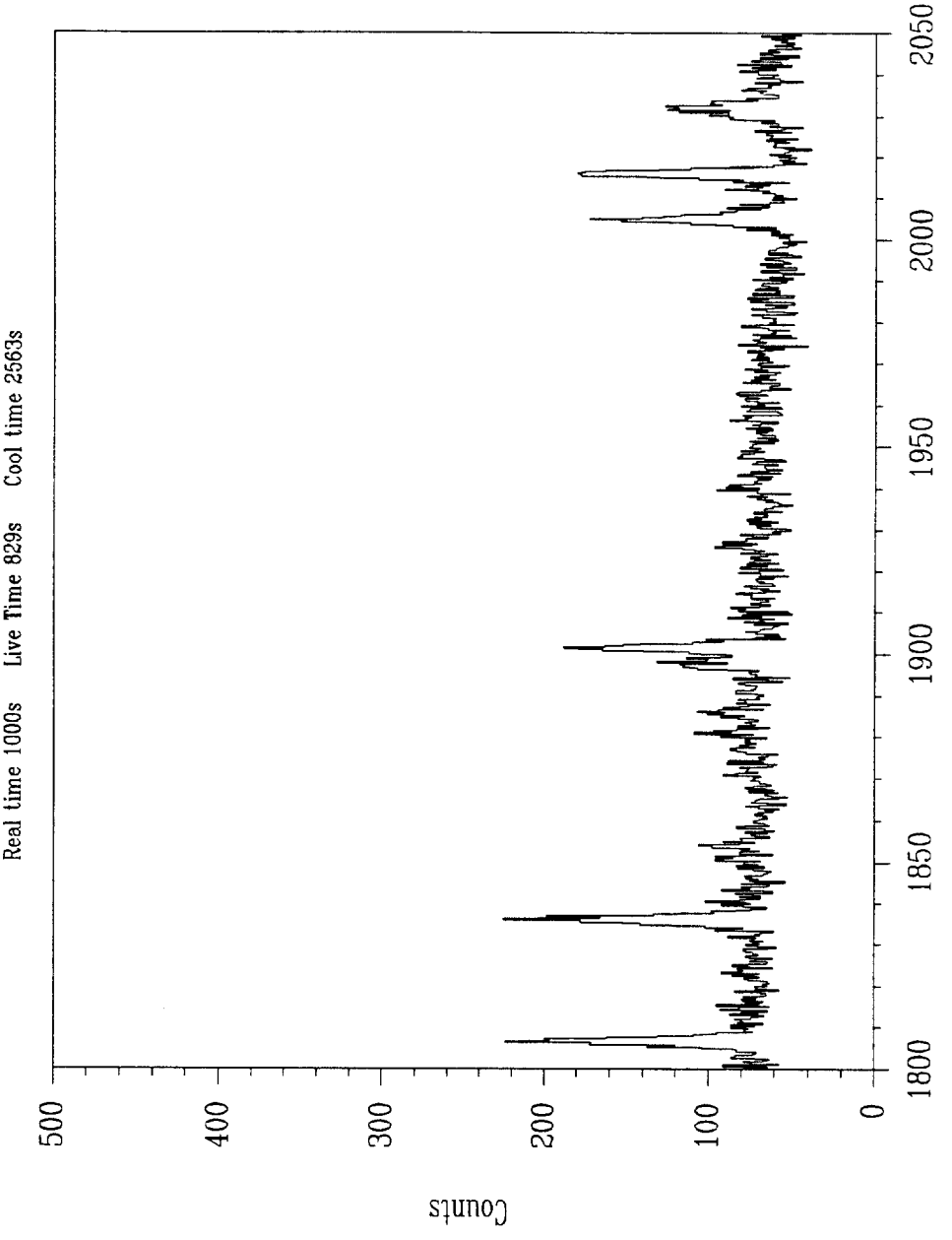

Figure C35. U-235 fission product gamma-ray spectrum from 1800 -2050 keV

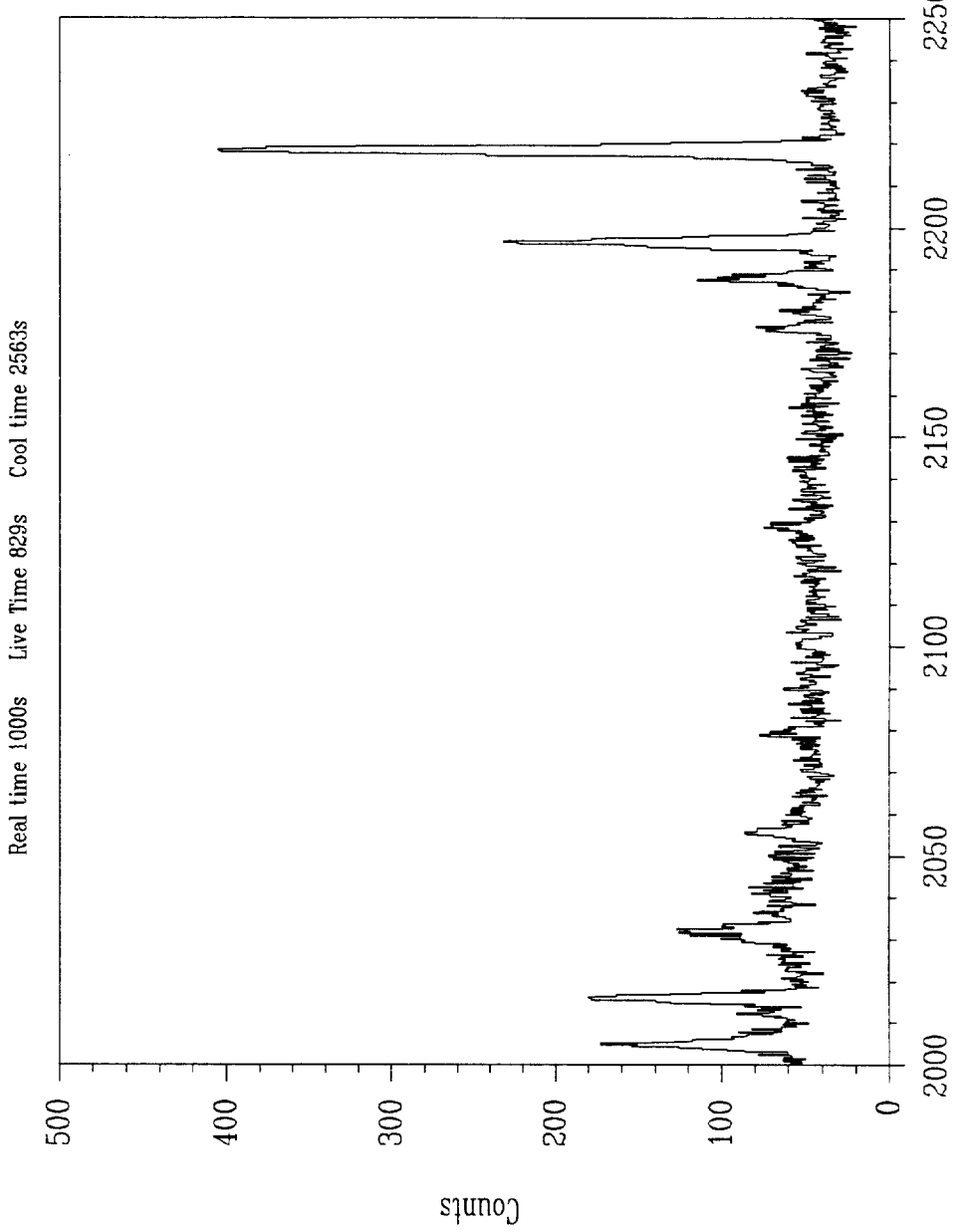

Figure C36. U-235 fission product gamma-ray spectrum from 2000 - 2250 keV

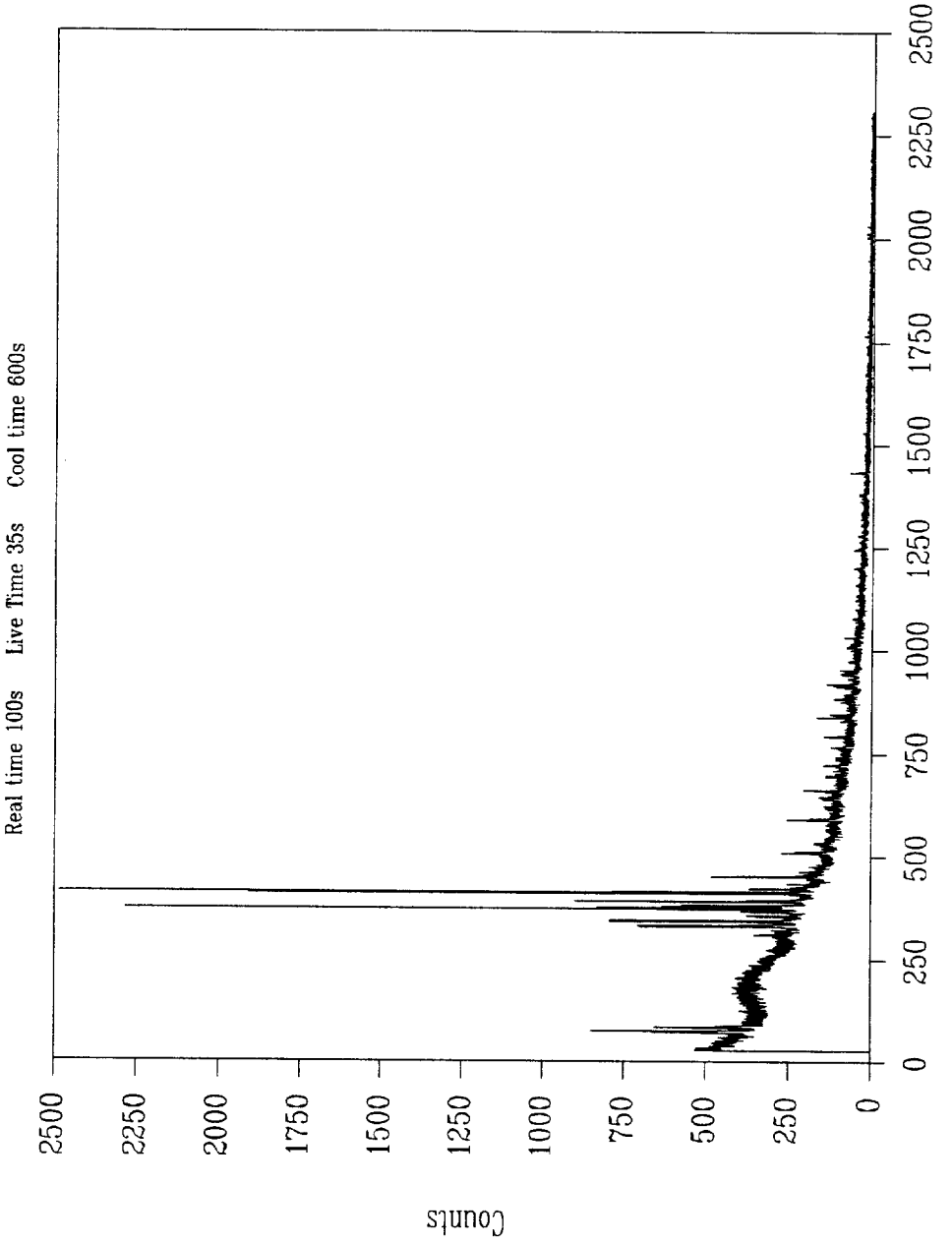

Figure C37. Entire Pu-239 fission product gamma-ray spectrum

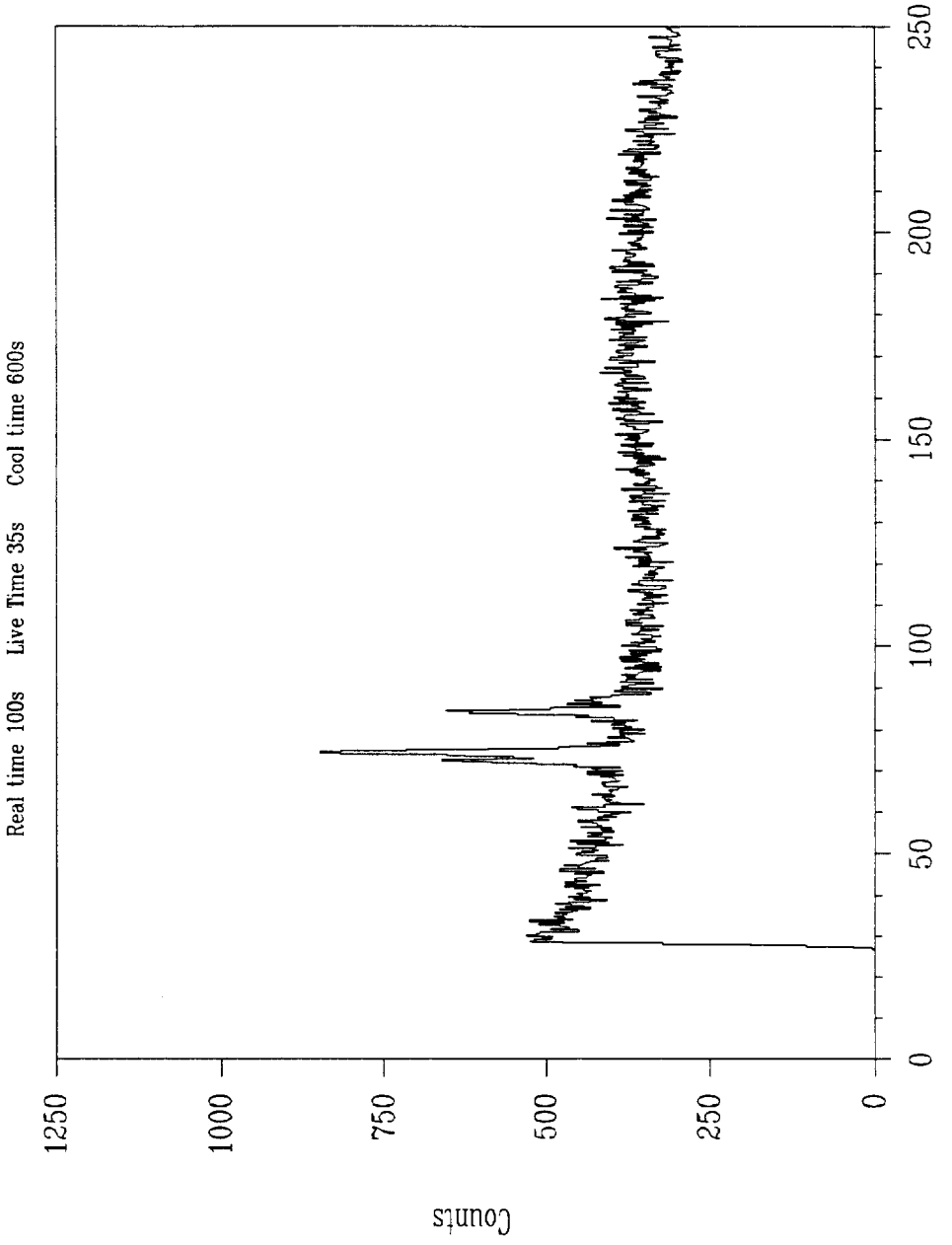

Figure C38. Pu-239 fission product gamma-ray spectrum from 0 - 250 keV

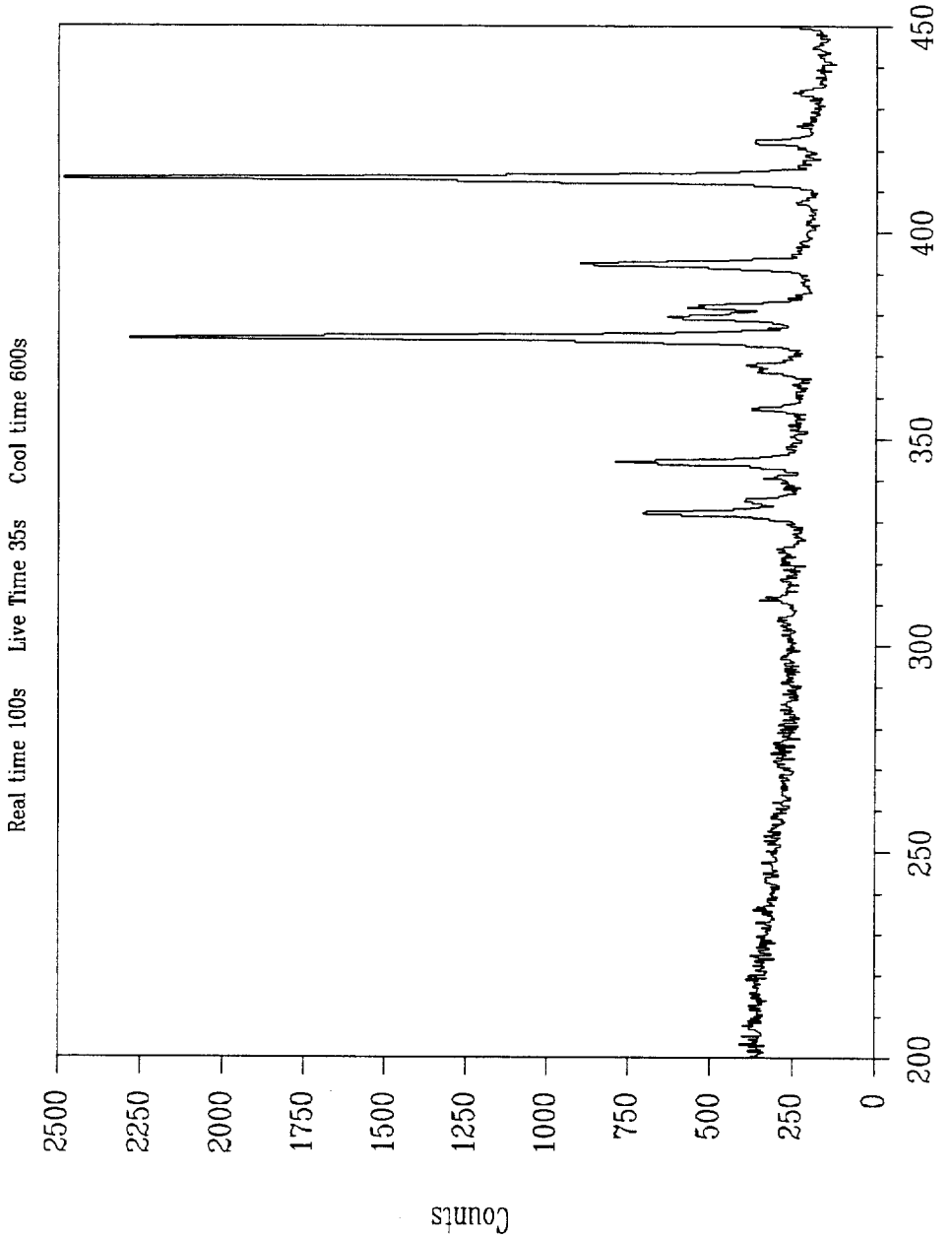

Figure C39. Pu-239 fission product gamma-ray spectrum from 200 -450 keV

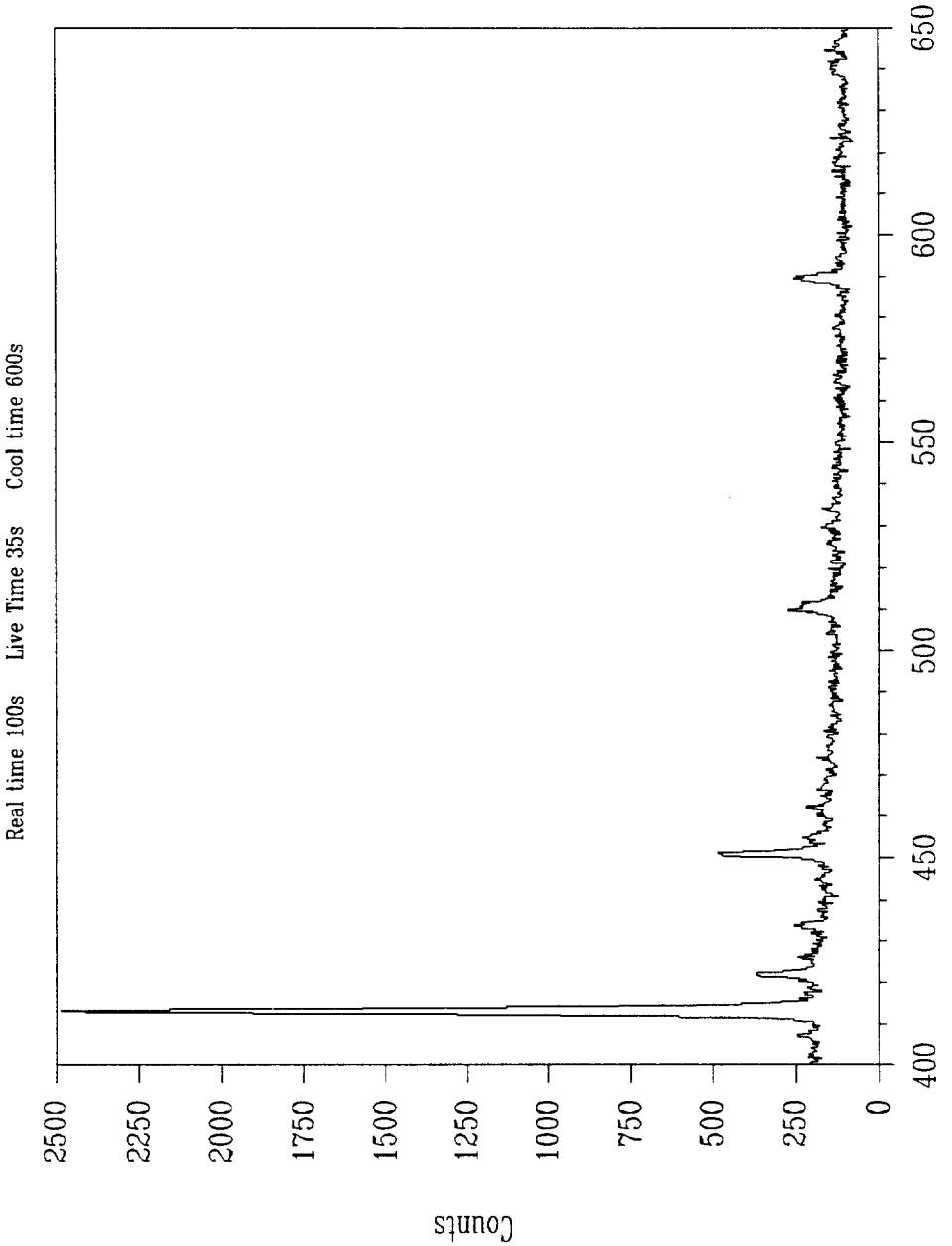

Figure C40. Pu-239 fission product gamma-ray spectrum from 400 -650 keV

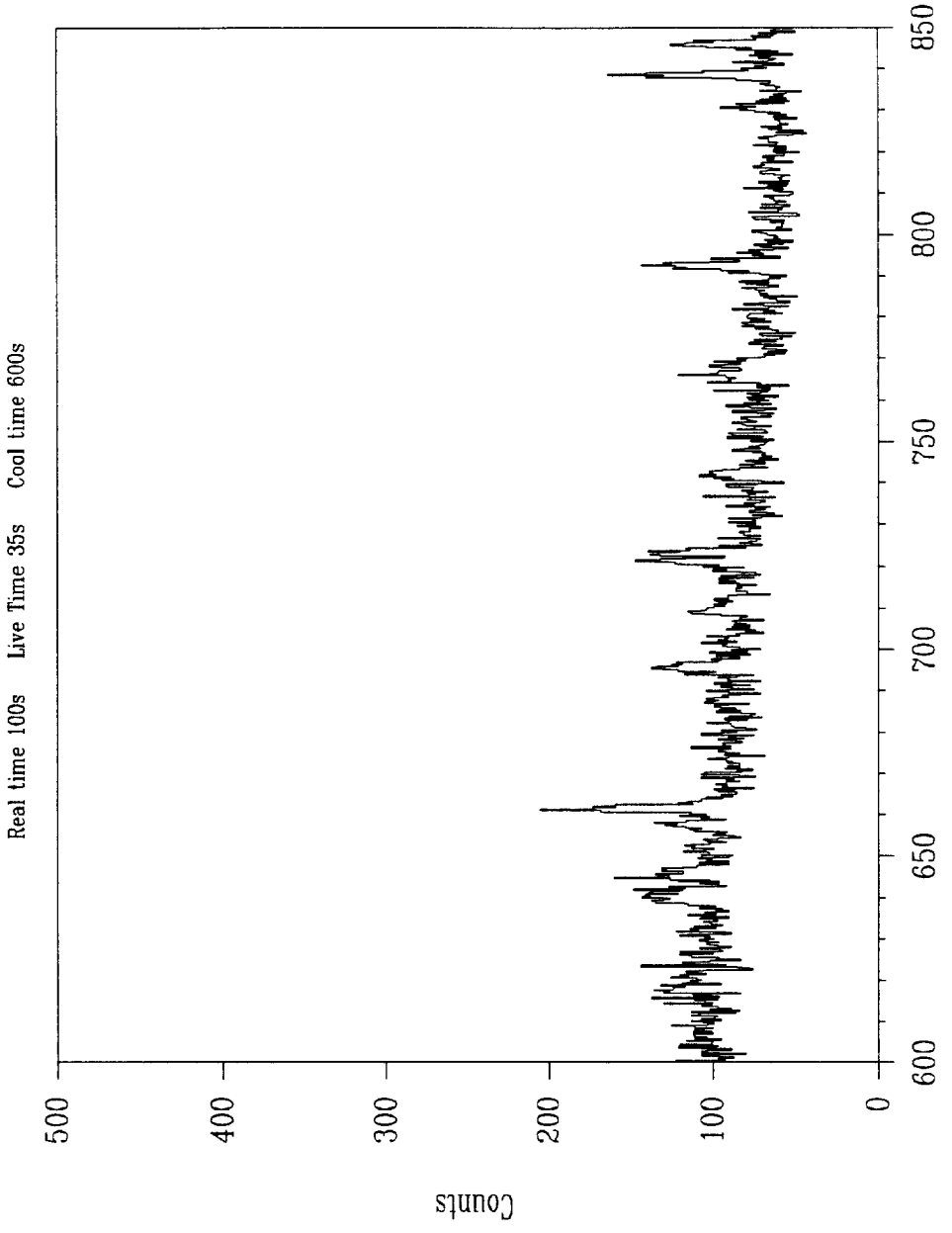

Figure C41. Pu-239 fission product gamma-ray spectrum from 600 -850 keV

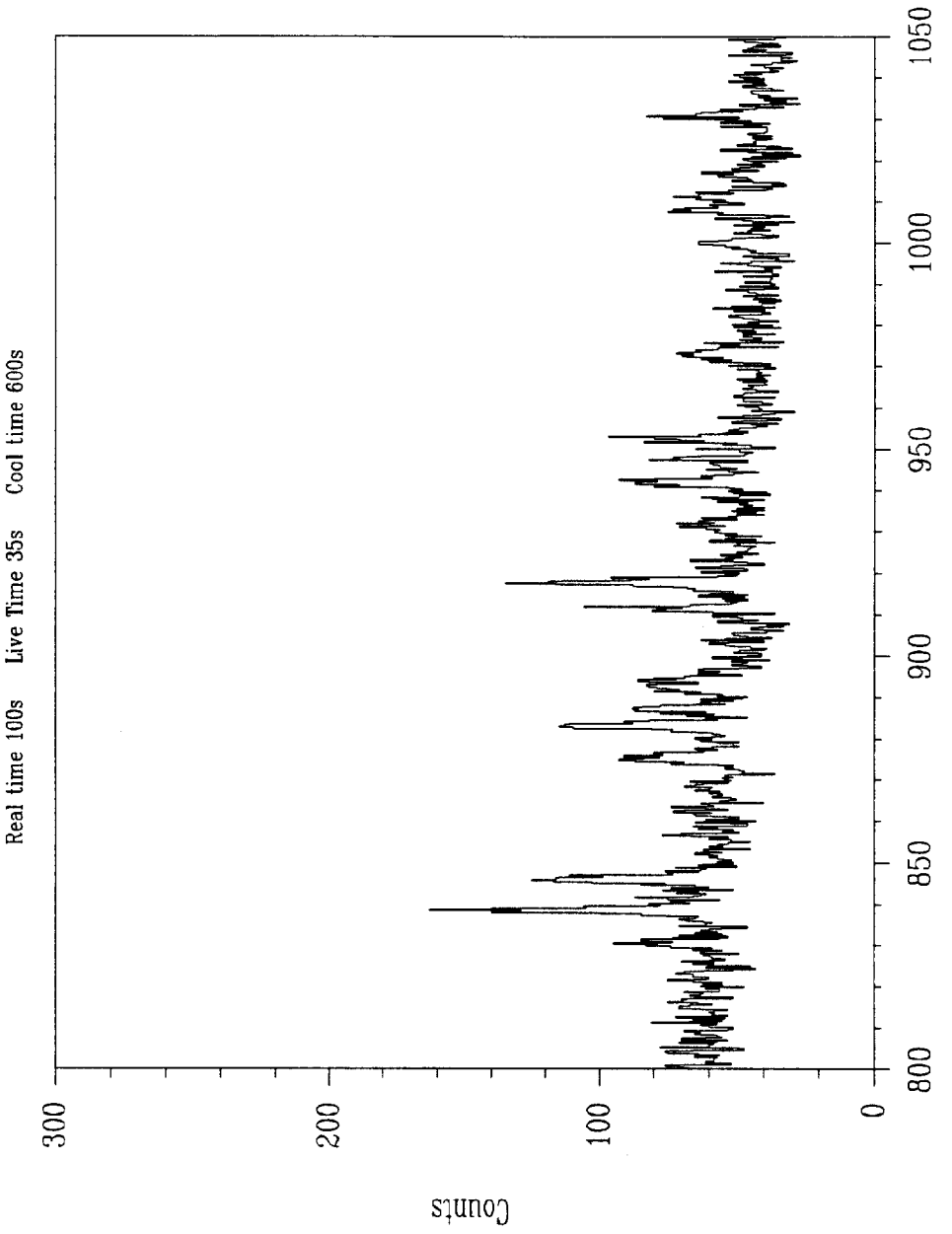

Figure C42. Pu-239 fission product gamma-ray spectrum from 800 -1050 keV

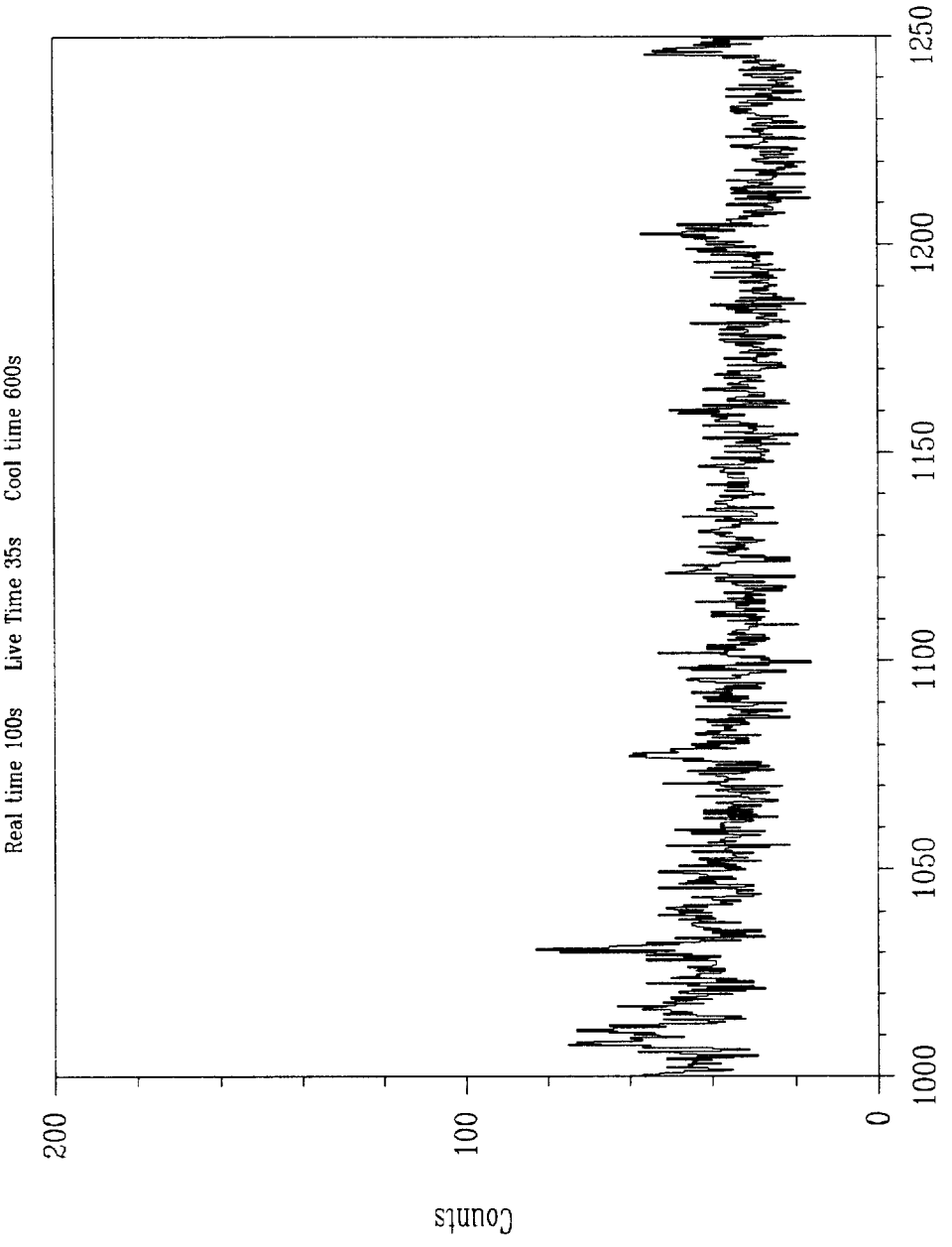

Figure C43. Pu-239 fission product gamma-ray spectrum from 1000 -1250 keV

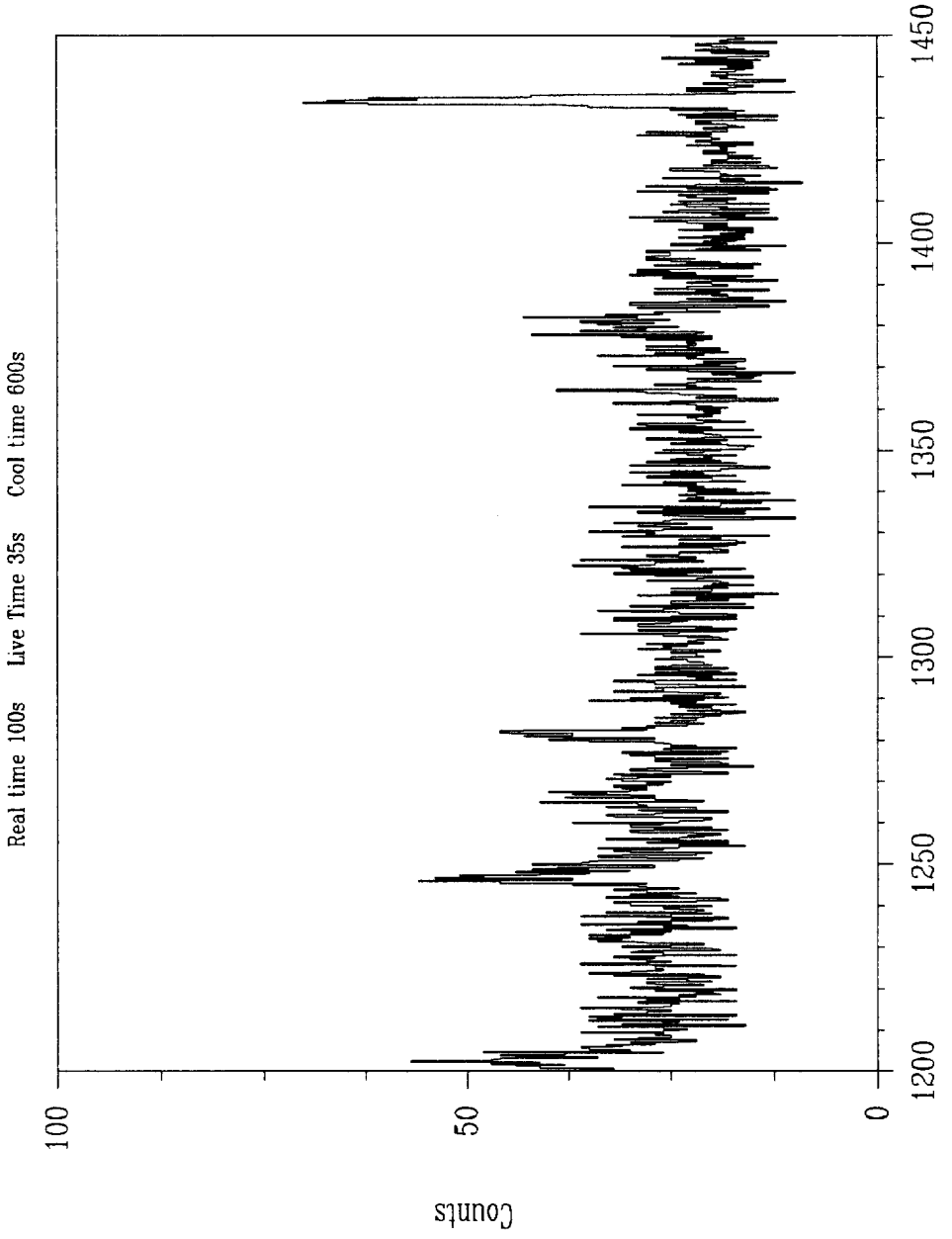

Figure C44. Pu-239 fission product gamma-ray spectrum from 1200 -1450 keV

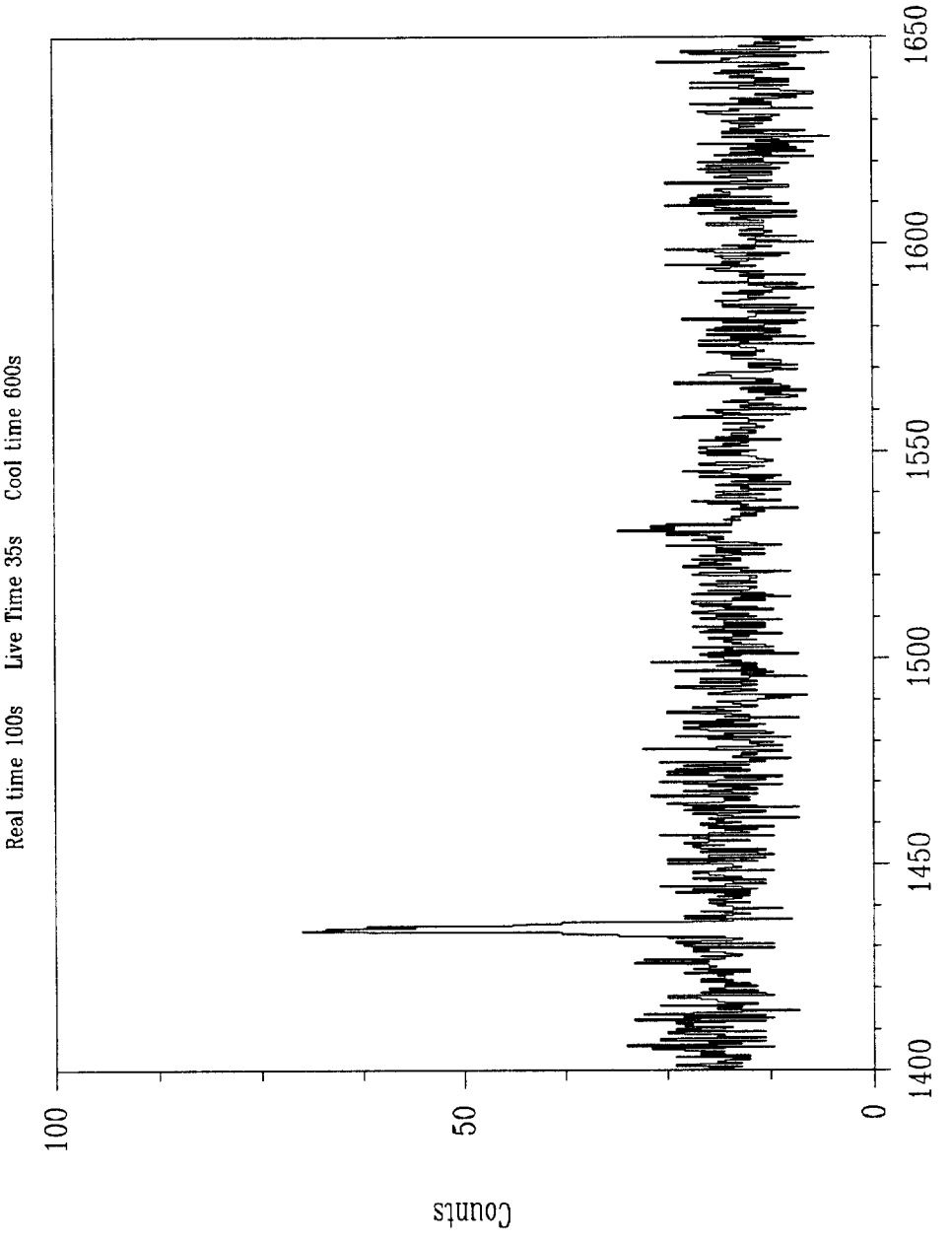

Figure C45. Pu-239 fission product gamma-ray spectrum from 1400 -1650 keV

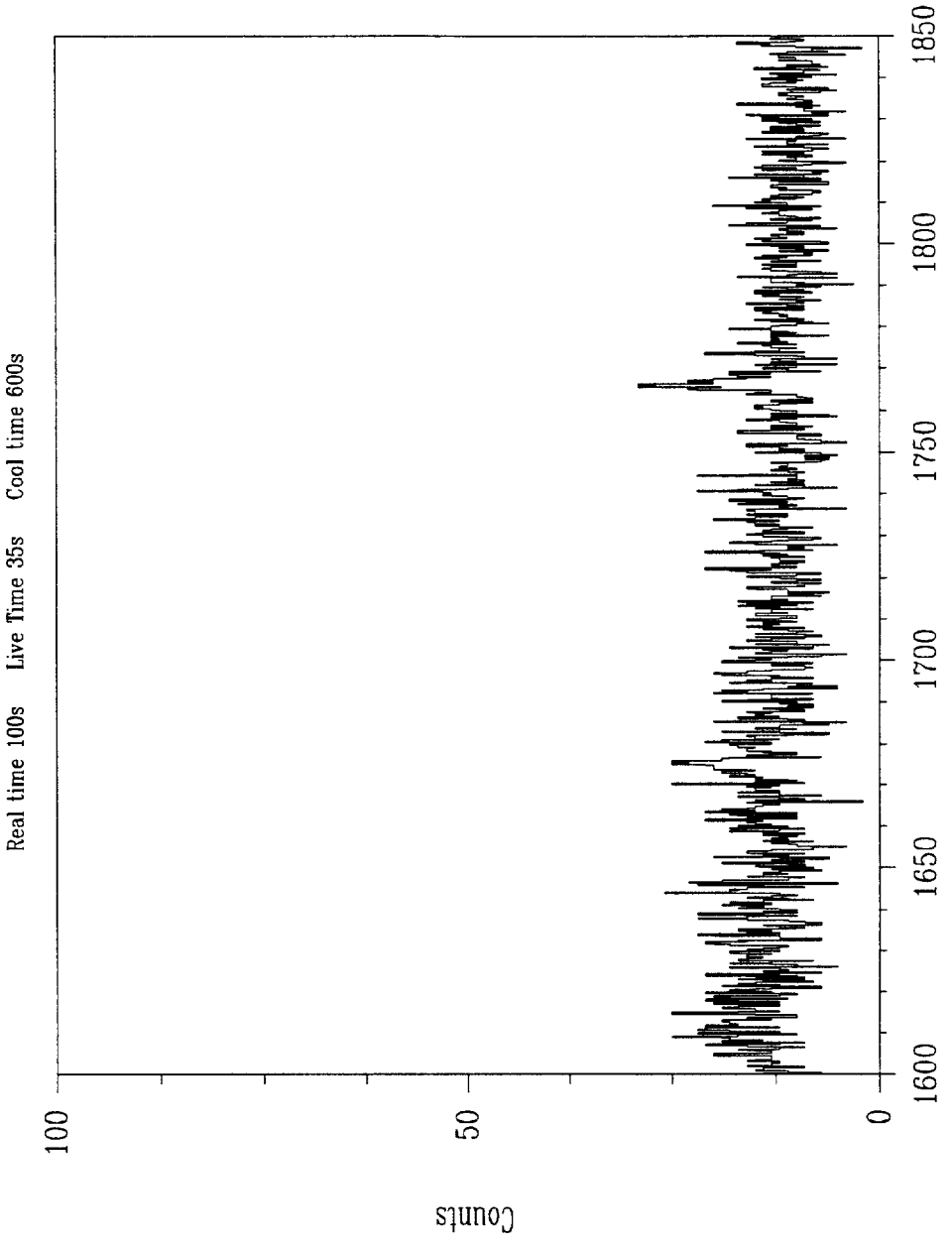

Figure C46. Pu-239 fission product gamma-ray spectrum from 1600 -1850 keV

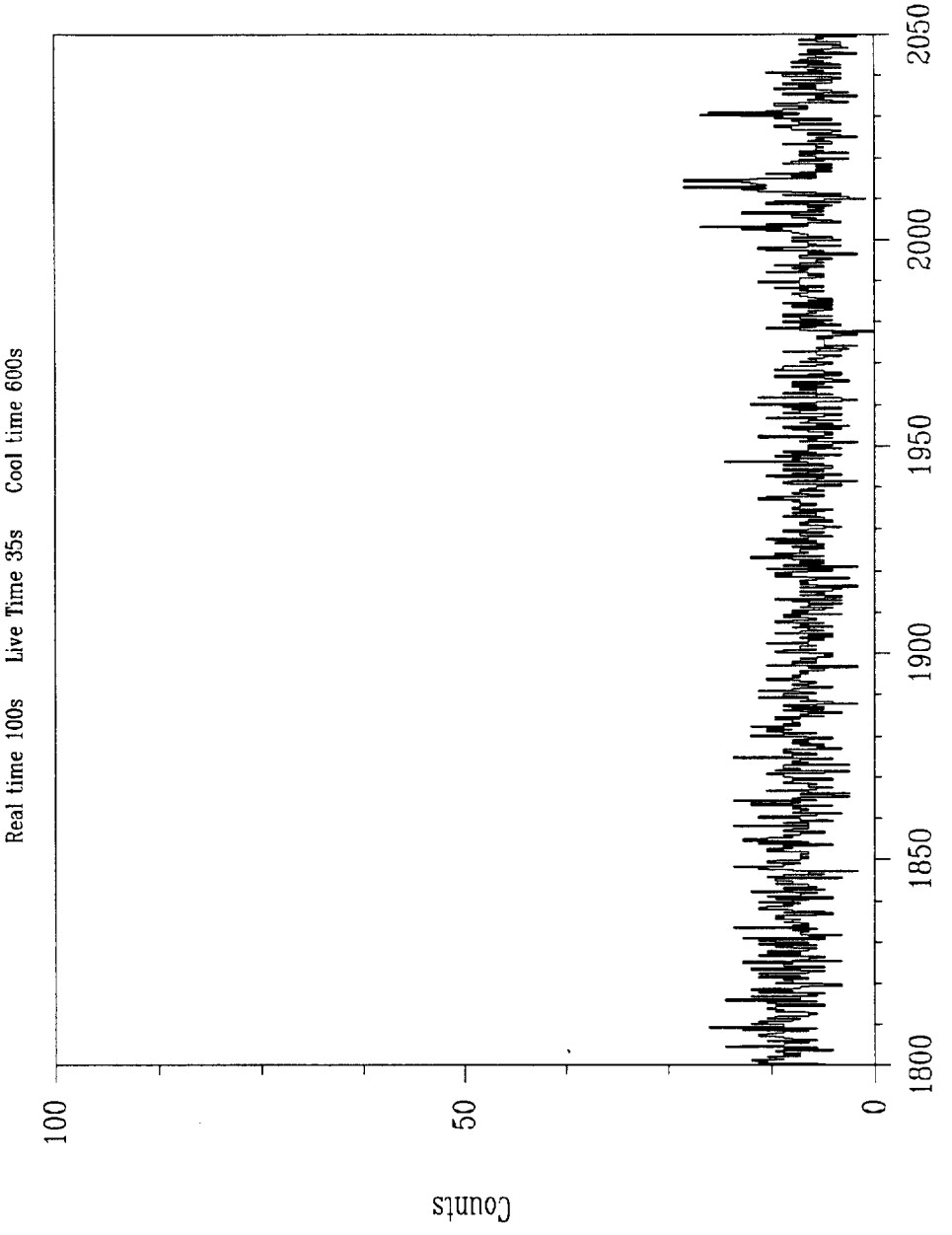

Figure C47. Pu-239 fission product gamma-ray spectrum from 1800 -2050 keV

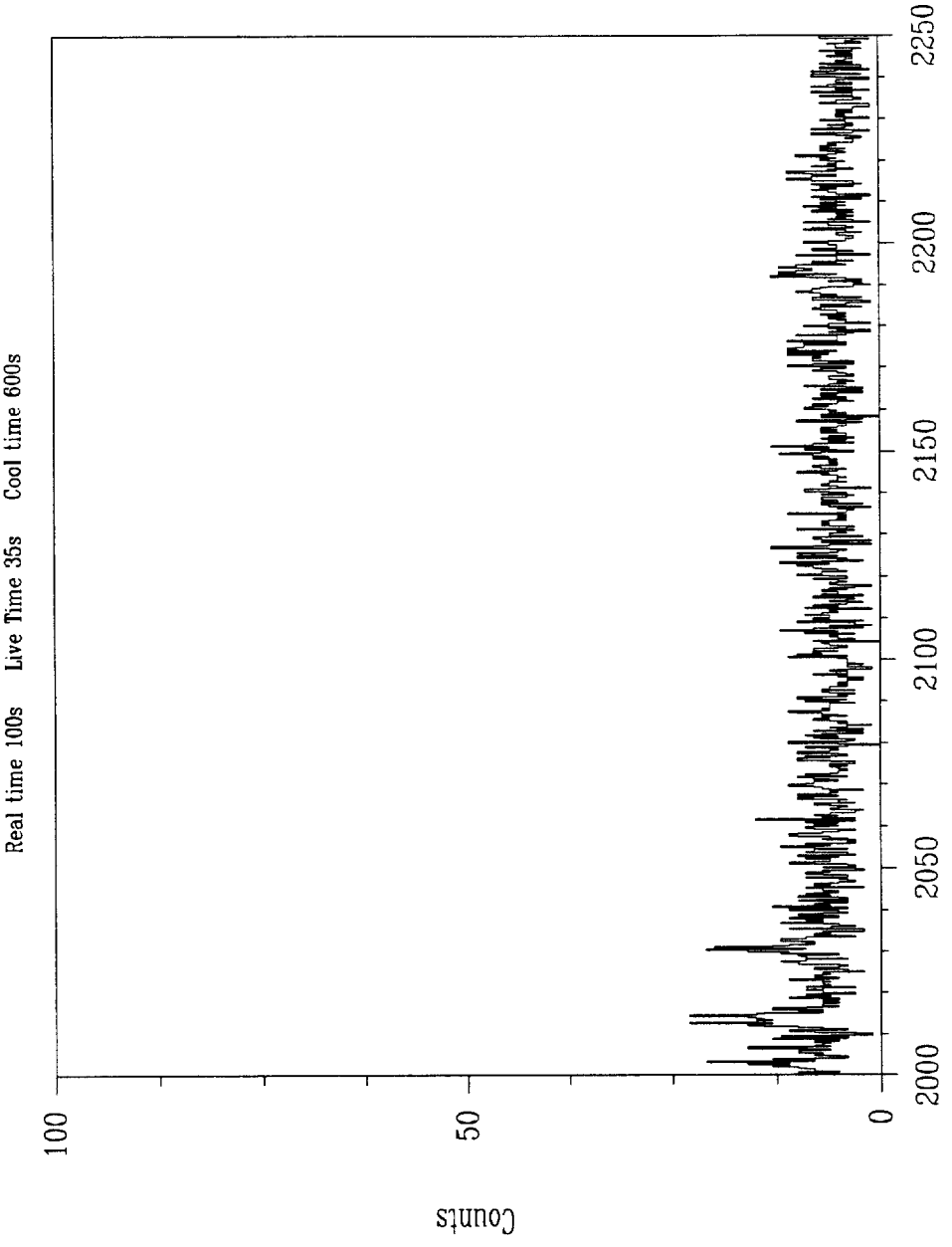

Figure C48. Pu-239 fission product gamma-ray spectrum from 2000 - 2250 keV

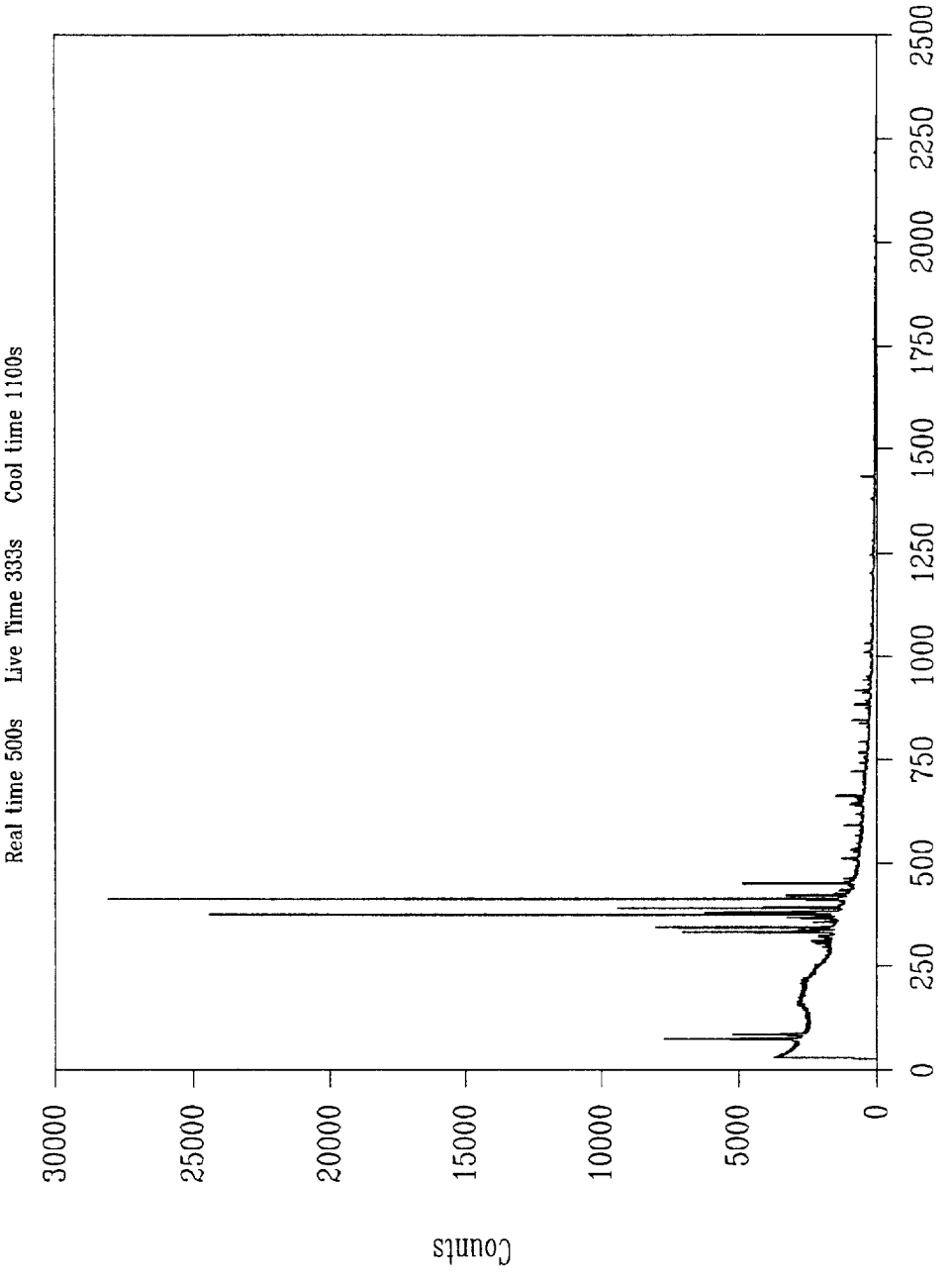

Figure C49. Entire Pu-239 fission product gamma-ray spectrum

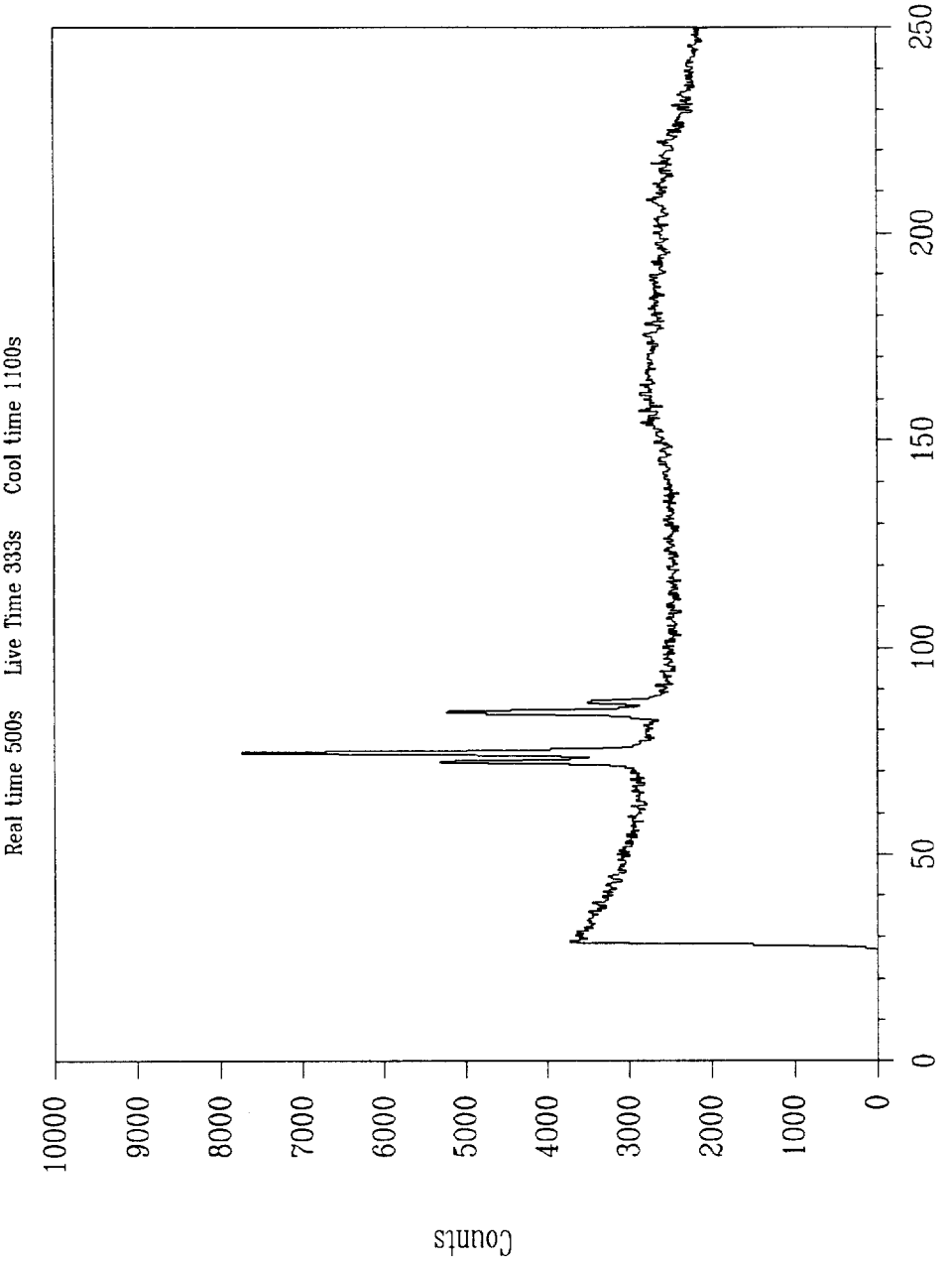

Figure C50. Pu-239 fission product gamma-ray spectrum from 0 - 250 keV

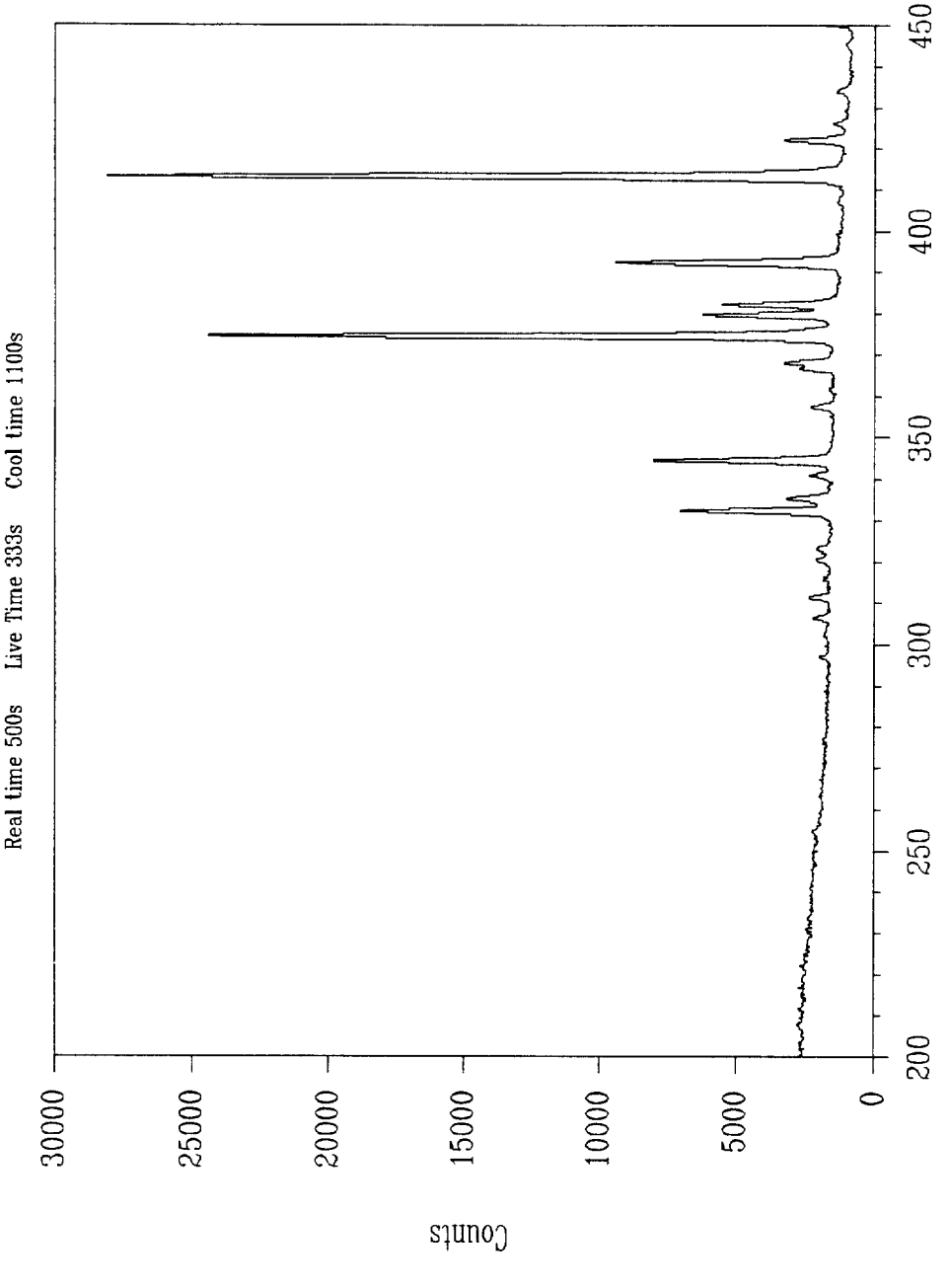

Figure C51. Pu-239 fission product gamma-ray spectrum from 200 - 450 keV

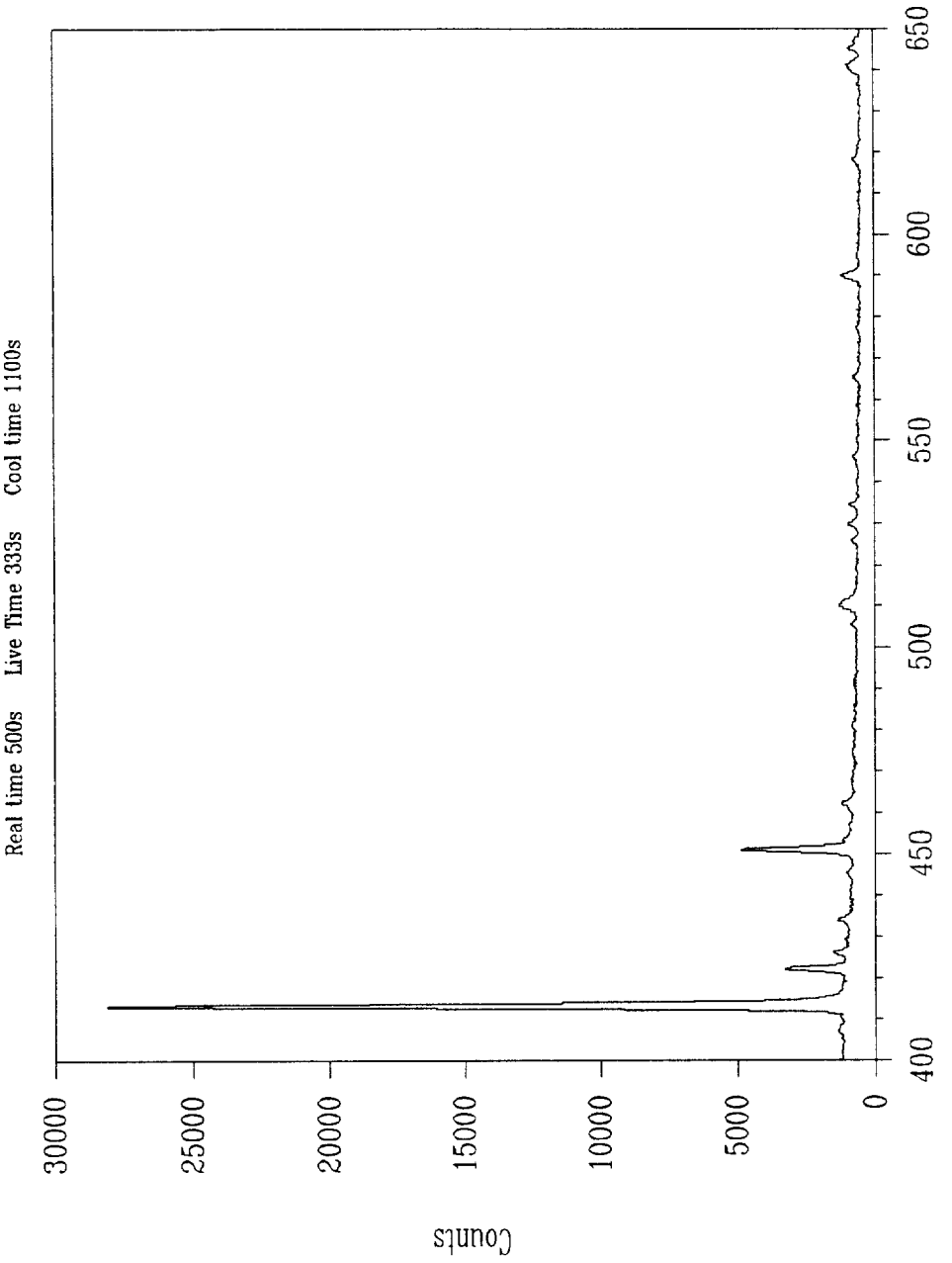

Figure C52. Pu-239 fission product gamma-ray spectrum from 400 - 650 keV

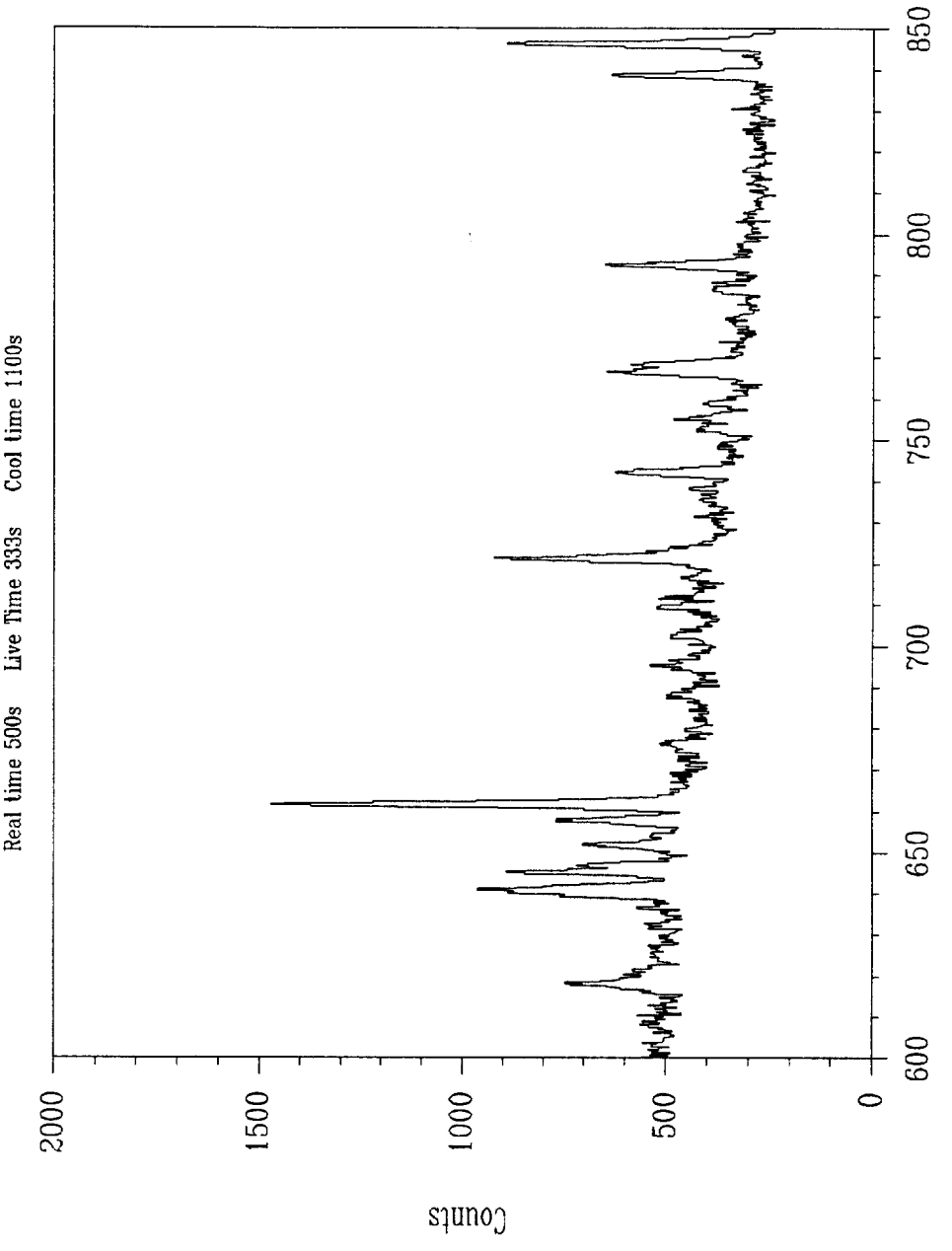

Figure C53. Pu-239 fission product gamma-ray spectrum from 600 - 850 keV

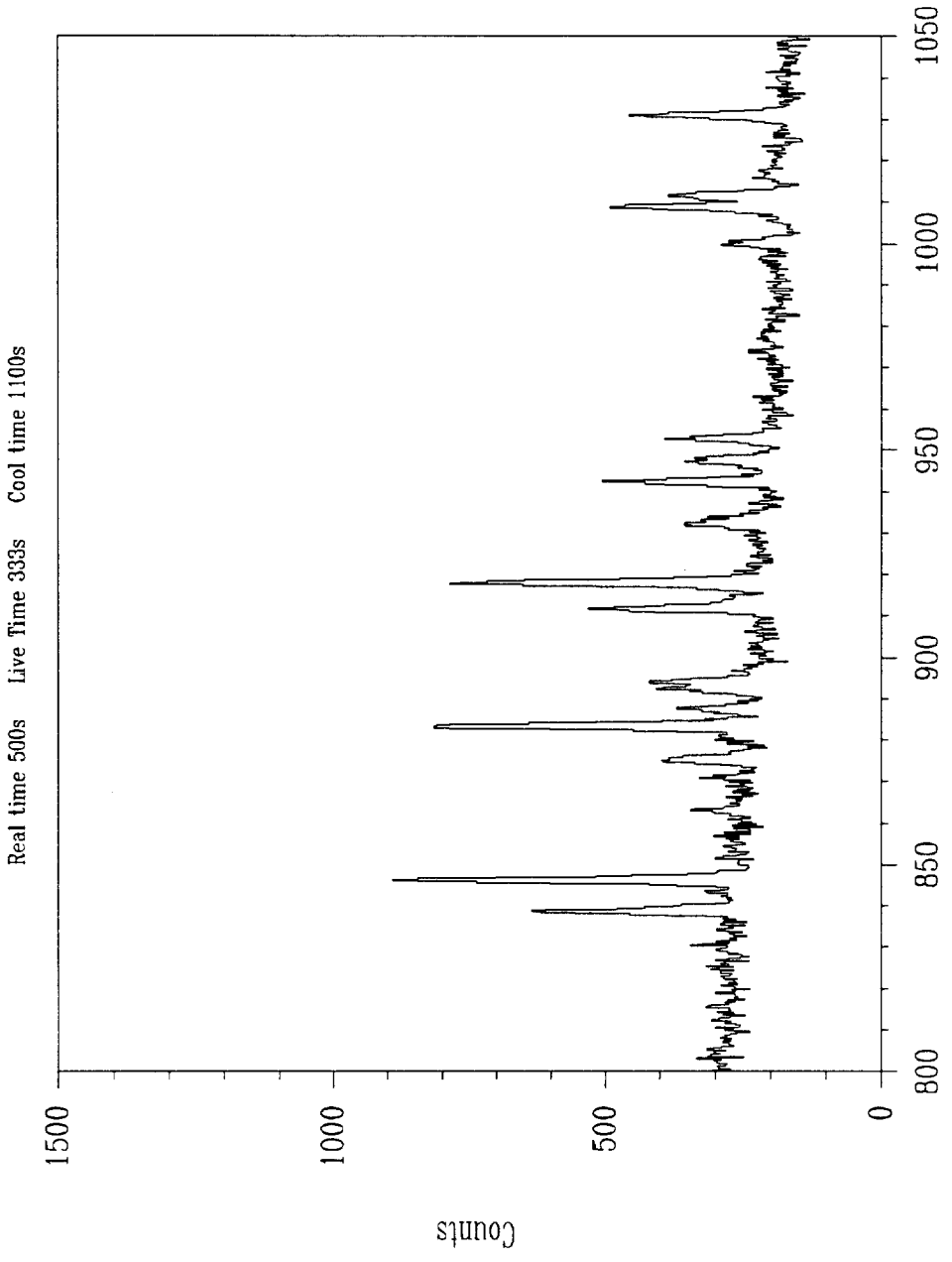

Figure C54. Pu-239 fission product gamma-ray spectrum from 800 - 1050 keV

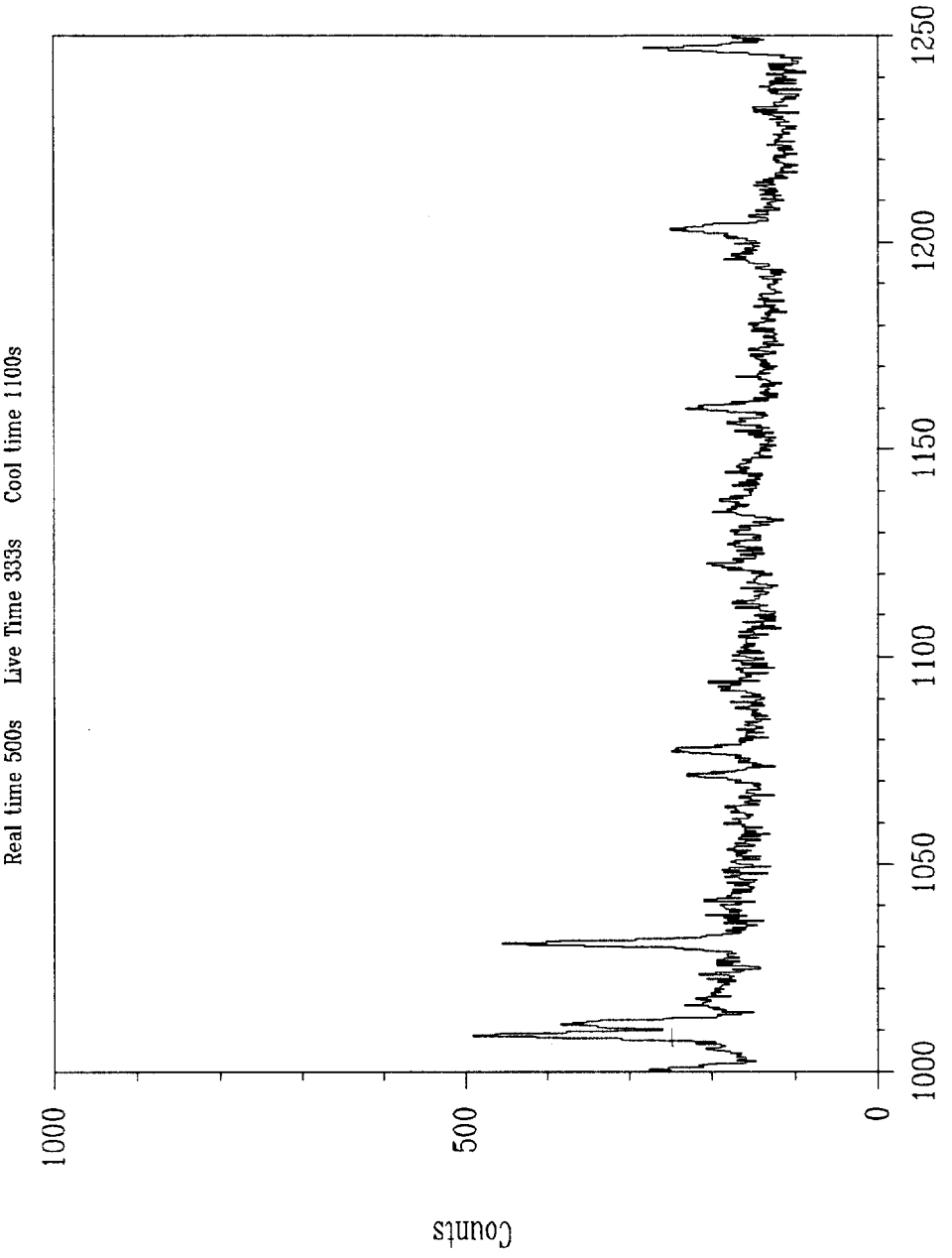

Figure C55. Pu-239 fission product gamma-ray spectrum from 1000 - 1250 keV

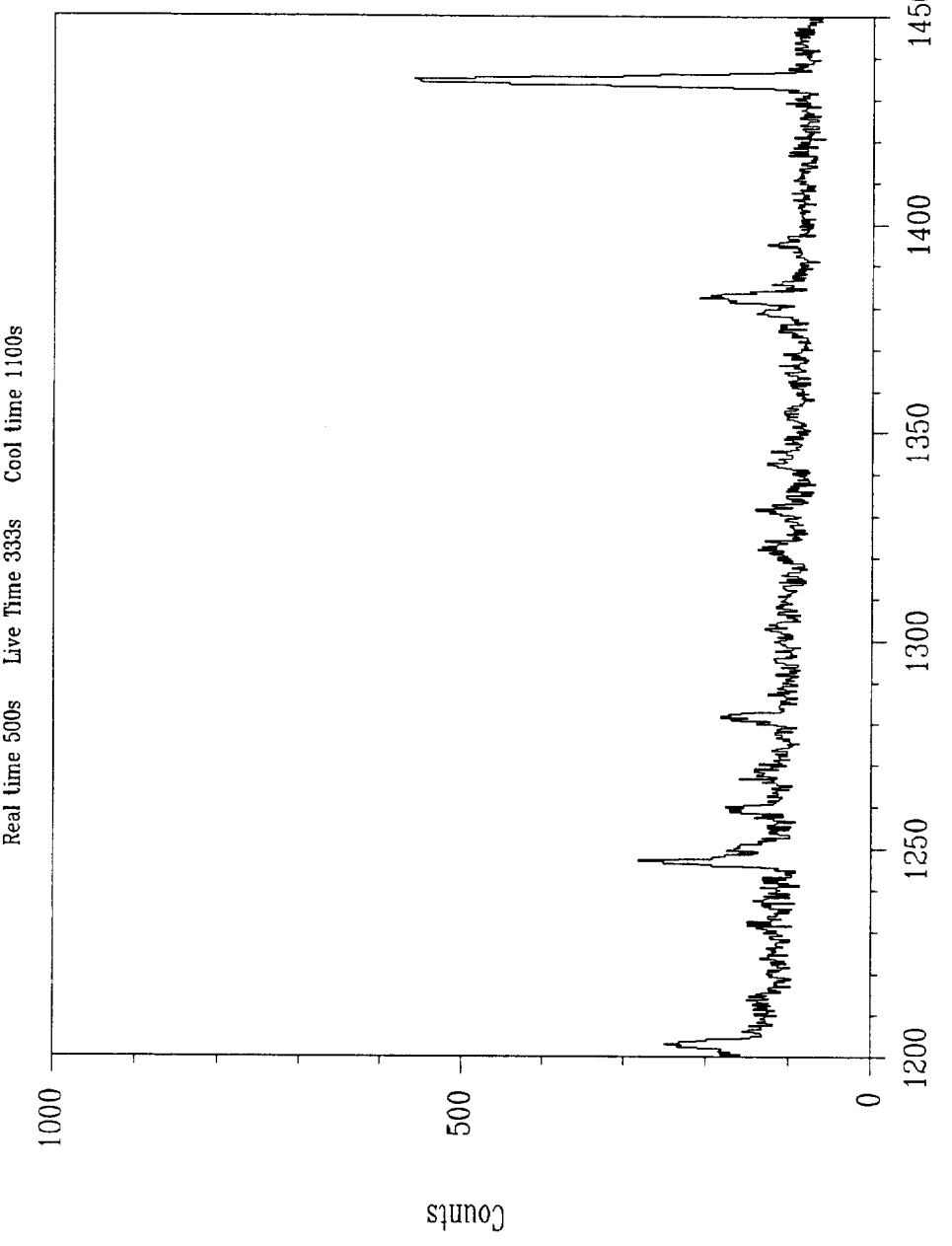

Figure C56. Pu-239 fission product gamma-ray spectrum from 1200 - 1450 keV

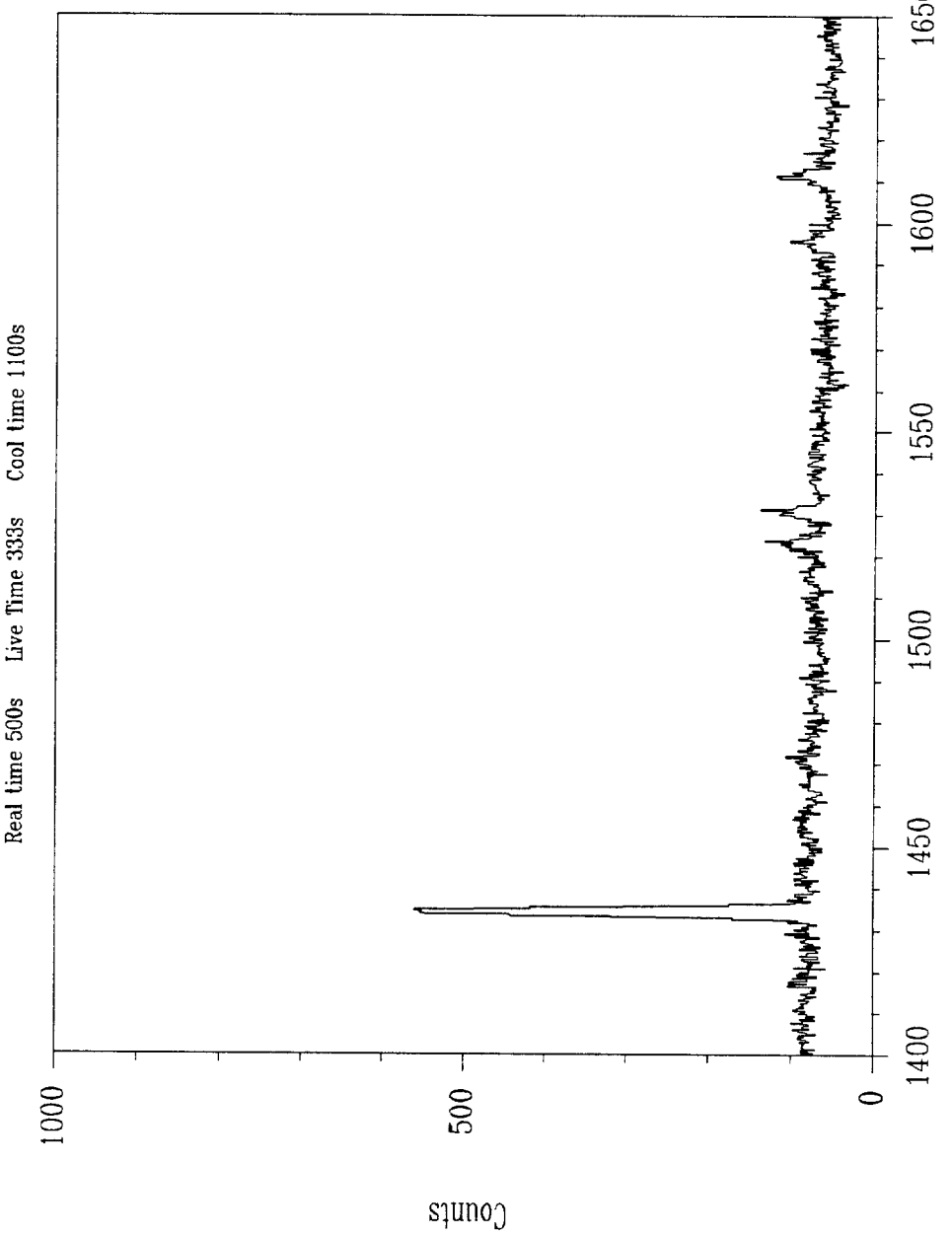

Figure C57. Pu-239 fission product gamma-ray spectrum from 1400 - 1650 keV

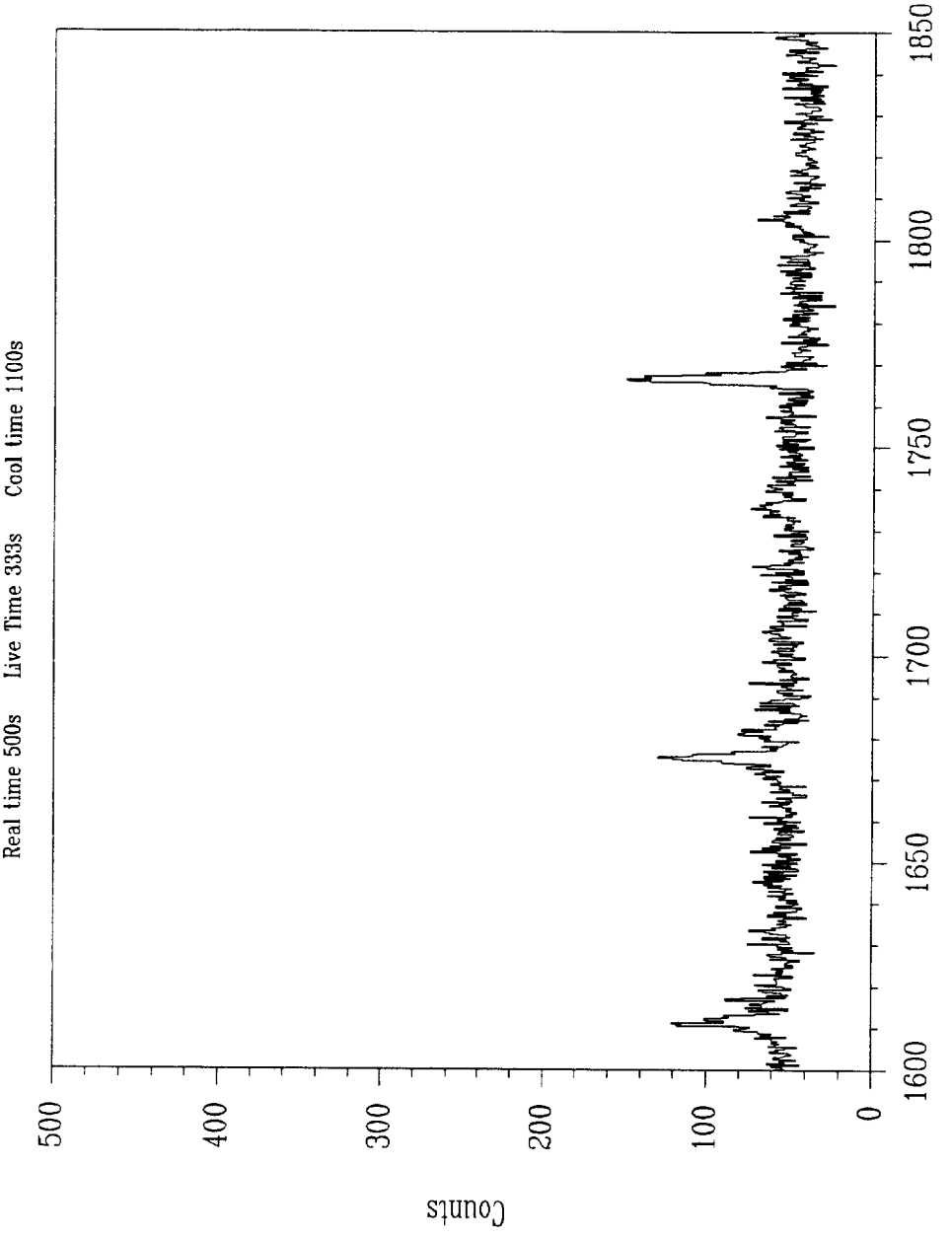

Figure C58. Pu-239 fission product gamma-ray spectrum from 1600 - 1850 keV

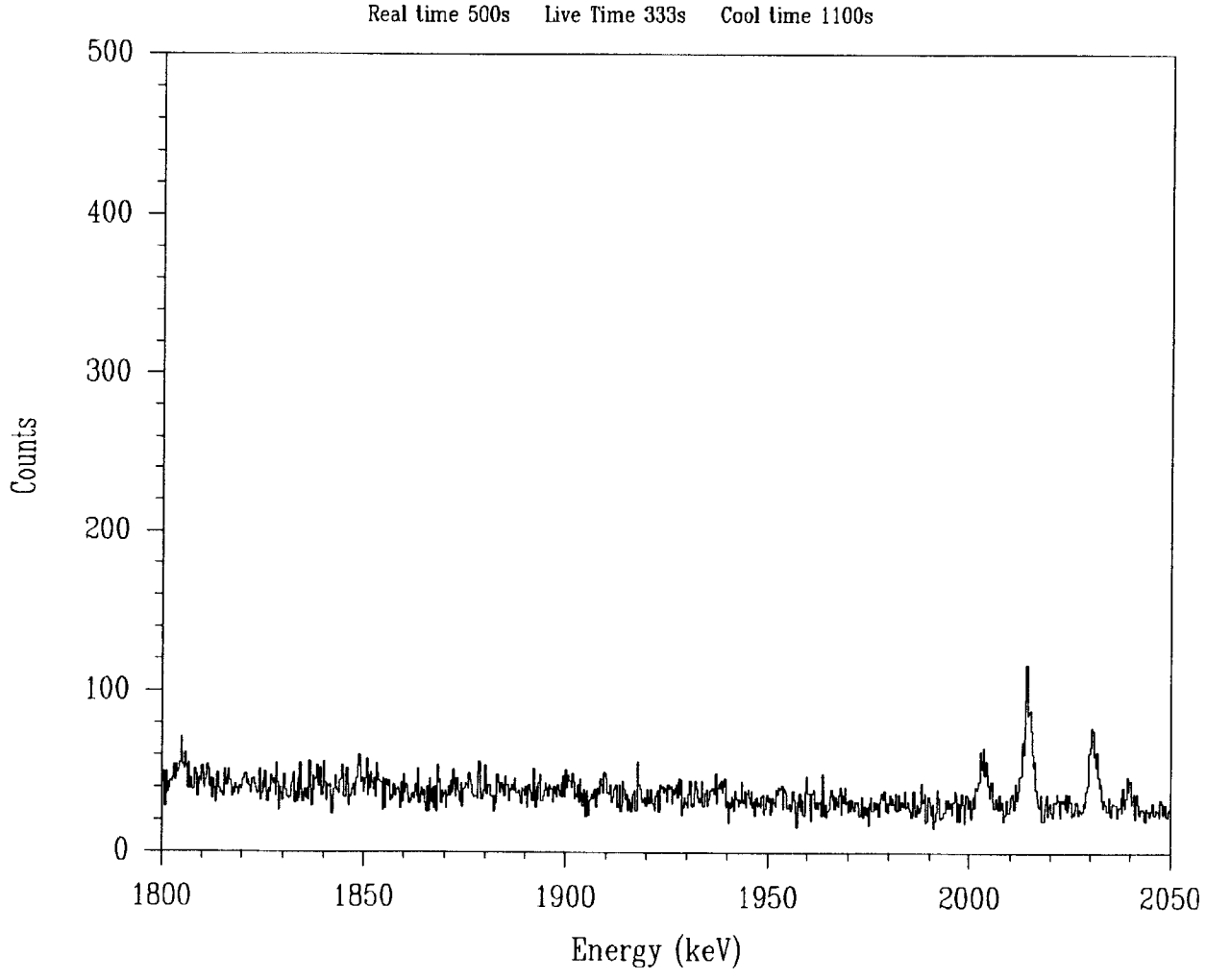

Figure C59. Pu-239 fission product gamma-ray spectrum from 1800 - 2050 keV

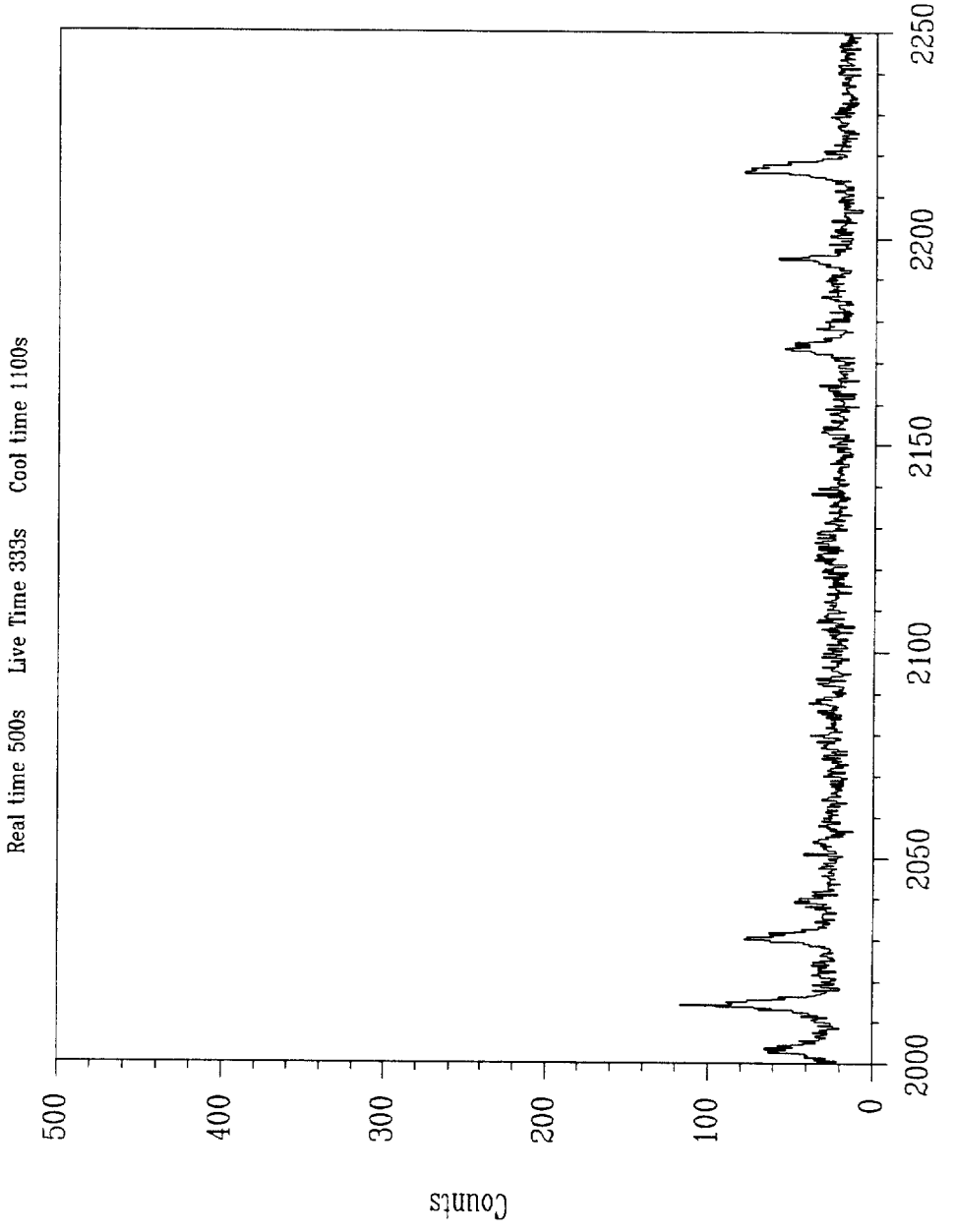

Figure C60. Pu-239 fission product gamma-ray spectrum from 2000 - 2250 keV

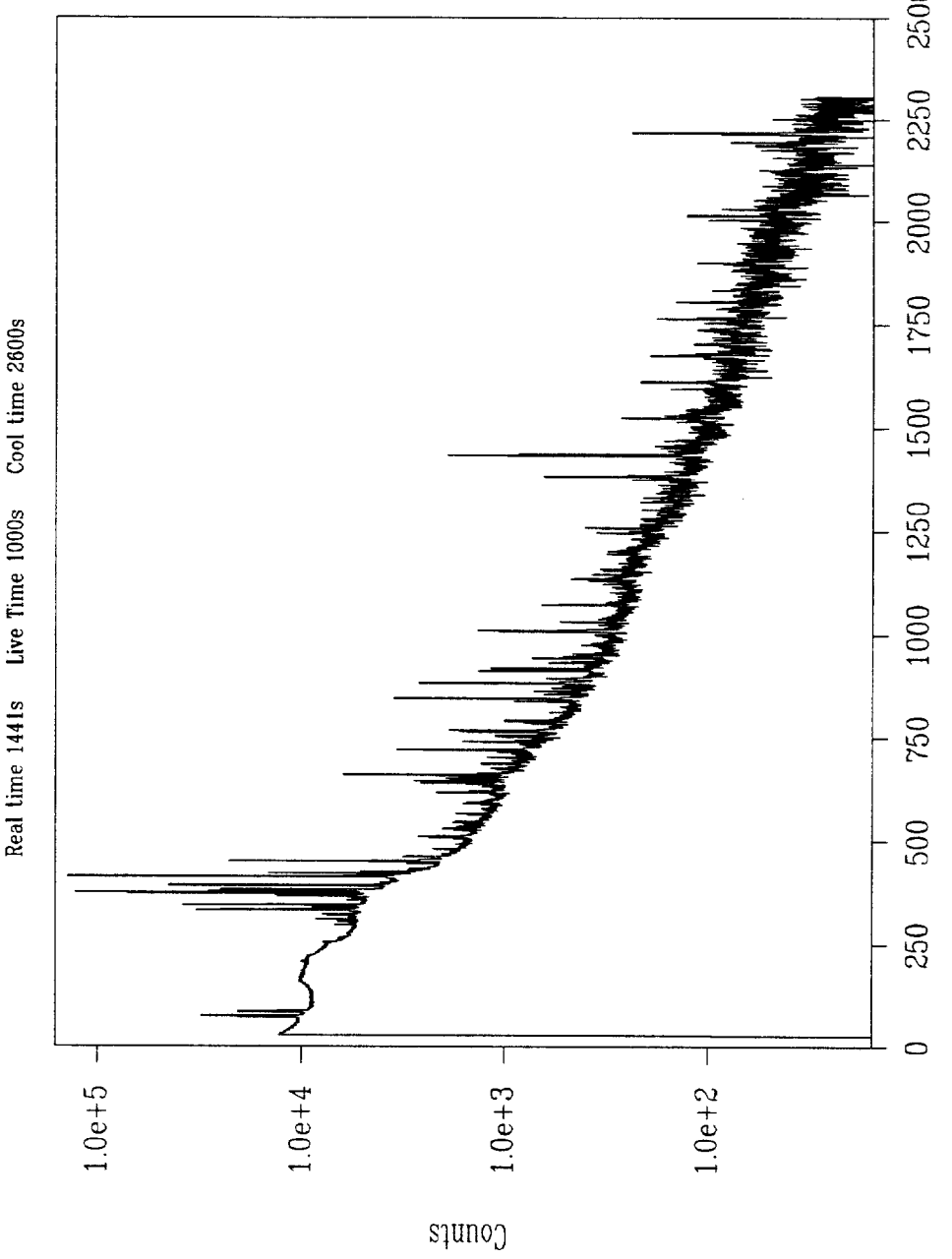

Figure C61. Entire Pu-239 fission product gamma-ray spectrum

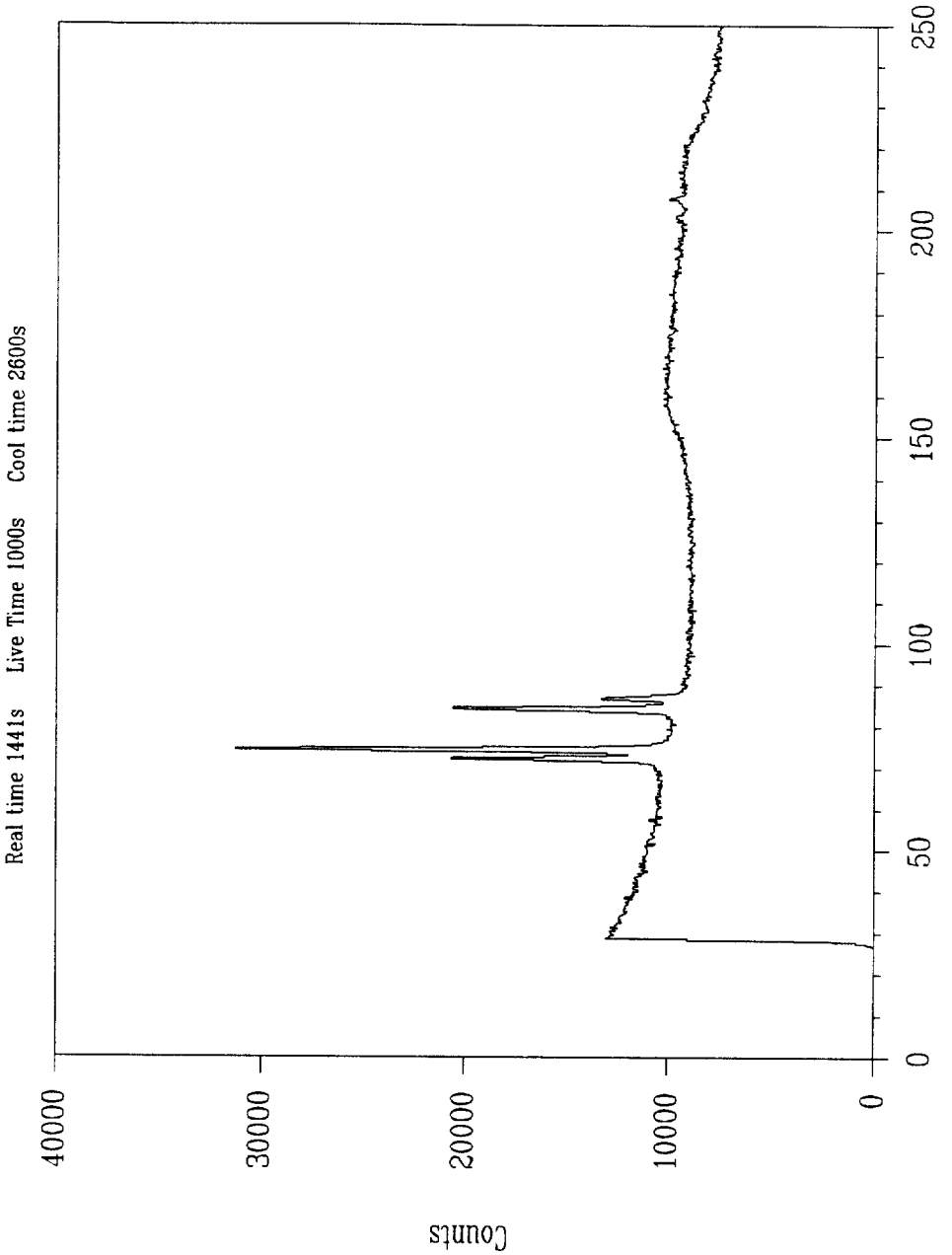

Figure C62. Pu-239 fission product gamma-ray spectrum from 0 - 250 keV

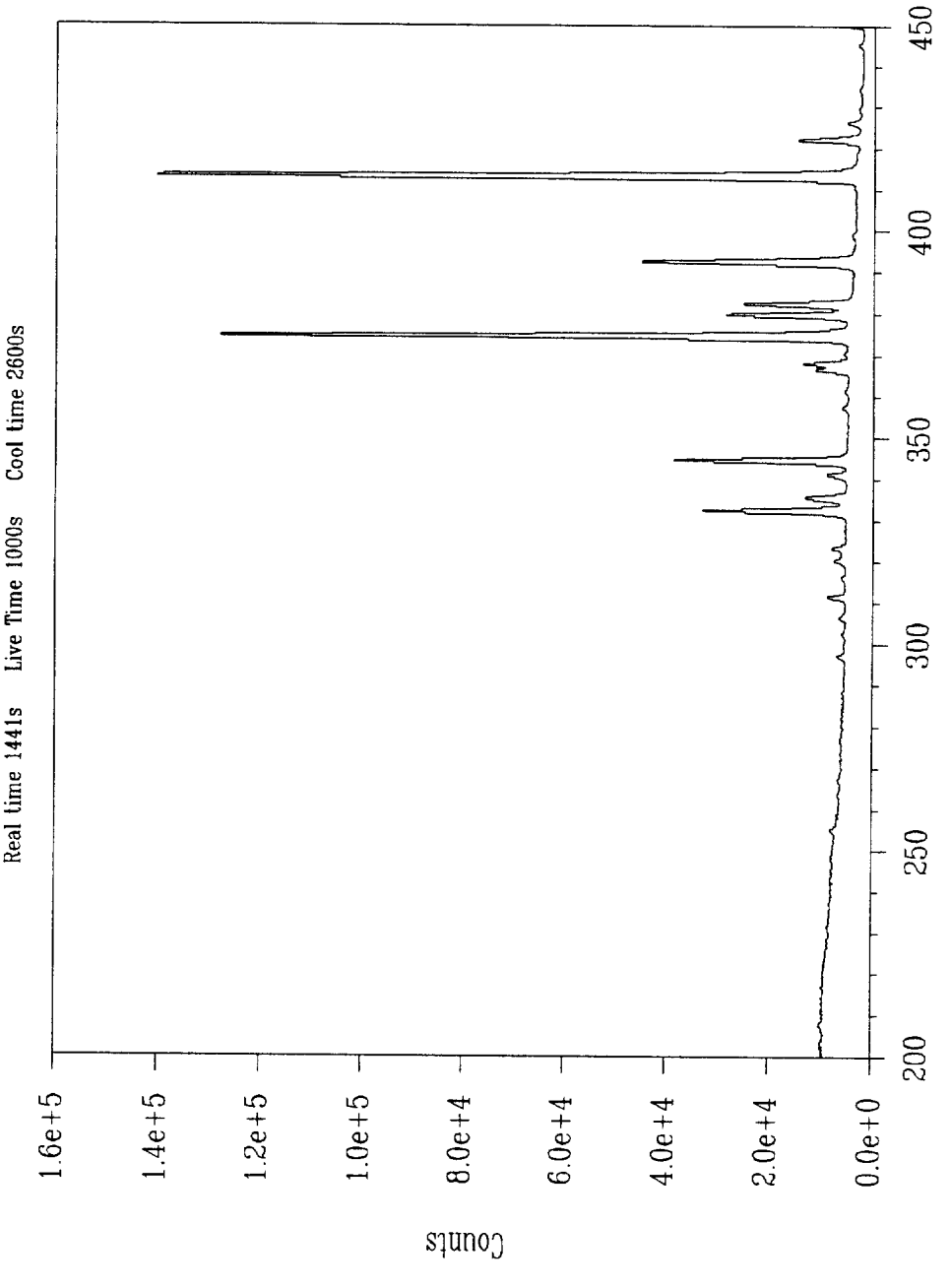

Figure C63. Pu-239 fission product gamma-ray spectrum from 200 - 450 keV

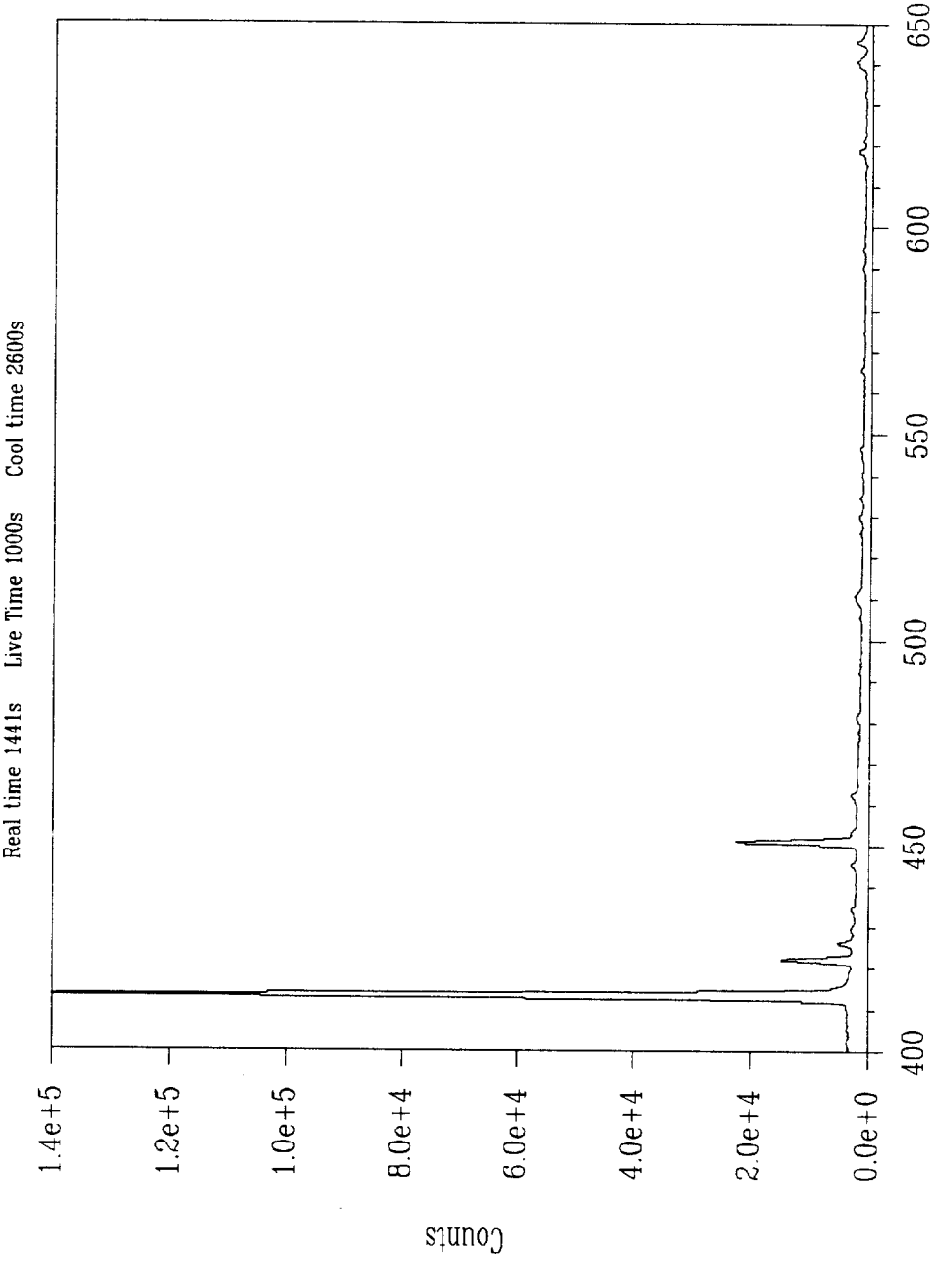

Figure C64. Pu-239 fission product gamma-ray spectrum from 400 - 650 keV

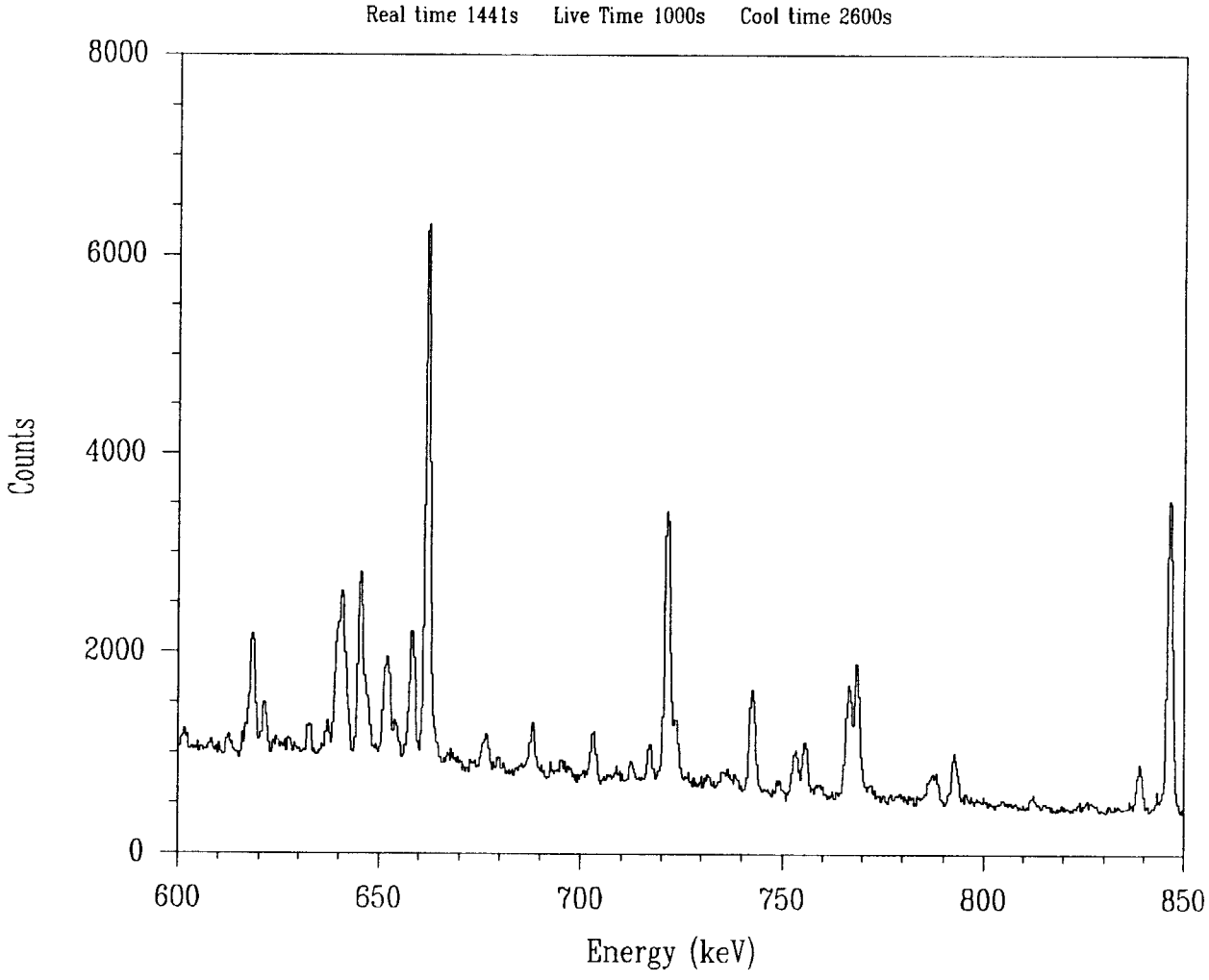

Figure C65. Pu-239 fission product gamma-ray spectrum from 600 - 850 keV

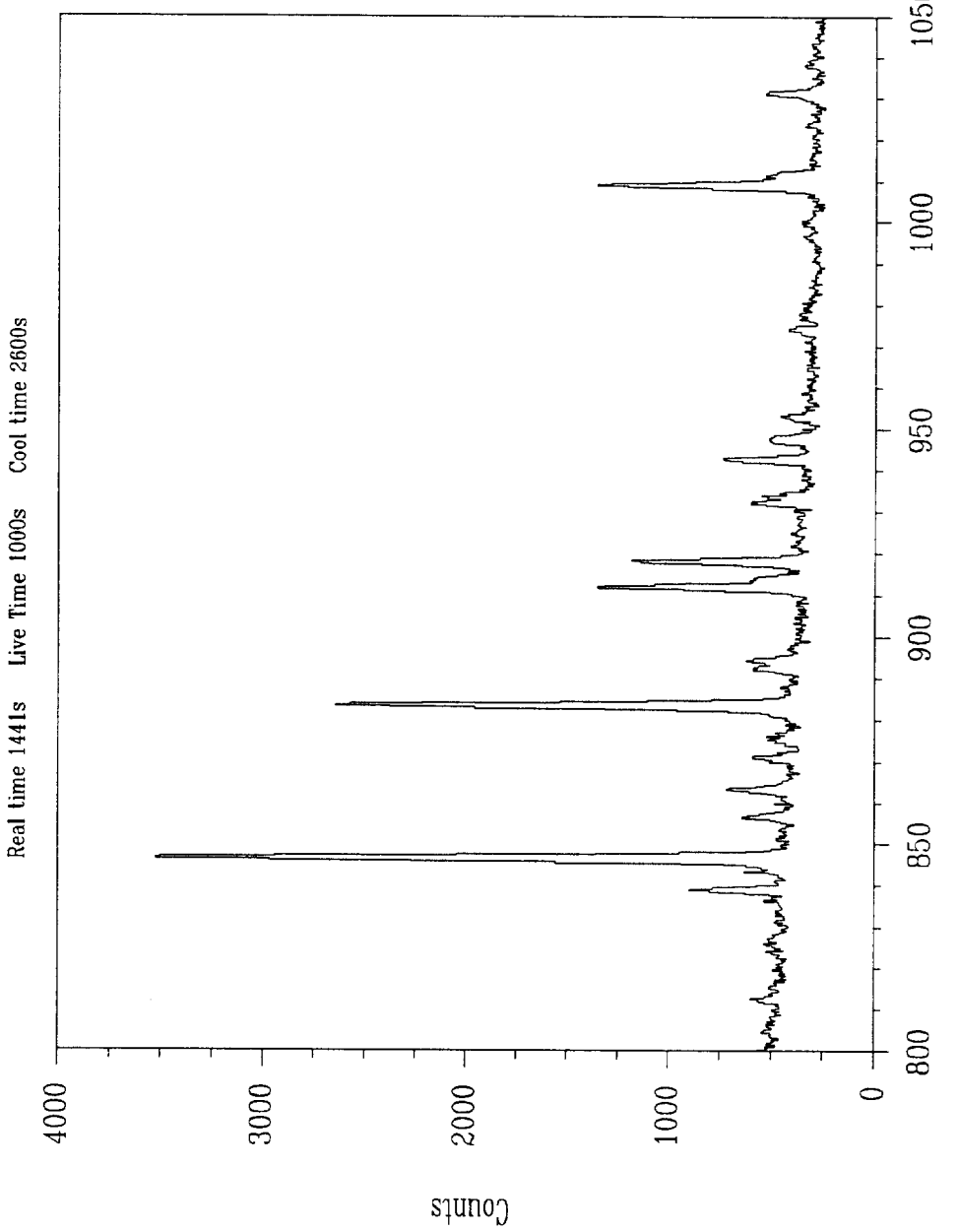

Figure C66. Pu-239 fission product gamma-ray spectrum from 800 - 1050 keV

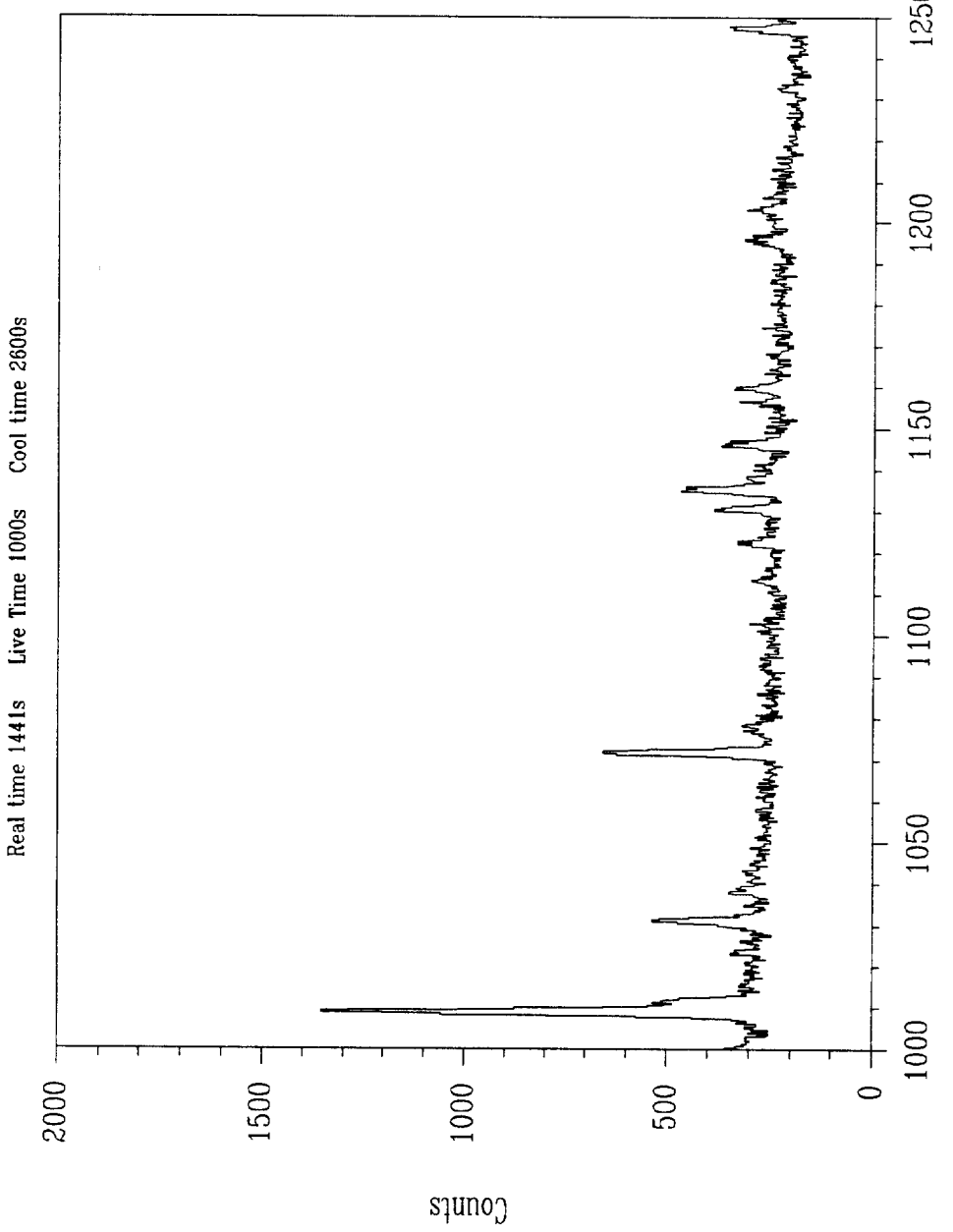

Figure C67. Pu-239 fission product gamma-ray spectrum from 1000 - 1250 keV

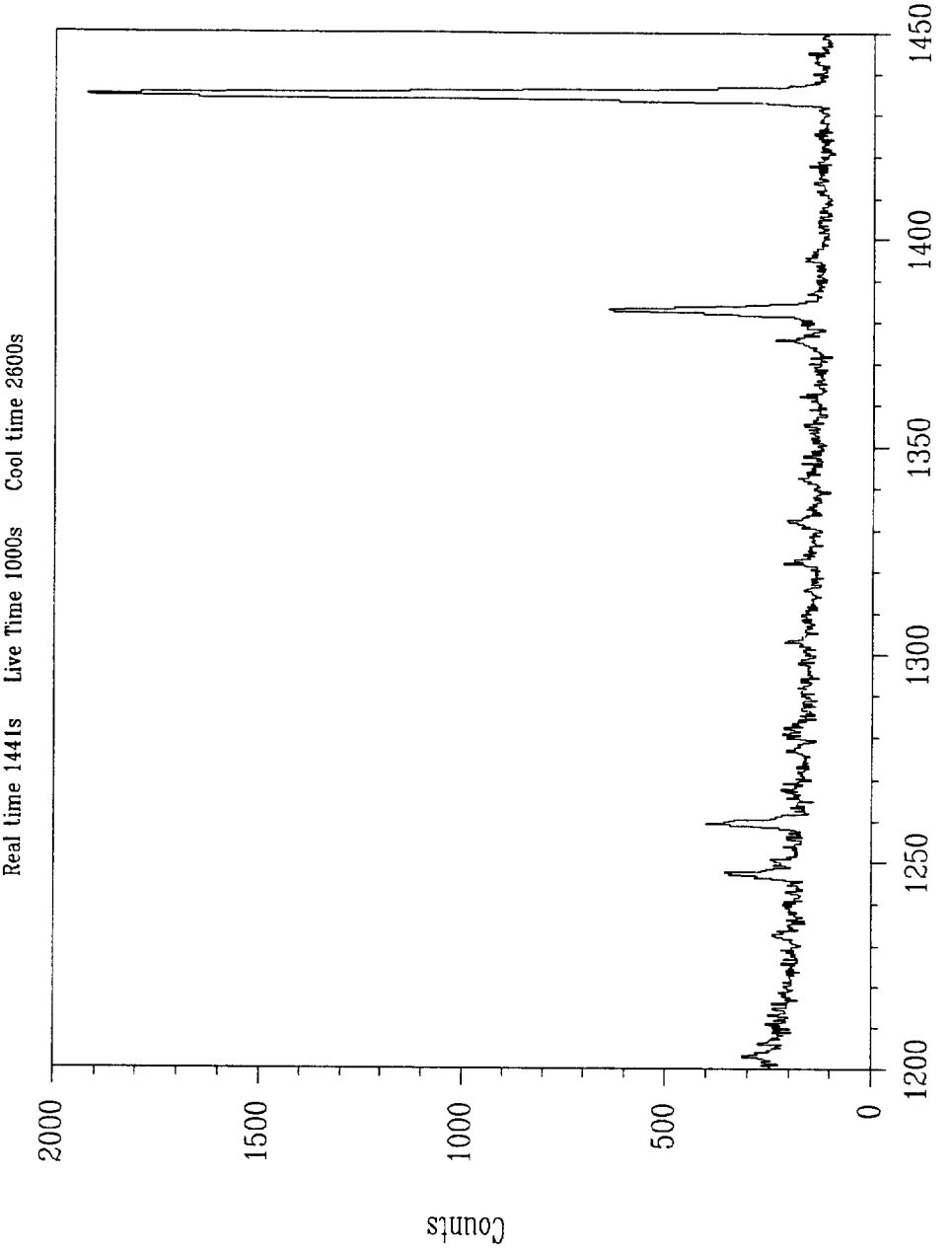

Figure C68. Pu-239 fission product gamma-ray spectrum from 1200 - 1450 keV

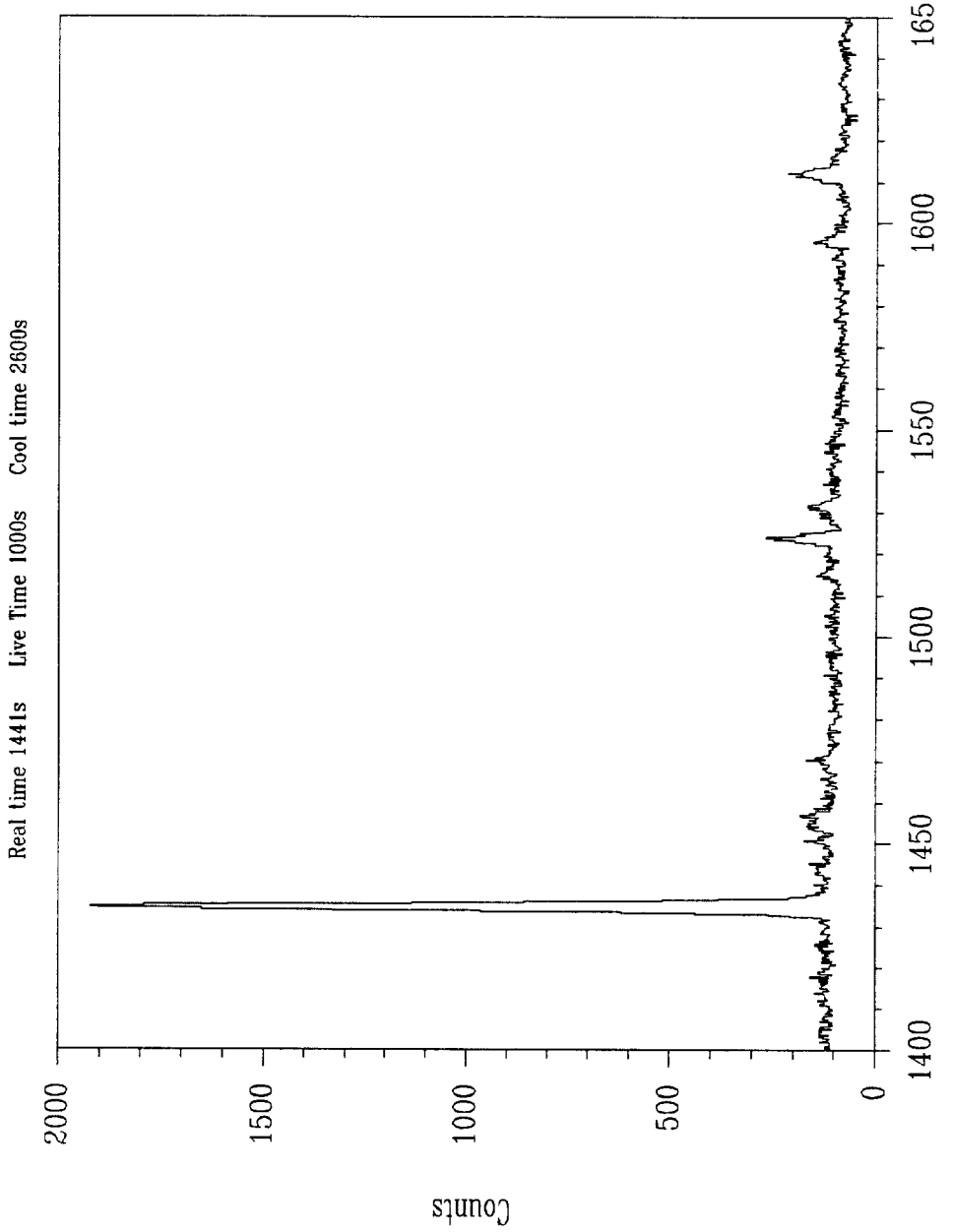

Figure C69. Pu-239 fission product gamma-ray spectrum from 1400 - 1650 keV

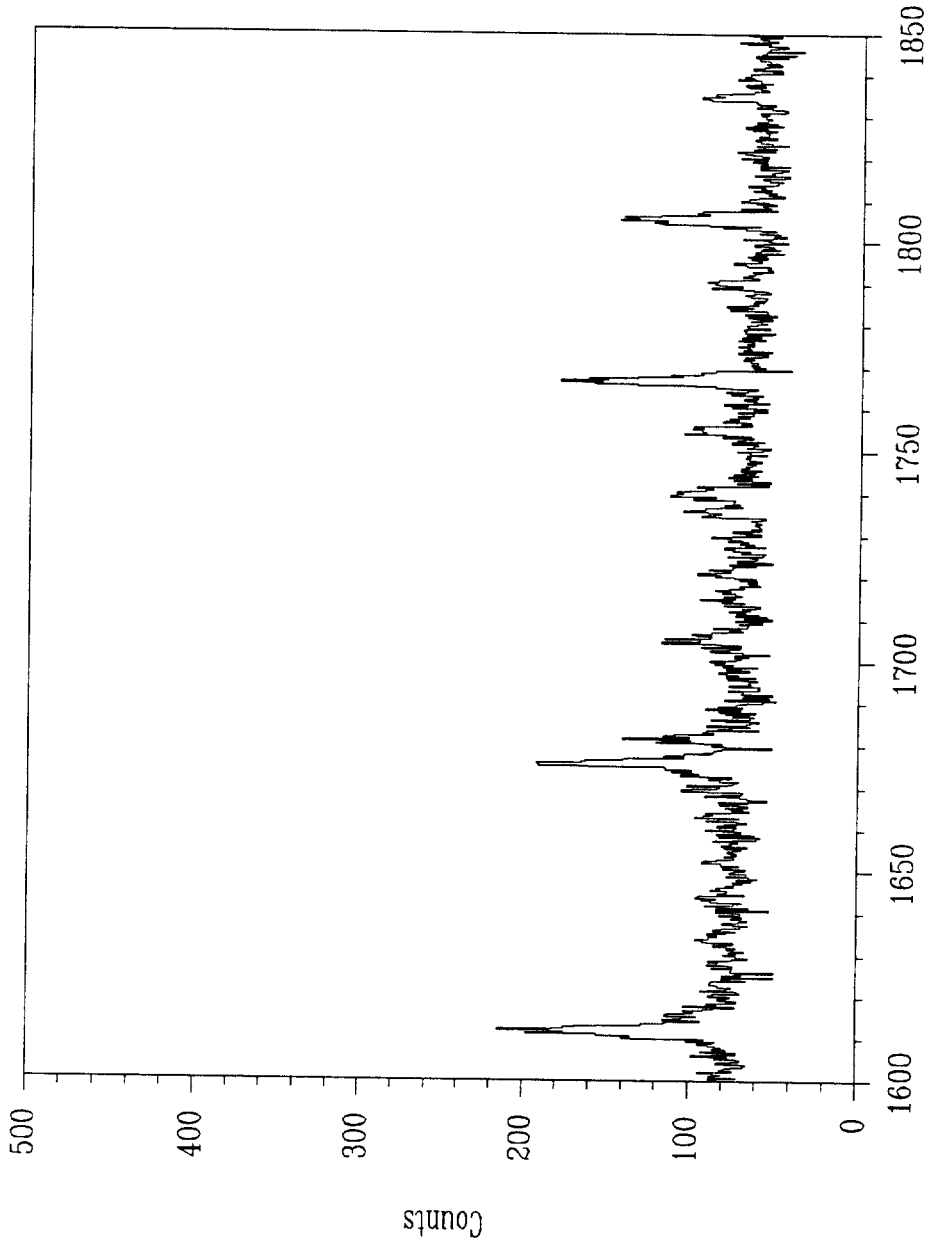

Figure C70. Pu-239 fission product gamma-ray spectrum from 1600 - 1850 keV

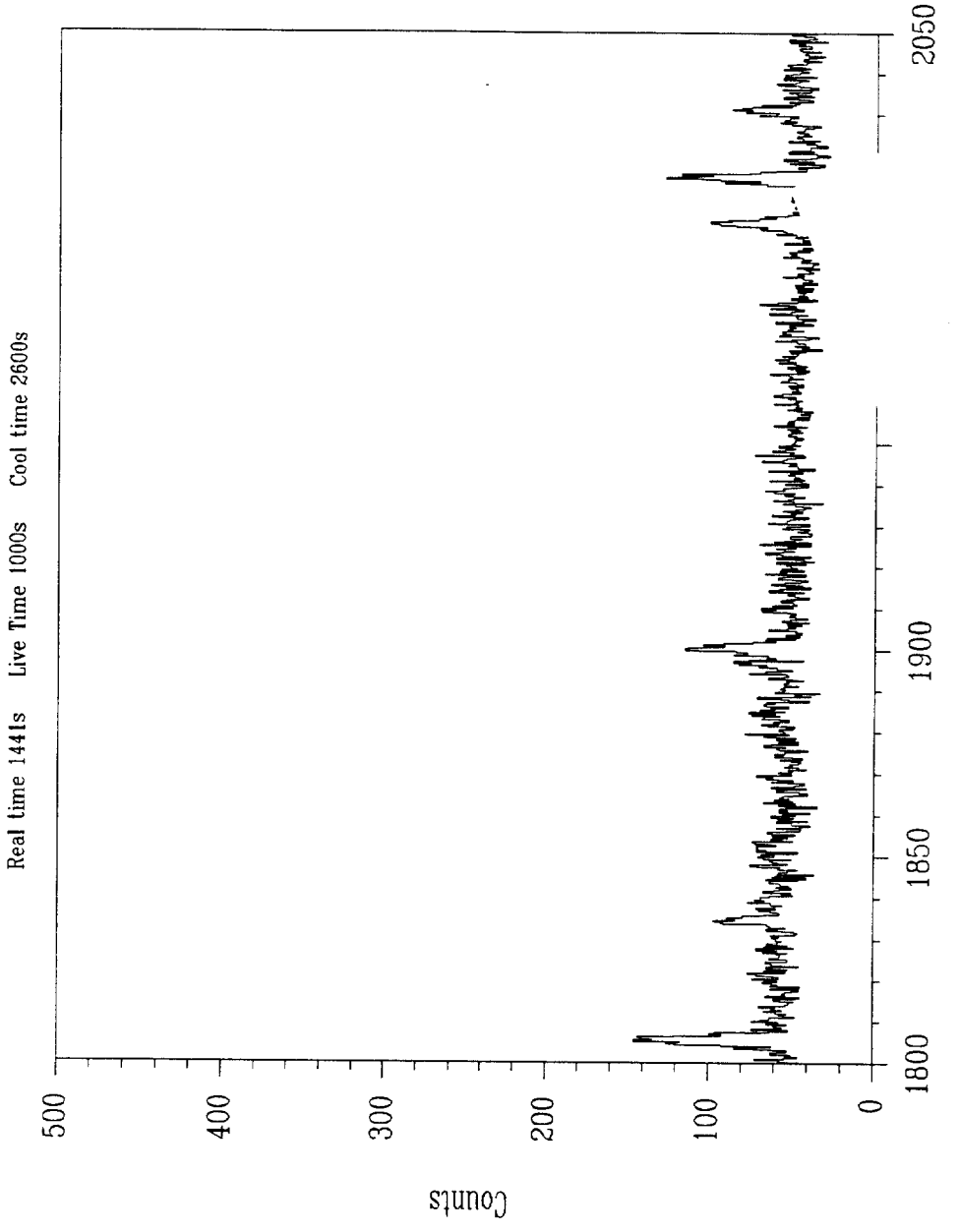

Figure C71. Pu-239 fission product ga

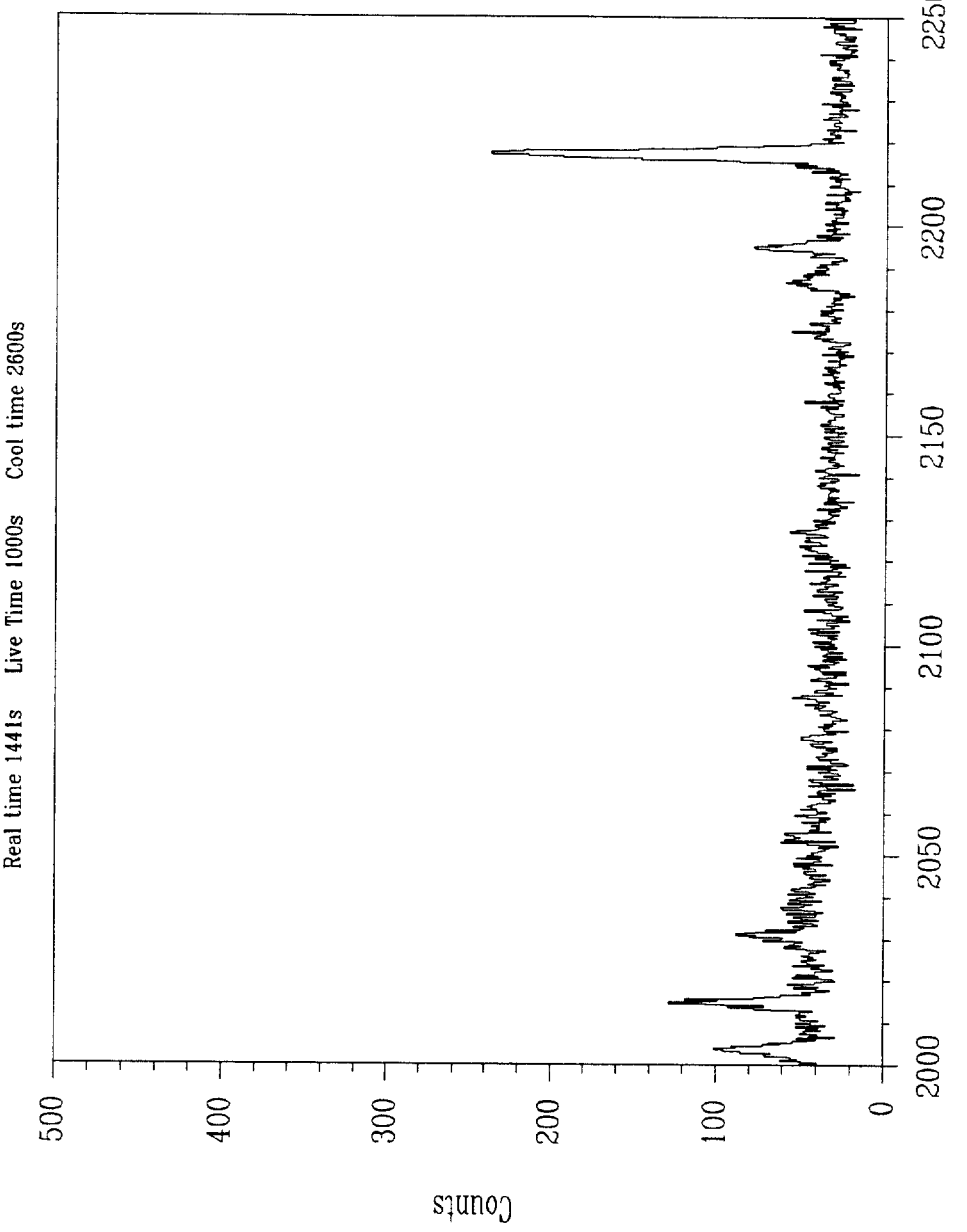

Figure C72. Pu-239 fission product gamma-ray spectrum from 2000 - 2250 keV

APPENDIX D

N_0 Correction Terms for Finite Irradiation Times

The following values should be used in place of the N_0 values in the serial decay equations from Appendix A when the irradiation period cannot be ignored. The decay scheme is the same as that depicted in Figure A1. These corrections accommodate the fact that the materials are decaying throughout their production.

It is helpful to introduce two functions to produce a more compact notation,

$$\alpha_X^0 \equiv 1 - \exp(-\lambda_X t_{irr}) \tag{D1}$$

and

$$\beta_{XY}^0 \equiv \frac{1}{\lambda_Y - \lambda_X}\left(\exp(-\lambda_X t_{irr}) - \exp(-\lambda_Y t_{irr})\right) \tag{D2}$$

where,

λ_X = the decay constant of isotope X,
t_{irr} = the irradiation time period.

The correction terms for isotope A are,

$$N_{A0} = f_{A1}^{IT} R_{A1}\left(\frac{\alpha_A^0}{\lambda_A} - \beta_{A1A}^0\right) + f_{A2}^{IT} R_{A2}\left(\frac{\alpha_A^0}{\lambda_A} - \beta_{A2A}^0\right) + R_A \frac{\alpha_A^0}{\lambda_A} \tag{D3}$$

$$N_{A10} = R_{A1} \frac{\alpha_{A1}^0}{\lambda_{A1}} \tag{D4}$$

and

$$N_{A20} = R_{A2}\frac{\alpha^{0}_{A2}}{\lambda_{A2}} \tag{D5}$$

where,

R_A, R_{A1}, R_{A2} = the production rate if isotopes A, A1 and A2 respectively, and other terms are as defined in Appendix A. The production rate of a given isotope is simply the fission rate times the fission yield of that isotope.

The correction terms for isotope B are,

$$\begin{aligned}
N_{B0} = {} & f_A^{\beta^-} f_{A1}^{IT} \lambda_A R_{A1}\left[\frac{1}{\lambda_A}\left(\frac{\alpha^{0}_{B}}{\lambda_B} - \beta^{0}_{AB}\right) - \left(\beta^{0}_{A1B} - \beta^{0}_{AB}\right)\right] \\
& + f_A^{\beta^-} f_{A2}^{IT} \lambda_A R_{A2}\left[\frac{1}{\lambda_A}\left(\frac{\alpha^{0}_{B}}{\lambda_B} - \beta^{0}_{AB}\right) - \left(\beta^{0}_{A2B} - \beta^{0}_{AB}\right)\right] \\
& + f_A^{\beta^-} R_A\left(\frac{\alpha^{0}_{B}}{\lambda_B} - \beta^{0}_{AB}\right) + f_{A1}^{\beta^-} R_{A1}\left(\frac{\alpha^{0}_{B}}{\lambda_B} - \beta^{0}_{A1A}\right) \\
& + f_{A2}^{\beta^-} R_{A2}\left(\frac{\alpha^{0}_{B}}{\lambda_B} - \beta^{0}_{A2B}\right) + f_{B1}^{IT} R_{B1}\left(\frac{\alpha^{0}_{B}}{\lambda_B} - \beta^{0}_{B1A}\right) \\
& + f_{B2}^{IT} R_{B2}\left(\frac{\alpha^{0}_{B}}{\lambda_B} - \beta^{0}_{B2B}\right) + R_B\frac{\alpha^{0}_{B}}{\lambda_B}
\end{aligned} \tag{D6}$$

$$N_{B10} = R_{B1}\frac{\alpha^{0}_{B1}}{\lambda_{B1}} \tag{D7}$$

and

$$N_{B20} = R_{B2}\frac{\alpha^0_{B2}}{\lambda_{B2}}. \tag{D8}$$

The correction terms for isotope C are,

$$\begin{aligned}
N_{C0} = {} & f_B^{\beta^-} f_A^{\beta^-} f_{A1}^{IT} \lambda_B R_{A1}\left[\frac{1}{\lambda_B}\left(\frac{\alpha^0_C}{\lambda_C} - \beta^0_{BC}\right) - \left(\beta^0_{AC} - \beta^0_{BC}\right)\right] \\
& - f_B^{\beta^-} f_A^{\beta^-} f_{A1}^{IT} \lambda_A \lambda_B R_{A1}\left[\left(\beta^0_{A1C} - \beta^0_{BC}\right) - \left(\beta^0_{AC} - \beta^0_{BC}\right)\right] \\
& + f_B^{\beta^-} f_A^{\beta^-} f_{A2}^{IT} \lambda_B R_{A2}\left[\frac{1}{\lambda_B}\left(\frac{\alpha^0_C}{\lambda_C} - \beta^0_{BC}\right) - \left(\beta^0_{AC} - \beta^0_{BC}\right)\right] \\
& - f_B^{\beta^-} f_A^{\beta^-} f_{A2}^{IT} \lambda_A \lambda_B R_{A2}\left[\left(\beta^0_{A2C} - \beta^0_{BC}\right) - \left(\beta^0_{AC} - \beta^0_{BC}\right)\right] \\
& + f_B^{\beta^-} f_A^{\beta^-} \lambda_B R_A\left[\frac{1}{\lambda_B}\left(\frac{\alpha^0_C}{\lambda_C} - \beta^0_{BC}\right) - \left(\beta^0_{AC} - \beta^0_{BC}\right)\right] \\
& + f_B^{\beta^-} f_{A1}^{\beta^-} \lambda_B R_{A1}\left[\frac{1}{\lambda_B}\left(\frac{\alpha^0_C}{\lambda_C} - \beta^0_{BC}\right) - \left(\beta^0_{A1C} - \beta^0_{BC}\right)\right] \\
& + f_B^{\beta^-} f_{A2}^{\beta^-} \lambda_B R_{A2}\left[\frac{1}{\lambda_B}\left(\frac{\alpha^0_C}{\lambda_C} - \beta^0_{BC}\right) - \left(\beta^0_{A2C} - \beta^0_{BC}\right)\right] \\
& + f_B^{\beta^-} f_{B1}^{IT} \lambda_B R_{B1}\left[\frac{1}{\lambda_B}\left(\frac{\alpha^0_C}{\lambda_C} - \beta^0_{BC}\right) - \left(\beta^0_{B1C} - \beta^0_{BC}\right)\right] \\
& + f_B^{\beta^-} f_{B2}^{IT} \lambda_B R_{B2}\left[\frac{1}{\lambda_B}\left(\frac{\alpha^0_C}{\lambda_C} - \beta^0_{BC}\right) - \left(\beta^0_{B2C} - \beta^0_{BC}\right)\right] \\
& + f_B^{\beta^-} R_B\left(\frac{\alpha^0_C}{\lambda_C} - \beta^0_{BC}\right) + f_{B1}^{\beta^-} R_{B1}\left(\frac{\alpha^0_C}{\lambda_C} - \beta^0_{B1C}\right) \\
& + f_{B2}^{\beta^-} R_{B2}\left(\frac{\alpha^0_C}{\lambda_B} - \beta^0_{B2C}\right) + f_{C1}^{IT} R_{C1}\left(\frac{\alpha^0_C}{\lambda_C} - \beta^0_{C1C}\right) \\
& + f_{C2}^{IT} R_{C2}\left(\frac{\alpha^0_C}{\lambda_C} - \beta^0_{C2C}\right) + R_C\frac{\alpha^0_C}{\lambda_C}
\end{aligned} \tag{D9}$$

$$N_{C10} = R_{C1}\frac{\alpha^{0}_{C1}}{\lambda_{C1}} \tag{D10}$$

and

$$N_{C20} = R_{C2}\frac{\alpha^{0}_{C2}}{\lambda_{C2}} \tag{D11}$$

The correction terms for isotope D are,

$$\begin{aligned}
N_{D0} = {} & f_C^{\beta-} f_B^{\beta-} f_A^{\beta-} f_{A1}^{IT} \lambda_C R_{A1}\left[\frac{1}{\lambda_C}\left(\frac{\alpha^0_D}{\lambda_D} - \beta^0_{CD}\right) - \left(\beta^0_{BD} - \beta^0_{CD}\right)\right] \\
& - f_C^{\beta-} f_B^{\beta-} f_A^{\beta-} f_{A1}^{IT} \lambda_B \lambda_C R_{A1}\left[\left(\beta^0_{AD} - \beta^0_{CD}\right) - \left(\beta^0_{BD} - \beta^0_{CD}\right)\right] \\
& - f_C^{\beta-} f_B^{\beta-} f_A^{\beta-} f_{A1}^{IT} \lambda_A \lambda_B \lambda_C R_{A1}\left[\left(\beta^0_{A1D} - \beta^0_{CD}\right) - \left(\beta^0_{BD} - \beta^0_{CD}\right)\right] \\
& + f_C^{\beta-} f_B^{\beta-} f_A^{\beta-} f_{A1}^{IT} \lambda_A \lambda_B \lambda_C R_{A1}\left[\left(\beta^0_{AD} - \beta^0_{CD}\right) - \left(\beta^0_{BD} - \beta^0_{CD}\right)\right] \\
& + f_C^{\beta-} f_B^{\beta-} f_A^{\beta-} f_{A2}^{IT} \lambda_C R_{A2}\left[\frac{1}{\lambda_C}\left(\frac{\alpha^0_D}{\lambda_D} - \beta^0_{CD}\right) - \left(\beta^0_{BD} - \beta^0_{CD}\right)\right] \\
& - f_C^{\beta-} f_B^{\beta-} f_A^{\beta-} f_{A2}^{IT} \lambda_B \lambda_C R_{A2}\left[\left(\beta^0_{AD} - \beta^0_{CD}\right) - \left(\beta^0_{BD} - \beta^0_{CD}\right)\right] \\
& - f_C^{\beta-} f_B^{\beta-} f_A^{\beta-} f_{A2}^{IT} \lambda_A \lambda_B \lambda_C R_{A2}\left[\left(\beta^0_{A2D} - \beta^0_{CD}\right) - \left(\beta^0_{BD} - \beta^0_{CD}\right)\right] \\
& + f_C^{\beta-} f_B^{\beta-} f_A^{\beta-} f_{A2}^{IT} \lambda_A \lambda_B \lambda_C R_{A2}\left[\left(\beta^0_{AD} - \beta^0_{CD}\right) - \left(\beta^0_{BD} - \beta^0_{CD}\right)\right] \\
& + f_C^{\beta-} f_B^{\beta-} f_A^{\beta-} \lambda_C R_A\left[\frac{1}{\lambda_C}\left(\frac{\alpha^0_D}{\lambda_D} - \beta^0_{CD}\right) - \left(\beta^0_{BD} - \beta^0_{CD}\right)\right] \\
& - f_C^{\beta-} f_B^{\beta-} f_A^{\beta-} \lambda_B \lambda_C R_A\left[\left(\beta^0_{AD} - \beta^0_{CD}\right) - \left(\beta^0_{BD} - \beta^0_{CD}\right)\right] \\
& + f_C^{\beta-} f_B^{\beta-} f_{A1}^{\beta-} \lambda_C R_{A1}\left[\frac{1}{\lambda_C}\left(\frac{\alpha^0_D}{\lambda_D} - \beta^0_{CD}\right) - \left(\beta^0_{BD} - \beta^0_{CD}\right)\right]
\end{aligned} \tag{D12}$$

$$
\begin{aligned}
&- f_C^{\beta^-} f_B^{\beta^-} f_{A1}^{\beta^-} \lambda_B \lambda_C R_{A1} \left[\left(\beta_{A1D}^0 - \beta_{CD}^0 \right) - \left(\beta_{BD}^0 - \beta_{CD}^0 \right) \right] \\
&+ f_C^{\beta^-} f_B^{\beta^-} f_{A2}^{\beta^-} \lambda_C R_{A2} \left[\frac{1}{\lambda_C} \left(\frac{\alpha_D^0}{\lambda_D} - \beta_{CD}^0 \right) - \left(\beta_{BD}^0 - \beta_{CD}^0 \right) \right] \\
&- f_C^{\beta^-} f_B^{\beta^-} f_{A2}^{\beta^-} \lambda_B \lambda_C R_{A2} \left[\left(\beta_{A1D}^0 - \beta_{CD}^0 \right) - \left(\beta_{BD}^0 - \beta_{CD}^0 \right) \right] \\
&+ f_C^{\beta^-} f_B^{\beta^-} f_{B1}^{IT} \lambda_C R_{B1} \left[\frac{1}{\lambda_C} \left(\frac{\alpha_D^0}{\lambda_D} - \beta_{CD}^0 \right) - \left(\beta_{BD}^0 - \beta_{CD}^0 \right) \right] \\
&- f_C^{\beta^-} f_B^{\beta^-} f_{B1}^{IT} \lambda_B \lambda_C R_{B1} \left[\left(\beta_{B1D}^0 - \beta_{CD}^0 \right) - \left(\beta_{BD}^0 - \beta_{CD}^0 \right) \right] \\
&+ f_C^{\beta^-} f_B^{\beta^-} f_{B2}^{IT} \lambda_C R_{B2} \left[\frac{1}{\lambda_C} \left(\frac{\alpha_D^0}{\lambda_D} - \beta_{CD}^0 \right) - \left(\beta_{BD}^0 - \beta_{CD}^0 \right) \right] \\
&- f_C^{\beta^-} f_B^{\beta^-} f_{B2}^{IT} \lambda_B \lambda_C R_{B2} \left[\left(\beta_{B2D}^0 - \beta_{CD}^0 \right) - \left(\beta_{BD}^0 - \beta_{CD}^0 \right) \right] \\
&+ f_C^{\beta^-} f_B^{\beta^-} \lambda_C R_B \left[\frac{1}{\lambda_C} \left(\frac{\alpha_D^0}{\lambda_D} - \beta_{CD}^0 \right) - \left(\beta_{BD}^0 - \beta_{CD}^0 \right) \right] \\
&+ f_C^{\beta^-} f_{B1}^{\beta^-} \lambda_C R_{B1} \left[\frac{1}{\lambda_C} \left(\frac{\alpha_D^0}{\lambda_D} - \beta_{CD}^0 \right) - \left(\beta_{B1D}^0 - \beta_{CD}^0 \right) \right] \\
&+ f_C^{\beta^-} f_{B2}^{\beta^-} \lambda_C R_{B2} \left[\frac{1}{\lambda_C} \left(\frac{\alpha_D^0}{\lambda_D} - \beta_{CD}^0 \right) - \left(\beta_{B2D}^0 - \beta_{CD}^0 \right) \right] \\
&+ f_C^{\beta^-} f_{C1}^{IT} \lambda_C R_{C1} \left[\frac{1}{\lambda_C} \left(\frac{\alpha_D^0}{\lambda_D} - \beta_{CD}^0 \right) - \left(\beta_{C1D}^0 - \beta_{CD}^0 \right) \right] \\
&+ f_C^{\beta^-} f_{C2}^{IT} \lambda_C R_{C2} \left[\frac{1}{\lambda_C} \left(\frac{\alpha_D^0}{\lambda_D} - \beta_{CD}^0 \right) - \left(\beta_{C2D}^0 - \beta_{CD}^0 \right) \right] \\
&+ f_C^{\beta^-} R_C \left(\frac{\alpha_D^0}{\lambda_D} - \beta_{CD}^0 \right) + f_{C1}^{\beta^-} R_{C1} \left(\frac{\alpha_D^0}{\lambda_D} - \beta_{C1D}^0 \right) \\
&+ f_{C2}^{\beta^-} R_{C2} \left(\frac{\alpha_D^0}{\lambda_D} - \beta_{C2D}^0 \right) + f_{D1}^{IT} R_{D1} \left(\frac{\alpha_D^0}{\lambda_D} - \beta_{D1D}^0 \right) \\
&+ f_{D2}^{IT} R_{D2} \left(\frac{\alpha_D^0}{\lambda_D} - \beta_{D2D}^0 \right) + R_D \frac{\alpha_D^0}{\lambda_D}
\end{aligned}
$$

$$
N_{D10} = R_{D1} \frac{\alpha_{D1}^0}{\lambda_{D1}} \tag{D13}
$$

and

$$N_{D20} = R_{D2}\frac{\alpha^{0}_{D2}}{\lambda_{D2}}. \qquad \textbf{(C14)}$$

The correction terms for isotope E are,

$$\begin{aligned}
N_{E0} = {} & f_D^{\beta^-} f_C^{\beta^-} f_B^{\beta^-} f_A^{\beta^-} f_{A1}^{IT} \lambda_D R_{A1}\left[\frac{1}{\lambda_D}\left(\frac{\alpha_E^0}{\lambda_E} - \beta^0_{DE}\right) - \left(\beta^0_{CE} - \beta^0_{DE}\right)\right] \\
& - f_D^{\beta^-} f_C^{\beta^-} f_B^{\beta^-} f_A^{\beta^-} f_{A1}^{IT} \lambda_C \lambda_D R_{A1}\left[\left(\beta^0_{BE} - \beta^0_{DE}\right) - \left(\beta^0_{CE} - \beta^0_{DE}\right)\right] \\
& - f_D^{\beta^-} f_C^{\beta^-} f_B^{\beta^-} f_A^{\beta^-} f_{A1}^{IT} \lambda_B \lambda_C \lambda_D R_{A1}\left[\left(\beta^0_{AE} - \beta^0_{DE}\right) - \left(\beta^0_{CE} - \beta^0_{DE}\right)\right] \\
& + f_D^{\beta^-} f_C^{\beta^-} f_B^{\beta^-} f_A^{\beta^-} f_{A1}^{IT} \lambda_B \lambda_C \lambda_D R_{A1}\left[\left(\beta^0_{BE} - \beta^0_{DE}\right) - \left(\beta^0_{CE} - \beta^0_{DE}\right)\right] \\
& - f_D^{\beta^-} f_C^{\beta^-} f_B^{\beta^-} f_A^{\beta^-} f_{A1}^{IT} \lambda_A \lambda_B \lambda_C \lambda_D R_{A1}\left[\left(\beta^0_{A1E} - \beta^0_{DE}\right) - \left(\beta^0_{CE} - \beta^0_{DE}\right)\right] \\
& + f_D^{\beta^-} f_C^{\beta^-} f_B^{\beta^-} f_A^{\beta^-} f_{A1}^{IT} \lambda_A \lambda_B \lambda_C \lambda_D R_{A1}\left[\left(\beta^0_{AE} - \beta^0_{DE}\right) - \left(\beta^0_{CE} - \beta^0_{DE}\right)\right] \\
& + f_D^{\beta^-} f_C^{\beta^-} f_B^{\beta^-} f_A^{\beta^-} f_{A2}^{IT} \lambda_D R_{A2}\left[\frac{1}{\lambda_D}\left(\frac{\alpha_E^0}{\lambda_E} - \beta^0_{DE}\right) - \left(\beta^0_{CE} - \beta^0_{DE}\right)\right] \\
& - f_D^{\beta^-} f_C^{\beta^-} f_B^{\beta^-} f_A^{\beta^-} f_{A2}^{IT} \lambda_C \lambda_D R_{A2}\left[\left(\beta^0_{BE} - \beta^0_{DE}\right) - \left(\beta^0_{CE} - \beta^0_{DE}\right)\right] \\
& - f_D^{\beta^-} f_C^{\beta^-} f_B^{\beta^-} f_A^{\beta^-} f_{A2}^{IT} \lambda_B \lambda_C \lambda_D R_{A2}\left[\left(\beta^0_{AE} - \beta^0_{DE}\right) - \left(\beta^0_{CE} - \beta^0_{DE}\right)\right] \\
& + f_D^{\beta^-} f_C^{\beta^-} f_B^{\beta^-} f_A^{\beta^-} f_{A2}^{IT} \lambda_B \lambda_C \lambda_D R_{A2}\left[\left(\beta^0_{BE} - \beta^0_{DE}\right) - \left(\beta^0_{CE} - \beta^0_{DE}\right)\right] \\
& - f_D^{\beta^-} f_C^{\beta^-} f_B^{\beta^-} f_A^{\beta^-} f_{A2}^{IT} \lambda_A \lambda_B \lambda_C \lambda_D R_{A2}\left[\left(\beta^0_{A2E} - \beta^0_{DE}\right) - \left(\beta^0_{CE} - \beta^0_{DE}\right)\right] \\
& + f_D^{\beta^-} f_C^{\beta^-} f_B^{\beta^-} f_A^{\beta^-} f_{A2}^{IT} \lambda_A \lambda_B \lambda_C \lambda_D R_{A2}\left[\left(\beta^0_{AE} - \beta^0_{DE}\right) - \left(\beta^0_{CE} - \beta^0_{DE}\right)\right] \\
& + f_D^{\beta^-} f_C^{\beta^-} f_B^{\beta^-} f_A^{\beta^-} R_A\left[\frac{1}{\lambda_D}\left(\frac{\alpha_E^0}{\lambda_E} - \beta^0_{DE}\right) - \left(\beta^0_{CE} - \beta^0_{DE}\right)\right] \\
& - f_D^{\beta^-} f_C^{\beta^-} f_B^{\beta^-} f_A^{\beta^-} \lambda_C R_A\left[\left(\beta^0_{BE} - \beta^0_{DE}\right) - \left(\beta^0_{CE} - \beta^0_{DE}\right)\right] \\
& - f_D^{\beta^-} f_C^{\beta^-} f_B^{\beta^-} f_A^{\beta^-} \lambda_B \lambda_C \lambda_D R_A\left[\left(\beta^0_{AE} - \beta^0_{DE}\right) - \left(\beta^0_{CE} - \beta^0_{DE}\right)\right] \\
& + f_D^{\beta^-} f_C^{\beta^-} f_B^{\beta^-} f_A^{\beta^-} \lambda_B \lambda_C \lambda_D R_A\left[\left(\beta^0_{BE} - \beta^0_{DE}\right) - \left(\beta^0_{CE} - \beta^0_{DE}\right)\right]
\end{aligned} \qquad \textbf{(D15)}$$

$$
\begin{aligned}
&+ f_D^{\beta-} f_C^{\beta-} f_B^{\beta-} f_{A1}^{\beta-} \lambda_D R_{A1} \left[\frac{1}{\lambda_D} \left(\frac{\alpha_E^0}{\lambda_E} - \beta_{DE}^0 \right) - \left(\beta_{CE}^0 - \beta_{DE}^0 \right) \right] \\
&- f_D^{\beta-} f_C^{\beta-} f_B^{\beta-} f_{A1}^{\beta-} \lambda_C \lambda_D R_{A1} \left[\left(\beta_{BE}^0 - \beta_{DE}^0 \right) - \left(\beta_{CE}^0 - \beta_{DE}^0 \right) \right] \\
&- f_D^{\beta-} f_C^{\beta-} f_B^{\beta-} f_{A1}^{\beta-} \lambda_B \lambda_C \lambda_D R_{A1} \left[\left(\beta_{A1E}^0 - \beta_{DE}^0 \right) - \left(\beta_{CE}^0 - \beta_{DE}^0 \right) \right] \\
&+ f_D^{\beta-} f_C^{\beta-} f_B^{\beta-} f_{A1}^{\beta-} \lambda_B \lambda_C \lambda_D R_{A1} \left[\left(\beta_{BE}^0 - \beta_{DE}^0 \right) - \left(\beta_{CE}^0 - \beta_{DE}^0 \right) \right] \\
&+ f_D^{\beta-} f_C^{\beta-} f_B^{\beta-} f_{A2}^{\beta-} \lambda_D R_{A2} \left[\frac{1}{\lambda_D} \left(\frac{\alpha_E^0}{\lambda_E} - \beta_{DE}^0 \right) - \left(\beta_{CE}^0 - \beta_{DE}^0 \right) \right] \\
&- f_D^{\beta-} f_C^{\beta-} f_B^{\beta-} f_{A2}^{\beta-} \lambda_C \lambda_D R_{A2} \left[\left(\beta_{BE}^0 - \beta_{DE}^0 \right) - \left(\beta_{CE}^0 - \beta_{DE}^0 \right) \right] \\
&- f_D^{\beta-} f_C^{\beta-} f_B^{\beta-} f_{A2}^{\beta-} \lambda_B \lambda_C \lambda_D R_{A2} \left[\left(\beta_{A2E}^0 - \beta_{DE}^0 \right) - \left(\beta_{CE}^0 - \beta_{DE}^0 \right) \right] \\
&+ f_D^{\beta-} f_C^{\beta-} f_B^{\beta-} f_{A2}^{\beta-} \lambda_B \lambda_C \lambda_D R_{A2} \left[\left(\beta_{BE}^0 - \beta_{DE}^0 \right) - \left(\beta_{CE}^0 - \beta_{DE}^0 \right) \right] \\
&+ f_D^{\beta-} f_C^{\beta-} f_B^{\beta-} f_{B1}^{IT} \lambda_D R_{B1} \left[\frac{1}{\lambda_D} \left(\frac{\alpha_E^0}{\lambda_E} - \beta_{DE}^0 \right) - \left(\beta_{CE}^0 - \beta_{DE}^0 \right) \right] \\
&- f_D^{\beta-} f_C^{\beta-} f_B^{\beta-} f_{B1}^{IT} \lambda_C \lambda_D R_{B1} \left[\left(\beta_{BE}^0 - \beta_{DE}^0 \right) - \left(\beta_{CE}^0 - \beta_{DE}^0 \right) \right] \\
&- f_D^{\beta-} f_C^{\beta-} f_B^{\beta-} f_{B1}^{IT} \lambda_B \lambda_C \lambda_D R_{B1} \left[\left(\beta_{B1E}^0 - \beta_{DE}^0 \right) - \left(\beta_{CE}^0 - \beta_{DE}^0 \right) \right] \\
&+ f_D^{\beta-} f_C^{\beta-} f_B^{\beta-} f_{B1}^{IT} \lambda_B \lambda_C \lambda_D R_{B1} \left[\left(\beta_{BE}^0 - \beta_{DE}^0 \right) - \left(\beta_{CE}^0 - \beta_{DE}^0 \right) \right] \\
&+ f_D^{\beta-} f_C^{\beta-} f_B^{\beta-} f_{B2}^{IT} \lambda_D R_{B2} \left[\frac{1}{\lambda_D} \left(\frac{\alpha_E^0}{\lambda_E} - \beta_{DE}^0 \right) - \left(\beta_{CE}^0 - \beta_{DE}^0 \right) \right] \\
&- f_D^{\beta-} f_C^{\beta-} f_B^{\beta-} f_{B2}^{IT} \lambda_C \lambda_D R_{B2} \left[\left(\beta_{BE}^0 - \beta_{DE}^0 \right) - \left(\beta_{CE}^0 - \beta_{DE}^0 \right) \right] \\
&- f_D^{\beta-} f_C^{\beta-} f_B^{\beta-} f_{B2}^{IT} \lambda_B \lambda_C \lambda_D R_{B2} \left[\left(\beta_{B2E}^0 - \beta_{DE}^0 \right) - \left(\beta_{CE}^0 - \beta_{DE}^0 \right) \right] \\
&+ f_D^{\beta-} f_C^{\beta-} f_B^{\beta-} f_{B2}^{IT} \lambda_B \lambda_C \lambda_D R_{B2} \left[\left(\beta_{BE}^0 - \beta_{DE}^0 \right) - \left(\beta_{CE}^0 - \beta_{DE}^0 \right) \right] \\
&+ f_D^{\beta-} f_C^{\beta-} f_B^{\beta-} \lambda_D R_B \left[\frac{1}{\lambda_D} \left(\frac{\alpha_E^0}{\lambda_E} - \beta_{DE}^0 \right) - \left(\beta_{CE}^0 - \beta_{DE}^0 \right) \right] \\
&- f_D^{\beta-} f_C^{\beta-} f_B^{\beta-} \lambda_C \lambda_D R_B \left[\left(\beta_{BE}^0 - \beta_{DE}^0 \right) - \left(\beta_{CE}^0 - \beta_{DE}^0 \right) \right] \\
&+ f_D^{\beta-} f_C^{\beta-} f_{B1}^{\beta-} \lambda_D R_{B1} \left[\frac{1}{\lambda_D} \left(\frac{\alpha_E^0}{\lambda_E} - \beta_{DE}^0 \right) - \left(\beta_{CE}^0 - \beta_{DE}^0 \right) \right] \\
&- f_D^{\beta-} f_C^{\beta-} f_{B1}^{\beta-} \lambda_C \lambda_D R_{B1} \left[\left(\beta_{B1E}^0 - \beta_{DE}^0 \right) - \left(\beta_{CE}^0 - \beta_{DE}^0 \right) \right] \\
&+ f_D^{\beta-} f_C^{\beta-} f_{B2}^{\beta-} \lambda_D R_{B2} \left[\frac{1}{\lambda_D} \left(\frac{\alpha_E^0}{\lambda_E} - \beta_{DE}^0 \right) - \left(\beta_{CE}^0 - \beta_{DE}^0 \right) \right]
\end{aligned}
$$

$$
\begin{aligned}
&- f_D^{\beta^-} f_C^{\beta^-} f_{B2}^{\beta^-} \lambda_C \lambda_D R_{B2} \left[\left(\beta_{B2E}^0 - \beta_{DE}^0 \right) - \left(\beta_{CE}^0 - \beta_{DE}^0 \right) \right] \\
&+ f_D^{\beta^-} f_C^{\beta^-} f_{C1}^{IT} \lambda_D R_{C1} \left[\frac{1}{\lambda_D} \left(\frac{\alpha_E^0}{\lambda_E} - \beta_{DE}^0 \right) - \left(\beta_{CE}^0 - \beta_{DE}^0 \right) \right] \\
&- f_D^{\beta^-} f_C^{\beta^-} f_{C1}^{IT} \lambda_C \lambda_D R_{C1} \left[\left(\beta_{C1E}^0 - \beta_{DE}^0 \right) - \left(\beta_{CE}^0 - \beta_{DE}^0 \right) \right] \\
&+ f_D^{\beta^-} f_C^{\beta^-} f_{C2}^{IT} \lambda_D R_{C2} \left[\frac{1}{\lambda_D} \left(\frac{\alpha_E^0}{\lambda_E} - \beta_{DE}^0 \right) - \left(\beta_{CE}^0 - \beta_{DE}^0 \right) \right] \\
&- f_D^{\beta^-} f_C^{\beta^-} f_{C2}^{IT} \lambda_C \lambda_D R_{C2} \left[\left(\beta_{C2E}^0 - \beta_{DE}^0 \right) - \left(\beta_{CE}^0 - \beta_{DE}^0 \right) \right] \\
&+ f_D^{\beta^-} f_C^{\beta^-} \lambda_D R_C \left[\frac{1}{\lambda_D} \left(\frac{\alpha_E^0}{\lambda_E} - \beta_{DE}^0 \right) - \left(\beta_{CE}^0 - \beta_{DE}^0 \right) \right] \\
&+ f_D^{\beta^-} f_{C1}^{\beta^-} \lambda_D R_{C1} \left[\frac{1}{\lambda_D} \left(\frac{\alpha_E^0}{\lambda_E} - \beta_{DE}^0 \right) - \left(\beta_{C1E}^0 - \beta_{DE}^0 \right) \right] \\
&+ f_D^{\beta^-} f_{C2}^{\beta^-} \lambda_D R_{C2} \left[\frac{1}{\lambda_D} \left(\frac{\alpha_E^0}{\lambda_E} - \beta_{DE}^0 \right) - \left(\beta_{C2D}^0 - \beta_{DE}^0 \right) \right] \\
&+ f_D^{\beta^-} f_{D1}^{IT} \lambda_D R_{D1} \left[\frac{1}{\lambda_D} \left(\frac{\alpha_E^0}{\lambda_E} - \beta_{DE}^0 \right) - \left(\beta_{D1E}^0 - \beta_{DE}^0 \right) \right] \\
&+ f_D^{\beta^-} f_{D2}^{IT} \lambda_D R_{D2} \left[\frac{1}{\lambda_D} \left(\frac{\alpha_E^0}{\lambda_E} - \beta_{DE}^0 \right) - \left(\beta_{D2E}^0 - \beta_{DE}^0 \right) \right] \\
&+ f_D^{\beta^-} R_D \left(\frac{\alpha_E^0}{\lambda_E} - \beta_{DE}^0 \right) + f_{D1}^{\beta^-} R_{D1} \left(\frac{\alpha_E^0}{\lambda_E} - \beta_{D1E}^0 \right) \\
&+ f_{D2}^{\beta^-} R_{D2} \left(\frac{\alpha_E^0}{\lambda_E} - \beta_{D2E}^0 \right) + f_{E1}^{IT} R_{E1} \left(\frac{\alpha_E^0}{\lambda_E} - \beta_{E1E}^0 \right) \\
&+ f_{E2}^{IT} R_{E2} \left(\frac{\alpha_E^0}{\lambda_E} - \beta_{E2E}^0 \right) + R_E \frac{\alpha_E^0}{\lambda_E}
\end{aligned}
$$

$$
N_{D10} = R_{D1} \frac{\alpha_{D1}^0}{\lambda_{D1}} \tag{D16}
$$

and

$$N_{E20} = R_{E2} \frac{\alpha^{0}_{E2}}{\lambda_{E2}}. \qquad \text{(D17)}$$